THERMALLY MODULATED FIBER SORBENTS FOR RAPIDLY CYCLED VACUUM-PRESSURE SWING ADSORPTION OF POST-COMBUSTION FLUE GAS

A Dissertation
Presented to
The Academic Faculty

by

Stephen J. A. DeWitt

In Partial Fulfillment
of the Requirements for the Degree
Doctor of Philosophy in the
School of Chemical and Biomolecular Engineering

Georgia Institute of Technology
December 2020

THERMALLY MODULATED FIBER SORBENTS FOR RAPIDLY CYCLED VACUUM-PRESSURE SWING ADSORPTION OF POST-COMBUSTION FLUE GAS

Approved by:

Dr. Ryan P. Lively, Advisor
School of Chemical & Biomolecular Engineering
Georgia Institute of Technology

Dr. Christopher W. Jones
School of Chemical & Biomolecular Engineering
Georgia Institute of Technology

Dr. David S. Sholl
School of Chemical & Biomolecular Engineering
Georgia Institute of Technology

Dr. Matthew J. Realff
School of Chemical & Biomolecular Engineering
Georgia Institute of Technology

Dr. Angus P. Wilkinson
School of Chemistry and Biochemistry
Georgia Institute of Technology

Dr. Pradeep Agrawal
Department of Chemical Engineering
Michigan Technological Institute

Date Approved: October 26th, 2020

To my family, for without their support none of this could be possible.

ACKNOWLEDGEMENTS

There are more people than I could probably list to whom I owe a great deal of thanks for their friendship and support throughout my life. While this document is the culmination of my past five years' work, this work was only possible because of a million different interactions with probably numerous people over my life. To all those people, whether directly acknowledged here or not, I say thank you.

To my advisor, Dr. Ryan Lively, thank you, first and foremost, for the opportunity to work with you on so many interesting problems. I'm not sure I have ever met someone with the combination of patience and unbridled joy for everything he does, characteristics that will always inspire me to better myself. I'm equally unsure how many advisors who could simply take in stride the number of times I just stopped by your office unannounced to talk through a challenge I was running into that day, a dumb off the wall research idea, or a random thing that happened in sports the night before. I'll always be grateful for your ability to pass on your passion for solving big problems to myself and the entire group, particularly allowing me to learn how to take the spark of an idea and turn it into a reality. There is no way I could have imagined when I joined the group the kind of person I'd develop into, and that would have been, without a doubt, impossible without you.

Thanks to the members of the Lively Lab, past and present, for inspiring me to always reach for more. To Melinda, Brian, and Erkang for building the lab. I am deeply indebted to Simon for being the kind of person to always make time to talk, even when its 9 PM on a Tuesday, and this annoying first year keeps talking. Many people have taught me about selflessness over the years. Still, your mentorship of me embodied a spirit of

selflessness I aspire to achieve one day. To Dong-Yeun, Guanghui, Eric, Yao, Achintya, Fengyi, Richelle, Leo, and Yun-Ho for showing me the breath and adaptability required of a great researcher. My thanks to Ronita for having the patience to talk through numerous small things and "not a big deal, buts do you think we could change this?'s." I owe a great deal to Conrad for innumerable coffees and conversations and being the first person to let me learn how to be a mentor. To Matt and Isaiah for going to random baseball games and tailgates and putting up with my Boston sports fandom. My thanks to Chunyi, Younghee, Pavithra, Hannah, Haley, Yi, Youngjoo, and Yacine, for their excitement as they just get started. As an older student who has a tendency to think he has it all figured out, seeing that new energy approaching these problems is humbling and inspiring.

I'd be remiss if I waited any longer to thank Andrew Alves for being the person to know me well enough to always call me out when I am full of it, regardless of the situation. I guess that happens when you have known someone since they were 10. Still, I'd have never survived this without the almost daily discussions about whatever is happening in the world. Having a friend that you can talk to about everything, without worrying about a filter, is one of many things I am grateful to you for.

I am indebted to innumerable individuals at Georgia Tech and across the world for numerous research discussions. Among them, I'd like to thank Eli, Krishna, and Professor Jones for their ability to rapidly switch between talking about research and talking about sports. My thanks to Adam and Matt for putting up with my imposter syndrome. To my committee members and the CryoMOF project team for their ideas and support throughout this work. To the many people I met across the country and world at conferences, particularly Aaron, Eugene, Rebecca, Max, and Eric, for continuing that relationship once

we all got back to work, from discussing entropy at 11 PM, or how to overcome a weird thing we're running into in an experiment.

I said there are more people than I could ever list at the beginning, and I am about to start the third page. I owe a great deal to the mentors who continue to inspire me even after I have moved miles away, and friends who continue to support me. To Professors Maase, White, and Dissinger for their incredible support of my academic development while at Lowell. At the same time, I have to mention Greg, CiCi, Mike, Liz, Neha, Ben, Daveed, Zoe, and countless others who struggled with me during that academic development. To Ray Morrison, Mike Bryant, George Dionne, Brian Lobao, Ernie Bostwick, and Dave McMenemey for their mentorship and guidance in Scouting, and to Bobby, Cam, Kevin, Zach, and Brian for inspiring me to never stop growing as a leader. KTSA.

Finally, to my parents and sister, for more than I could ever list on paper. Their guidance, sacrifices, and loving support for me in all that I do are, without a doubt, the most important things to any successes I have ever had or will ever have. To my Mom for putting up with what is probably hundreds of hours (and counting) of me just pacing (and procrastinating) at the edge of her bed to figure out what I would do next. To my Dad, for always being able to approach all problems in the most controlled manner, and challenging me to improve and be better. To Carolynn for being the kind of person to message out of the blue just to make sure I am doing ok 1500 miles from home, for making time for breakfasts and/or (usually and) ice cream whenever I did come home.

TABLE OF CONTENTS

LIST OF TABLES

LIST OF FIGURES

LIST OF SYMBOLS AND ABBREVIATIONS

Letters and letter-like symbols

$\mathit{\Delta H}$	Heat of Adsorption	[kJ/mol]
c	BET Constant, concentration in gas phase	[-]
C	Concentration or composition	[mol/mol]
C_s, C_f	Heat Capacity of Solid and Fluid phase	[J K^{-1}]
m	Mass of sorbent	[grams]
n^A	Total moles of gas in stream A	[moles]
n_i^A	Total moles of component i in stream A	[moles]
P	Pressure	[bar]
q	uptake	
R	Ideal Gas Constant	[J mol^{-1} K^{-1}]
T	Temperature	[K]
t_{cycle}	PSA Cycle Time	[seconds]
V, v	Quantity of gas adsorbed, volume	[ccSTP]
y_i^A	Average mole fraction of component i in stream A	[-]

Superscripts and Subscripts

0   Initial or inlet

BD   Relating to the blowdown step of the PSA

Evac   Relating to the evacuation step of the PSA

F-in   Relating to the inlet stream of the Feed step of the PSA

F-out   Relating to the outlet stream of the Feed step of the PSA

m   molar

P   Relating to the pressurization step of the PSA

q   Uptake, at constant uptake

Greek Symbols

Δ Difference, Change in

η Dimensionless thermal front to Mass front velocity

SUMMARY

The continued rise in the concentration of CO_2 in the Earth's atmosphere driven by society's rising standard of living and continued reliance on carbon-containing fossil fuels has led to several significant environmental challenges, which will continue to face humanity in the coming decades and centuries. Developing technological solutions to accelerate the reduction of carbon dioxide emissions and curtail the effects of climate change will continue to serve one of the critical directions society will pursue to combat these effects. The capture of CO_2 from point sources like coal-fired power plants will likely be a direction for the short and long-term reduction in emissions needed to stabilize the environment. With this in mind, developing technologies to serve this purpose with the least impact on people's way of life serves as a critical challenge over the coming decades.

The removal of CO_2 from point sources has been an area of interest for a number of years now, with absorption technology appears best suited to make an immediate impact with pilot and full-scale plants currently being built. In the future, methods of separating and capturing CO_2 will look to technologies with the potential to be considerably lower energy requirements, like adsorption and membranes, and these are still in the early stages of development. While these approaches lag behind absorption in technology readiness for CO_2 capture today, the potential impact of their adoption in terms of cost reduction has led to considerable research investment in developing new materials and processes to enable their application. In this dissertation, a novel strategy is proposed, and materials are developed to enable the proposed process for post-combustion CO_2 capture from coal. As part of this dissertation, four objectives were pursued to understand and enable this process.

i) A process model was created and studied to develop a deeper understanding of the approach's potential and the necessary materials developments to enable it. **ii)** Promising materials were synthesized and manufactured into ready-made devices for bench-scale testing. **iii)** Fundamental challenges of adsorptive separations related to heat management were considered in detail, and a novel manufacturing approach was developed to enable improvement in materials performance. **iv)** The potential of fiber sorbents for sub-ambient CO_2 capture was examined through the operation of single bed PSA cycles using the manufactured materials from previous objectives.

The first objective showed that a sub-ambient pressure-driven separation process, coupled with downstream liquefaction, could be used without the need for external refrigeration. Excess low-quality cooling could also be used for the dehydration of the flue gas, a key challenge facing adsorptive CO_2 capture. This process would be significantly limited by its capital costs, consistent with expectation. Regardless of the separation considered, the capital and energy costs of pre- and post-treatment of CO_2 lead to costs of CO_2 capture exceeding \$47/tonne$_{CO2}$, and the best case study of sub-ambient pressure swing adsorption led to costs of capture around \$60/tonne$_{CO2}$. Preliminary analysis shows a more complicated process, where the post-treatment liquefaction is removed or replaced with a low-cost membrane or adsorbent system that could allow for additional cost reductions.

The second objective focused on the production and spinning of MOF fiber sorbents, which showed the potential, in simulation, when combined with the work from objective 3 to reach 8-10x the performance of traditional pellet packed bed systems. Work here focused on the development of scale-up and manufacture of multiple MOF fiber

sorbents, overcoming challenges in dope composition formulation and particle size resulting in sorbent leaching not previously reported in fiber sorbent spinning.

The third objective focused on the development of a passive internal heat management strategy for pressure swing adsorption in the fiber sorbent morphology. Microencapsulated phase change materials were, for the first time, incorporated into fiber sorbents in the spinning step, allowing for a reduction in the manufacturing complexity of heat management in PSA systems. A 20-25% improvement in the breakthrough capacity of the sorbent and 30-40% reduction in amplitude of the thermal front prove the manufacturing process works and will enable more efficient sorbent performance.

The final objective looked at the operation of a pressure swing adsorption unit for the removal of CO_2 from simulated flue gas within the sub-ambient process framework. MOF fiber sorbents with and without phase change materials were compared in terms of the tradeoffs between purity, recovery, and CO_2 productivity. This preliminary analysis showed there was much potential for sub-ambient CO_2 capture, with productivities as high as 0.01 mol kg^{-1} sec^{-1} achieved using MOF fibers. Due to the single bed cycles used in these experiments, the recovery of the system suffered (never exceeding 45%), but future work focused on optimizing more complex cycles should allow for improvements in this area. Thermally modulated fiber adsorbents were also considered in the sub-ambient PSA system, showing higher purities and productivities than fibers without heat management at comparable recovery levels.

CHAPTER 1.   INTRODUCTION

1.1   Carbon Capture as a Solution to Global Climate Change

The rising concentration of CO_2, driven by emissions due to human industrialization, has widely been related to the Earth's increasing temperatures. **Figure 1-1** shows this relationship simply; since industrialization, we have seen ever-increasing concentrations in the atmosphere, which offer a good correlation with a disturbing increase in the Earth's temperatures.
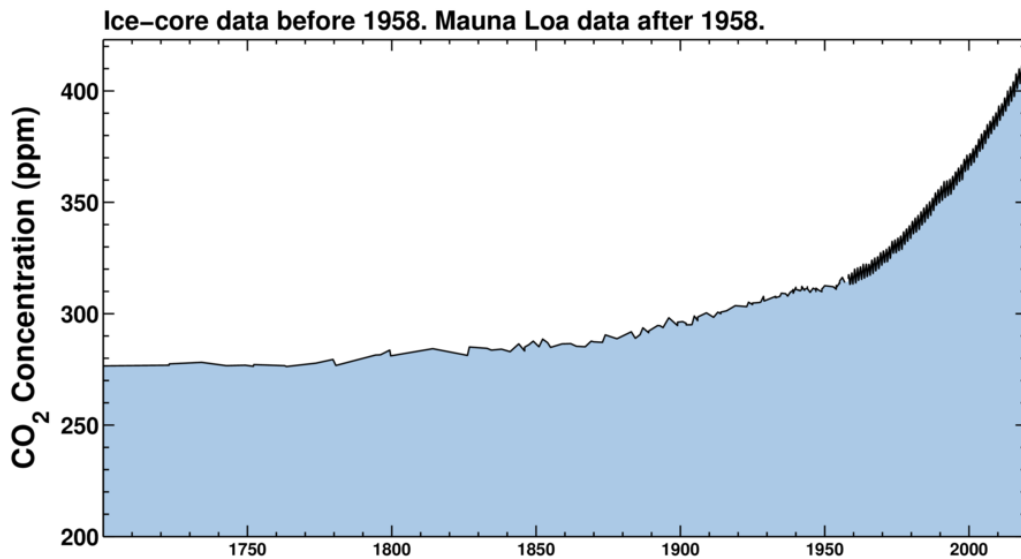
Figure 1-1. Keeling Curve of CO_2 Concentration in the atmosphere since 1700 AD. Reprinted with permission of Scripps Institution of Oceanography[1-2]

Sokolow and Pacala, noting this relationship, stated the solution to such a complex problem would not come as one societal change or technological advancement. Instead, many actions (both societal and technological) would be required to combat the issue of the world carbon emissions.[3] Fifteen decisions/technologies/changes were identified, each considering 1 million tons of carbon removed from world emissions per year (e.g., 1

million in year 1, 2 million in year two), which, if implemented, would act as a single "wedge." Had eight of these wedges been enacted at the time and enacted over the next 50 years, they projected global emissions would be stabilized, and the effects of global climate change could be curtailed. In the time since, additional stabilization wedges have been identified, but progress and commitment have lagged behind need.

While the developed world has made considerable inroads on curtailing global climate change in their communities (ex. Natural gas prices enabling widespread *fuel switching* in the US electrical grid, several policies across the European Union including more stringent fuel standards for vehicles), four global carbon emissions continue to rise due to industrial and quality of life improvements in the developing world.[4-5] These countries (China, India, Indonesia, and eventually, African nations) make up the vast majority of the world's population. One must imagine their development to a similar quality of life to that of western countries will entail the adoption of the same sorts of carbon-emitting technologies the developed world has already used to reach the quality of life we demand. With that understanding, it stands as a significant challenge to the global community, especially the scientific community, to develop new policies and technologies to enable their industrialization while keeping within the environmental needs of the Earth.

Returning to Sokolow's wedges, acknowledging these challenges the world community faces, it may prove imperative to identify the wedges that can both be adopted in the developed world but also in the developing world to limit carbon emissions. A number of the wedges may be considered in this context, but for this dissertation, the focus centers on one in particular: the capture of 90% of CO_2 from coal-fired power plants. While the US may be moving away from coal as the economical choice of fuel, coal still appears

to be the cheapest and most available form of energy in many nations worldwide, particularly China.

1.2   Methods of Carbon Capture From Point Sources

Three primary process approaches have been considered as methods of removing CO_2 from a coal-fired power plant.[6-8] These paths to energy production follow a similar general process scheme, coal, air, makeup water enter the system as inputs, electricity leaves the system as an output, along with some concentration of CO_2, O_2, N_2, water, and other trace byproducts. **Figure 1-2** gives this fundamental high-level viewpoint, along with the three methods more precisely. The three process approaches include post-combustion capture of CO_2 from flue gas, pre-combustion, or gasification of coal, oxy-fired combustion.
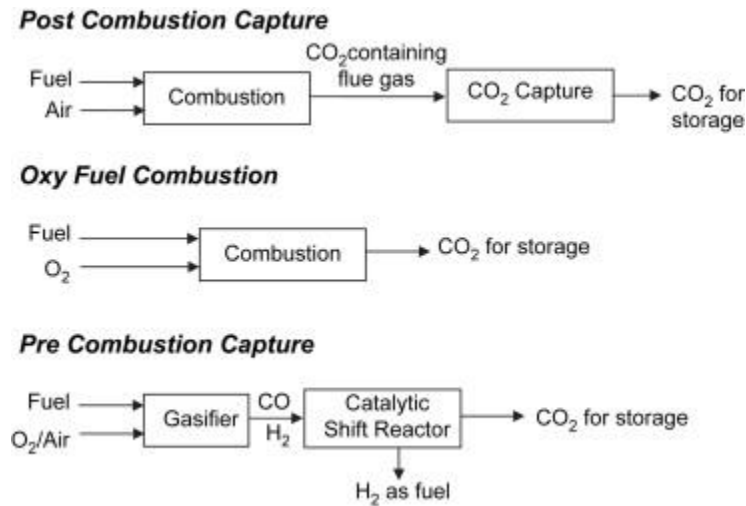
Figure 1-2. Methods of CO_2 capture are most often discussed in the power production industry[9]. Reprinted with permission[9] Elsevier 2009

From a carbon capture perspective, each of these methods involves a different combination of separations to remove CO_2 from the coal fed power production system.

Post-combustion capture involves (ideally) retrofitting existing coal-fired power plants with a "drop-in" separation process.[8] The other two approaches require the energy production system to be effectively changed, either through pre-treatment of the coal (pre-combustion) or pre-treatment of the air (oxy-fired). In either case, the goal of changing over the fundamental power production process is to simplify the separation process such that the removal of carbon dioxide from the process as a whole will be simplified at the cost of making the power production process more complicated.

Post-combustion capture is widely considered the most straightforward approach to be implemented at the plant and national scales, as it does not necessitate the disturbance of the power generation process to enable the carbon removal process. The existing flue gas, at compositions near those listed in **Table 1-1**, is sent to a separation process, where a purified CO_2 stream is removed from the stream. In contrast, the remainder of the gas (predominantly N_2, O_2, and H_2O) are vented to the atmosphere. From a pure separations perspective, post-combustion capture is considered the most challenging approach, due to the dilute nature of the CO_2 in the flue gas. While the separation of CO_2 from this mixture is more complicated than the other process options, the ability to utilize existing infrastructure, hopefully extending its life for a carbon-constrained future, makes post-combustion capture an attractive option for the decarbonization of the fossil power industry.

Table 1-1. Typical Flue Gas Composition[10]

Component	Mole %
CO_2	13.5
SO_2	0.016
SO_3	0.00325
N_2	74.7
NO_2	0.0025
NO_x	0.06
HCl	0.00525
O_2	4
H_2O	7.7

Pre-combustion capture utilizes fuel pre-treatment, in particular coal gasification technology (widely used in South Africa as an upstream process for fuel production), to simplify the separation to one similar (though on a much larger scale) to that of a water-gas shift reaction[11]. Carbon-rich coal is reacted at high temperatures with steam to produce CO and H_2 gas (colloquially known as syn-gas); the CO can then be further converted to CO_2 with additional water to make even more hydrogen gas. This CO_2 and H_2 rich gas could then be separated to produce pure CO_2 and H_2 products. The H_2 is then combusted (possibly in the presence of some inert gas like N_2) to produce energy for power production, along with a *green* water product ($H_2 + 1/2\ O_2 \rightarrow H_2O$) from the combustion. The separation of CO_2 from H_2 gas has been developed elsewhere (as part of gasification processes), though the scale of separation necessary to operate a power plant would still be a significant challenge. The concentration of CO_2 being relatively higher in these pre-combustion streams as compared to post-combustion is one of the main benefits of this approach for CO_2 capture from power systems.

Oxy-fired combustion operates as the name implies; an oxygen feed is utilized in the combustion as opposed to an air feed to produce a far higher purity CO_2 product leaving the combustion chamber.[12-13] This does significantly reduce the energy requirement and simplify the separation of CO_2 from the oxy-fired flue gas but at the cost of employing an enormous air separation unit to produce the pure O_2 gas. While the O_2/N_2 separation has been widely employed in industrial applications and is a mature technology, it is still energy-intensive.[14-16] Like pre-combustion capture, oxy-fired combustion approaches require a significant overhaul of the combustion system for appropriate heat management when steam is being produced. Looping of the purified CO_2 product and other advanced combustion approaches have been considered to reduce the risk of oxy-fired systems.[17] In general, both Pre- and Oxy-fired combustion approaches work in such a way as to simplify the CO_2 separation as compared to post-combustion approaches, utilizing more mature separation technologies upstream to reconfigure the heat production process.

As post-combustion technology may prove the simplest to drop into existing plants and plants being built in the immediate future, it has been the main point of emphasis on the carbon capture community. While other approaches may prove more fruitful in the future, existing and newly built plants have lifetimes spanning the next 20-30 years. Expecting these large capital endeavors to simply shut down because a new, more desirable approach has been developed is probably not reasonable. For that reason, development of new post-combustion capture processes, separating CO_2 from the dilute flue gas, will continue to be a significant focus of those interested in reducing and eventually decarbonizing the electricity production industry worldwide, as well as its application to other industries where similar flue gas compositions can be expected.

1.3   Methods of Post-Combustion CO_2 Capture

Several separations processes are being considered as possibilities to enable the separation of CO_2 from post-combustion coal flue gas.[18-19] Four approaches: 1. Absorption 2. Cryo-Distillation 3. Membrane 4. Adsorption, are being pursued at different levels of development as technologies for adoption for post-combustion capture.

1.3.1   *Absorption*

Absorption processes show great promise for widespread adoption as post-combustion CO_2 capture processes, primarily due to it being the closest to deployable technology for these kinds of separations. Indeed, absorptive separations are already used in coal-fired power plants for the removal of harmful acid gases (SO_x particularly).[20]

Absorption processes use a two-stage process (absorption and stripping) to separate one component from the others.[21] In the absorption stage, the gas of interest is put into continuous contact with a liquid phase, which is depleted in CO_2. The CO_2, based on the chemical affinity of the liquid phase for CO_2 at those conditions, is absorbed into the liquid phase from the gas phase. The CO_2 enriched liquid is then moved to the stripping column, where it is heated to free the CO_2 from the liquid phase. The CO_2 is recovered as hot gas and compressed and sent to the pipeline for storage. Absorption columns are usually considered the most technically mature technology of the options available for CO_2 capture. Like all technologies considered for post-combustion capture, scaling absorption to the sizes necessary to deal with the vast flows of flue gas is a problem. Because of absorption's maturity in separations, particularly in terms of power plant operation, some

companies have already begun to explore the scaling of these technologies to the scale required for power plants.

While perhaps the closest to widespread deployment, absorption technologies do still have many technical challenges researchers are working to solve. Perhaps the largest challenge remains the high-energy demand of the stripping column. As water is usually used as the carrier for the absorbent material (monoethanolamine as an example absorbent), the energy required to regenerate the absorbent also includes the latent heat associated with a portion of the liquid evaporates. Water lean absorption processes have gained significant interest, as have alternative process configurations, to drive down the high-energy demand of absorption.

The other sizeable technical issue is the volatility of the absorbent at elevated temperatures. Vaporous absorbent compounds becoming entrained in the pure CO_2 product of the stripper leads to many economic and environmental challenges. From an economics perspective, any loss of solvent needs to be made up with new absorbent being added to the process. If high regeneration temperatures are required to enable efficient utilization of absorbent, those temperatures will also lead to significant demand for makeup absorbent. Environmentally, the volatilization of the absorbent means it must either be separated from the CO_2 rich product or risk it leaching out to the atmosphere.

1.3.2   Cryo-distillation

Distillation processes form the backbone of the chemical and petroleum industries due to their significant maturity in the field as well as their ease of control and design to reach process requirements. Cryo-distillation processes have not gained the acclaim of the

other three processes, as the vast volumes of flow lead to significant concerns over any type of pre-treatment process of flue gas for downstream separation. Distillation, while widely used industrially, is seen as extremely energy-intensive, even with the immense institutional knowledge of heat and energy recovery.

Little exists in published literature looking at distillation as a stand-alone technology for CO_2 capture.[22-23] However, a few industrial endeavors exist to explore the possibility of CO_2 separation via low-temperature distillation. Through cooling and compressing the flue gas, the CO_2 can be selectively liquefied from the stream, leaving the inert gases behind. The compression of flue gas is widely viewed as a non-starter, so that alone limits the support of cryo-distillation in the engineering community. Additional concerns over the energetic cost of flue gas dehydration as an unrecoverable energy demand of these distillation processes stand in the way of engineering acceptance.[24]

Where cryo-distillation approaches have gained some headway has been when it is taken as a final step of the separation process. Most industrial separations are not carried out in a single unit, often to reach the process specification for sale or additional actions, a final separation may be necessary. Cryo-distillation (often called CO_2 liquefaction when performed following another separation) has been seen as a very promising possibility to help membranes and adsorption processes reach final desired purity specifications. With the majority of the separation occurring in a lower energy process (membranes or adsorption), the cost of compression and cooling is seen as acceptable energy demand.[25]

1.3.3   Membranes

Membrane technologies are one of the chief non-thermal separations gaining headway in the separations community as an option for debottlenecking and, in theory replacing distillation as widespread industrial separations equipment. Membranes, estimated to require 10-15% of the energy of traditional thermal separations, may be considered for a wide range of separations. The adoption of membrane technologies may be seen as especially desirable as membranes have shown the potential to reach nearest to the thermodynamic limit of separation (the Gibbs Free Energy of Demixing) of components. Membranes rely on a chemical potential driving force across a selective layer. This chemical potential driving force is generally driven by a partial pressure driving force (really a fugacity driving force) produced through the introduction of a pressure gradient across the membrane surface.[26] Performance characterization of membrane materials are generally driven by comparison of two parameters, permeability, an intrinsic property related to the potential productivity of the material, and perm-selectivity, its potential for separating one component from another. [27]

For membranes, the challenges of post-combustion CO_2 capture are the same as they would be for any other separation.[28-29] The partial pressure of the CO_2 in the flue gas leaving a coal plant is low, meaning a large pressure gradient will, in theory, be required to reach the desired performance of the membrane. The presence of water in the stream serves as a second significant challenge, as the co-transport of water through the membrane can lead to vastly different performance than whatever is discovered for dry streams. Like all other separations considered for CO_2 capture, harmful acid gases (SO_x, NO_x) are

expected to be detrimental to the performance of the material in the short term and the stability of the material in the long run.

Novel membrane materials are still being developed to overcome the inherent challenges membrane processes face[29]. Classes of membrane materials include inorganic (challenging to manufacture in a scalable way, high-performance characteristics) and polymer (well developed scalable manufacturing methods, performance limited by tradeoff between selectivity and permeability). The development of hybrids of these materials, so-called mixed matrix membranes, has gained a wide following in literature due to their idealized vision of combining the manufacturability of polymer membranes with an enhancement in performance due to the cooperative effects of an inorganic filler.

1.3.4 *Adsorption*

The last strongly considered option for separating CO_2 from flue gas is the use of adsorptive separations.[30-31] Adsorption processes rely on the affinity of a sorbate (a component of a mixture in the fluid phase) to form a new phase on the surface of a solid, usually porous, adsorbent. Porosity is desired to increase the available surface area, as adsorption processes rely on the interaction between the sorbate and sorbent at the surface. The strength of the affinity of the sorbed phase (made up of a mixture of the sorbates) is widely used to categorize the nature of sorption. Comparatively weaker adsorption, primarily driven by forces such as Van der Waals interactions, is referred to as physisorption, while stronger sorption, where strong bonds (or bond-like forces) appear between the surface and sorbed phase, is referred to as chemisorption. The calculated heat of adsorption, the amount of energy required to free a quantity of (pure, single component)

sorbate from the surface, is broadly used to determine the strength of the surface interaction and characterize the adsorption process as either chemisorption or physisorption.

Adsorptive separations are run with a series of adsorbent "beds," each cycling between adsorption (treating the inlet gas) and desorption (regenerating the adsorbent material and recovering adsorbed product). The desorption step can be carried out via either increasing the temperature (Temperature Swing adsorption) or decreasing the pressure (Pressure Swing adsorption), examples are shown in **Figure 1-3**.[32] For post-combustion CO_2 capture applications, both approaches have been widely considered, and depending on the composition of the flue gas and the adsorbent selected, either approach may prove advantageous.[33] The time it takes to complete one cycle of adsorption and desorption informs the size of the adsorption unit, as for continuous processing, one or more beds must always be performing the adsorption step.
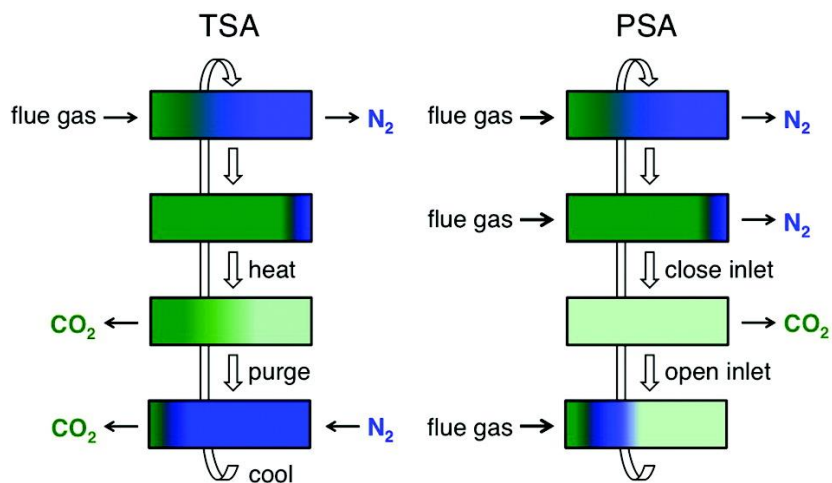
Figure 1-3. Schematic Diagrams of idealized temperature, pressure, and vacuum swing fixed bed adsorption processes. Adapted with permission[32] Copyright © 2012, American Chemical Society.

As with the previously mentioned processes, adsorption processes equally struggle with impurities, both water and trace acid gases, and the scale of the post-combustion CO_2

capture problem. Water and trace acid gases are, in most cases, more strongly adsorbed than CO_2, leading to a reduction in the performance of the sorbent.[34] Water removal has been seen to be a showstopper from an economics perspective,[35] so significant work has gone into finding and developing sorbents that either act cooperatively with water (e.g., supported amines) or are selective for CO_2 over water.[34, 36] Acid gas co-adsorption or poisoning has been the point of emphasis on several studies.[37]

A number of classes of porous materials are being developed as options for adsorptive post-combustion capture, including zeolites, activated carbons, and metal-organic frameworks (MOFs). Zeolites and carbons are the primary materials used industrially for other adsorptive separations, with zeolites moderate capacities and high selectivity's, and carbon's larger capacities and generally simpler synthesis allowing both groups of materials to serve specific applications.[34] Metal-organic frameworks are an emerging class of adsorbent materials with tunable pore size and pore chemistries offering the potential for a wide range of applications, including post-combustion capture.

The development of new techniques for forming absorbent structures, such as polymeric fibers or honeycomb monolith, has also been an area of focus in adsorbent separations to enable economic post-combustion capture.[38] These *structured adsorbent contactors* help to reduce pressure drop in the bed, allowing for potentially faster cycling of adsorbent materials to help reduce the size of adsorbent materials significantly. The fiber adsorbent platform, with an example separation module pictured in **Figure 1-4**, has also allowed for the development of heat management strategies within the structured contactor itself, leading to significant improvements in adsorbent performance.[39-40]

Figure 1-4. An example lab scale fiber sorbent module, packed parallel to the flow direction

The issue of the scale of post-combustion capture is an equally enormous challenge to be overcome. The primary approach considered throughout the literature has focused on materials improvements that have been increasing the amount of CO_2 per unit mass (or volume) that can be capture by the sorbent material. Increasing the capacity of the adsorbent means less adsorbent should be necessary for each cycle, thus leading to reductions in the size of the facility. In parallel, some researchers have been looking into methods to cycle the adsorbent more efficiently. If these approaches could be combined, it would help to drive down the massive size of the adsorbent unit required for post-combustion capture.

1.4 Sub-Ambient CO_2 Capture

While all four of the previously described methods have merit, the limitations of typical post-combustion CO_2 capture from flue gas remain challenging to all of them. As a consequence, several norms developed within the CO_2 capture research community building on the significant experience of all involved. Chief amongst these was the idea that any "pre-treatment" of flue gas would result in too large a capital and operating cost to overcome, even were that pre-treatment to improve the performance of the separation

significantly. Both compression and water removal were, therefore, widely considered intolerable in the area of CO_2 capture to economic operation.

In the late 2000s, building in part on the work of Merkel et al.[29], Haase and colleagues at Air Liquide began to develop a process for CO_2 capture using membranes that used compression, water removal, and feed cooling to enable significant improvements in membrane performance.[41-42] While that alone was interesting from a scientific perspective, when this group performed the preliminary economic analysis, they found that the entire pre- and post-treatment process could reasonably be expected to operate at costs of capture near \$40/tonne$_{CO2}$. A key reason for the reasonable economics of this process was the extensive heat integration making an external cooling utility unnecessary for sub-ambient operation. Refrigeration on the scale of CO_2 capture had not been discussed in great detail elsewhere, outside of cryo-distillation of CO_2. However, the high costs of process refrigeration had been widely noted elsewhere. A number of groups have built off of the concept developed by Air Liquide, working with different CO_2 feed compositions and membrane materials to apply this approach to other post-combustion applications besides the coal work performed by Air Liquide. As hollow fiber membranes were allowing for much of this potential for sub-ambient CO_2 capture, the question of whether this approach could be extended to adsorbent materials as well has not yet been considered in the literature. With the numerous breakthroughs in adsorbent material chemistry and structuring, the application of this pre-treatment strategy to a pressure swing adsorption system could lead to further cost reductions, combined to overcome many of the challenges adsorptive separations face in post-combustion CO_2 capture.

1.5 Thesis Objectives

The overall objective of this thesis is to develop a deeper understanding of the limitations and opportunities of sub-ambient CO_2 capture via a pressure-driven process, mainly pressure swing adsorption (PSA). This thesis will work to combine process design and optimization, materials development, scale-up, and optimization, and novel heat management in PSA systems, culminating in lab-scale testing of thermally modulated, scalable adsorbent contactors for application to sub-ambient post-combustion CO_2 capture.

1.5.1 Objective 1

Development of a process model for sub-ambient pressure-driven separation and exploration of its economic and energetic potential for post-combustion CO_2 capture from coal combustion derived flue gas.

To understand the properties of materials to best suit the capture of CO_2 from flue gas, it is essential to probe different processes and separations performance parameters to inform the selection of materials and understand process tradeoffs. Case studies are carried out looking at two MOF materials and one zeolite material to provide insight into the potential of this approach to CO_2 capture. Accompanying these case studies, the effects of varying a single process parameter on the overall process economics and energetics are carried out. The highly energy integrated nature of this process makes it likely variation of a single parameter may prove to have compounding effects on other parts of the system, both positive and negative. Gaining a deeper understanding of process parameters on the economics and energetics of the process helps to inform materials decisions. Accompanying the process understanding, a preliminary analysis of the

economics of thermally managed fiber sorbents for pressure swing adsorption is carried out to again assist in decision-making as to the best materials for sub-ambient CO_2 capture. The knowledge base developed in this objective can help to guide future work on materials and PSA process development primarily in their application to this and similar processes.

1.5.2   Objective 2

Scale-up and manufacture of high capacity MOF fiber sorbents for sub-ambient CO_2 capture

MOF materials show promise for sub-ambient CO_2 capture due to the wide range of chemistries and structures that can be produced, offering the possibility for exceptional capacities for CO_2 at relevant operating conditions. A MOF material (MIL-101(Cr)) was identified as a potential candidate for application to CO_2 capture due to its high surface area and pore volume, enabling large "swing capacities," advantageous for increasing sorbent productivity. MIL-101(Cr) was scaled up to 15-20 g scales building off prior work in the area, and spun into fiber sorbents. Sorbent leaching during manufacture was discovered, and two approaches were developed to overcome this potential manufacturing challenge.

1.5.3 Objective 3

Development of internal passive thermal management solutions for fiber sorbent contactors

One of the chief benefits of the fiber sorbent contactor to adsorption applications has been the development of internal solutions to the deleterious effects of undesired heat swings within the adsorbent bed. Past work has focused on active approaches, where heat is removed from or added to the adsorbent bed to balance out the thermal fronts developed during swing adsorption processes. The goal of this objective was to develop an alternative, passive approach, which could better suit pressure swing adsorption processes. A new hybrid fiber sorbent, containing both sorbent and heat management inside the structure was developed for application towards sub-ambient CO_2 capture.

1.5.4 Objective 4

Bench Scale Sub-ambient CO_2 capture using MOF Fiber Sorbents

In this final objective, MIL-101(Cr) fiber sorbents were tested in a bench-scale PSA unit to determine their potential in the sub-ambient CO_2 capture process. Using fibers beds both with and without thermal management, a wide range of PSA operating conditions for a single bed process will begin to provide insight into the application of this process. Variables like pressure, vacuum level, temperature, feed time, and feed rate were tested, and their effects on the purity and recovery of CO_2 from simulated flue gas was considered.

1.6 References

1.   MacFarling Meure, C.; Etheridge, D.; Trudinger, C.; Steele, P.; Langenfelds, R.; van Ommen, T.; Smith, A.; Elkins, J., Law Dome CO_2, CH_4 and N_2O ice core records extended to 2000 years BP. *Geophysical Research Letters* **2006,** *33* (14).

2.   Keeling, R. F.; Keeling, C. D., Atmospheric Monthly In Situ CO_2 Data - Mauna Loa Observatory, Hawaii. Atmospheric Monthly In Situ CO_2 Data - Mauna Loa Observatory, H., Ed. C San Diego Library Digital Collections: In Scripps CO_2 Program Data, 2017.

3.   Pacala, S.; Socolow, R., Stabilization Wedges: Solving the Climate Problem for the Next 50 Years with Current Technologies. *Science* **2004,** *305* (5686), 968-972.

4.   Clarke, L., Assessing Transformation Pathways. In: Climate Change 2014: Mitigation of Climate Change. Contribution of Working Group III to the Fifth Assessment Report of the Intergovernmental Panel on Climate Change. 2014.

5.   *British Petroleum Energy Outlook 2020 Edition*; 2020.

6.   IPCC, W., Climate change 1995: The science of climate change. Cambridge University Press Cambridge: 1996.

7.   Xu, M.; Yu, D.; Yao, H.; Liu, X.; Qiao, Y., Coal combustion-generated aerosols: Formation and properties. *Proceedings of the Combustion Institute* **2011,** *33* (1), 1681-1697.

8.   Benson, S. M.; Orr, F. M., Carbon dioxide capture and storage. *MRS bulletin* **2008,** *33* (4), 303-305.

9.   Thiruvenkatachari, R.; Su, S.; An, H.; Yu, X. X., Post combustion CO_2 capture by carbon fibre monolithic adsorbents. *Progress in Energy and Combustion Science* **2009,** *35* (5), 438-455.

10.   Last, G.; Shmick, M., Identification and Selection of Major Carbon Sioxide Stream Compositions. **2011,** *PNNL-20493*.

11.   Damen, K.; Troost, M. v.; Faaij, A.; Turkenburg, W., A comparison of electricity and hydrogen production systems with CO_2 capture and storage. Part A: Review and selection of promising conversion and capture technologies. *Progress in Energy and Combustion Science* **2006,** *32* (2), 215-246.

12.   Toftegaard, M. B.; Brix, J.; Jensen, P. A.; Glarborg, P.; Jensen, A. D., Oxy-fuel combustion of solid fuels. *Progress in Energy and Combustion Science* **2010,** *36* (5), 581-625.

13.   Wall, T.; Liu, Y.; Spero, C.; Elliott, L.; Khare, S.; Rathnam, R.; Zeenathal, F.; Moghtaderi, B.; Buhre, B.; Sheng, C., An overview on oxyfuel coal combustion—State of the art research and technology development. *Chemical Engineering Research and Design* **2009,** *87* (8), 1003-1016.

14.   Burdyny, T.; Struchtrup, H., Hybrid membrane/cryogenic separation of oxygen from air for use in the oxy-fuel process. *Energy* **2010,** *35* (5), 1884-1897.

15.   Smith, A. R.; Klosek, J., A review of air separation technologies and their integration with energy conversion processes. *Fuel Processing Technology* **2001,** *70* (2), 115-134.

16.   Vinson, D. R., Air separation control technology. *Computers & Chemical Engineering* **2006,** *30* (10), 1436-1446.

17.   Toporov, D.; Bocian, P.; Heil, P.; Kellermann, A.; Stadler, H.; Tschunko, S.; Förster, M.; Kneer, R., Detailed investigation of a pulverized fuel swirl flame in CO_2/O_2 atmosphere. *Combustion and Flame* **2008,** *155* (4), 605-618.

18.   Leung, D. Y.; Caramanna, G.; Maroto-Valer, M. M., An overview of current status of carbon dioxide capture and storage technologies. *Renewable and Sustainable Energy Reviews* **2014,** *39*, 426-443.

19.   Zhang, X.; Singh, B.; He, X.; Gundersen, T.; Deng, L.; Zhang, S., Post-combustion carbon capture technologies: Energetic analysis and life cycle assessment. *International Journal of Greenhouse Gas Control* **2014,** *27*, 289-298.

20.   Rao, A. B.; Rubin, E. S., A technical, economic, and environmental assessment of amine-based CO_2 capture technology for power plant greenhouse gas control. *Environmental Science & Technology* **2002,** *36* (20), 4467-4475.

21.   Hasan, M. F.; Baliban, R. C.; Elia, J. A.; Floudas, C. A., Modeling, simulation, and optimization of postcombustion CO_2 capture for variable feed concentration and flow rate. 2. Pressure swing adsorption and vacuum swing adsorption processes. *Ind. Eng. Chem. Res.* **2012,** *51* (48), 15665-15682.

22.   Meratla, Z., Combining cryogenic flue gas emission remediation with a CO_2O_2 combustion cycle. *Energy Conversion and Management* **1997,** *38*, S147-S152.

23.   Yuan, L. C.; Pfotenhauer, J. M.; Qiu, L. M., A preliminary investigation of cryogenic CO_2 capture utilizing a reverse Brayton Cycle. *AIP Conference Proceedings* **2014,** *1573* (1), 1107-1114.

24.   Baxter, L.; Baxter, A.; Burt, S., Cryogenic CO_2 Capture as a Cost-Effective CO_2 Capture Process. In *Pittsburgh Coal Conference*, 2009.

25.   Song, C.; Liu, Q.; Ji, N.; Deng, S.; Zhao, J.; Li, Y.; Song, Y.; Li, H., Alternative pathways for efficient CO_2 capture by hybrid processes—A review. *Renewable and Sustainable Energy Reviews* **2018,** *82*, 215-231.

26.   Sholl, D. S.; Lively, R. P., Seven chemical separations to change the world. *Nature* **2016,** *532* (7600), 435-437.

27.   Robeson, L. M., Correlation of separation factor versus permeability for polymeric membranes. *J. Membr. Sci.* **1991,** *62* (2), 165-185.

28.   Xu, J.; Wang, Z.; Qiao, Z.; Wu, H.; Dong, S.; Zhao, S.; Wang, J., Post-combustion CO_2 capture with membrane process: Practical membrane performance and appropriate pressure. *J. Membr. Sci.* **2019,** *581*, 195-213.

29.   Merkel, T. C.; Lin, H. Q.; Wei, X. T.; Baker, R., Power plant post-combustion carbon dioxide capture: An opportunity for membranes. *J. Membr. Sci.* **2010,** *359* (1-2), 126-139.

30.   Mukherjee, A.; Okolie, J. A.; Abdelrasoul, A.; Niu, C.; Dalai, A. K., Review of post-combustion carbon dioxide capture technologies using activated carbon. *Journal of Environmental Sciences* **2019,** *83*, 46-63.

31.   Ruthven, D. M., *Principles of Adsorption and Adsorption Processes*. Wiley: New York, 1984.

32.   Sumida, K.; Rogow, D. L.; Mason, J. A.; McDonald, T. M.; Bloch, E. D.; Herm, Z. R.; Bae, T.-H.; Long, J. R., Carbon Dioxide Capture in Metal–Organic Frameworks. *Chemical Reviews* **2012,** *112* (2), 724-781.

33.   Lively, R. P.; Realff, M. J., On thermodynamic separation efficiency: Adsorption processes. *AIChE Journal* **2016,** *62* (10), 3699-3705.

34.   Choi, S.; Drese, J. H.; Jones, C. W., Adsorbent Materials for Carbon Dioxide Capture from Large Anthropogenic Point Sources. *ChemSusChem* **2009,** *2* (9), 796-854.

35.   Zanco, S. E.; Joss, L.; Hefti, M.; Gazzani, M.; Mazzotti, M., Addressing the Criticalities for the Deployment of Adsorption-based CO_2 Capture Processes. *Energy Procedia* **2017,** *114*, 2497-2505.

36.   Li, S.; Chung, Y. G.; Snurr, R. Q., High-Throughput Screening of Metal–Organic Frameworks for CO_2 Capture in the Presence of Water. *Langmuir* **2016,** *32* (40), 10368-10376.

37.   Bhattacharyya, S.; Han, R.; Kim, W.-G.; Chiang, Y.; Jayachandrababu, K. C.; Hungerford, J. T.; Dutzer, M. R.; Ma, C.; Walton, K. S.; Sholl, D. S.; Nair, S., Acid Gas Stability of Zeolitic Imidazolate Frameworks: Generalized Kinetic and Thermodynamic Characteristics. *Chemistry of Materials* **2018,** *30* (12), 4089-4101.

38.   DeWitt, S. J. A.; Sinha, A.; Kalyanaraman, J.; Zhang, F.; Realff, M. J.; Lively, R. P., Critical Comparison of Structured Contactors for Adsorption-Based Gas Separations. *Annual Review of Chemical and Biomolecular Engineering* **2018,** *9* (1), 129-152.

39.   Lively, R. P. Hollow Fiber Sorbents for Post-Combustion CO_2 Capture. Georgia Institute of Technology, 2011.

40.   Lively, R. P.; Chance, R. R.; Kelley, B. T.; Deckman, H. W.; Drese, J. H.; Jones, C. W.; Koros, W. J., Hollow Fiber Adsorbents for CO_2 Removal from Flue Gas. *Ind. Eng. Chem. Res.* **2009,** *48* (15), 7314-7324.

41.   Hasse, D.; Kulkarni, S.; Sanders, E.; Corson, E.; Tranier, J. P., CO_2 capture by sub-ambient membrane operation. In *Ghgt-11*, Dixon, T.; Yamaji, K., Eds. Elsevier Science Bv: Amsterdam, 2013; Vol. 37, pp 993-1003.

42.   Hasse, D.; Ma, J. F.; Kulkarni, S.; Terrien, P.; Tranier, J. P.; Sanders, E.; Chaubey, T.; Brumback, J., CO_2 Capture by Cold Membrane Operation. In *12th International Conference on Greenhouse Gas Control Technologies, Ghgt-12*, Dixon, T.; Herzog, H.; Twinning, S., Eds. Elsevier Science Bv: Amsterdam, 2014; Vol. 63, pp 186-193.

CHAPTER 2.   BACKGROUND AND THEORY

This chapter discusses the background knowledge related to the fields of adsorptive separations, porous materials synthesis, and design and manufacture of structured contactors. The chapter begins with a general discussion of adsorptive separations, particularly focusing on approaches considered for CO_2 capture. This discussion is followed by a broader discussion of adsorbent materials considered for CO_2 capture that then focuses more fully on Metal-Organic Frameworks, discussing properties and synthesis strategies employed to produce these materials. With a deeper understanding of the materials considered in this process, the next section focuses on the development of structured sorbent contactors, particularly focusing on the fiber sorbent platform. Finally, this section concludes with a discussion of the intricacies of Pressure Swing Adsorption (PSA) processes, including a discussion of usual design considerations made when considering the application of such systems.

The section discussing structured sorbent contactors is adapted from DeWitt et al. "Critical Comparison of Structured Contactors for Adsorption-Based Gas Separations." Adsorption and Pressure Swing Adsorption Fundamentals draw strongly from a number of seminal texts in the field, including Ruthven's "Fundamentals of Adsorption" and "Pressure Swing Adsorption."[1-2] These texts are highly recommended to those looking for deeper discussions of the background and theory of adsorption science.

2.1 Fundamentals of Adsorption and Adsorptive Separations

Adsorptive separations serve as one approach to the separation and purification of gas or liquid mixtures for a wide range of applications, from pharmaceuticals and medical devices to large-scale gas separation and purification systems. While adsorption science is integral to a wide range of fields, from catalysis to membrane separations, adsorption can also be applied more directly for the separation of materials. Adsorption separations can be applied to both batch (chromatographic separations are driven by adsorption) or continuous (traditional adsorption separations), as well as more complex combinations of the two (simulated moving bed chromatography)[1].

Broadly, speaking separations via adsorption rely on a difference in the strength of the intermolecular interaction between the surface of a solid (usually porous) material and the different components of a mobile (gas or liquid) phase. At equilibrium, this interaction leads to the creation of a separate (3rd) phase (the "adsorbed" phase), with all three phases existing in chemical equilibrium. Since one or more components in the adsorbate phase prove to be more prevalent in the adsorbed phase, usually due to the relative strength of its interaction as compared to the other adsorbates, allowing that component to be partially (or fully) removed from the mixture. There are a number of cases where the adsorbed phase composition can be controlled by the rate of diffusion and adsorption to the solid surface, rather than the equilibrium adsorption properties. This is oftentimes termed "kinetic adsorption" (size exclusion chromatography is the corollary of this approach to chromatographic separations) and has been shown to be highly effective in the separation of multicomponent mixtures where one component is significantly larger than another.[1, 3]

Both "equilibrium" and "kinetic" adsorption processes can prove highly effective at separating and purifying mixtures depending on the composition of the mixture and the physical and chemical properties of the solid adsorbent. In either case, the main products of adsorptive separations are purified product of the more poorly adsorbed component (in kinetic case, this would be the component which diffuses more slowly) and a second purified product of the more strongly adsorbed component. The recovery of the second product is typically combined with the regeneration of the adsorbent. The shift in the chemical environment (and chemical potential) to regenerate the adsorbent and recovery the "heavy product" is generally carried out either through the increase of the temperature of the system (Temperature Swing Adsorption) or the reduction in the partial pressure of the heavy component in the mobile phase (Pressure Swing Adsorption). Either of these approaches drives the equilibrium of the system in the direction of returning the sorbed phase back to the free adsorbate phase.[3]

2.1.1 *Adsorption Equilibrium*

Adsorption equilibrium is most frequently described in the form of an adsorption *isotherm*, where the amount of material in the adsorbed phase (uptake) is plotted versus the partial pressure of the adsorbate at some desired constant temperature. The collection of adsorption isotherms can be carried out using a variety of methods, particularly volumetric and gravimetric techniques.[3]

2.1.1.1 Methods of Determining Single Component Adsorption Isotherms

Two approaches are typically used to determine the amount of adsorption occurring on a solid at a given partial pressure, volumetric and gravimetric. In either case, a known

mass of adsorbent is exposed to an environment of gas of interest (at some known or monitored partial pressure), and the total uptake is determined by the change in some monitored variables. Regardless of the technique, the removal of all other possible adsorbing species, commonly termed "activation," is necessary prior to perform the experiment. This activation condition depends greatly on the class of material under consideration; its thermal and chemical stability is particularly important. The use of vacuum or flowing dry gas at elevated temperatures allows for the removal of water and other impurities that may remain in the adsorbent pores prior to performing the experiment.

Volumetric adsorption techniques use the change in pressure of a known volume of gas to determine the total amount of gas adsorbed. The volume is usually determined for every experiment through the collection of a "free space" using a non-adsorbing gas like Helium. As this gas is assumed not to adsorb at all, the pressure change experienced when dosing a known volume of gas into the measurement chamber allows for the determination of the amount of volume in the measurement chamber. Determining isotherm points of interest follows a similar method, where a known volume of adsorbate (gas) at a determined pressure is dosed into the measurement chamber, and the pressure of the combined volume is monitored to determine a change in pressure. The deviation of this change in pressure from that expected value based on the volume determined from the free space measurement enables the calculation of the number of moles of gas that were adsorbed. It is extremely important in adsorption measurements (both volumetric and gravimetric) that the parameter used to determine when equilibrium is taken, pressure in the case of volumetric techniques, is well defined for the system. As these systems are typically automated, if the *equilibrium condition* is set too broadly, the experiment will move on before the actual

equilibrium is reached. In volumetric measurements, the adsorbed amount value is recorded at the final pressure the system settled at, and the next point can then be determined. As each individual point only determined the additional amount of gas adsorbed from the previous point, it is imperative that each point reaches equilibrium, as any error in earlier measurements will propagate to later points as well. This error is typically observable when collecting the desorption branch of an isotherm, where small positive differences (higher uptake at desorption than adsorption), which still follow the general trend of the isotherm, would indicate either the adsorption or desorption measurements were not reaching equilibrium. Volumetric techniques, when operated correctly, typically allow for a higher degree of certainty than gravimetric techniques, largely due to the ability to monitor pressures with more significant digits than typical mass measurements with microbalances used in gravimetric techniques. This greater degree of certainty usually comes at the cost of experiments taking longer, so gravimetric techniques will often be used for screening applications. This is especially true when only one partial pressure is of interest or necessary to judge success or failure.

Gravimetric techniques use a constant gas environment, typically through the flowing of a gas or gas mixture. A sample is placed on a calibrated microbalance, and its mass is monitored to determine the mass change as a function of the environment. For isotherm collection, the adsorbate gas, or a gas mixture (with the adsorbate at some partial pressure and a non-adsorbing carrier) flows through the sample chamber, and the change in mass is recorded. This change in mass can be compared to an empty pan if there are concerns about the effects of buoyancy on the microbalance mass recording. The change in mass of the adsorbent is assumed to be entirely due to the adsorbing species. An

equilibrium condition of some incremental change in mass over a given time period is used to determine the time when equilibrium has been reached. For isotherm collection, the gas pressure, mixture composition, or both, must then be adjusted to allow for the determination of weight change at a new condition. The weight change, as compared to the original activated sample mass, can then be used to calculate the amount adsorbed directly.

Gravimetric approaches have also been applied for the collection of isobars instead of isotherms, where instead of changing the gas species' partial pressure, the temperature is changed while the partial pressure remains constant. This approach allows for the rapid collection of uptake information over a range of temperatures, and is less reliant on having many gas mixtures available to determine all uptakes; instead, a single gas composition can probe the adsorption over a wide range of conditions.

While volumetric and gravimetric approaches are the two most typically used for the determination of single-component isotherms, approaches based on studying the change in gas composition during flow, like breakthrough or desorption, could also be used. These experiments tend to be slightly less reliable, as pressure transducers and microbalances allow for measurement that is more exact. Due to this comparative lower precision and higher complexity, these experimental techniques are oftentimes used for fast screening of multicomponent adsorption in place of the above techniques, which are less well suited for those applications. These techniques are discussed in more detail in section 2.1.2 Adsorption Process Dynamics, as the results of these experiments may also be used to determine the effects of various transport limitations along with single or multi-component adsorption equilibria.

2.1.1.2   Application of Adsorption Isotherms to Characterize Porous Materials

While single component isotherms alone are useful for understanding the potential

of a material for an application, the collected information may also be used for the

determination of a wide range of other characteristics of adsorbent materials. Properties

like pore volume, surface area, pore size distribution, and isosteric heat of adsorption can

all be determined using collected isotherm(s) using models from the literature. These

properties are especially useful in the literature for comparisons both between materials

and to confirm repeatability between synthesis. As they are agreed-upon metrics, they have

also been used as parameters to draw trends in performance metrics and inform structure-

property relationships.

2.1.1.3   Swing Capacity

An adsorbent's swing (or working) capacity is defined as the difference in uptake

of the adsorbent between the anticipated process's adsorption condition and the process'

desorption condition. The graphical definition of the swing capacity is shown in **Figure

2-1** as the difference between q_{ads} and q_{des}. In this figure, both pressure swing and

temperature swing adsorption approaches are considered, each displayed having the same

swing capacity. For adsorption processes expected to be controlled by adsorption

equilibrium and not kinetics, the swing capacity can be considered the thermodynamic

upper ceiling on the performance of the sorbent to capture a given adsorbate.

As these processes are inherently dynamic, the swing capacity serves best as a

descriptive variable for the active comparison of materials. Since typically, each cycle

(PSA or TSA) does not begin with an entirely regenerated bed, and the bed is not typically

completely saturated at the end of the adsorption step, the swing capacity will not be capable of actually capturing the real performance. Still, swing capacity is regularly used as a performance metric for comparison between sorbents because of its ease of collection and calculation.[1,3] A number of authors have compared swing capacity to other experimental and computational performance metrics, and while imperfect, it does offer a good baseline for simple comparison of materials.[4-5]
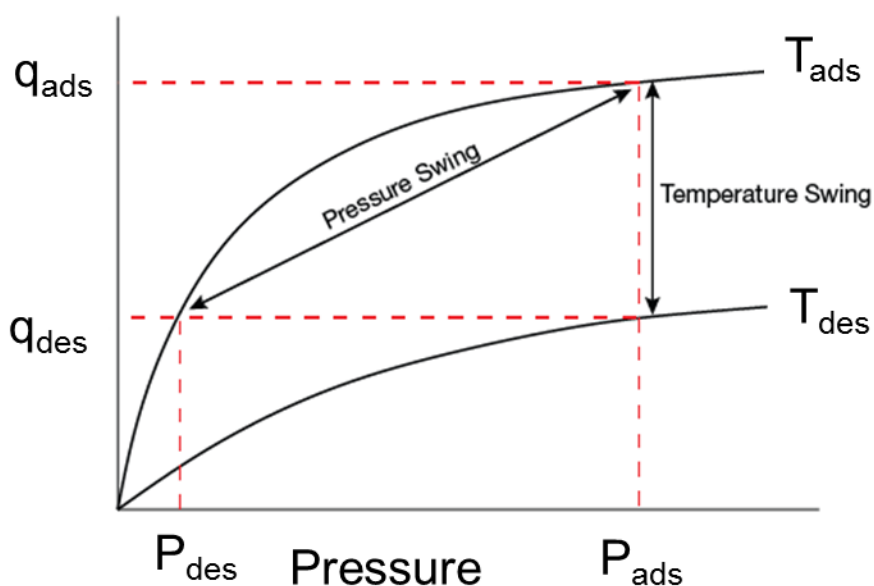
Figure 2-1. Example of two isotherms showing adsorption and desorption conditions for pressure and temperature swing adsorption, Adapted with permission[3] Copyright © 2018 American Institute of Chemical Engineers (AIChE)

2.1.1.4   Surface Area

The determination of a porous materials surface area is perhaps the most prevalent calculation carried out in literature to determine the quality of the material. As adsorption processes directly involve the surface, it is easy to see why being able to characterize and compare properly is a key area of the field. Most often used in the literature are the Langmuir[6] and the Brunauer-Emmett Teller (BET) surface area calculation.[7] While both

methods can be appropriate in many applications, some of the underlying assumptions of each limit their accuracy as measures of the *real* surface area of a material. These approaches remain the most prevalent approach to calculating and comparing synthesized material's surface areas. Both approaches rely on the collection of isotherms at low relative pressures (p/p_0) and are most often carried out using Nitrogen gas as an adsorbent. Nitrogen is advantageous for this application for a number of reasons; it is non-polar and weakly adsorbing on most surfaces being the main key. Additionally, the prevalence, cost efficiency, and relative safety of liquid nitrogen in laboratory settings make it one of the more desirable gases for the collection of low relative pressure isotherms. Argon (87 K boiling point)[8] and CO_2 (at ice bath or dry ice conditions) [9]have also been considered in some detail in the literature, primarily for applications where there may be diffusion rate limitations in the collection of N_2 isotherms at 77K that those higher temperatures and smaller molecules can better be applied. Still, N_2 remains the main fluid used for these characterizations.

The Langmuir surface area calculation is the older of the two, relying upon multiple assumptions, which proved to be relatively rare as new porous materials were developed. The five main assumptions of the Langmuir surface area model are as follows:[6]

1. The gas phase is perfectly ideal

2. The surface of the solid is perfectly flat

3. The adsorbing gas is immobile once it adsorbs to the surface

4. All surface sites are identical (have equal surface energy) and so the heat of adsorption is constant across all sites

5. Each surface site can only hold a single molecule (a monolayer is formed)

31

As the field of porous materials developed, many materials were developed where one or more of these assumptions did not hold, and so the Langmuir model offered limited insights to the actual characteristics of the material. The fourth and fifth assumption is challenging to find in complex pore geometries, where multiple active sites can be identified. Heterogeneous surface chemistries will lead to the formation of second and third layers prior to the completion of the monolayer across all sites. As with many models used to characterize materials (including BET to be discussed in the following paragraphs), the Langmuir model is still used to compare materials even when one or more of the assumptions do not hold. The idea being, so long as the model is always followed the same way for all materials the values calculated, though not necessarily descriptive of the reality of the surface, can still be compared.

The Brunauer-Emmett Teller (BET) surface area helps to overcome some of the issues of the Langmuir surface area calculation by extending the concept of the Langmuir calculation to the formation of multilayers.[7] This has allowed for the calculation of surface area values for more complex surfaces where multilayer formation occurs at low relative pressures. The basic approach to calculating a BET surface area from an N_2 physisorption isotherm at 77K is as follows, using the criteria defined by Rocquerol.[10]

1. The N_2 isotherm (uptake vs. pressure) is replotted using the BET Equation (1)

$$\frac{1}{v\left(\left(\frac{p_0}{p}\right) - 1\right)} = \frac{c-1}{v_m}\left(\frac{p}{p_0}\right) + \frac{1}{v_m c} \tag{2-1}$$

2. The range where the BET surface area is linear and increasing is identified (typically between $0.05 < p/p_0 < 0.30$)

3. The BET isotherm is plotted, and the slope and intercept of the BET equation are determined. From these values, the parameter C and v_m can be determined. The range of values used to calculate should result in the value of C is greater than 0, if not a new range must be selected.

4. The calculated monolayer loading v_m derived from the slope and intercept should correspond to a value of v within the pressure range used for the calculation.

5. The approximate relative pressure (p/p_0) value corresponding most closely to the value v_m should be within a tolerance (typically 20%) of the estimation of that value using the C parameter ($p/p_0 = 1/ (\sqrt{C} +1) \pm$ tolerance)

6. The surface area can then be calculated by combining the monolayer loading and the surface area of a nitrogen molecule.

For microporous materials, this method has proven to offer great insight into the surface area of materials, though there have been a number of follow up studies of the method which have shown it may not be the most accurate. Still, it is widely embraced in the field of microporous materials for comparison of materials surface areas.

Isosteric Heat of Adsorption

One of the most fundamental quantities that can be measured or calculated using equilibrium adsorption experiments is the heat of adsorption. As the process of adsorption is an inherently exothermic process, the heat given off as a molecule moves from the free gas phase to the adsorbed phase is an essential thermodynamic quantity to understand about a material.

The heat of adsorption of an adsorbent on a surface is oftentimes used as a proxy for comparisons of the strength of adsorption relative to other surfaces with the same sorbate or other sorbates on the same surface. As determining the actual competitive adsorption behavior of mixtures on a surface can be experimentally challenging, the heat of adsorption serves as a useful proxy.

The determination of heat of adsorption can be carried out using one of two methods, microcalorimetry or Van't Hoff analysis. Of the two methods, microcalorimetry can be more accurate to the actual performance of the material, as it uses the direction collection of the heat of adsorption for material and sorbate. As calorimetry is carried out in the catalysis field, calorimetry in adsorption relies on the experimental determination of the heat released as a known volume of sorbate is introduced into the system. Through monitoring of a thermal sink that surrounds the adsorption chamber, one is able to determine the amount of heat released as a sorbate is dosed into the system. By also monitoring the pressure in the chamber, the total number of moles of gas adsorbed during each dosing step may be determined. Combining these two pieces of information allows for the determination of the heat of adsorption. [3]

Van't Hoff analysis relies on the fundamental thermodynamics of adsorption to determine the isosteric heat of adsorption from adsorption isotherms. To perform Van't Hoff analysis, one must first have a number (typically >3) of adsorption isotherms for the same material and sorbate collected at different temperatures. Since adsorption equilibrium follows the known Clausius Clapeyron relationship,[11] replotting the isotherm data as isosteres (constant uptake) on an ln(P) vs. 1/T basis allows for the calculation of the heat of adsorption.

$$\left(\ln\frac{P_2}{P_1}\right)_q = \frac{-\Delta H_{ads}}{R}(T_2 - T_1) \qquad (2\text{-}2)$$

It is worth noting that Van't Hoff analysis allows for the heat of adsorption to change with loading, which is typical in adsorption but also relies on there being no temperature dependence on the heat of adsorption. The heat of adsorption in nearly all cases has been shown to be consistent regardless of temperature, though cases have been reported where this behavior does not appear to be consistent. [12]

2.1.2   Adsorption Process Dynamics

While adsorption equilibrium is highly useful for the characterization of materials and beginning to probe their potential for application to adsorption systems many adsorption separations are operated in a dynamic regime where transport effects can dominate[1,13]. Especially in the case of CO_2 capture requiring high throughput, understanding the system dynamics at relevant operating conditions will be critical to efficient operation. A number of different transport effects exist in the operation of the adsorption system, which will briefly be reviewed in the following sections.

A number of experiments may be carried out to study the different transport effects on the performance of adsorbents. In this dissertation, the primary experimental approach to observe these effects is the *fixed bed breakthrough* (breakthrough) *experiment.* The breakthrough experiment, in its simplest form, simulates the ideal Adsorption step of a pressure or temperature swing adsorption process. In the experiment, a bed of adsorbent, which has been previously activated to remove all impurities, is saturated with a weakly adsorbing gas underflow. The feed is then switched to a gas mixture of interest containing

one or more adsorbing gas species, and sometimes a non-absorbing tracer, and the composition of the effluent is monitored. [1-2, 14-16]

An example breakthrough profile for one analysis gas and a tracer for two adsorbent materials is given in **Figure 2-2a** below, where time has been normalized to the moment the tracer appears in the effluent. While breakthrough profiles can be used to study kinetics within the fixed bed, the experiment can also offer insight into the mixed gas adsorption capacity of different adsorbents. The area bound between the tracer and adsorbate breakthrough profiles can be used to calculate the amount of gas adsorbed. So in the case of the experiments run in **Figure 2-2a**, a later breakthrough time relative to the tracer of "Sorbent 3" as compared to "Sorbent 2" (with all other experimental parameters held constant (i.e., pressure, feed composition, sorbent mass, temperature, flow rate) indicates qualitatively that Sorbent 3 has more capacity for the adsorbate than Sorbent 2. The areas bound between the adsorbate and tracer curves can be calculated to quantify uptake, as shown in **Figure 2-2b**, and then normalized per gram of adsorbent and per molar flowrate of adsorbate in the inlet(the exact procedure is outlined in Chapter 3). This calculated value allows for quantitative comparison between adsorbent(s) performance at different operating conditions as well.[15]
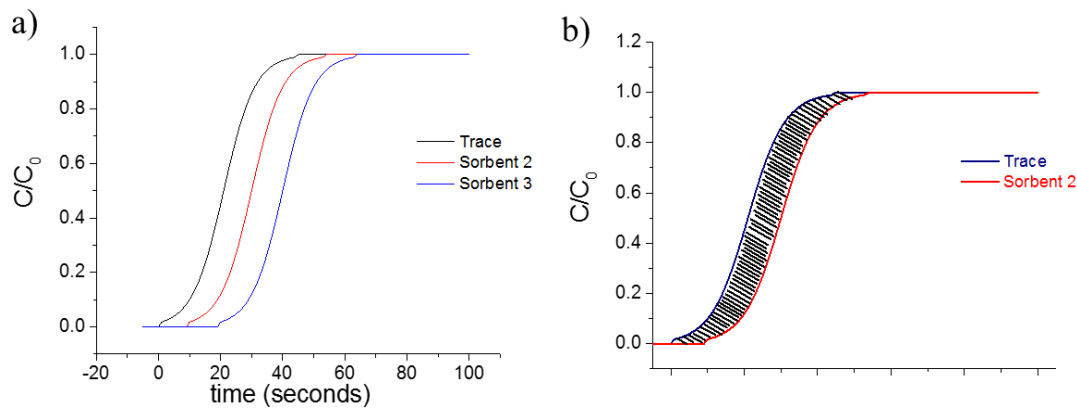
Figure 2-2. Example Breakthrough profiles (a) for two adsorbents in one adsorbate, one tracer system. (b) illustration of the calculation of the area bound between the tracer profile and the adsorbate breakthrough profile for one sorbate.

While the breakthrough profile is the main piece of data collected in the breakthrough experiment, the experiment is probing the behavior of the fluid component's concentration profile as a function of time and location within the bed. **Figure 2-3** offers one graphic interpretation of these profiles as a function of normalized bed length at a number of different times post introduction of adsorbate fluid to the bed. A perfect adsorption breakthrough effluent profile, with no transport limitations and a linear isotherm, would be a perfect square wave, (like t=0 in **Figure 2-3**).[1, 17] All deviations from that perfect square wave response then are due to transport limitations and curvature of the isotherm. Conceptually, analysis of breakthrough profiles collected at the effluent is used to back out the different phenomena occurring within the bed leading to the different broadening and sharpening behaviors shown at different times as the concentration front propagates the bed. Each of the green and red profiles indicates the concentration profile in the bed at a given time prior to the actual breakthrough of tracer and sorbate, which is collected to produce the profiles in **Figure 2-2**. The discussion, which follows, focuses on a number of the different effects on the breakthrough profile that may be observed.
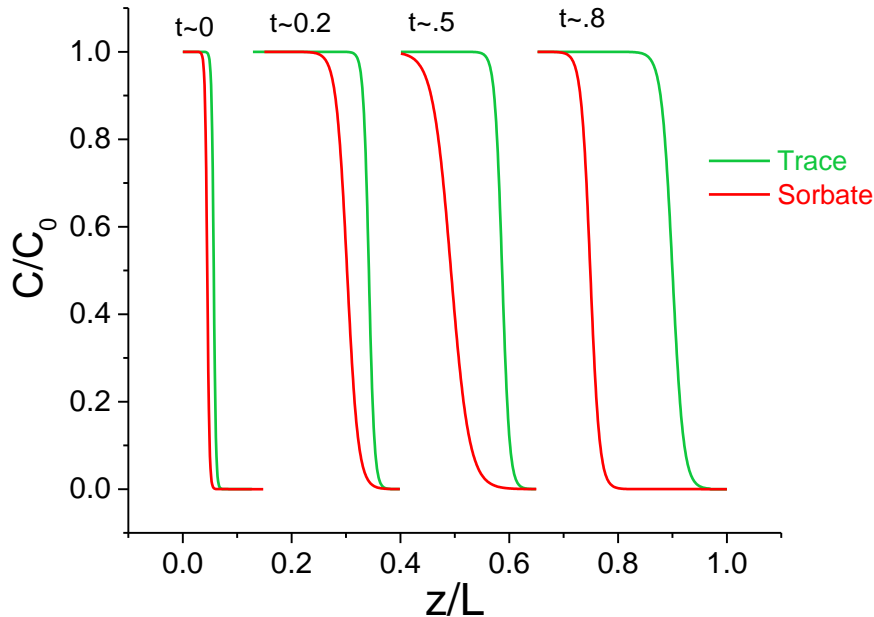
Figure 2-3. Example of two concentration fronts propagating a fixed bed at different times and axial locations. (green) non-adsorbing tracer (red) adsorbing species

2.1.2.1   Mass Transfer Resistances in Fixed Beds

Three main mass transfer existences will be experienced in fixed beds, external diffusion, internal diffusion resistances, and intraparticle/pore limitations. All of these effects lead to the broadening of the breakthrough profile, as these effects limit the rate at which the adsorbate in the free fluid phase can reach a given adsorption site within the bed. Design decisions in cycles, macro-structuring of adsorbent, or adsorbent microstructure will all play a role in which of these three effects may control the rate of adsorption. [1]

The external diffusion limitation is controlled by the size of the laminar boundary layer formed between the bulk gas phase traversing the bed and the surface of the adsorbent

structure (i.e., pellet, fiber, monolith). The size of the boundary layer is correlated to the Sherwood number, which in turn is strongly correlated to the Reynolds and Schmidt numbers, so adjusting the size of the adsorbent structure or increasing the velocity of the fluid phase in the bed will play a vital role in the shape of the breakthrough. Overcoming the external resistance via either of these methods can be challenging in traditional adsorbent beds because smaller particle sizes and higher fluid velocities can lead to fluidization of the adsorbent pellets.

Internal diffusion resistances in a structured contactor typically means the transfer of adsorbate molecules from the surface of the structure to the solid adsorbent. This should typically be pore diffusion, as most structured adsorbents (pellets, fibers, monoliths) will have some form of internal pore structure to allow for more rapid transport of the adsorbate from the surface of the structure to the adsorbent particles themselves. Minimizing internal diffusion typically involves the shrinking of the particle size, which will increase the pressure drop in the system, and increase the chances of fluidization. The other option is to introduce more pores into the structure, which will help to reduce internal diffusion limitations. Introducing more porosity into a structured contactor will reduce the overall density of the structure, which may lead to larger bed volumes unless the system is very strongly internally controlled.

Intraparticle diffusion can be thought of as the diffusion of the fluid adsorbate inside the adsorbent, so it is primarily controlled by the pore size and connectivity of the adsorbent particle. Intraparticle diffusion limitations can be a desirable characteristic of an adsorbent to be leveraged when operating a kinetic pressure swing adsorption system. Reducing intraparticle diffusion effects can be accomplished by shrinking the particle size of the

adsorbent or via the selection of a new adsorbent with a microporous structure more conducive to Knudsen pore flow.

2.1.2.2   Axial Spreading

As a fluid mixture flows through a packed bed, there is the opportunity for mixing axially as the mass transfer front develops, making the separation less efficient.[1] In beds where channeling is not an issue (occurring primarily in shorter beds when there is non-uniformity of packing of adsorbent throughout the bed), there are two primary components of axial spreading, molecular diffusion and turbulent mixing. Molecular diffusion, driven by the random flow of individual molecules (Brownian motion), is always going to control, though it has been correlated to the bed's voidage. Turbulent mixing can be related back to the Reynolds number of the flow and will depend greatly on the structure of the adsorbent bed.

2.1.2.3   Heat Effects

Heat effects can play a significant role in the performance of an adsorption system as adsorption's inherently exothermic nature leads to the release of a significant amount of heat (20-40 kJ/mol for CO_2 in a typical physisorbent)[1, 14]. This heat release in breakthrough experiment results in the creation of a thermal wave, generated within the bed as the concentration front propagates the bed. The rate of propagation of the concentration wave is related to the relative rates of heat generation and thermal capacity of the system, which can be denoted in the variable η below[1]. η is the relative rate of propagation of the thermal front in the fixed bed generated by one adsorbate as compared to the rate of propagation of that adsorbate's mass transfer front.

$$\eta = \frac{C_s/\Delta q - C_f/\Delta c}{R\left(\frac{-\Delta H}{RT_0}\right)^2} \tag{2-3}$$

When η is negative, as would almost always be the case with larger $\Delta q/\Delta c$ (as seen in the Langmuir isotherm) and relatively smaller C_s/C_f, the thermal front races ahead of the mass transfer front, leading to front broadening, like that shown in the "some adiabatic" case shown in **Figure 2-4**. These effects can be mitigated by heat leakage through the walls of the column, but in the case of most industrial systems, the heat generation rate far exceeds the heat losses through the wall, resulting in more front broadening, as shown by the adiabatic case. The effects of heat generation in broadening the profile are shown in **Figure 2-3** in the sorbate fronts broadening between t=0 and t=0.5.
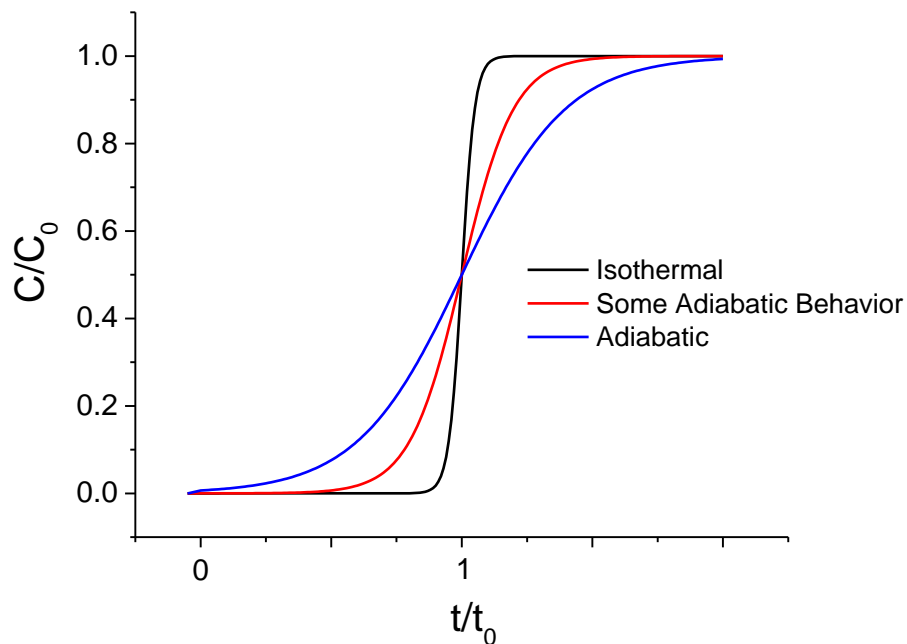
Figure 2-4. Effects of heat on adsorbate breakthrough profiles

2.1.2.4   Constant Pattern and Self Sharpening Behavior

While mass and heat transfer effects will generally lead to front broadening, some of the adverse effects of these limitations are actually counteracted by the thermodynamics of the system[1]. With an ideal isotherm (one which the second derivative of the isotherm decreases with increasing concentration, like the Langmuir isotherm) the concentration front propagates the bed and is spread by mass and heat transfer effects, there are fewer adsorbate molecules in the local fluid phase than the adsorbent particle wants to have adsorbed. As such, adsorption equilibrium acts to counteract the spreading of the concentration front at the beginning of the front resulting in what is referred to as "self-sharpening" behavior, illustrated between t=0.5 and t=0.8 in **Figure 2-3**.

The result of self-sharpening is the eventual development of constant pattern behavior, where self-sharpening and the different spreading effects offset one another, and the front is said to be fully developed. It is in this fully developed state that the study of the different effects in the bed can be studied, as all of the different effects within the bed are no longer changing the shape of the front.

2.1.3   *Methods of Regeneration and Desorption*

The nature of traditional adsorption processes relies on a cyclic operation where multiple beds are operating in parallel on a schedule always to be treating the feed and (ideally) producing the different products. As was mentioned earlier about different methods of performing the separation (diffusion-dominated kinetic vs. equilibrium-dominated thermodynamic), there are also different methods for regenerating the adsorbent bed and capturing the desorption product. As briefly overviewed in *Section 2.1.1.2*, the

driving force for the removal of adsorbate from the adsorbent surface is typically carried out via a temperature swing or pressure swing.

Temperature swing adsorption relies on the fact that adsorption is an inherently exothermic process, so increases in the adsorbent temperature results in a shift in the equilibrium of the three phases, moving adsorbate from the sorbed phase to the free gas phase. So, a bed of adsorbent, having been charged with a mixture of adsorbates, upon heating, will release some of the adsorbed phases. How much adsorbate will be removed depends on the shape of the isotherm, the heat of adsorption, and the change in temperature. Generally, temperature swing adsorption is considered the more energy-efficient method of recovering the adsorbed phase in a cyclic adsorption process, as might be desired in CO_2 capture. This is because the energy put into the process only acts on the mass in the system at the end of the adsorption step and is thus acting only on the product. In doing so, energy is not wasted on the undesired product. The purity and recovery of the products of temperature swing adsorption will be primarily controlled by the conditions used in desorption, with purge using high-temperature product gas from previous cycles oftentimes used to boost purity. Industrial TSA cycles suffer from long cycle times, as heating and cooling the immense beds of adsorbent can be a slow process.[18-19]

Pressure swing adsorption relies on shifting the local equilibrium of the three phases by removing gas (partial pressure of the adsorbate(s)) from the free gas phase, liberating the product from the adsorbed phase. The bed of adsorbent having been saturated at a given partial pressure of adsorbate having its overall pressure reduced will free molecules of the adsorbed phase. Like TSA, the amount desorbed will depend on how much had been adsorbed, as well as how much the pressure has been reduced. PSA cycles

can be operated at very rapid rates (>10 seconds), mainly when operating in a diffusion-controlled regime[15,20]. As TSA is seen as ideal for recovering high quality strongly adsorbed species, PSA is seen as the more efficient way to recover high quality weaker adsorbing species. Since PSA processes are often run near ambient pressures with recovery at vacuum conditions where the Henry's regime offers the highest selectivity for the strongly adsorbed species over the weakly adsorbed species. [2, 21]

2.2   Adsorbent Materials for CO_2 Capture

Adsorption, as the separation process for post-combustion capture, requires the optimization of three relatively different areas: materials, structures, and cycle design. Adsorbent materials are the surfaces that perform the separation. Structures deal with the manufacturing of the sorbents into handle-able macrostructures like pellets, fibers, and honeycomb monoliths.[22-26] Cycle design, therefore, deals with how energy, feeds, and products are integrated throughout the system to allow each bed to produce the products to the specification of the process. Each of these areas of separation and adsorption science feed-back and forward into each other, as a breakthrough in one area, may require considerable optimization in the other areas to realize the full potential of the discovery fully. As an example, the discovery of a new adsorbent material for the separation of ethane and ethylene may require the development of a new approach to structuring the material into a contactor while maintaining or enabling scalable manufacturing techniques, an in-depth study of conceivable cycle designs to optimize its application. Of the three, adsorbent materials are likely the most robust research area, where new materials are regularly being developed for separation applications.[27]

This section deals with developments in the area of adsorbent materials for application to CO_2 capture, particularly post-combustion capture from coal plants. A wide range of organic, inorganic, and hybrid materials are available for post-combustion capture, using both temperature and pressure swing adsorption. As the focus of this thesis is on sub-ambient adsorption via PSA, an abridged primer on the adsorbent properties desired for sub-ambient CO_2 capture adapted from Park et al. is included. That discussion is followed by a discussion of some of the major classes of adsorbent materials considered for CO_2 capture via adsorption, including carbons, zeolites, amine appended and impregnated materials, and metal-organic frameworks. A number of thorough reviews of these materials can be found in the literature[27-29], highlighting the benefits of each adsorbent for adsorptive CO_2 capture. A number of factors have been identified as desirable, including high selectivity for CO_2 over N_2 at relevant operating conditions, high capacity for CO_2, low-cost materials, and rapid adsorption kinetics.

2.2.1   *Desired Material Characteristics for Sub-Ambient CO$_2$ Capture*

As this work focuses primarily on the potential of sub-ambient CO_2 capture, it is useful to get an idea of the structural and sorption characteristics, which may prove to be especially desirable. The main advantage of operating at sub-ambient conditions versus closer to ambient conditions is the sharpening of the isotherm that leads to very high swing capacities. As noted earlier, swing capacities are not a performance parameter of the separation process itself, but increases in swing capacity will lead to higher potential productivities, a key parameter to the economic operation of adsorption systems. In *Establishing upper bounds on CO_2 swing capacity in sub-ambient pressure swing adsorption via molecular simulation of metal-organic frameworks*,[30] Park and co-workers

investigated some of the relationships between the structure of one class of adsorbent materials, Metal-Organic Frameworks (more general properties on these materials will be discussed later in this section), and the swing capacity of those adsorbents. This dissertation builds upon this analysis, taking the information about the desired adsorbent properties to inform the selection of the material for later sections. As such, this subsection offers a brief primer to the information gathered in that work and highly recommended that all readers further investigate the paper.

While a number of geometric characteristics of the MOF sorbents were investigated, two key parameters appeared to have a strong positive correlation with swing capacity at sub-ambient conditions. **Figure 2-5** shows the relationship between (a) pore volume and (b) accessible surface area and the swing capacity between an adsorption condition of 2 bar and a desorption condition of 0.1 bar and at a temperature of 243K. In both cases, with very few exceptions, increases in these variables result in increases in swing capacity. It is worth noting the accessible surface area is a different surface area measurement than those discussed earlier, as it is calculated *in-silico* through the rolling of a probe molecule along the porous surface of the structure. While there is some variance in the gains of additional surface area in the 477 materials considered, with few exceptions, materials having high pore volume and surface area result in very high swing capacities, exceeding those of some of the state of the art materials (Zeolite 13X and Mg-MOF-74) at room temperature, by as much as five times. Interestingly, the pore volume-swing capacity relationship becomes clearer when moving to lower temperatures (213K shown in Figure 2 of the referenced text), with the highest pore volume material having a swing capacity of >40 mol/kg.
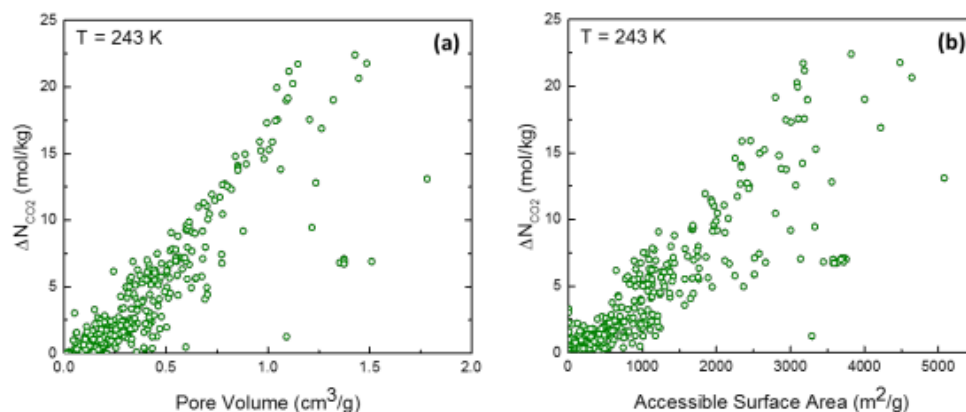
Figure 2-5. Effects of crystal geometry parameters on swing capacity (left) pore volume, (right) accessible surface area. Reprinted with permission © 2017 Royal Society of Chemistry

Other geometric parameters of the structure were also considered, in particular the material's largest cavity diameter and pore limiting diameter, each of which showed a positive trend as compared to swing capacity, but with more variance in the structure-property relationship. As this work was carried out *in-silico,* the authors were able to compare swing capacity to other adsorption parameters, particularly the heat of adsorption. Looking at the heats of adsorption which corresponded to materials exhibited very high (>10 mol/kg) swing capacities when their heats of adsorption were between 22-32 kJ/mol at 243 K. While there was some variability over the exact range as a function of temperature (some materials only had those capacities over small temperature ranges), regardless of temperature these materials.

2.2.2   *Solid supported amines*

One promising class of adsorbent materials for CO_2 capture are chemisorbent materials containing amine chemistries that act as solid adsorbent analogs to the promising materials used in absorption capture.[27] These materials allow for very high CO_2/N_2 selectivity due to the strong chemisorption driven by the amine's strong basicity interacting

with the acid CO_2 molecule. The amine and CO_2 molecule combine to form a zwitterion structure (**Figure 2-6**), which can then interact with another basic molecule, like a neighboring amine group, to form a stabilized carbamate. In a dried flue gas, two amines are required to form an adsorbed carbamate, but in humid atmospheres, the water molecule can act as the second base, allowing for more efficient utilization of the amine for the capture of CO_2.
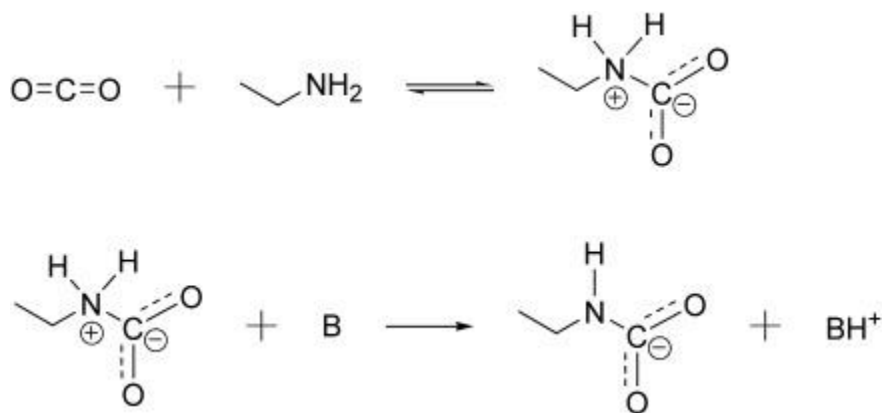
Figure 2-6. Chemistry of the formation of zwitterion and carbamate structure for solid-supported amine-based CO_2 capture.[27] Reprinted with permission Copyright © 2009 WILEY-VCH Verlag GmbH & Co.

A variety of different approaches have been taken to the creation of these amine supported materials, whether that be the filling or impregnation of the porous solid support with an amine, the chemical tethering of the amine to a structure, or the synthesis of support to introduce the amine. The first approach usually involves the soaking of porous support in amine or polyamine, where the amine molecule diffuses into the pore. Evaporation, whatever carrier solvent, is used leaves the amine trapped within the porous support allowing for capture. These impregnated amines are then available for adsorption. This impregnation approach is the easiest from a manufacturing perspective and can result in very high per volume uptakes of CO_2 per amine group added. Similar to absorption

processes, there are concerns about the volatilization of the amine under a temperature swing, though this has been limited to some extent through the use of polyamines, which tend to be less volatile. A drawback to the use of polyamines, and high loading of amines via impregnation in general, is the increased internal diffusion limitations, which may appear due to the decreased pore size of the amine loaded systems

A second approach to supported amines is the chemical tethering of amines to the pores of solid support. A variety of different chemical approaches can be taken to producing this second class of amine materials, particularly the use of silane chemistry or reactive surface polymerization. These approaches are slightly more complex from a scalable manufacturing perspective in comparison to the previously discussed impregnation methods but benefit from reductions in the volatility of the amines, as there is significantly better adhesion between the support and amines in the case of chemical tethering.

2.2.3   Carbons

Carbon materials, activated carbons, along with zeolites and metal oxides, remain the workhorses of adsorbent materials in industrial separations. The advantages of carbonaceous materials lie primarily in its relative cost efficiency as compared to zeolite materials, and their high surface areas as compared to other inexpensive sorbents. Depending on the application, activated carbons can be applied to a wide range of problems, due to their advantages in high surface area and low cost. Still, activated carbons typically have relatively homogenous surface chemistry's leading to less steep isotherm shapes for adsorption. Due to their wide availability over the past century, there has been

a great deal of time for the development of new structures and internal chemistries, which have been well-reviewed in the literature. [27, 31-34]

Activated carbons can be produced from a wide range of sources, like coal, biomass, to more complex sources of carbon like ionic liquids. The general approach to the production of activated carbons centers on a two-step process, involving first carbonization, then some form of activation. The procedures followed for these steps can vary widely depending on the carbon precursor, the desired morphology, and any chemistries that may be desired. The carbonization process involves the controlled heating of the carbon source in an oxygen-depleted environment, releasing the non-carbon species like hydrogen and oxygen as products. What is then left behind is an interconnected carbon structure, commonly referred to as "char." The char is then further converted and activated through some combination of additional heating to very high temperatures (1100-1250K), or chemical washing in strong

Unmodified activated carbons tend to have lower uptakes and swing capacities for dilute CO_2 separation as compared to MOFs, zeolites, and due to the weaker interactions between CO_2 and the carbon surface as compared to materials with stronger sorbing sites like MOFs or zeolites. This property makes them possibly better suited for applications working at very high partial pressures, like pre-combustion CO_2 capture. In such cases, their large pore volumes and surface areas allow for significantly higher capacities than many other microporous materials. [31]

The main area of interest in carbons for CO_2 capture has focused on Nitrogen-doped activated carbons, which work in a similar vein to the previously discussed solid-supported

amines. The acid-base interactions between the basic nitrogen groups and acidic CO_2 create a strongly sorbed CO_2 phase with heats of adsorption from 40-70kJ/mol. These heats of adsorption and typically weak sorption of nitrogen combine to make these materials ideal for temperature swing adsorption applications.

2.2.4 Zeolites

Zeolites are porous crystalline materials made up of a framework of SiO_4 and AlO_4 tetrahedron connections (sharing oxygen atoms so that a typical stoichiometric zeolite will be made up of SiO_2 and AlO_2 units). The tetrahedral connections form regular repeating patterns that are repeatedly produced synthetically through the use of organic structure-directing agents. The ratio of Si to Al is a critical parameter in the design of zeolite sorbents, where the ratio is no less than one and can be very high as desired, with aluminum-rich zeolites resulting in very hydrophilic structures. The typical synthesis of zeolites is via a solvothermal reaction of sodium silicates and sodium aluminates (sometimes as hydrogels) in a basic environment, where variables like mixing time, pH, temperature, reaction time, and the addition of organic additives (structure-directing agents.). The product zeolite can then be dried and calcined to produce final zeolite powders. [1, 27]

Due to the well-defined rigid crystal structures which can be produced as a part of a synthesis, zeolites have proven highly desirable for catalysis and adsorptive separations where a specific pore size might be desired. This tunability can be augmented post-synthetically with the incorporation or exchange of additional metal ions within the structure. A variety of ions (i.e., Li, Na, K) can be exchanged into different zeolite

structures post-synthetically for the purposes of either boosting the uptake and selectivity of the adsorbent or adjusting its pore volume to allow for molecular sieving like behavior.

Zeolite 13X has so far been the leading candidate for CO_2 capture[35], while a number of other zeolite materials, including 4A, 5A, NaY, and LiX, have also been considered.[36-37] X type zeolites exhibit higher uptakes of CO_2 at relevant pressures and very high sorption selectivity for CO_2 and N_2 makes it the ideal candidate among zeolite materials. Still, these materials suffer from abysmal sorption performance when the zeolite has been saturated with water, as the incorporation of H_2O within the structure removes selective sites from the zeolite cage, which would otherwise adsorb CO_2. Both temperature and pressure swing adsorption processes are considered options for post-combustion CO_2 capture using zeolite materials, as the materials show good regenerability characteristics, whether through increasing temperature or pulling vacuum.

2.2.5 *Metal-Organic Frameworks*

A developing area of adsorbent materials is Metal-Organic Frameworks (MOFs), organic-inorganic 2- and 3-D porous solid materials formed by coordination bonds formed between organic linkers and inorganic metal or metal-oxo clusters. MOFs have been formed from a wide variety of metals and linkers, allowing for the development of customizable pore geometries and pore chemistries, making them desirable for a wide range of applications like catalysis and gas storage along with adsorptive separations. [38-40]

MOFs are typically synthesized via solvothermal or hydrothermal methods where a metal or metal salt, an organic linker, are mixed in a solvent (or aqueous environment) and heated to elevated temperatures where the crystals form. A number of modifications

to this procedure have been adapted to control particle size, introduce or control crystalline defects in the structure, or produce crystals with multiple metals or linker chemistries. Post-synthesis, the product is typically washed repeatedly in a strong solvent environment to remove any unreacted metal or linker. Activation at elevated temperatures is usually required to remove any excess washing solvent from the pores. [40]

A number of different approaches have been taken for the purposes of producing MOF materials with ideal sorption performance for CO_2 capture via different adsorption performance. Variation in linker chemistry to introduce different functional groups (NH_2, NO_2, OH) within a MOF pore has been shown to offer one potential avenue to improving the strength of CO_2 sorption. MOFs with unoccupied metal sites, either by structural design or defect engineering, enable local, strong adsorption upon removal of adsorbed solvent from the pore. [41]

Recent work has worked on combining MOF materials with amines post-synthetically, either through impregnation with amines,[42] or via binding an amine to an unoccupied metal site within the structure. The second approach has proven particularly interesting for CO_2 capture applications as it has been shown to lead to CO_2 sorption isotherms exhibiting a "step," shown in **Figure 2-7**.[43] These step type isotherms, shown to form due to a chemical insertion of the CO_2 molecule between the amine and the open metal site and subsequent chain reaction down the pore of the structure, have shown significant potential for temperature swing adsorption applications. The location of the step as a function of CO_2 partial pressure has been shown to be tunable with the choice of amine, allowing for fine-tuning of the adsorbent performance for CO_2 capture. While the step in the isotherm leads to a very high selectivity for CO_2 over nitrogen, it also leads to a more

complex adsorption step, with the so-called "shock-wave-shock" behavior. Still, the developments of materials like this, taking advantage of the tunable chemistry of MOFs offers a window into potential future developments of these materials particularly for CO_2 capture applications.
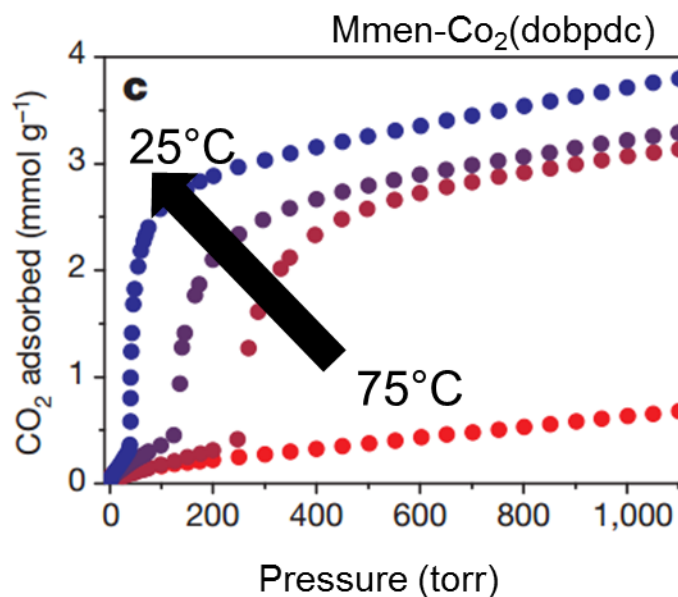
Figure 2-7. CO_2 Isotherms on Mmen-CO_2(DOPBDC) MOF adsorbent, showing "step" in isotherm at reduced temperatures. Reprinted with permission Copyright © 2015, Springer Nature

A significant challenge facing MOF's application to post-combustion CO_2 capture is the poor water stability exhibited by many MOF materials when interacting with humid environments. One of the first MOFs, MOF-5, is an excellent example of this poor stability, as when left out in ambient air, it will lose nearly all its porosity over 8-24 hours. Finding MOF materials with good humid stability remains a challenge for these materials for CO_2 capture, though the tunability of the pore and surface chemistry allows many pathways to be taken to produce materials with good stability in humid conditions. Like other adsorbent materials, many MOFs suffer significant performance losses when more complex mixtures containing simulating coal-fired flue gas are included in the CO_2 capture mixture. Typically

this leads to irreversible degradation of the structure, though approaches have been developed to regenerate the structure via solvothermal methods, and new materials are being developed, which offer greater stability in acid gas environments.[44-45]

2.3   Structured Sorbent Contactors

As new challenges in separations have emerged, a great deal of focus in the adsorptive separations community has centered upon the development of novel porous materials capable of achieving both high operating capacity and selectivity for the separation of interest.[27, 33, 43-44, 46-47] While these materials offer the opportunity for game-changing performance; this performance cannot be realized without considering the more practical methods of deployment. Indeed, factors including packing efficiency, pressure drop, sorption enthalpy management, and thermal integration will all play a role in the cycle time, size, energy demand, and ultimate performance of the sorbent.[1] Structured sorbent contactors like monoliths and fiber sorbents (**Figure 2-8**) offer an improvement over traditional pellet packed bed structures as they introduce additional degrees of freedom in bed design that enable efficient management of deleterious heat, mass, and momentum transport limitations present in traditional systems.
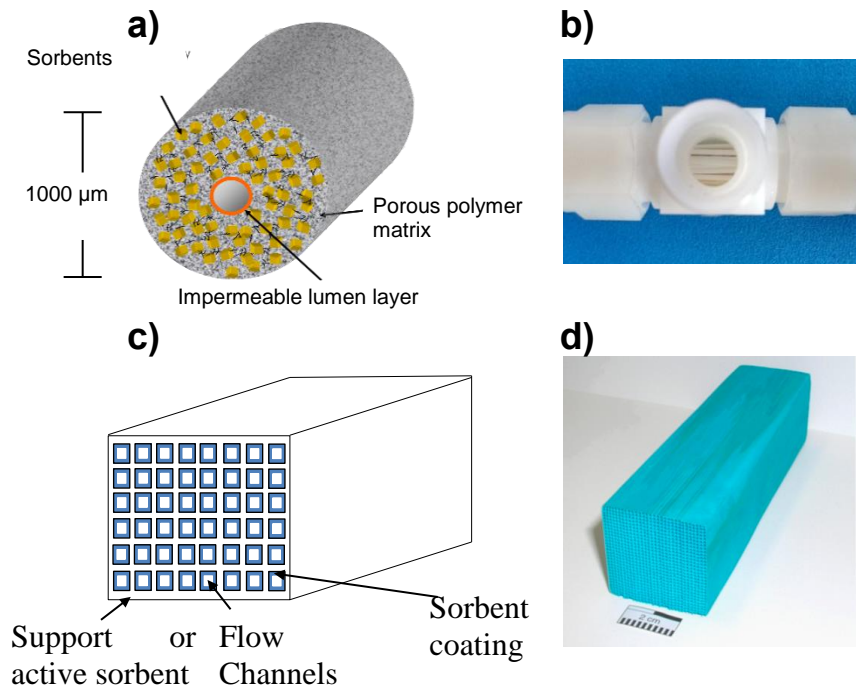
Figure 2-8. (a) Schematic cross-section of hollow fiber sorbent with impermeable lumen layer. (b) Example shell-side view of hollow fiber sorbent module comprising a 1" tube diameter module containing ~80 fibers. (c) Schematic cross-section of monolith contactor. (d) HKUST-1 extruded monolith Reprinted with permission, © 2018 Annual Reviews[22]

Koros, Lively, and coworkers first conceived the concept of hollow fiber sorbent contactors in 2009.[48-51] At a high level, hollow fiber sorbents are constructed in a fashion similar to mixed matrix polymeric hollow fiber membranes. In place of the selective skin layer that enables molecular separations in the asymmetrically porous membrane structure, the fiber sorbent structure is instead filled with adsorbent particles, dispersed throughout the asymmetrically porous polymer matrix. The porous matrix and absence of the skin layer allow for rapid transport of gas from the bulk phase outside the fiber to the sorbent particles supported within the matrix. These fibers can be packed parallel or perpendicular to fluid flow, enabling high sorbent packing fractions that exhibit straight channels between fibers in the former case, which significantly reduce pressure drop relative to particle-packed systems. The most critical benefit of the fiber sorbent platform is the availability of two

56

distinct fluid flow paths, i.e., through the bore of the fibers and about the shell of the fiber module. Incorporation of the impermeable lumen or sheath layers on hollow fiber sorbents has enabled novel localized thermal management in fiber sorbent systems.

Monoliths are solid contactors composed of parallel channels resembling a honeycomb structure. Monolithic contactors were first applied as three-way catalytic converters in the automotive industry for NOx reduction.[52] Monoliths have several advantages over packed beds, such as higher mass transfer rates, good attrition properties, and lower pressure drop, but this is balanced against typically a lower loading of sorbent per unit volume. Beyond catalytic converters, there have been several applications of monoliths for separations and reactions, such as chromatography,[53] catalytic combustion,[54] bioseparation and bioconversion,[55] gas adsorption processes[25, 42, 56] and multi-phase reactions.[57] Lower pressure drop in the case of monoliths is particularly favorable in gas separation processes[58] since it results in lower energy consumption associated with physically moving larger volumes of gas through the contactor. Monoliths can either be made entirely of the sorbent material, as when the sorbent material is directly extruded with no binder, or with some fraction of sorbent dependent on ratios of binder/sorbent/monolith body, as is the case with many deposition or growth methods.[25, 34] A variety of geometric and material properties, like wall and channel dimensions, wall porosity, and heat capacity, among others, play a significant role in the performance of monolith contactors.[26]

2.3.1 Manufacture of Fiber Sorbents

Traditional methods of production where the sorbent is incorporated during fabrication of the contactor generally are less manufacturing intense but require high

mechanical and chemical stability of the sorbent. Recent advances focused on incorporating the sorbent material into the adsorption device post-fabrication of the contactor help overcome stability limitations associated with traditional methods. In the case of hollow fiber sorbents, the installation of the impermeable barrier layer and its effects on the adsorbent activity or stability needs to be carefully considered. Nevertheless, this additional fabrication step is a crucial enabler for many of the advantages of hollow fiber sorbents (i.e., advanced heat management solutions).

Fiber sorbent production is similar to that of hollow fiber membranes, i.e., a polymeric dope containing polymer, solvent, non-solvent, pore-forming agent, and sorbent particles is mixed to form a dispersion of particles within a polymer solution, with compositions falling on a ternary phase diagram like that shown in **Figure 2-9**. This dope is then extruded through a spinneret through an air gap, into a nonsolvent bath (typically water), where it undergoes rapid phase inversion and forms a porous polymer network with sorbent particles dispersed throughout.[48, 59] For fiber sorbent spinning, the primary key is reducing the time in the air gap as much as possible, to reduce the likelihood of vitrification at the filament surface. This is the most significant divergence from membrane spinning (outside of the adsorbent addition to the dope at high volume loadings), as this vitrification is required for membrane performance.

The method of producing the sorbent-containing dope is somewhat more complicated than a membrane dope preparation, primarily due to the repeated sonication and stirring steps required to provide a good dispersion of sorbent particles within the dope. A "prime" dope is produced in advance, containing some fraction of the polymer-solvent-nonsolvent-pore former. This prime dope is incorporated after preliminary dispersion of

the sorbent in the remaining solvent and non-solvent to increase the viscosity and stabilize the dispersion via adsorption of polymer chains onto the surface of the sorbent particles.[49-50] The as-spun sorbent-containing fibers undergo solvent exchange in nonsolvent to remove any residual solvent and are finally dried to remove non-solvent. A complete flow diagram, including the steps involved in introducing a barrier layer and any additional sorbent production and modification steps, is given in **Figure 2-10**.
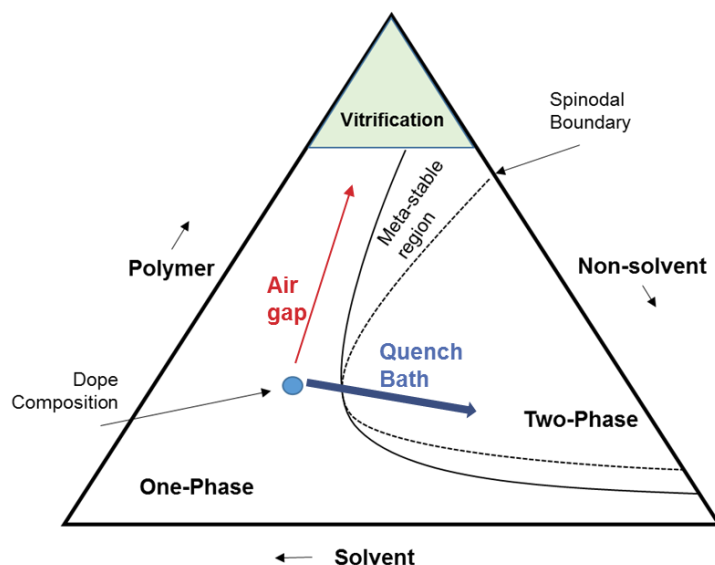
Figure 2-9. Example ternary phase diagram for fiber spinning

The first fiber sorbents were spun in this direct manner utilizing zeolite 13X[51, 60-61], and later zeolite NaY[62] with sorbent loadings as high as 75 weight fraction (wt.%). MOFs with stability in the presence of water, solvents, and sonication can also be spun in this manner; Chen et al. fabricated UiO-66 MOF fiber sorbents at 75 wt.% MOF loading for mercaptan removal from natural gas streams.[63] Other MOFs, such as MIL-53(Al) and HKUST-1, were found not to be fully resistant to the spinning process, thus highlighting the importance of MOF stability to the rapid fabrication of structured sorbents.

Methods exist to synthesize the adsorbent after fabrication of the contactor, a useful workaround for promising materials that are not sufficiently stable for spinning but are likely stable under process conditions. Post-fabrication synthesis of the adsorbent has been utilized to create hollow fiber sorbents with oxide-supported amine materials supported within the walls of the fiber. Labreche et al. discovered that both "Class 1" and "Class 2" type solid-supported amines[27] wash out of their mesoporous silica supports during the hollow fiber spinning process, thus rendering the hollow fiber sorbent device inactive.[64] The authors hypothesized this was likely due to some combination of sonication in spinning solvents and prolonged exposure to water in the quench bath. This loss of active adsorbent was overcome by introducing the amine molecules into the hollow fiber solvent exchange step of the spinning process. This approach was found to yield amine loadings in the hollow fiber sorbent that were comparable to amine loadings in control powder samples, thus highlighting the utility of this technique. This procedure was the first instance of post-spinning sorbent modification in fiber sorbents and was extended to a number of other polymers, [65] porous solids,[66-67], and amine functionalizations. [68]
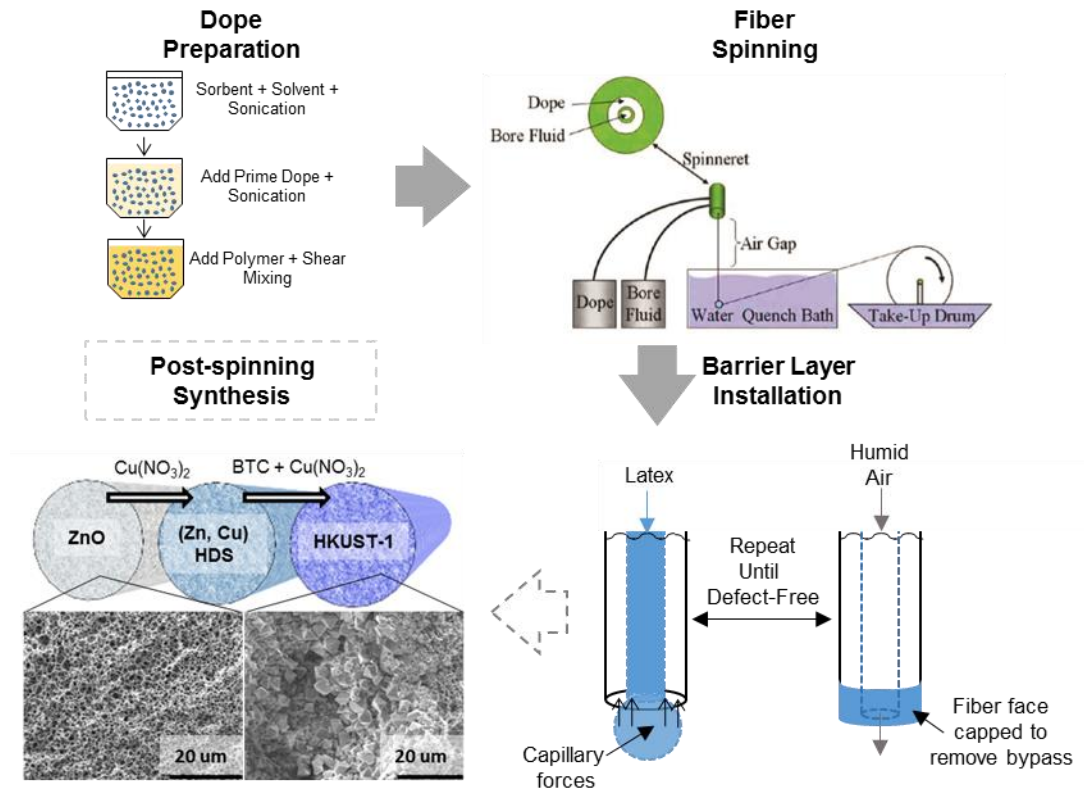
Figure 2-10. Flow diagram describing the processing steps involved in hollow fiber sorbent production. Reprinted with permission, © 2018 Annual Reviews[22]

Other work focused on using the polymer backbone of a fiber as a site for amine functionalization. Working with polyamide-imide hollow fibers, Li and co-workers utilized a ring-breaking mechanism to graft PEI into the polymeric matrix directly.[69] Although successful, the limited surface area and pore volume of the polymer-only fiber sorbent resulted in relatively low CO_2 capacities with substantial mass transfer resistance. Work by Pang et al. overcame this issue by utilizing polymers of intrinsic microporosity (PIMs) fiber sorbents as "binderless" support for polyamines.[70]   Here, PIM-1 was fabricated into a hollow fiber sorbent and was infused with PEI during the solvent exchange process. The resulting CO_2 capacity and uptake kinetics rivaled powder forms of oxide-

supported amine materials, but with the clear advantage of already possessing the structured contactor morphology.

More recent work focusing on post-fabrication adsorbent synthesis has centered on the synthesis of MOF within pre-made fiber sorbents containing a solid precursor that serves as a precursor for MOF crystallization. Parsons and coworkers utilized such a strategy to grow water-sensitive MOFs onto the external surfaces of electrospun nonwoven fiber mats.[71] Metal oxide was converted to a reactive intermediate, called a hydroxy-double salt (HDS), which upon mixing with the linker solution, rapidly converted to MOF. Pimentel et al. utilized this HDS intermediate approach to convert oxide-loaded fiber sorbents into MOF-loaded fiber sorbents shown as post-spinning synthesis **Figure 2-10**.[16] In this work, HKUST-1 was utilized as a "proof of concept" of the post-fabrication synthesis technique. The traditional spinning of HKUST-1 resulted in the dissolution of the MOF and an inactive fiber sorbent. Cellulose acetate-ZnO fibers were spun and then loaded into the adsorption module and the ZnO was subsequently converted to HKUST-1 via the hydroxy-double-salt intermediate, attaining extremely high weight loadings (85 wt.%). As conversion was carried out inside the adsorption bed, the sorbent was kept in a moisture free environment throughout bed activation and utilization. The HKUST-1 containing bed is the first instance of a water instable MOF being incorporated into the fiber sorbent platform. Importantly, this approach showcases that water-sensitive MOFs can be grown directly into an adsorption module and subsequently flushed with inert gas for storage before being put into service. This is analogous to the activation and storage of water-sensitive zeolite materials (e.g., LiX), and suggests that the path to

commercialization of certain MOF materials is more straightforward than originally thought.

Both during and post fiber spinning fiber sorbent contactors can be augmented with an impermeable lumen on the outer or inner wall of a hollow fiber sorbent to enable heat management. In analogy to the installation of the adsorbents, the barrier layer either can be directly spun along with the hollow fiber sorbent structure or can be installed post-fabrication in secondary post-treatment steps. Bhandari et al. directly fabricated the barrier layer and the porous core together using a dual-layer using a co-extrusion process.[72] They studied the impact of various spinning process parameters on the quality of the obtained barrier layer, finding high viscosity sheath dopes were best for producing a thin, dense sheath layer. The impermeable layer produced during spinning was extremely defective, producing near Knudsen selectivity of O_2/N_2. Labreche et al. explored methods to directly spin the barrier layer on the lumen-side of the fiber.[73] While effective at drastically reducing gas transport rates from the bore side of the fiber to the shell side of the fiber, these fibers ultimately required secondary post-treatments to seal the lumen-side barrier layer fully. Indeed, the direct spinning of a lumen-side barrier layer does not remove the "lumen layer bypass," a leakage pathway identified by Lively and co-workers that must be mitigated to avoid contamination of the shell- and bore-side fluids during operation[51]. Secondary post-treatments of the fiber sorbents typically involve repeated flowing of a barrier polymer latex or solution (comprised of a solvent that acts as a non-solvent for the fiber sorbent matrix) through the bore of the fiber, which creates the lumen-side barrier layer (**Figure 2-10**).[74] Critical consideration must be given for the cases where thermal modulation is not a paramount issue in the adsorptive separation, as, in these situations, the

63

extra costs associated with installing the barrier layer (which enable thermal management) may not be justified.

Sorbent loadings in fiber and monolithic contactors can vary greatly depending on the methods of manufacture, and with few exceptions, sorbent loading when compared to traditional systems like pellet packed beds drops when moving to either fiber or monolithic sorbent contactors. This is a critical point to consider in the design of adsorption systems— if parameters such as pressure drop (loss of energy) and heat effects (reduced efficiency of the adsorbent) are not paramount features to mitigate in the separation process, then it is likely that the added complexity of the structured contactor is not necessary.

2.3.2   *Sorbent Loading*

Traditional adsorption systems utilizing pellets or powders can reach 100 wt.%, therefore volumetric loading (the actual figure of merit for sorbent loading) is then only a function of packing density. Incorporating organic or inorganic binders in these systems to give additional mechanical stability results in a direct reduction in volumetric loading. Fiber sorbents can generally reach 50-75% w/w solid sorbent, depending on the properties of the sorbent utilized. MOF and zeolite species have generally been shown to be spinnable up to 75% w/w[51, 63], while porous ceramics, e.g., mesoporous silica, have only been able to reach sorbent loadings slightly exceeding 58% w/w[64]. The maximum loading of sorbent in the fiber is determined when the polymeric dope can no longer be spun into continuous fibers spinnable, usually due to high viscosity dopes leading to line breaks. This upper ceiling of solids loading has been exceeded in cases of post-spinning sorbent growth (Section 3.1), where solid loadings of as high as 85% w/w were reached. Like fibers,

monolith sorbent loading can vary depending on the method of manufacture, direct extrusion of the sorbent will result in high loadings rivaling traditional systems, and activated carbon monoliths may exceed traditional systems if their void fraction may be reduced beyond pellets[25]. Coating honeycomb monoliths will lead to lower volumetric loading then direct extrusion due to the required mass of inactive support.

Taking as a base case, the use of zeolite 13X structured sorbents and assuming identical void fraction (0.43) allows us to compare approximate volumetric loadings for each structure. For the pellet case, with no binder, volumetric loadings of 0.86 g/cm^3 are achievable. Extruded monoliths with 10.5% binder had a similar volumetric loading of 0.77 g/cm^3, while wash coated 1200cpsi monoliths with a 10µm adsorbent layer (7.5% w/w) give loadings of ~0.05 g/cm^3. Fiber sorbents with 75 w/w loading and 50% porosity in the fiber give 0.38 g/cm^3. These differences in volumetric loading are essential factors in the design of an adsorption process and clearly show that mitigation of one or all of the aforementioned deleterious effects (e.g., pressure) must be the driver for the selection of structure contactors.

2.3.3 *Mass transfer in structured sorbents*

The mass transfer rate of sorbate from the gas phase to the adsorbed phase is the key parameter that determines the efficiency of the sorption process, or more specifically, the efficient utilization of the adsorbent material. In both the conventional bed as well as the structured sorbents, two major diffusion resistances that the adsorbate are encountered prior to sorption in the adsorbent material. One is the diffusion resistance in the gas phase, often referred to as external diffusion resistance, and the other is the diffusion resistance

within the composite sorbent structure, commonly referred to as internal diffusion resistance. Depending upon the structure within the sorbent, the internal diffusion again can have different components, each having different orders of diffusion resistance. For example, in the pellet sorbent, the internal diffusion includes the diffusion through the macropores that exist between the binders and the sorbent particles and between the sorbent particles, as well as diffusion through the micropores that exist within the sorbent particle. The macropores that are formed during the pellet formation are typical of diameter (0.1 μm - 1 μm) [75]. In addition to the diffusion resistance, the rate is directly proportional to the interfacial area, i.e., surface area per unit volume of the sorbent. Although the pellets have a higher interfacial area ($A_{bead} = 3/r_p$) compared to the structured sorbents ($A_{fiber} = 2r_f$, $A_{monolith} = \frac{2r_{im}}{r_{om}^2 - r_{im}^2}$) at equivalent characteristic lengths, this is more than compensated by the smaller characteristic length in the structured sorbents enabled by significantly reduced pressure drops in these systems relative to the pellets. As an illustrative calculation, reduction of the characteristic length of a fiber sorbent by 4x relative to a pellet increases the pressure drop by a factor of 15, which is still well below that of the pelleted system of 1x size, while realizing higher mass transfer areas per unit volume than the pellets.

The external diffusion resistance can be reduced by flowing the gas at higher velocities as the gas film mass transfer coefficient is directly proportional to Reynold's number. However, the pressure drop of the pelleted sorbents in packed beds is prohibitive at higher velocities and therefore enforces limitations to the extent to which the external mass transfer resistance can be minimized. In the case of structured sorbents, to the contrary, it is possible to design the contactor dimensions such that external diffusion

resistance can be minimized. The internal diffusion is limited by the size of the macropore in both the structured and pellet sorbents. Here again, there exists a trade-off that needs to be balanced between the size of the pore dimension that can be achieved while simultaneously not sacrificing sorbent loading density in the pellet or in the fiber/monolith. In addition to increasing the size of the macropore, the diffusion length also needs to be minimized to minimize the internal diffusion resistance. In the case of pellets, the size of the pellet/pellet determines the diffusion length, and in the case of the hollow fiber, it is the thickness of the fiber or the diameter of fiber for a solid fiber. For a monolith, the film thickness (if porous) determines the total diffusion length; otherwise, the half wall thickness determines the total diffusion length. In each of these cases, although it is beneficial to have the smallest diffusion length as possible, it may be either physically challenging in synthesizing as in the case of very thin fibers and thin-film coating for the monolith, or it may pose additional challenges in terms of mechanical strength as in case of small pellets.

2.3.4   *Pressure Drop*

One of the main advantages of structured contactors relative to traditional conventional pellet-based packed beds is the lower pressure drop of the structured system. The structured contactors, as the name suggests, offers a more regular passageway for gas flow, as opposed to the highly tortuous passageway involving higher viscous drag for gas flow in the pellet case. A quantitative comparison of the pressure drop incurred in both the types of structured contactors against the packed bed is provided in **Figure 2-11**. The characteristic particle size is maintained at the same value among all the contactors. By characteristic dimension, we mean the particle diameter in the case of packed bed; the

channel diameter in the case of the monolith and the outer fiber diameter in the case of hollow fiber are all maintained at the same value of 2.5 mm. In addition, the length of the contactor and the void fraction are maintained at 1 m and 0.43, respectively, in the comparison. However, in the case of the monolith, the void fraction of the entire monolith has no bearing on the pressure drop as the gas flows through the hollow channel and therefore is dependent only on the channel inner diameter. The pressure drop for the monoliths is calculated using the Hagen Poiseulle equation,[42], which is applicable for the low-pressure gases considered in this proof-of-concept analysis. The void fraction of the hollow fiber sorbent module $\left(\phi_m = \frac{A_{fibers}}{A_{module}}\right)$ determines the cross section through which the gas flows. Therefore, the void fraction is kept at 43% as in case of the packed bed and Happel's equation is used to calculate the pressure drop for fiber sorbents[76]. Finally, for the packed bed, the Ergun equation is used. As seen in **Figure 2-11**, both the structured contactors exhibit significantly reduced pressure drops compared to packed beds, whose value is nearly higher by a factor of 15-40 times compared to that of structured contactors, and this effect grows at higher gas throughputs. In essence, at constant pressure drop, structured contactors can realize gas throughputs that are 15-30x found in pellet-packed beds, which is typically sufficient to offset any differences in adsorbent loading between the structured vs. pellet systems.
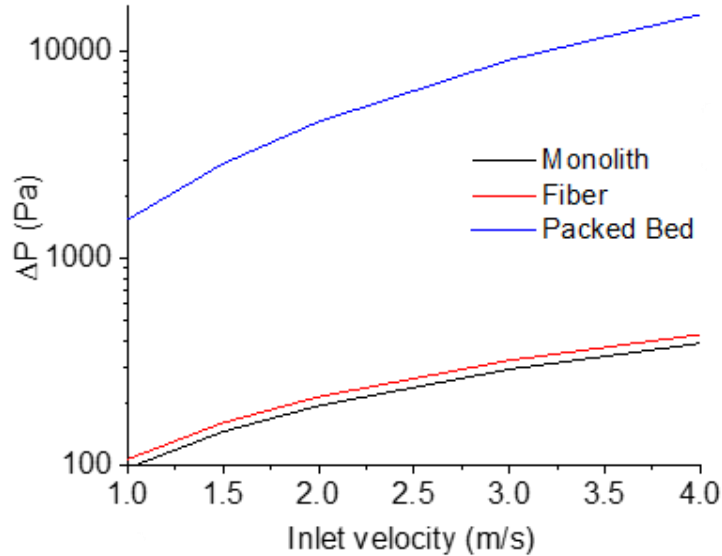
Figure 2-11. Comparison of pressure drop in differently structured sorbent contactors with the same characteristic dimension ($d_p = d_o = d_{im} = 2.5$ mm) and bed void fraction =0.43 for CO_2 sorption with zeolite 13X. Reprinted with permission, © 2018 Annual Reviews[22]

2.3.5   Sorption Enthalpy Management in Cyclic Adsorption Systems

Thermal fronts develop as a result of the sorption enthalpy generated or consumed during adsorption-desorption cycling, and these lead to substantial inefficiencies in practical adsorption processes. At the lab scale, the effects of thermal fronts are minimized by small module size allowing wall leakage to dominate, which often leads to researchers neglecting the importance of heat effects in adsorptive separation processes. At industrial scales, the process approaches adiabatic behavior, and the rate of heat transfer from the bed cannot keep up with the rate of heat generation.[1-2] Novel adsorbent contactor architectures enable efficiency gains via incorporation of thermal modulation or other advanced heat transfer solutions capable of containing or removing sorption enthalpy from the system. Successfully controlling thermal excursions in the system reduce mass transfer

inefficiencies, reduces cycle times, improves capacity, and can enable heat integration of the sorption system with other systems requiring process heat.

Hollow fiber sorbents have shown great promise for the effective management of sorption enthalpy, as the introduction of a bore region in the fiber allows heat transfer fluids to be flowed down the center of the fiber, thus removing the sorption enthalpy as it is generated. The installation of the impermeable lumen layer on the fiber keeps the heat transfer fluid (most often water) contained within the bore such that heat is transferred from the sorbent-packed annular region of the fiber to the flowing heat transfer fluid, which effectively keeps the fiber isothermal during adsorption/desorption. Lively and co-workers showed that for zeolite 13X/cellulose acetate hollow fibers with a polyvinylidene chloride barrier layer installed on the bore side, flowing water through the bore allowed for the isothermal or near isothermal operation of 1/4" tube modules during CO_2 adsorption. Additionally, the use of bore cooling in their hollow fibers allowed for consistent breakthrough capacity even at higher superficial gas velocities, thus enabling shorter cycle times without sacrificing capacity.[60] It was postulated this generated heat could be used as a heat source elsewhere within the separation so long as the quality of the generated heat would be applicable to the separation process in question[13].

Enabling the efficient use of new sorbent materials with high capacities will require engineered systems to contain and manage heat, as the amount of sorption enthalpy released scales directly with operating capacity and adsorbate flow rate. With this in mind, some authors have considered strategies to manage or remove this heat. The heat released during adsorption and withdrawn during desorption, termed sorption enthalpy, causes a broadening of the adsorbate breakthrough front due to the temperature increase. This

inefficiency in the sorption dynamics leads to additional sorbent being required to reach separation targets. Management of the heat to improve sorption dynamics may serve as one approach to drive down sorbent requirements for adsorptive separations. This need is even more necessary in sub-ambient CO_2 capture from coal plants, where high flow rates and high sorption enthalpies are the norms. The expectation is these effects will be exacerbated at the industrial scale for sub-ambient capture, where convection to the surroundings will no longer manage the heat release[25]. Indeed, in the case of sub-ambient CO_2 capture, where energy is being expended to operate at cold conditions, heating inside the process is effectively wasted energy.

Methods for managing sorption-induced heat generation use a variety of factors, ranging from bed geometry and sorbent structure to regeneration methodology and utility availability. To simplify the discussion, we propose broadly categorizing different heat management methods based on the nature of the management strategy (i.e., "active" versus "passive") and the nature of the contact with the sorbent (i.e., "internal" versus "external"), as visualized in **Figure 2-12**. Distinguishing between active and passive strategies may be done by drawing a system boundary around the sorbent bed (black dotted lines in **Figure 2-12**). If any material streams besides those involved directly in adsorption (i.e., the stream containing the adsorbate) cross the system boundary, the management method is defined as "active." Conversely, a passive method will only have adsorbate streams cross system boundaries; i.e., no heat transfer fluids cross the boundary. Distinguishing between internal and external methods involves drawing a boundary around an individual sorbent contactor (pellet, monolith, laminate, fiber) inside the bed (green dotted lines). If the management method is located inside the boundary, regardless of which pellet or other structure inside

the bed is selected, the method can be classified as "internal." As an example, a traditional heating jacket on a zeolite pellet bed would be considered active external thermal management. A heating jacket with tubes running through the bed would still be considered active and external because not all sorbent structures experience the same effect of the strategy.
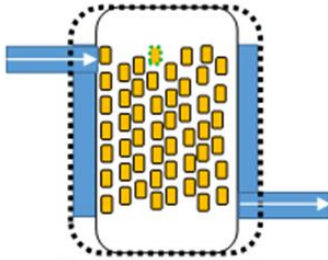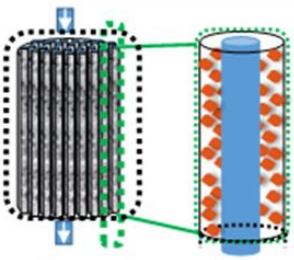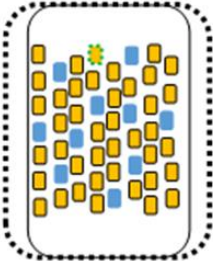
Figure 2-12. Methods of heat management in adsorption systems

For thermal management in PSA systems, passive thermal management methods may be preferred to simplify the installation and operation of the unit. Incorporation of a phase change material (PCM) into the sorbent bed to trap sorption enthalpy has garnered interest in the patent literature[77-80], as well as several recent process modeling studies[81-82]. Conceptually, the phase change material works as a thermal ballast, melting at or near the

operating temperature of the adsorption device, and storing the heat of adsorption in the heat of fusion of the PCM. Upon depressurization and desorption, heat is withdrawn from the PCM, solidifying it, thus keeping the system close to the desired operating temperature. This coupled adsorption-melting / desorption-freezing cycling should help to manage effectively thermal fronts generated by the sorption process in the bed. In traditional pellet systems, large containers of phase change material are loaded into the bed with the sorbent pellets to help contain the heat released; however, the heat transfer efficiencies in such systems may be lacking, so that the additional cost of the PCM may not always be justified.

In a study looking at phase change material application in a CH_4 storage system, Toledo et al. found that spheres of PCM allowed for more rapid pressurization and managed the heat near the PCM, but could not capture the heat from further away[83]. Several authors have considered how to improve the distribution of PCM throughout the adsorbent bed. Regardless of approach, incorporation of PCM results in a natural tradeoff: the volume the PCM takes up in the bed cannot be used for sorbent. The use of smaller PCM capsules has been considered before, but the use of microencapsulated phase change material (μPCM) has been dismissed in traditional packed beds as the small size leads to excessive pressure drop or may become entrained in the flow[81].

To circumvent this PCM distribution problem, Lively and co-workers[84] used zeolite-NaX-containing hollow fibers packed in a shell-and-tube configuration to distribute sorbent and PCM throughout the bed. In the shell-and-tube modules, a feed gas of CO_2 and He were fed through the bore of the fibers, while the PCM packing in the interstitial space surrounding the fibers in the module helped contain the sorption enthalpy release. They found the PCM was able to keep the fibers almost entirely under isothermal conditions. In

73

these thermally modulated fiber sorbents, sorption performance was enhanced, with increased CO_2 capacities and sharper breakthrough fronts.

2.3.6 Integrated Temperature Swing

A key enabler for energy-efficient temperature swing adsorption processes is the ability to introduce the heat and cooling of the bed required to regenerate the bed and return it to adsorption conditions, respectively. The amount of heat required to reach bed regeneration conditions makes up the majority of the energy demand of such systems, so providing heat to the sorbent in an efficient manner is key to driving down costs.[85] Structured sorbent contactors allow for new approaches to heating and cooling the bed, as the incorporation of new materials and hierarchical structures into the bed may allow for more localized heating and cooling of the sorbent, thus driving down cycle times and lowering net energy requirements. Competing with this more efficient heat delivery or removal is the additional thermal mass incorporated into the system to give it structure, for fibers the polymer, for monoliths any binder or support[42], as shown in **Figure 2-13**.
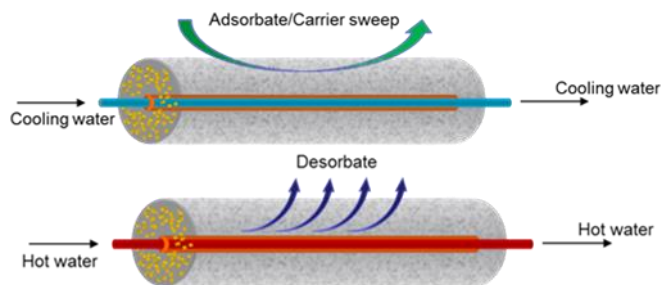
Figure 2-13. Schematic illustration of hollow fiber RTSA[51]. Adapted with permission Copyright © 2009, American Chemical Society

In the case of hollow fiber sorbents,[51] the sensible heat of the beds can be efficiently transferred to water flowing through the bore side of the fiber such that this heat is

effectively recovered and can be used elsewhere in the TSA process. Similarly, hot fluid or steam can be provided to the bores to heat the fibers, allowing for more rapid cycling86 locally. Eisenberger proposed the idea of utilizing steam as a stripping agent for monolith contactors, where the condensation of steam on the monolith surface provided rapid localized heating for TSA processing. [86-87]

2.4   Fundamentals of Pressure Swing Adsorption

Commercial gas separations with solid adsorbents using pressure swing adsorption have been developed since the 1960s, used for the separation of gas mixtures where significant differences exist between either adsorption isotherms or diffusion of the different components[2, 21, 88]. In a typical PSA system, the products are two separate gas streams, an elevated pressure "light product," which is the weakly adsorbed species found in the effluent of the gas produced during the feed or adsorption step, and a lower pressure "heavy product" made up of purified strongly adsorbing species recovered when the bed is regenerated. At a fundamental level, a cyclic steady state, the mass transfer front of the strongly adsorbing species (described in Section 2.1.2) transverses the bed axially, effectively oscillating closer (feed step) and further (regeneration step) from the end of the bed, as shown in **Figure 2-14**.
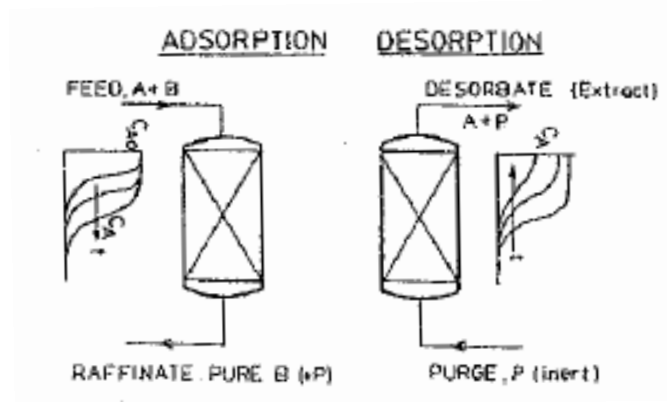
Figure 2-14. A simple schematic of the PSA process, illustrating adsorption and desorption steps and the concentration profiles expected in each step. Copyright VCH Publishers 1994 [2]

Industrially PSA processes are used primarily for the purification of the light product (N_2 in the case of CO_2 capture), as the oscillation of the mass transfer front inside the bed can enable very high purities of that product if the heavy product front is never allowed to leave the bed. Typical industrial applications of this behavior in PSA systems would be oxygen generation from the air using zeolite adsorbents. In that case, the N_2 mass transfer front is never allowed to leave the adsorbent bed, enabling very high (99.9999%) purity oxygen products.[2]

PSA processes have been under development since as early as the 1930's via the use of a vacuum swing, though the application of these processes is most often attributed to Skarstrom, who patented a process using a gas purge for regeneration. As compared to other separation processes like distillation absorption, or membrane processes, perhaps the most significant difference is, in fact, PSA (and all adsorption processes) operate as cyclic processes and are thus inherently transient non-steady state in nature. This introduces additional complexity into their operation and control, but also offers opportunities for the optimization of the cycle to enable better performance without requiring significant

changes to the actual process. Methods of improving performance will be reviewed in the following sections, and generally focus on connecting different beds to reduce losses or improve energy efficiency.

2.4.1   *The Skarstrom and Linde Processes, Simplified PSA for light product purification*

The two original PSA processes, Skarstrom and Linde, can be thought of as virtually the same, except for a slight variation in the final regeneration step.[2] The Skarstrom cycle was used for dehydration of gas streams, where the recovery of water was of no concern. So that the feed gas was continually being treated, the Skarstrom cycle used two beds so that when one bed was treating gas, the second bed would be in some stage of regeneration. The process was a four-step cycle: 1. Pressurization with feed, 2. Feed, where dehydrated gas was produced, and water was held up in the bed, 3. Blowdown, where the column's pressure was reduced to atmospheric, and 4. Light product purge, where some of the product from the feed step of the second bed was swept over the blown down bed to regenerate it. This process resulted in very high purity light product gas at the cost of reduced recovery due to the sweeping with the product. The use of the light product purge to regenerate the bed made sense in the case of dehydration, as the humid final product was of no value, so the purged gas would simply be vented. This was, and remains the main challenge of PSA processes, they are very good at purifying the poorly adsorbing light product, but the quality of the strongly adsorbing product is limited by the adsorbent itself.

The Linde Process, developed around the same time, was developed in part to be able to also capture the heavy product through regeneration through reducing the pressure further through pulling a vacuum on the sample. By pulling the vacuum in place of the

light product purge, more light product could be captured, increasing recovery. At the same time, recovering the heavy product with vacuum meant that product was less dilute and closer to the composition of the adsorbed phase, enabling higher purity of the heavy product. The main cost to such a process as compared to the Skarstrom cycle then is the additional capital and energy required in operating the evacuation step, which ideally is offset by the increased recovery of the light product as well as the increased purity of the heavy vacuum product.

2.4.2 Cycle design to improve performance

These two basic approaches serve as the baseline designs for pressure-swing-adsorption systems[2]. Neither process alone is expected to be especially good at the purification of the heavy product, as is the goal of a CO_2 capture process, but a number of additional steps to these cycles have been developed to improve the performance for either purification of the light product or the heavy product. Four performance parameters are used throughout the PSA literature to judge the quality of the process for a given application the purity, recovery, productivity (or bed size factor), and the specific energy. Each of these parameters can be determined for either or both of the products depending on the goals of the cycle (for CO_2 capture, they would typically be discussed per mole of CO_2 product produced in the heavy product stream).

The purity and recovery are likely the most straightforward parameters to understand, as they are variables that determine the quality of the separation focused on the product. The purity is defined as the mole fraction of the product stream, which is made up of the desired molecule (mole %). The recovery then is defined as the moles of product in

the product stream versus the moles of that component, which enters the system in each cycle (mole %). Generally the higher these values are the better. For post-combustion CO_2 capture, they can be defines as follows:

$$Purity = \frac{moles\ of\ CO_2\ in\ product\ step}{total\ moles\ of\ gas\ in\ product\ step} \qquad (2\text{-}4)$$

$$Recovery = \frac{moles\ of\ CO_2\ in\ product\ step}{moles\ of\ CO_2\ in\ feed\ and\ pressurization\ steps} \qquad (2\text{-}5)$$

The productivity is a parameter designed to determine how efficiently the product gas is being produced per mass of adsorbent or volume of adsorbent bed, per unit time. Sometimes the inverse of the productivity termed the *bed size factor* is used for comparisons instead, but this distinction is purely a matter of preference. Like purity and recovery, increasing productivity is generally desired for any application, as improvements in productivity mean the system size can be reduced (less adsorbent used). There are generally two approaches to increasing productivity, either a new adsorbent can be used with a more desirable isotherm or better adsorption kinetics, enabling higher recovery of product per unit mass or volume, or the cycle time is reduced.

$$Productivity = \frac{moles\ of\ CO_2\ in\ product\ of\ one\ cycle}{mass\ of\ adsorbent \times cycle\ time} \qquad (2\text{-}6)$$

Finally, the specific energy is the parameter designed to capture how energy efficient the process is per mole of gas produced. Unlike the previous three values, ideally, this value is as small as possible. The energy required to perform a cycle can be estimated given the high and low-pressure conditions and the total number of moles of gas expected to enter and leave within those steps (for TSA, this can be estimated as the heat energy put

into the process, plus the energy required to overcome pressure drop) assuming no energy recovery of the high-pressure product. For post-combustion CO_2 capture using both elevated pressure and vacuum, the specific energy can be defined as:

$$Specific\ Energy = \frac{Energy\ required\ to\ pressurize\ the\ bed\ and\ feed + Energy\ required\ to\ pull\ vacuum}{moles\ of\ CO_2\ in\ product\ of\ one\ cycle} \tag{2-7}$$

When considering developing a PSA process for any application, the goal is to optimize these parameters, reaching at least the minimum required values of product purity, recovery with the highest productivity and lowest specific energy. A number of intrinsic tradeoffs exist when trying to optimize, but in general, higher purities are expected to result in lower recoveries and vice versa. Similarly, higher productivities are expected to be higher operating pressure, and lower vacuum pressures usually improve the result of more energy being put into the process, as sorbent performance. Similarly, more complex cycles can be operated to reduce the specific energy, but will typically increase the cycle time or reduce the total amount of gas treated as a byproduct.

As the most basic PSA cycles are designed more for the production of high purity light product (expected to N_2, O_2, Ar in a post-combustion CO_2 capture process), it is very likely a more complex PSA cycle will need to be employed to allow for the high purities and recoveries to be enabled. Outside of changing operating conditions like the high and low-pressure conditions and different feed rates, a number of other decisions about the cycle design will be considered in the application of PSA to post-combustion capture to boost the performance for heavy product purification, a number of which are listed below.

In comparing these strategies, it is worth noting all of them involve trading off losses in one or more performance parameters to boost another.

2.4.2.1   Pressurization with feed or light product

In multi-bed PSA's where the product is semi-continuously being produced from one or more beds, it is possible to redirect the high-pressure light product to a neighboring bed for its pressurization. This approach referred to as light product pressurization, can be performed either by connecting the end of one bed to the beginning of another near the end of the operating cycle (in cases where the bed's high-pressure condition is near ambient pressure) or by feeding gas from a downstream product storage tank back to the PSA. In either case, the goal of light product pressurization is to have the subsequent adsorption or feed step begin with a very light product enriched bed, enabling a sharper heavy product mass transfer front. This approach is typically used when very high purity light product is desired, which in the case of CO_2 capture applications may be desired to boost the recovery of CO_2. Since the already treated light product is being reused in the process, this generally increases the cycle time, as the breakthrough of the heavy product will take longer.

Pressurizing with feed gas, as the alternative, should lead to shorter cycle times, increasing the productivity, with possible losses in the purity and recovery of the heavy product due to the spreading of the front during pressurization. This spreading phenomena with the feed can be offset somewhat if the pressurization step is performed at slower rates, but that results in prolonging the cycle time in a similar (though perhaps let drastic) way to light product pressurization.

2.4.2.2   Pressure Equalization

A pressure equalization step involves the connection of two beds at different pressures and allowing them to share the gas until a standard pressure is reached. An example cycle, where pressure equalization is carried out upon the completion of the feed step in one bed and the evacuation step in a second bed is shown in **Figure 2-15**. Pressure equalizations are oftentimes utilized when too much of the product is being lost in the blowdown step, whether light or heavy product. As the pressure equalization is usually very fast, pressure equalizations usually capture the interstitial gas of the fixed bed primarily, allowing it to pressurize a neighboring bed partially and that gas can be captured or purified in a later step.
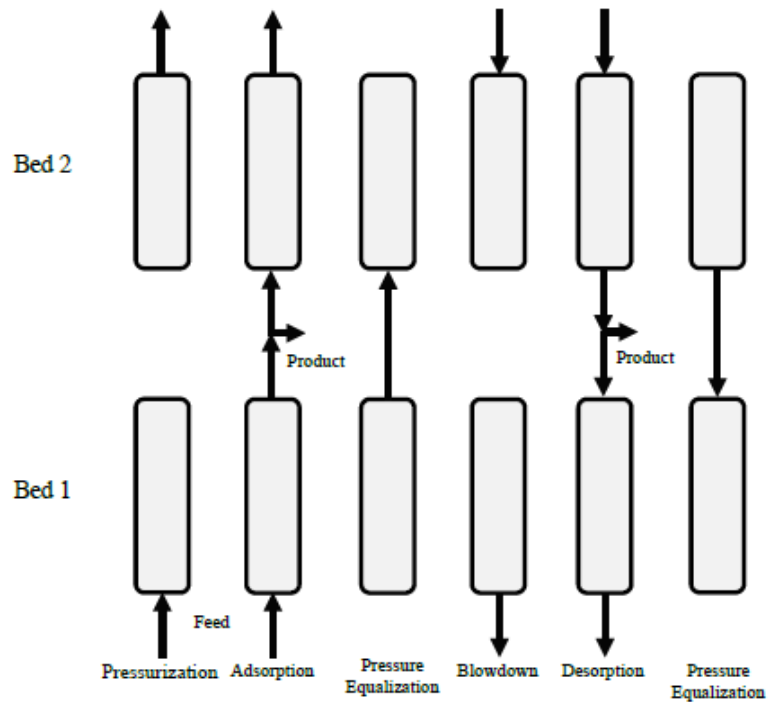
Figure 2-15. Example Multi-Bed PSA with pressure equalization. Copyright © Pimentel 2018[15]

The main benefit of pressure equalization steps is in boosting the specific energy of the process, as less high-pressure gas needs are expended to repressurize the bed.

Multiple pressure equalizations can be used in more complex PSA systems to help alleviate this concern. For CO_2 capture, where the CO_2 product is expected to be captured only in the evacuation step, pressure equalization steps between multiple beds help to reduce the total amount of CO_2 vented in the blowdown step, which ideally boosts the recovery of the system.[89] Like light product pressurization, pressure equalization steps tend to increase the overall cycle time, though this can be partially offset by the fact the pressurization step may be sped up considerably. Its effect on the purity of the light and heavy product depends on the composition of the gas used to equalize, as the rapid depressurization of the bed can lead to some spreading of the concentration fronts of the heavy product.

2.4.2.3   Evacuation Product Recovery at Above Ambient Pressures

While a typical pressure swing adsorption cycle using a vacuum will try to reduce the amount of gas that is evacuated in an effort to reduce total energy expenditure, sometimes the evacuation step may be initiated at higher pressures (also termed incomplete blowdown by some) to improve the recovery of the heavy product. By halting the blowdown early and recovering more of the adsorbed product, the recovery and productivity are enhanced. This approach also will reduce the purity of the heavy product stream, as more of the interstitial gas at the feed composition or lower heavy product concentration will be recovered with the evacuation product. The increases in energy and reduction in purity for improved productivity and recovery of this approach make it an interesting parameter to tune in PSA processes, particularly in cases with especially weak physisorption of the heavy product (lower selectivity's), where desorption of product during the blowdown step near ambient pressure leads to effective purification of the blowdown product. By halting the blowdown early and recovering, more of the adsorbed

product, more heavy product, and the light product is recovered, increasing recovery at the cost of purity.

2.5   References

1.   Ruthven, D. M., *Principles of Adsorption and Adsorption Processes*. Wiley: New York, 1984.

2.   Ruthven, D. M.; Farooq, S.; Knaebel, K. S., *Pressure Swing Adsorption*. VCH Publishers Inc: New York, NY, 1994.

3.   Brown, D., Characterization of Adsorbents for Gas Separations. *Chemical Engineering Progress* 2018.

4.   Bae, Y.-S.; Snurr, R. Q., Development and Evaluation of Porous Materials for Carbon Dioxide Separation and Capture. *Angewandte Chemie International Edition* **2011,** *50* (49), 11586-11596.

5.   Park, J.; Rubiera Landa, H. O.; Kawajiri, Y.; Realff, M. J.; Lively, R. P.; Sholl, D. S., How Well Do Approximate Models of Adsorption-Based CO_2 Capture Processes Predict Results of Detailed Process Models? *Ind. Eng. Chem. Res.* **2020,** *59* (15), 7097-7108.

6.   Langmuir, I., The Adsorption of Gases on Plane Surfaces of Glass, Mica and Platinum. *Journal of the American Chemical Society* **1918,** *40* (9), 1361-1403.

7.   Brunauer, S.; Emmett, P. H.; Teller, E., Adsorption of Gases in Multimolecular Layers. *Journal of the American Chemical Society* **1938,** *60* (2), 309-319.

8.   Payne, D. A.; Sing, K. S. W.; Turk, D. H., Comparison of argon and nitrogen adsorption isotherms on porous and nonporous hydroxylated silica. *Journal of Colloid and Interface Science* **1973,** *43* (2), 287-293.

9.   Kim, K. C.; Yoon, T.-U.; Bae, Y.-S., Applicability of using CO_2 adsorption isotherms to determine BET surface areas of microporous materials. *Microporous and Mesoporous Materials* **2016,** *224*, 294-301.

10.   Rouquerol, J.; Llewellyn, P.; Rouquerol, F., Is the bet equation applicable to microporous adsorbents? In *Studies in Surface Science and Catalysis*, Llewellyn, P. L.; Rodriquez-Reinoso, F.; Rouqerol, J.; Seaton, N., Eds. Elsevier: 2007; Vol. 160, pp 49-56.

11.   Smith, J. M.; Van Ness, H. C.; Abbott, M. M., *Introduction to chemical engineering thermodynamics*. 7th ed. / ed.; McGraw-Hill: Boston, 2005.

12.   Hyla, A. S.; Fang, H.; Boulfelfel, S. E.; Muraro, G.; Paur, C.; Strohmaier, K.; Ravikovitch, P. I.; Sholl, D. S., Significant Temperature Dependence of the Isosteric Heats of Adsorption of Gases in Zeolites Demonstrated by Experiments and Molecular Simulations. *The Journal of Physical Chemistry C* **2019,** *123* (33), 20405-20412.

13.   Lively, R. P.; Chance, R. R.; Koros, W. J., Enabling Low-Cost CO_2 Capture via Heat Integration. *Ind. Eng. Chem. Res.* **2010,** *49* (16), 7550-7562.

14.   Farooq, S.; Hassan, M. M.; Ruthven, D. M., Heat-Effects in Pressure Swing Adsorption Systems. *Chemical Engineering Science* **1988,** *43* (5), 1017-1031.

15.   Pimentel, B. Control of Diffusive Time Scales in Zeolite Imidazolate Frameworks for the Kinetic Separation of Light Hydrocarbons. Georgia Institute of Technology, Atlanta, GA, 2018.

16.   Pimentel, B. R.; Fultz, A. W.; Presnell, K. V.; Lively, R. P., Synthesis of Water-Sensitive Metal-Organic Frameworks within Fiber Sorbent Modules. *Ind. Eng. Chem. Res.* **2017,** *56* (17), 5070-5077.

17.   Lively, R. P. Hollow Fiber Sorbents for Post-Combustion CO_2 Capture. Georgia Institute of Technology, 2011.

18.   Joss, L.; Gazzani, M.; Mazzotti, M., Rational design of temperature swing adsorption cycles for post-combustion CO_2 capture. *Chemical Engineering Science* **2017,** *158*, 381-394.

19.   Merkel, T. C.; Lin, H. Q.; Wei, X. T.; Baker, R., Power plant post-combustion carbon dioxide capture: An opportunity for membranes. *J. Membr. Sci.* **2010,** *359* (1-2), 126-139.

20.   Garg, D. R.; Ruthven, D. M., Linear Driving Force Approximations for Diffusion Controlled Adsorption in Molecular Sieve Columns. *Aiche Journal* **1975,** *21* (1), 200-202.

21.   Anna, H. R. S.; Barreto, A. G.; Tavares, F. W.; do Nascimento, J. F., Methane/nitrogen separation through pressure swing adsorption process from nitrogen-rich streams. *Chemical Engineering and Processing* **2016,** *103*, 70-79.

22.   DeWitt, S. J. A.; Sinha, A.; Kalyanaraman, J.; Zhang, F.; Realff, M. J.; Lively, R. P., Critical Comparison of Structured Contactors for Adsorption-Based Gas Separations. *Annual Review of Chemical and Biomolecular Engineering* **2018,** *9* (1), 129-152.

23.   Kusgens, P.; Zgaverdea, A.; Fritz, H. G.; Siegle, S.; Kaskel, S., Metal-Organic Frameworks in Monolithic Structures. *Journal of the American Ceramic Society* **2010,** *93* (9), 2476-2479.

24.   Rezaei, F.; Grahn, M., Thermal Management of Structured Adsorbents in CO_2 Capture Processes. *Ind. Eng. Chem. Res.* **2012,** *51* (10), 4025-4034.

25.   Rezaei, F.; Webley, P., Structured adsorbents in gas separation processes. *Separation and Purification Technology* **2010,** *70* (3), 243-256.

26.   Rezaei, F.; Webley, P., Optimum structured adsorbents for gas separation processes. *Chemical Engineering Science* **2009,** *64* (24), 5182-5191.

27.   Choi, S.; Drese, J. H.; Jones, C. W., Adsorbent Materials for Carbon Dioxide Capture from Large Anthropogenic Point Sources. *ChemSusChem* **2009,** *2* (9), 796-854.

28.   Sumida, K.; Rogow, D. L.; Mason, J. A.; McDonald, T. M.; Bloch, E. D.; Herm, Z. R.; Bae, T.-H.; Long, J. R., Carbon dioxide capture in metal–organic frameworks. *Chemical reviews* **2012,** *112* (2), 724-781.

29.   Sayari, A.; Belmabkhout, Y.; Serna-Guerrero, R., Flue gas treatment via CO_2 adsorption. *Chemical Engineering Journal* **2011,** *171* (3), 760-774.

30.   Park, J.; Lively, R. P.; Sholl, D. S., Establishing upper bounds on CO_2 swing capacity in sub-ambient pressure swing adsorption via molecular simulation of metal-organic frameworks. *Journal of Materials Chemistry A* **2017**.

31.   Chen, Z. H.; Deng, S. B.; Wei, H. R.; Wang, B.; Huang, J.; Yu, G., Activated carbons and amine-modified materials for carbon dioxide capture - a review. *Frontiers of Environmental Science & Engineering* **2013,** *7* (3), 326-340.

32.   Choma, J.; Stachurska, K.; Marszewski, M.; Jaroniec, M., Equilibrium isotherms and isosteric heat for CO_2 adsorption on nanoporous carbons from polymers. *Adsorption-Journal of the International Adsorption Society* **2016,** *22* (4-6), 581-588.

33.   Jones, C. W., CO_2 Capture from Dilute Gases as a Component of Modern Global Carbon Management. In *Annual Review of Chemical and Biomolecular Engineering, Vol 2*, Prausnitz, J. M., Ed. 2011; Vol. 2, pp 31-52.

34.   Akhtar, F.; Andersson, L.; Ogunwumi, S.; Hedin, N.; Bergstrom, L., Structuring adsorbents and catalysts by processing of porous powders. *Journal of the European Ceramic Society* **2014,** *34* (7), 1643-1666.

35.   Wilcox, J.; Haghpanah, R.; Rupp, E. C.; He, J. J.; Lee, K., Advancing Adsorption and Membrane Separation Processes for the Gigaton Carbon Capture Challenge. In *Annual Review of Chemical and Biomolecular Engineering, Vol 5*, Prausnitz, J. M.; Doherty, M. F.; Segalman, R. A., Eds. 2014; Vol. 5, pp 479-+.

36.   Chen, S. J.; Zhu, M.; Fu, Y.; Huang, Y. X.; Tao, Z. C.; Li, W. L., Using 13X, LiX, and LiPdAgX zeolites for CO_2 capture from post-combustion flue gas. *Applied Energy* **2017,** *191*, 87-98.

37.   Mulgundmath, V.; Tezel, F.; Saatcioglu, T.; Golden, T., Adsorption and separation of CO_2/N_2 and CO_2/CH_4 by 13X zeolite. *The Canadian Journal of Chemical Engineering* **2012,** *90* (3), 730-738.

38.   Britt, D.; Furukawa, H.; Wang, B.; Glover, T. G.; Yaghi, O. M., Highly efficient separation of carbon dioxide by a metal-organic framework replete with open metal sites. *Proceedings of the National Academy of Sciences of the United States of America* **2009,** *106* (49), 20637-20640.

39.   Furukawa, H.; Cordova, K. E.; O'Keeffe, M.; Yaghi, O. M., The Chemistry and Applications of Metal-Organic Frameworks. *Science* **2013,** *341* (6149), 1230444.

40.   Zhou, H. C.; Long, J. R.; Yaghi, O. M., Introduction to Metal-Organic Frameworks. *Chemical Reviews* **2012,** *112* (2), 673-674.

41.   Belmabkhout, Y.; Guillerm, V.; Eddaoudi, M., Low concentration CO_2 capture using physical adsorbents: Are metal-organic frameworks becoming the new benchmark materials? *Chemical Engineering Journal* **2016,** *296*, 386-397.

42.   Sinha, A.; Darunte, L. A.; Jones, C. W.; Realff, M. J.; Kawajiri, Y., Systems Design and Economic Analysis of Direct Air Capture of CO_2 through Temperature Vacuum Swing Adsorption Using MIL-101(Cr)-PEI-800 and mmen-Mg-2(dobpdc) MOF Adsorbents. *Ind. Eng. Chem. Res.* **2017,** *56* (3), 750-764.

43.   McDonald, T. M.; Mason, J. A.; Kong, X. Q.; Bloch, E. D.; Gygi, D.; Dani, A.; Crocella, V.; Giordanino, F.; Odoh, S. O.; Drisdell, W. S.; Vlaisavljevich, B.; Dzubak, A. L.; Poloni, R.; Schnell, S. K.; Planas, N.; Lee, K.; Pascal, T.; Wan, L. W. F.; Prendergast, D.; Neaton, J. B.; Smit, B.; Kortright, J. B.; Gagliardi, L.; Bordiga, S.; Reimer, J. A.; Long, J. R., Cooperative insertion of CO_2 in diamine-appended metal-organic frameworks. *Nature* **2015,** *519* (7543), 303-+.

44.   Burtch, N. C.; Jasuja, H.; Walton, K. S., Water Stability and Adsorption in Metal-Organic Frameworks. *Chemical Reviews* **2014,** *114* (20), 10575-10612.

45.   Bhattacharyya, S.; Han, R.; Kim, W.-G.; Chiang, Y.; Jayachandrababu, K. C.; Hungerford, J. T.; Dutzer, M. R.; Ma, C.; Walton, K. S.; Sholl, D. S.; Nair, S., Acid Gas Stability of Zeolitic Imidazolate Frameworks: Generalized Kinetic and Thermodynamic Characteristics. *Chemistry of Materials* **2018,** *30* (12), 4089-4101.

46.   Ilic, B.; Wettstein, S. G., A review of adsorbate and temperature-induced zeolite framework flexibility. *Microporous and Mesoporous Materials* **2017,** *239*, 221-234.

47.   Li, H.; Eddaoudi, M.; O'Keeffe, M.; Yaghi, O. M., Design and synthesis of an exceptionally stable and highly porous metal-organic framework. *Nature* **1999,** *402* (6759), 276-279.

48.   Lively, R. P., Chance, Ronald R., Koros, William J., Deckman, Harry W., Kelley, Bruce T. Sorbent fiber compositions and methods of temperature swing adsorption 2012.

49.   Koros, W. J., Bhandari, Dhaval A. Fiber sorbents. 2013.

50.   Koros, W. J. Sorbent fiber compositions and methods of using the same. 2014.

51.   Lively, R. P.; Chance, R. R.; Kelley, B. T.; Deckman, H. W.; Drese, J. H.; Jones, C. W.; Koros, W. J., Hollow Fiber Adsorbents for CO_2 Removal from Flue Gas. *Ind. Eng. Chem. Res.* **2009,** *48* (15), 7314-7324.

52.   Gulati, S. T., 1998. Ceramic catalyst supports for gasoline fuel. In: Cybulski, A., Moulijn, J.A. (Eds.), Structured Catalysts and Reactors. Marcel Dekker, New York.

53.   Mallik, R.; Hage, D. S., Affinity monolith chromatography. *Journal of Separation Science* **2006,** *29* (12), 1686-1704.

54.   Corella, J.; Toledo, J. M.; Padilla, R., Catalytic hot gas cleaning with monoliths in biomass gasification in fluidized beds. 2. Modeling of the monolithic reactor. *Ind. Eng. Chem. Res.* **2004,** *43* (26), 8207-8216.

55.   Jungbauer, A.; Hahn, R., Monoliths for fast bioseparation and bioconversion and their applications in biotechnology. *Journal of Separation Science* **2004,** *27* (10-11), 767-778.

56.   Ribeiro, R.; Sauer, T. P.; Lopes, F. V.; Moreira, R. F.; Grande, C. A.; Rodrigues, A. E., Adsorption of CO_2, CH_4, and N_2 in Activated Carbon Honeycomb Monolith. *J. Chem. Eng. Data* **2008,** *53* (10), 2311-2317.

57.   Kreutzer, M. T.; Kapteijn, F.; Moulijn, J. A.; Heiszwolf, J. J., Multiphase monolith reactors: Chemical reaction engineering of segmented flow in microchannels. *Chemical Engineering Science* **2005,** *60* (22), 5895-5916.

58.   Kopaygorodsky, E. M.; Guliants, V. V.; Krantz, W. B., Predictive dynamic model of single-stage Ultra-Rapid Pressure Swing Adsorption. *Aiche Journal* **2004,** *50* (5), 953-962.

59.   Li, S. G.; Koops, G. H.; Mulder, M. H. V.; Vandenboomgaard, T.; Smolders, C. A., Wet Spinning of Integrally Skinned Hollow-Fiber Membranes by a Modified Dual-Bath Coagulation Method using a Triple Orifice Spinneret. *J. Membr. Sci.* **1994,** *94*, 329-340.

60.   Lively, R. P.; Chance, R. R.; Mysona, J. A.; Babu, V. P.; Deckman, H. W.; Leta, D. P.; Thomann, H.; Koros, W. J., CO_2 sorption and desorption performance of thermally cycled hollow fiber sorbents. *International Journal of Greenhouse Gas Control* **2012,** *10*, 285-294.

61.   Lively, R. P.; Leta, D. P.; DeRites, B. A.; Chance, R. R.; Koros, W. J., Hollow fiber adsorbents for CO_2 capture: Kinetic sorption performance. *Chemical Engineering Journal* **2011,** *171* (3), 801-810.

62.   Bhandari, D. A.; Bessho, N.; Koros, W. J., Hollow Fiber Sorbents for Desulfurization of Natural Gas. *Ind. Eng. Chem. Res.* **2010,** *49* (23), 12038-12050.

63.   Chen, G.; Koros, W. J.; Jones, C. W., Hybrid Polymer/UiO-66(Zr) and Polymer/NaY Fiber Sorbents for Mercaptan Removal from Natural Gas. *Acs Applied Materials & Interfaces* **2016,** *8* (15), 9700-9709.

64.   Labreche, Y.; Lively, R. P.; Rezaei, F.; Chen, G.; Jones, C. W.; Koros, W. J., Post-spinning infusion of poly(ethyleneimine) into polymer/silica hollow fiber sorbents for carbon dioxide capture. *Chemical Engineering Journal* **2013,** *221*, 166-175.

65.   Labreche, Y.; Fan, Y. F.; Rezaei, F.; Lively, R. P.; Jones, C. W.; Koros, W. J., Poly(amide-imide)/Silica Supported PEI Hollow Fiber Sorbents for Postcombustion CO_2 Capture by RTSA. *Acs Applied Materials & Interfaces* **2014,** *6* (21), 19336-19346.

66.   Rownaghi, A. A.; Kant, A.; Li, X.; Thakkar, H.; Hajari, A.; He, Y. X.; Brennan, P. J.; Hosseini, H.; Koros, W. J.; Rezaei, F., Aminosilane-Grafted Zirconia-Titania-Silica Nanoparticles/TorIon Hollow Fiber Composites for CO_2 Capture. *Chemsuschem* **2016,** *9* (10), 1166-1177.

67.   Rownaghi, A. A.; Rezaei, F.; Labreche, Y.; Brennan, P. J.; Johnson, J. R.; Li, F. S.; Koros, W. J., Insitu Formation of a Monodispersed Spherical Mesoporous Nanosilica-Torlon Hollow-Fiber Composite for Carbon Dioxide Capture. *Chemsuschem* **2015,** *8* (20), 3439-3450.

68.   Fan, Y. F.; Rezaei, F.; Labreche, Y.; Lively, R. P.; Koros, W. J.; Jones, C. W., Stability of amine-based hollow fiber CO_2 adsorbents in the presence of NO and SO_2. *Fuel* **2015,** *160*, 153-164.

69.   Li, F. S.; Qiu, W. L.; Lively, R. P.; Lee, J. S.; Rownaghi, A. A.; Koros, W. J., Polyethyleneimine-Functionalized Polyamide Imide (Torlon) Hollow-Fiber Sorbents for Post-Combustion CO_2 Capture. *Chemsuschem* **2013,** *6* (7), 1216-1223.

70.   Pang, S. H.; Jue, M. L.; Leisen, J.; Jones, C. W.; Lively, R. P., PIM-1 as a Solution-Processable "Molecular Basket" for CO_2 Capture from Dilute Sources. *Acs Macro Letters* **2015,** *4* (12), 1415-1419.

71.   Zhao, J. J.; Nunn, W. T.; Lemaire, P. C.; Lin, Y. L.; Dickey, M. D.; Oldham, C. J.; Walls, H. J.; Peterson, G. W.; Losego, M. D.; Parsons, G. N., Facile Conversion of Hydroxy Double Salts to Metal-Organic Frameworks Using Metal Oxide Particles and Atomic Layer Deposition Thin-Film Templates. *Journal of the American Chemical Society* **2015,** *137* (43), 13756-13759.

72.   Bhandari, D.; Olanrewaju, K. O.; Bessho, N.; Breedveld, V.; Koros, W. J., Dual layer hollow fiber sorbents: Concept, fabrication and characterization. *Separation and Purification Technology* **2013,** *104*, 68-80.

73.   Labreche, Y.; Fan, Y. F.; Lively, R. P.; Jones, C. W.; Koros, W. J., Direct dual layer spinning of aminosilica/Torlon (R) hollow fiber sorbents with a lumen layer for CO_2 separation by rapid temperature swing adsorption. *Journal of Applied Polymer Science* **2015,** *132* (17).

74.   Lively, R. P.; Mysona, J. A.; Chance, R. R.; Koros, W. J., Formation of Defect-Free Latex Films on Porous Fiber Supports. *Acs Applied Materials & Interfaces* **2011,** *3* (9), 3568-3582.

75.   Ackley, M. W.; Barrett, P. A.; Stephenson, N. A.; Kikkinides, E. S., High Rate Compositions. Google Patents: 2013.

76.   Kalyanaraman, J.; Fan, Y.; Lively, R. P.; Koros, W. J.; Jones, C. W.; Realff, M. J.; Kawajiri, Y., Modeling and experimental validation of carbon dioxide sorption on hollow fibers loaded with silica-supported poly(ethylenimine). *Chemical Engineering Journal* **2015,** *259*, 737-751.

77.   Gueret, V.; Monereau, C.; Pullumbi, P., Mixture of an adsorbent and a phase change material with an adapted density. Google Patents: 2016.

78.   Viramontes-Brown, R.; Villarreal-Trevino, J. A., Method for producing direct reduced iron utilizing a reducing gas with a high content of carbon monoxide. Google Patents: 1997.

79.   Py, X.; Goetz, V., Composite material and use thereof for controlling thermal effects in a physicochemical process. Google Patents: 2010.

80.   Hufton, J. R.; Quinn, R.; White, V.; Allam, R. J., Carbon Dioxide Separation Via Partial Pressure Swing Cyclic Chemical Reaction. Google Patents: 2009.

81.   Gueret, V.; Monereau, C.; Pullumbi, P., Particle of a phase change material with coating layer. Google Patents: 2014.

82.   Horstmeier, J. F.; Gomez Lopez, A.; Agar, D. W., Performance improvement of vacuum swing adsorption processes for CO_2 removal with integrated phase change material. *International Journal of Greenhouse Gas Control* **2016,** *47*, 364-375.

83.   Toledo, M.; Rojas, C.; Montes, E.; Veloso, J.; Sáez, A., Use of phase change materials on an adsorbed carbon dioxide storage system. *Applied Thermal Engineering* **2013,** *51* (1), 512-519.

84.   Lively, R. P.; Bessho, N.; Bhandari, D. A.; Kawajiri, Y.; Koros, W. J., Thermally moderated hollow fiber sorbent modules in rapidly cycled pressure swing adsorption mode for hydrogen purification. *Int. J. Hydrog. Energy* **2012,** *37* (20), 15227-15240.

85.   Pirngruber, G. D.; Guillou, F.; Gomez, A.; Clausse, M., A theoretical analysis of the energy consumption of post-combustion CO_2 capture processes by temperature swing adsorption using solid sorbents. *International Journal of Greenhouse Gas Control* **2013,** *14* (Supplement C), 74-83.

86.   Eisenberger, P. Carbon dioxide capture/regeneration method using monolith 2016.

87.   Esisenberger, P., Chichilnisky Graciela System and method for removing carbon dioxide from an atmosphere and global thermostat using the same 2014.

88.   Reynolds, S. P.; Ebner, A. D.; Ritter, J. A., New Pressure Swing Adsorption Cycles for Carbon Dioxide Sequestration. *Adsorption* **2005,** *11* (1), 531-536.

89.   Bui, M.; Adjiman, C. S.; Bardow, A.; Anthony, E. J.; Boston, A.; Brown, S.; Fennell, P. S.; Fuss, S.; Galindo, A.; Hackett, L. A.; Hallett, J. P.; Herzog, H. J.; Jackson, G.; Kemper, J.; Krevor, S.; Maitland, G. C.; Matuszewski, M.; Metcalfe, I. S.; Petit, C.; Puxty, G.; Reimer, J.; Reiner, D. M.; Rubin, E. S.; Scott, S. A.; Shah, N.; Smit, B.; Trusler, J. P. M.; Webley, P.; Wilcox, J.; Mac Dowell, N., Carbon capture and storage (CCS): the way forward. *Energy Environ. Sci.* **2018,** *11* (5), 1062-1176.

CHAPTER 3.   MATERIALS AND METHODS

This work has focused on the development of structured sorbent contactors for use in post-combustion CO_2 capture separations operating at sub-ambient conditions. Different parts of this work focus on understanding the economics of the sub-ambient capture process to help guide the development of new materials. The methods used for estimating the energetics and economics are reviewed here. In later chapters, simulated Pareto performance of the materials developed throughout this work will be discussed, and while those results add great value to the economic discussion, those methods are left to Appendix A. The materials and experimental methodologies used to develop and understand the performance of the newly manufactured materials are discussed in some detail in this chapter.

3.1   Methods of Estimating the Economics of Sub-ambient CO_2 capture

This section focuses on an extended discussion of how the capital costs and other economic factors were estimated for the separations plant in the base case, as well as the sensitivity analysis and various case studies. The section is broken down into three subsections: 3.1.1 Estimating Economic Indicators, 3.1.2 Capital Cost Estimation, and 3.1.3 Cost of Thermally Managed Fiber Sorbents.

A process model was created in Aspen Plus. The Volume Translated Peng-Robinson equation of state (VTPR) property set was used throughout the CO_2 capture process, while the International Association for the Properties of Water and Steam 1995 (IAPWS-95) property set was used to model the generation of BFW preheater steam using

available heat from the pulverized coal power cycle. DOE Case 11a from *Cost and Performance Baseline for Fossil Energy Plants Volume 1*[1] for post-combustion CO_2 capture from a supercritical pulverized coal power plant was used as a model baseline for the CO_2 product feed. For this analysis, the flue gas composition was simplified only to include CO_2, N_2, and H_2O. The ~1% other contaminants (O_2 and Ar) were not considered in the analysis and were grouped in with N_2.

Pressure drops through heat exchangers in this preliminary analysis were taken as 0.1 bar, while the pressure drops through the pressure-driven separation unit (membrane or adsorbent) was take as 0.2 bar. The adsorbent drier bed, pressure-driven separation unit, and the downstream vacuum pump were assumed to operate isothermally. The vacuum pump was modeled as a compressor followed by a heater to simulate the operation of an actual isothermal vacuum pump as Aspen Plus does not have a built-in vacuum pump model. System compressors and expanders acting on the feed and N_2 rich product were assumed axial compressors operating at a 90% polytropic efficiency sharing a joint driveshaft. The volumetric flow rates of flue gas entering the system are on the scale where axial compressors would be viable, and polytropic efficiencies ranging from 88-92% are typical for these systems.[2] The vacuum pump, liquefaction compressor, and recycle pressure changer (compressor or turbine depending on the required pressure change) were not in the required size range for axial compressors, so centrifugal compressors were considered instead (efficiencies of 80%).

3.1.1 Estimation of Economic Indicators

Two leading economic indicators were used throughout the analysis: (i) the energy per tonne of CO_2 captured, and (ii) the cost in dollars per tonne of CO_2 captured.

As no external cooling utility was required for the sub-ambient process, the energy demand of the process was estimated to be made up of the net energy associated with the compression, expansion, and pumping of streams throughout the process. The sum of these values after giving credit for the 16 MW saved by the boiler feedwater (discussed in Chapter 4) integration is divided by the amount of CO_2 captured by the process per hour.

$$\begin{aligned} Energy\ demand\ of\ process \\ = Compression\ and\ pumping\ Energy - Turbine\ Energy - BFW\ credit \end{aligned} \qquad (3\text{-}1)$$

$$Energy\ demand\ of\ process = 298.513\ \text{MW} - 91.455\ \text{MW} - 16\ \text{MW} = 191.07\ \text{MW}$$

$$Energy\ per\ tonne\ CO_2 = \frac{Energy\ Demand\ of\ Process}{Tonnes\ of\ CO2\ per\ hour} = \frac{191068\ kW}{10774\frac{kmol}{hr}} \times \frac{kmol_{CO2}}{44\ kg_{CO2}} \times 1000\frac{kg}{tonne}$$

$$= \mathbf{403.05}\ \boldsymbol{kWh/tonne_{CO2}}$$

Estimating the cost per tonne of CO_2 required the calculation of installed capital cost, as well as the cost of the energy displaced by the process that would otherwise be sold to the grid. An installation factor of 2 was used to take the raw capital costs to total installed capital. A five year equipment lifetime was taken for all equipment, understanding much of the large equipment would likely last significantly longer, while the PSA system may have a shorter lifetime. A cost of electricity of $0.04/kWh was taken as a basis for all calculations.

Sum of Capital Costs

$$= \$198{,}984{,}375 + \$34{,}085{,}722 + \$2{,}243{,}341 + \$13{,}260 + \$15{,}471$$

$$+ \$167{,}346{,}834$$

Sum of capital costs= **\$398,687,888**

The cost of capture per tonne can then be calculated, using:

$$
\begin{aligned}
\textit{Cost of Capture} \\
= [((\textit{Capital Cost} \times \textit{Installation factor}))/((\textit{Equipment Lifetime}))] \quad (3\text{-}2) \\
+ \textit{Cost of Electricity} \times \textit{Process Energy} \\
\times \textit{hours per year}]/(\textit{CO}\_2 \ \textit{Captured per year})
\end{aligned}
$$

where the CO_2 captured per year can be estimated using a capacity factor of 0.85

and an operating basis of 350 days, viz.,

$$
\begin{aligned}
CO_2 \ \textit{Captured per year} \\
= (CO_2 \ \textit{Captured per hour}) * \textit{Operating Days} \quad (3\text{-}3) \\
* \textit{Capacity Factor}
\end{aligned}
$$

$$CO_2 \ \textit{Captured per year} = \left(474.05\,\frac{tonne}{hour}\right) \times \left(24\,\frac{hours}{day}\right) \times \left(350\,\frac{days}{year}\right) \times (0.85)$$

$$= 3{,}384{,}759 \ tonne/year$$

$$\textit{Cost of Capture} = \frac{\left[\frac{(\$398{,}687{,}888*2)}{(\textit{Five years})} + \frac{\$0.04}{kWh} \times 191{,}068 \times 8760\right]}{3384759 \ tonne} = \frac{[\$159{,}475{,}155 + \$66{,}950{,}227]}{3384759 \ tonne} = \textbf{\$66.89/tonne}$$

3.1.2   Capital Cost Estimation

The analysis of capital costs of the sub-ambient CO_2 capture process was broken down into six major equipment categories: 1. Rotating Equipment (compressors, expanders, and vacuum pumps), 2. Heat Exchangers, 3. Direct Contact Chiller, 4. Liquid CO_2 pump, 5. Dryer Bed, and 6. Primary Separator. Example capital cost calculations for

each of these categories are carried out in the following sections for the base case conditions outlined in the chapter.

3.1.2.1   Rotating Equipment

The cost of all the rotating equipment was estimated by summing all energy consumption (kW) in each unit. The sum of the energy expended for compression and the vacuum pump (modeled as a compressor in Aspen), COMP1-COMP5 and VACPUMP in **Figure 3-1**, and the energy generated for the expansion of nitrogen (TURB 1 and 2) was then multiplied by a scaling factor to determine the cost of the equipment.
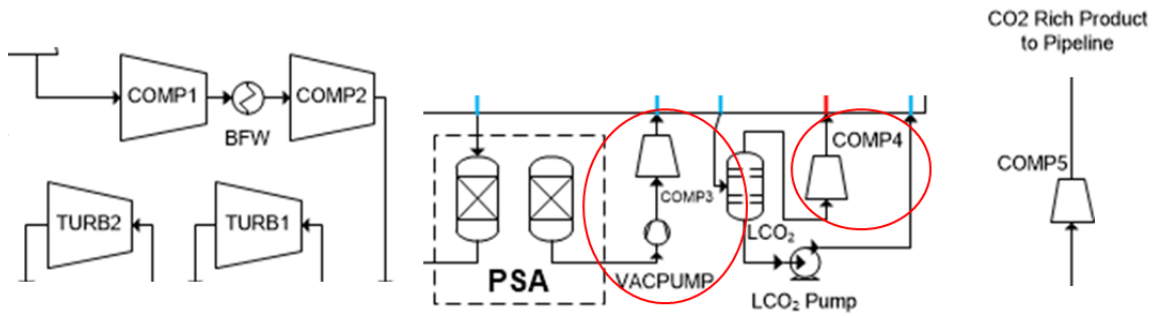
Figure 3-1. Unit Operations used in the Aspen Model for compression and expansion estimated as part of rotating equipment expenses

$$Rotating\ Equip\ Cost = \left(\frac{\$500}{kW_e}\right) \times (Sum\ of\ Compression\ and\ Expansion\ Energy) \quad \text{(3-4)}$$

$$\boldsymbol{Cost\ of\ Rotating\ Equipment\ in\ Base\ case} = \left(\frac{\$500}{kW_e}\right) \times (298513\ kW + 91455\ kW)$$

=$198,984,375

3.1.2.2 Heat Exchangers

Two different approaches were utilized to estimate the cost of the heat exchangers in the CO_2 capture process, one for the sub-ambient heat exchange network and the liquefaction column, and one for the BFW and cooling water exchangers. The sub-ambient heat exchanger network was estimated as a sum of the overall energy used for heating and cooling within the sub-ambient heat exchangers and the liquefaction column, multiplied by a cost estimate of $100/kW_{th}$.

$$\begin{aligned} Cost\ of\ SA\ HX\ Network \\ = \left(\frac{\$100}{kW_{th}}\right) \times (Heater\ Thermal\ Load \\ + Cooler\ Thermal\ Load) \end{aligned} \tag{3-5}$$

$$\boldsymbol{Cost\ of\ SA\ HX\ Network} = \left(\frac{\$100}{kW_{th}}\right) \times (181{,}241.2\ kW_{th} + 130{,}998.6\ kW_{th}) = \boldsymbol{\$31{,}223{,}977}$$

The BFW preheater and Cooling Water exchangers were priced as gas-liquid shell and tube heat exchangers using methods from Perry's Chemical Engineering Handbook. An overall heat transfer coefficient of 40 BTU°F^{-1} ft^{-2}hr^{-1} (227 W*°C^{-1}*m^2) was selected for water/air-like streams. This estimate is likely an underestimate of the overall heat transfer coefficient for the BFW exchangers, as the generation of steam in the exchanger should improve the performance beyond that of the correlation utilized. The log mean temperature difference of 43.25°C taken from the average of 6 different pressurization conditions from the sensitivity was used as a placeholder for all the exchangers throughout the remainder of the sensitivity analysis. These two values were used to estimate the total heat exchanger area for the four exchangers.

$$Area\ of\ Exchangers = \frac{Q}{U*\Delta T_{LM}} = \frac{247.14\text{x}10^6\ W_{th}}{227\frac{W}{°C*m^2}\times43.25°C} = 25,172\text{m}^2 \tag{3-6}$$

A cost per area of exchangers was then taken from Perry's Chemical Engineering Handbook of $2.30/ft^2 ($24.76/m^2)[3]. That cost was based on numbers from 1971, so the CEPCI was used to adjust for modern-day. CEPCI in 1971 was 321.3, while 2019 CEPCI was 607.5

$$Cost\ of\ Exchangers = (Area) \times Cost\ per\ area \times \left(\frac{2019\ CEPCI}{1971\ CEPCI}\right) \tag{3-7}$$

$$Cost\ of\ Exchangers = 25,172\ m^2 \times \frac{\$24.76}{m^2} \times \left(\frac{607.5}{321.3}\right) = \mathbf{\$2,861,745}$$

Combining these two costs gives the capital estimate for heat exchangers of **\$34,085,722**

3.1.2.3   Direct Contact Chiller

The cost of the direct contact chiller was determined via scaling analysis using the 6/10th's rule. [4]
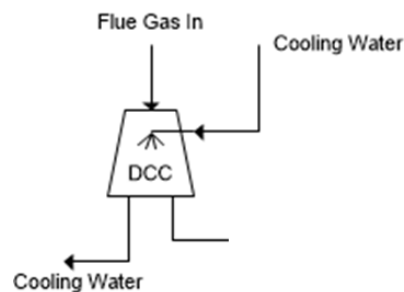
Figure 3-2. The direct contact chiller removes much of the water in the flue gas.

$$Cost\ of\ DCC = Cost\ of\ Known\ DCC \times \left(\frac{Modelled\ Size}{Known\ Size)}\right)^{6/10} \tag{3-8}$$

$$Cost\ of\ DCC = \$1{,}700{,}000 \times \left(\frac{11{,}113{,}273.9\ \text{kg/hour}}{7{,}000{,}000\ \text{kg/hour}}\right)^{6/10} = \mathbf{\$2{,}243{,}341}$$

3.1.2.4   Liquid CO₂ Pump

The liquid CO_2 pump cost was estimated using the known equation for the price as a function of the size factor. [31]

$$Size\ Factor = (Flow\ in\ gal/min) \times (Head\ in\ ft)^{\wedge}0.5 \qquad \text{(3-9)}$$

$$Cost = \exp((9.7171 - 0.6019 \times ln(SIZE\ FACTOR) + 0.0519 \\ \times ln(SIZE\ FACTOR)^2) \qquad \text{(3-10)}$$

So for the base case:

$$Size\ Factor = \left(1906.6\ \frac{gal}{min}\right) \times (1505.2\ ft)^{0.5} = 73970$$

$$Cost = \exp((9.7171 - 0.6019 \times ln(73970) + 0.0519 \times ln(73970)^2)$$

$$Cost\ of\ Liquid\ CO_2\ Pump\ in\ Base\ Case = \mathbf{\$13{,}260}$$

3.1.2.5   Dryer Bed

The dryer bed was priced for the sorbent required to run a 2-bed temperature swing adsorption for the final drying of the inlet after compression and preliminary cooling to 2°C, shown in **Figure 3-3**. The dryer bed was assumed to be running on a 1 hour cycle time with a silica sorbent with a capacity of 0.5 kg_{H2O}/kg sorbent[5], and a price of sorbent $10/kg.
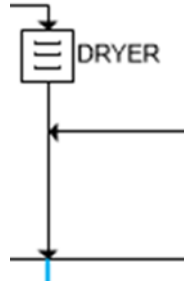
Figure 3-3. Drying of the cooled flue gas inlet prior to final cooling to the operating temperature was carried out via an adsorbent dryer bed.

$$Sorbent\ Required = \frac{Water\ Removed\ Per\ Cycle}{Sorbent\ Capacity} \qquad (3\text{-}11)$$

$$Sorbent\ Required = \frac{42.97\,\frac{kmol}{hr} \times 18\,\frac{kg}{kmol} * 1\ hour}{0.5\ kg_{H2O}/kg_{sorbent}} = 1{,}547.1\ kg\ of\ sorbent$$

$$Cost\ of\ Dryer\ Bed = Sorbent\ Cost * Sorbent\ Demand \qquad (3\text{-}12)$$

$$\boldsymbol{Cost\ of\ Dryer\ Bed} = \frac{\$10}{kg} \times 1{,}547.1\ kg = \mathbf{\$15{,}471}$$

3.1.3   Cost of Thermally Managed Fiber Sorbents

Estimating the cost of thermally managed fiber sorbents requires the cost analysis of the three main components of the fibers: sorbent, microencapsulated phase change material, and manufacture of the fiber modules, a conceptual schematic of the fiber module and fiber microstructure is given in **Figure 3-4**. Sorbent cost will vary from sorbent to sorbent, with specialized sorbents being significantly more expensive than more well-developed sorbents. Microencapsulated phase change materials are produced at the tonne scale for their use in construction materials and shipping. The manufacturing cost for fiber

sorbents was taken to be similar to that of fiber membranes, which are estimated based on the unit area of the external surface ($/m^2).
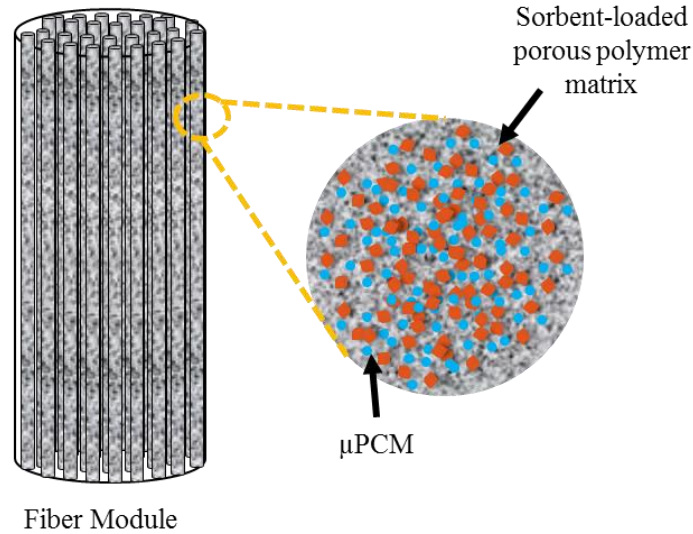
Figure 3-4. Schematic representation of an ideal thermally modulated fiber sorbent containing μPCM and adsorbent

Estimating the size of the PSA unit required for the CO_2 capture basis is most easily done by solving for the amount of sorbent required. If the sorbent requirement, the ratio of sorbent to microencapsulated phase change material, and the overall solids fraction of the fiber is known, the other relevant quantities were calculated.

$$CO_2 \ Captured \ by \ adsorbent = CO_2 \ treated * PSA \ CO_2 recovery \qquad (3\text{-}13)$$

$$CO_2 \ Captured \ by \ adsorbent = \left(14{,}896 \frac{kmol}{hr}\right) \times 0.92 \times \left(1000 \frac{mol}{kmol}\right) \times$$

$(60 \frac{min}{hr})^{-1} = 228{,}405 \text{ mol } CO_2/\text{min}$

From the known amount of CO_2 captured per some time basis, we can calculate the amount of sorbent required to treat the stream for the given cycle time and sorbent capacity.

This value is the same as the bed size factor or the inverse of the expected productivity of the system

$$Sorbent\ required =$$
$$CO_2\ captured\ by\ adsorbent\ \left(\frac{mol}{min}\right) \times \frac{cycle\ time\ (\text{min})}{sorbent\ capacity\ (\frac{mol}{kg})} \qquad (3\text{-}14)$$

$$Sorbent\ required = 228405 \left(\frac{mol}{min}\right) \times \frac{6.0(\text{min})}{5.0\left(\frac{mol}{kg}\right)} = \boldsymbol{274,086\ kg\ sorbent}$$

With the known sorbent requirement, we can use the PCM: sorbent weight ratio of 1.25:1 and solids: polymer ratio of 3:1 of the fibers to determine the PCM and polymer requirements.

$$\mu PCM\ requried = 274,086\ kg\ sorbent \times \frac{1.25\ kg\ \mu PCM}{1\ kg\ sorbent} = \boldsymbol{342,608\ kg\ \mu PCM}$$

$$Polymer\ Required$$
$$= Total\ Fiber\ Mass\ - Sorbent\ Mass - \mu PCM\ Mass \qquad (3\text{-}15)$$

$$Total\ Fiber\ Mass = \frac{Sorbent\ Mass + \mu PCM\ Mass}{Sorbent\ Fraction}$$

$$Total\ Fiber\ Mass = \frac{616694\ kg\ Solid\ Additives}{0.75\ Solid\ additives/_{Fiber}} = \textbf{822,259 kg Fiber}$$

$$Polymer\ Required = 822259\ - 616694 = \textbf{205,565 kg polymer}$$

The last step is transferring the polymer mass to fiber external surface area. For this step, we assume a polymer density of 1300 kg/m^3, a fiber void fraction of 0.5, and a diameter of 650 μm to determine the external surface area requirement of the fibers.

$$Volume\ of\ fiber = \frac{Mass\ of\ fiber}{density\ of\ polymer \times (1 - void\ fraction)} \qquad \text{(3-16)}$$

$$Volume\ of\ fiber = \frac{822{,}259\ kg}{1300\frac{kg}{m3} * 0.5} = 1265\ m^3$$

The surface area to volume ratio of a cylindrical fiber where the length is much greater than the cross-section can be defined as

$$\frac{Surface\ Area}{Volume} = \frac{\pi DL}{\frac{\pi}{4}D^2 L} = \frac{4}{D} \qquad \text{(3-17)}$$

$$\frac{Surface\ Area}{Volume} = \frac{4}{650\mu m} = 6154\ m^{-1}$$

Applying this value to our known fiber volume for the PSA gives the required external surface area of the fiber sorbents.

$$\begin{aligned} External\ &Surface\ Area\ of\ Fiber \\ &= Fiber\ Volume \times Surface\ area\ to\ volume\ ratio \end{aligned} \qquad \text{(3-18)}$$

$$External\ Surface\ Area\ of\ Fiber = 1265\ m^3 \times 6154\ m^{-1} = \mathbf{7{,}784{,}895\ m^2\ fiber}$$

With the known masses of sorbent and microencapsulated phase change material and the external surface area of all the fiber known, the total cost of the PSA unit can be estimated.

$$Sorbent\ Cost = 274086\ kg\ sorbent \times \frac{\$30}{kg} = \mathbf{\$8{,}222{,}580}$$

$$\mu PCM\ Cost = 342608\ kg\ \mu PCM \times \frac{\$10}{kg} = \mathbf{\$3{,}426{,}080}$$

$$Fiber\ Manufacturing\ Cost = 7,784,895\ m^2\ fiber \times \frac{\$20}{m^2} = \mathbf{\$155,697,904}$$

Adding these three costs gives our estimate of the thermally managed fiber sorbent PSA unit of **$167,346,834.**

3.2 Materials

With few exceptions, the materials used throughout this work were purchased directly from commercial sources, with little to no processing required upon delivery. The one exception is the MIL-101(Cr) materials used in Chapters 5 and 7. Due to unexpected circumstances related to the delivery of these materials from our partners at Inmondo Tech, this material needed to be synthesized at a relatively large scale in the lab setting (~15-20 gram per batch).

3.2.1 Polymers

Cellulose acetate (CA, MW 50,000, Sigma-Aldrich) was used as the polymer support for the fiber spinning of adsorbents. Cellulose acetate has probably been the most spun fiber support for adsorbent spinning due to its inexpensive cost and simplicity in spinning as compared to other polymers. Polyvinylpyrrolidone (PVP, K30 MW 40,000, TC and MW 55,000 Sigma-Aldrich) was used as a viscosity-enhancing additive for fiber spinning.

All polymers were dried overnight at 80°C under vacuum before incorporation in polymeric dopes to remove any sorbed water, which would otherwise be unaccounted for in the dope composition.

3.2.2 Reactants for the adsorbent formation

Chromium Nitrate Nonahydrate, $Cr(NO_3)_3 \cdot 9H_2O$, (97% reactant grade, Alfa Aesar), and Terephthalic Acid (BDC, 99% ACS grade, Sigma Aldrich) were used for the synthesis of MIL-101(Cr) with no additional purification.

3.2.3 Solvents

Several solvents were used throughout this work as a part of the adsorbent synthesis and fiber formation efforts. N-methyl-2pyrrolidone (NMP) (ACS Grade, VWR) was used as the spinning solvent for fiber manufacture, due to its well-established performance in cellulose acetate spinning processes. Methanol (ACS Grade, VWR) and Hexanes (ACS Grade, VWR) were used for the solvent exchange of the fiber sorbents post-spinning.

Deionized water was used as the primary reaction solvent for MIL-101(Cr) synthesis. Nitric Acid (70% reagent grade, Sigma Aldrich) was used as an acid modulator in the synthesis of MIL-101(Cr) to control the pH of the solution. N, N-Dimethylformamide (DMF, ACS Grade Alfa Aesar), Methanol, and Ethanol (200 proof, Fischer Scientific)were used for washing of the synthesized MIL-101(Cr) and the delivered UiO-66. DMF is one of two solvents with which terephthalic acid is known to be soluble with at room temperature and thus was used primarily to remove excess reactant from the MIL-101(Cr) and UiO-66 materials. Ethanol was reported as the solvent to be used in the solvent exchange of scaled-up MIL-101(Cr), but it was determined as part of the work that methanol could be substituted with no loss in performance.

3.2.4 Adsorbents

Two Metal-Organic Framework (MOF) adsorbents were used throughout this work. Each adsorbent was dried overnight at 80°C under vacuum before incorporation in spinning dopes.

UiO-66 was purchased from Inmondo Tech at a ~250-gram scale. UiO-66—made up of $Zr_6O_4(OH)_4$ nodes and terephthalic acid linkers—has drawn extensive interest for its outstanding chemical and thermal stability. A graphical representation of UiO-66's crystal structure is given in **Figure 3-5**. UiO-66's stability, high surface area (BET surface areas of approximately 1100 m^2/g are typical), and well-developed synthesis procedure[6] make it an interesting material to probe adsorption device performance[7-9]. Indeed, its high water stability allowed it to be spun into a fiber morphology and analyzed for its application to remove trace mercaptan and other sulfur species from natural gas[10].

The powders delivered were ~1-2 µm in size. The as-delivered UiO-66 was found to have significant terephthalic acid remaining in its pores, as shown by its sublimation on the walls of vacuum ovens during its activation at 200°C. To control this behavior, the powders were washed repeatedly (2-3x) in DMF (~100g of UiO-66 to 1L of DMF) via stirring overnight. The washed UiO-66 was either vacuum filtered or centrifuged (10,000 rpm for 10 minutes) after each subsequent wash and redispersed in DMF for further washing. Post washing, the UiO-66 was activated at 200°C to remove any residual DMF.

MIL-101(Cr) was synthesized in the lab so that this synthesis will be reviewed in Section 3.3 Materials Synthesis and Manufacture. MIL-101(Cr) is a metal-organic framework made up of Chromium-oxo clusters and terephthalic acid linkers, typically

synthesized in water. Methods of synthesis have been widely explored using both acid and basic linkers to control morphology and particle size[11-14]. An image of a typical cage is given in **Figure 3-5**. The crystal is made up of 2.9, and 3.4 nm pores connected by 1.4 nm windows and has had BET surface area's recorded as high as 4100 m^2/g, though typical synthesis in literature usually has values lying between 2700-3200 m^2/g[15]. It has well-reported stability in liquid water, and its stability in acid gases has been probed in the literature.
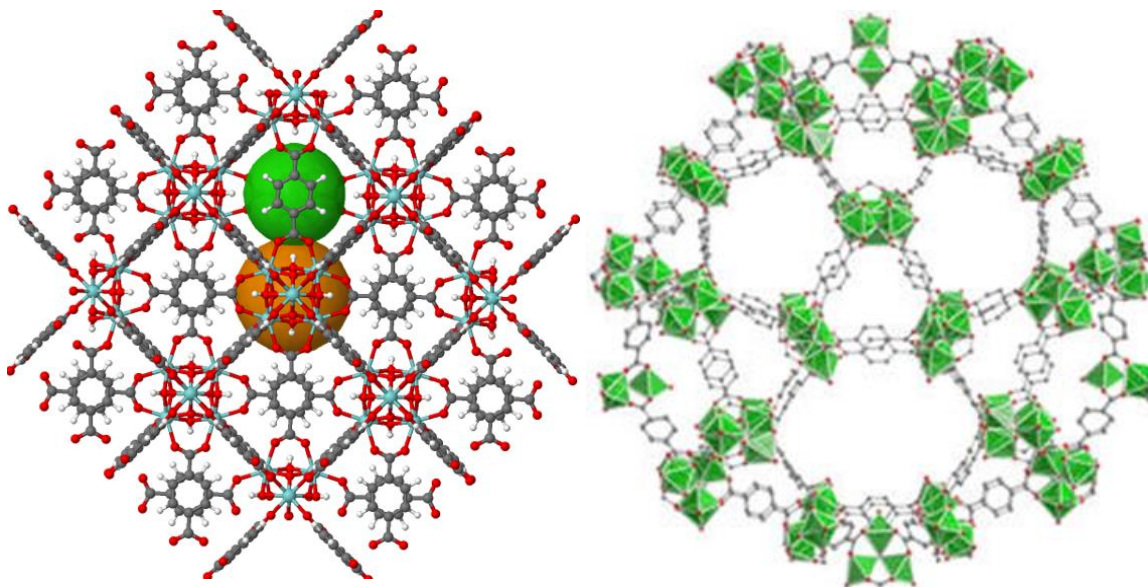
Figure 3-5. Crystal structures of UiO-66[16](left) and MIL-101(Cr) [17](right), the two MOF adsorbents used in this work. Reprinted with permission. Copyright The American Association for the Advancement of Science 2005

3.2.5 *Analysis Gases*

For isotherm collection, Research Grade Carbon Dioxide (CO_2) and Nitrogen were used. Ultra-High Purity Helium (He) was used by the volumetric adsorption systems for the calculation of free space.

For breakthrough experiments, simulated dry flue gas with a helium tracer (12.5% CO_2, 12.5% He, 75% N_2) was purchased from Matheson Gas. Research grade Nitrogen, used for bed purging and pressurization, was purchased from Airgas.

For desorption experiments, research-grade simulated flue gas (13.5% CO_2, 86.5% N_2) and ultra-high purity helium were purchased from Airgas. That simulated flue gas was also used for pressure swing adsorption experiments.

3.2.6 *Microencapsulated Phase Change Materials*

Commercial microencapsulated phase change material (μPCM), microPCM -30D and microPCM 28D (Microtek Laboratories, Inc.) were purchased as a suitable material for this work, as its size (~20 microns) is reasonable for spinning and their respective phase change temperatures occur within the region of interest for this application. The purchased microencapsulated phase change material is composed of a melamine-formaldehyde shell enclosing an organic phase change material made up of mixtures of branched-chain hydrocarbons.

3.3   Materials Synthesis and Manufacture

3.3.1 *MIL-101(Cr) Synthesis*

The scale-up synthesis of MIL-101(Cr) was adapted from a procedure developed by Zhao and co-workers[18]. A solution of Chromium Nitrate Nonahydrate (63.992 g, 0.16 mol) and deionized water (200mL) was mixed in an Erlenmeyer flask for ~30 minutes. A second dispersion containing terephthalic acid (27.103g, 0.16 mol), deionized water (500mL), and Nitric acid (10mL) were mixed for ~30 minutes in a second Erlenmeyer

flask. While water is used as the solvent for the hydrothermal reaction, terephthalic acid is not soluble in water at room temperature. The chromium-containing solution was added to the terephthalic acid dispersion, and the combined reaction mixture was stirred for an additional hour. At this point, the reaction mixture was a dark purple with white particulate (terephthalic acid) dispersed throughout. The reactant mixture was then added to a 2L Teflon lined autoclave. The walls of the reactant mixing flask were flushed with a total of 100 mL of deionized water (800 mL total water) to recover any of the terephthalic acids which lined the walls during pouring into the reaction vessel.

The autoclave was placed in a convection oven heated to 200°C for 15 hours. After the reaction period, the convection oven was set to cool to room temperature, and the autoclave was removed from the oven when room temperature to the touch for more than an hour (~8 hours total cooling time). The recovered reaction solution/dispersion was a pale green upon stirring. If allowed to settle, the pale green product and excess reactant would settle to the bottom, leaving a transparent, deep purple, liquid phase above. Photographs taken at different steps within the synthesis and washing are shown in **Figure 3-6**. The reaction product was mixed until well dispersed, then centrifuged at 12,000 rpm for 20 minutes. The solid product of centrifugation (green in color with white rods (BDC)) was recovered from the centrifuge tube and washed for 30 minutes with ~400 mL of DMF. The subsequent solution was centrifuged and dispersed and stirred in ~1L of DMF overnight (at least 8 hours). The DMF exchange was carried out twice more (with at least 20 hours between exchanges). After DMF exchange, the dispersion of particles was deep green in color. The product was then solvent exchanged using the same centrifuge procedure (30-minute first exchange, two subsequent overnight exchanges). Solvent

exchange to methanol resulted in a pale green dispersion of the MIL-101(Cr) particles. Solvent exchange to ethanol produced a slightly darker color, but no difference in adsorption performance was noted when the solvent exchange was in either alcohol.

Upon completion of the solvent exchanges, the dispersion was centrifuged to remove the solvent and allowed to dry in a hood at ambient conditions for 48 hours. The solid product was recovered from the centrifuge tubes, lightly crushed with a mortar and pestle to break up the centrifuge shaped agglomerates, and left in the hood to dry an additional 48 hours. The final MIL-101(Cr) product was activated in a vacuum oven under a dynamic vacuum overnight at 150°C to remove any remaining solvent.
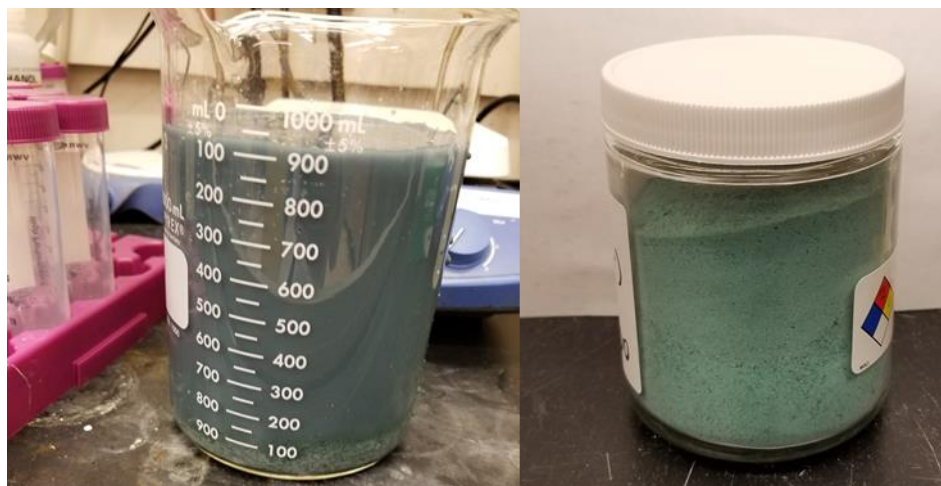
Figure 3-6. Photographs of MIL-101(Cr) Synthesis (Left) Product solution post-synthesis appeared as a blue-green color with significant particulate mass settling to the bottom. (Right) the powder product of approximately eight batches (~100 grams)

3.3.2   Fiber Spinning

3.3.2.1   <u>Confirmation of Solvent and Spinning Stability</u>

When trying to incorporate a new adsorbent or other solid filler in the fiber spinning process, it is imperative first to confirm the stability of the solid dispersant in all solvents

and all steps of the spinning process. The term dispersant here is used so that it is clear this is true not only for adsorbents, rather any solid filler that is desired to be dispersed throughout the porous polymer structure. Since this process can be carried out on very small scales ($< 500mg$) of active material, it is imperative to confirm this before attempting a full-scale spin.

The general procedure followed in this work is as follows. A known mass of dispersant was soaked for a prolonged period (1-3 days) in water. The dispersion was then vacuum filtered, and the solid is collected on filter paper. The filter paper was stored in a small (20 mL) vial covered by a kim wipe overnight in a fume hood to allow for most of the water to evaporate and is then dried at 60°C overnight under a dynamic vacuum. The weight of the dry filter paper and the empty vial was recorded before filtration of the sample and used to determine the mass of the dispersant which survived the exchange. The survival of the dispersant can be confirmed by comparison of the starting weight to the final weight, as well as other characterization methods (XRD, N_2 physisorption, SEM) to confirm other characteristics remain.

Water was used as the first solvent to check as once water stability is confirmed, water can act as a solvent exchange step from the testing of later solvents. After water, the same procedure can be followed for other solvents (e.g., NMP, Methanol, Ethanol, Hexanes), with an added solvent exchange to water carried out in the vacuum filtration funnel. Similar determination of weight loss and material characterization should be carried out for each solvent.

111

If the desired solvent stability has been confirmed, the process of dope preparation can be carried out, excluding the polymer as an added precaution to be doubly sure of the dispersant's survivability. With this stability confirmed, the next step is to perform syringe extrusions

3.3.2.2   Syringe Extrusions

Syringe extrusions are effectively small scale (1-5g of dispersant required) spinning experiments to determine an ideal polymer dope composition (solvent, non-solvent, polymer, additive(s)) needed for full-scale spinning.

The process of dope preparation for syringe extrusions mirrors that of full-scale spinning. A prime dope containing solvent, non-solvent, polymers, and soluble additives, is prepared 1-3 days in advance via the mixing of components. This mixing was either performed by hand, stirring the mixture with a small spatula, mixed on a vortex mixer, or some combination of the two. A dispersion dope containing the dispersant solid, along with solvent and non-solvent, is mixed and sonicated using a sonic horn repeatedly to break up agglomerates. A small amount of the prime dope (the fraction aligning with the missing solvent and non-solvent of the dispersion dope) is added to the dispersion dope and mixed by a combination of rolling, manual mixing, and vortex mixing. The prime added dispersion solution is then sonicated multiple times (usually 3) to break up any agglomerates that may still exist in the mixture, and the remaining polymer is added, mixed, and left to mix on a roller for an additional 1-3 days.

Due to the small size of syringe dopes, sometimes it proves infeasible to measure the prime dope adequately. In these cases, the prime dope preparation was eliminated from

the process, and the small amount of polymer that would have otherwise been added in the priming step was instead added to the dispersion, mixed, and allowed to roll for a period of hours, sonicating periodically to break up any forming agglomerates. This process allows for more precise control of the dope composition, with a bit of added risk of the formation of insoluble additive agglomerates.

Regardless of the preparation method employed, the syringe dope post-rolling to eliminate any air bubbles were loaded into a (5-20 mL) syringe. Depending on the viscosity of the dope, the syringe was left to rest for a period of hours at room temperature or elevated temperatures (in a convection oven within secondary containment) to eliminate any air bubbles. The syringe was then extruded (through a needle in some cases desired) into a prepared water bath. To confirm the ability of the fibers to handle the stress of being drawn, fiber extrudates were sometimes drawn using a pair of tweezers or small spatula. Following a 30 minute to 2-hour solvent exchange in water, the fibers were solvent exchanged with DI water for 24-72 hours, and typically solvent exchanged through methanol and hexanes before drying first in a fume hood and then under dynamic vacuum at elevated temperatures.

Syringe fibers were beneficial for probing spinning parameters before full-scale spinning. The process of syringe extrusion can offer some qualitative insights into the appropriateness of the dope for spinning. This may be combined with the characterization of the formed fiber segments with SEM, TGA, and physisorption can offer insight into the dope quality and processing stability of any dispersants. Usually, these fiber segments are too small to be used for dynamic adsorption testing, where the length of the bed plays a crucial role in the study of the system.

3.3.2.3   Fiber Sorbent Spinning

Fiber sorbents were created via a non-solvent induced phase separation technique, known as dry-jet wet-quench spinning. In this process, a polymer solution with well-dispersed sorbent particles known as a dope is extruded through an orifice known as a spinneret into a non-solvent quench bath. A schematic describing typical spinning was given in Chapter 2 and is also given in **Figure 3-7**. The polymer dope filament, leaving the spinneret, briefly transverses an air gap where it is drawn via tension derived from the take-up drum. It then enters a water quench bath, where the water rapidly exchanges with the solvent in the filament to produce a solid fiber filament, which is taken up on the neighboring take-up drum.
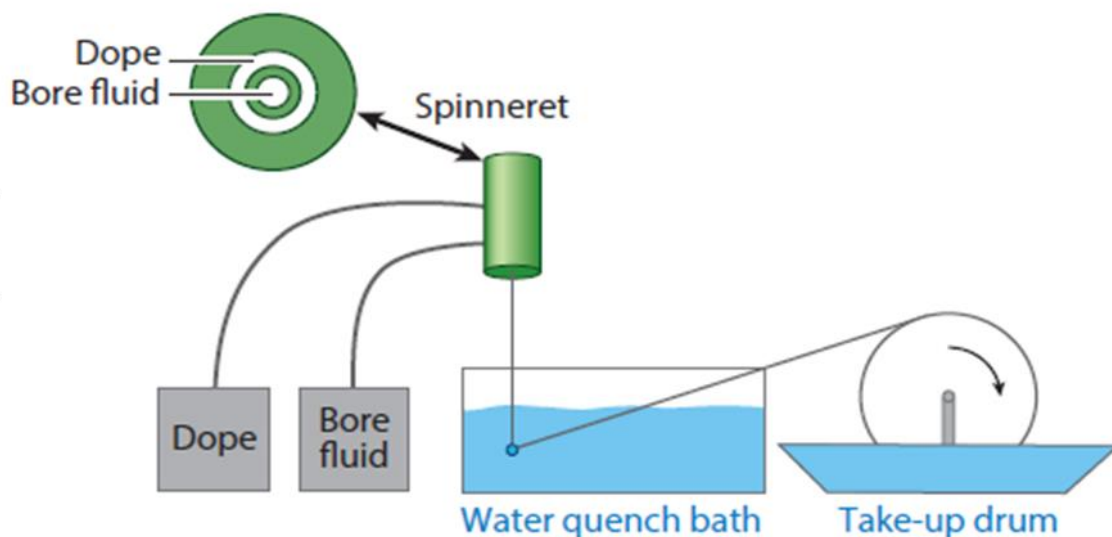
Figure 3-7. Fiber sorbent spinning system schematic where a polymer dope containing adsorbent particles is extruded through a spinneret into a water quench bath and taken up on a take up drum

Dopes were prepared in a similar manner described for syringe extrusions described above. A prime dope containing ~30% of the required polymer (CA), solvent (NMP), non-

114

solvent (water), and soluble additives (PVP in this work) was prepared via mixing in a 250 ml glass jar with a sealed cap and rolled on a dope roller for one to two days in advance of the dope preparation. A dispersion dope containing 80% of the required NMP and water and all of the required sorbent material was prepared in a 1L glass jar sealed with a cap. The dispersion dope underwent repeated stirring (with an impeller) and sonication (1000 W max horn) cycles to confirm the good dispersion of the adsorbent material. Typically in this work, the stirring-sonication cycling was as follows:

1. Stir dispersion dope for five minutes with impeller
2. Sonicate five times at 30% intensity on the sonication horn for thirty seconds, with a thirty-second break between each sonication
3. repeat steps 1 and 2 three times

Once the dispersion dope was well dispersed, 2/3rd's of the prepared prime dope (equivalent to 20% of the expected total dope's polymer, solvent, non-solvent, and soluble additives) was poured into the dispersion dope and allowed to mix on the impeller for at least 30 minutes. The primed dispersion dope then underwent three additional stirring sonication cycles. Upon completion of those cycles, the remaining CA and PVP were added to the primed dispersion dope resulting in the final dope composition. This dope was mixed for 3-8 hours with the impeller at room temperature until no solid polymer was notable in the mixture, then left to mix on a roller until all air bubbles had been degassed (typically 24 hours, no longer than 72 hours). The degassed dope was then loaded into a Teledyne Isco pump and allowed to degas overnight at 50°C in the sealed pump chamber.

Upon completion of spinning, the fibers were solvent exchanged for 72 hours in deionized water, exchanging the bath three times in total. The fibers are then solvent exchanged through Methanol and Hexanes to reduce the surface tension inside the pores of the polymer matrix to reduce the chance of pore collapse upon drying. Finally, the fibers are hung and dried in air for 24 hours before being dried in at elevated temperatures and under a dynamic vacuum in a vacuum oven.

3.3.2.4 Spinning of Thermally Modulated Fiber Sorbents

Fiber spinning with multiple insoluble additives (e.g., two sorbents) may require changes to the dope preparation process to realize good dispersion of both materials throughout the entirety of the dope. In the case of spinning microencapsulates phase change materials (µPCM), a minor change to the dope preparation process was required. To prepare a cellulose acetate dope of containing µPCM and UiO-66 insoluble additives, the dispersion dope preparation step described in the previous section was expanded. The µPCM being non-porous, had a significantly lower density (0.7-0.9 g/cc) than the solvent mixture when in the melted state, and relatively large particle size, which led to it settling more rapidly than other additives.

When preparing the dispersion dope, all of the requisite µPCM was added first and dispersed in the NMP-water mixture before any of the UiO-66 was added. The UiO-66 was then added in 25% increments with sonication, and stirring cycles followed similar to that described in the prior section. The addition of UiO-66 had a thickening effect on the *dispersion* dope, similar to what is experienced when the prime dope is added, which helped to reduce the settling and agglomeration of the µPCM.

Also, the μPCM was found to be unstable in methanol, leading to the collapse of the microcapsule shell. The methanol and hexane exchanges described in the earlier section were eliminated from the drying process. The drying of the fibers in the vacuum oven was carried out at ambient temperature for 4 hours before ramping to 60°C for the regular overnight drying.

3.3.2.5   Spinning of Adsorbent Agglomerates

To overcome issues related to sorbent leaching, a procedure was developed to spin adsorbent agglomerates of MIL-101(Cr). To try to allow the natural agglomerates of sorbent (estimated 20-100μm in diameter), the sonication steps described in the traditional process were eliminated. Out of concern over clogging of the spinneret, the spinning of fibers desiring adsorbent agglomerates exchanged the triple orifice spinneret for a Swagelok® ¼"-1/8" port adapter, extruding through the 1/8" end.

3.3.3   Materials Characterization

3.3.3.1   Scanning Electron Microscopy

Scanning Electron Microscopy (SEM) was used to observe the structure of sorbents and fibers synthesized and manufactured in this work. Powders were dispersed in acetone or methanol and dropped via pipetting of the dispersion onto a carbon tape covered sample stage. Fiber samples post solvent exchange and drying were cryofractured in LN_2 to produce clean cross-sections and mounted on a 90" sample stage. Experiments were carried out on a Hitachi 8230 Field Emission Scanning Electron Microscope. Fiber samples were sputter-coated for 20 seconds, each using a Hummer 6 Gold Sputterer.

3.3.3.2   Thermogravimetric Analysis

Thermogravimetric analysis (TGA) was used throughout this work to confirm the loading of fillers within fiber sorbents, as well as the quality of synthesized or delivered MOF samples. TGA was carried out on a TA Instruments TGA-500 with an autosampler.

The typical calculation of MOF loading was carried out via residual mass analysis. This approach is useful for determining the weight loading of materials containing some inorganic material (like MOF or zeolites), which will not be fully decomposed during ramped heating under flowing air. For residual mass analysis, the following experimental method was carried out from ambient temperature, given in **Table 3-1**.

Table 3-1. Example thermogravimetric analysis (TGA) method used for residual mass analysis

STEP	TEMPERATURE CONTROL	ANALYSIS GAS
1	Ramped at 5°C/min from room temperature to 110°C	Dry Nitrogen
2	Temperature soak at 100°C for at least 1 hour	Dry Nitrogen
3	Temperature ramped up to 900°C	Air
4	Temperature ramped down to room temperature	Air

The mass of the sample is recorded throughout the process in the TGA. To determine a weight loading of inorganic within a fiber, the remaining mass after step 4 is normalized to the weight of the dried sample (the recorded weight at the end of step 2). This value represents the fraction of the dry weight of the material, which was retained during the experiment.
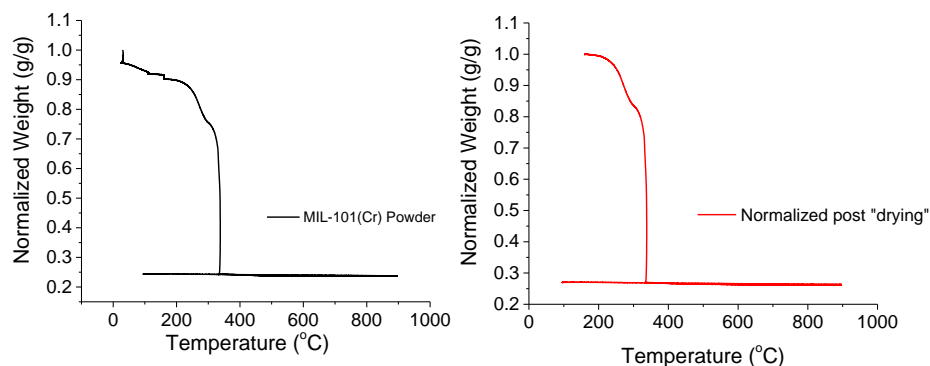
Figure 3-8. Example of collected TGA profiles for a MOF powder, with and without evaporation of water normalized away

Determining the weight loading of an adsorbent loaded fiber where the adsorbent contains some inorganic mass (MOFs or Zeolites) can be carried out by taking the ratio of the residual mass of the fiber-containing sorbent to the residual mass of the sorbent alone.[10, 19] One key parameter to keep in mind is that all of the water should be removed before calculating a dry weight. Without normalizing to a standard dry weight condition, some retained water may be accounted for in one of the residual mass calculations but not the other.

3.3.3.3 N_2 Physisorption at 77 K

N_2 physisorption at 77 K was carried out on MOF and fiber samples to assist in the determination of the weight loading of the adsorbent. All N_2 physisorption experiments performed in this work were performed on a Microtrak Belsorp-max or a Quantachrome Quadrasorb.

For the determination of the weight loading of sorbent within a fiber, one of two approaches was followed. One method involved comparing the quantity adsorbed at a designated relative pressure ($P/P_0 = 0.5$) of fiber adsorbent and powder adsorbent materials,

where the ratio of these values was considered the weight loading. The second method used the comparison of the calculated BET surface areas of the powder adsorbent and fiber adsorbent. Both methods result in effectively the same value being compared, as they both follow the same principle, i.e., that the uptake values of the isotherm should scale linearly with the weight loading of MOF material.

The first method was preferred for the calculation of MIL-101(Cr) loading due to an irregularity in the MIL-101(Cr) isotherm that can lead to significant errors in calculating the BET surface area. Because MIL-101(Cr) 's N_2 isotherm has an inflection in the BET plot in the middle of the microporous range, the value of the BET surface area is correctly calculated at the lower pressure range (below the step). The number of points available for the calculation of the BET surface area when working with the fibers was significantly fewer than that of the powders, determining in the fiber samples have a slightly larger error depending on the points selected. With that in mind, the first method, using the uptake at $P/P_0 = 0.5$, was used instead.

3.3.3.4   CO$_2$ and N$_2$ isotherm collection

Sub-ambient CO_2 and N_2 isotherms were collected using an HPVA-II from Particulate systems with a Cryostat attachment. Temperature control was maintained using a ColdEdge cold head, connected to a helium compressor-chiller with a Lakeshore 336 temperature controller. Samples were activated under a high vacuum (0.004 mbar) and elevated temperature using a temperature-controlled furnace and a turbomolecular pump attached to the system. Between experiments, samples were reactivated for 6 hours at 110-200°C, depending on the sample under a dynamic vacuum.

3.3.3.5 Differential Scanning Calorimetry

Determination of the weight loading of phase change material inside the thermally modulated fiber sorbents required a new form of fiber sorbent characterization. As microencapsulated phase change materials neither adsorb significant gas to have a tangible sorption isotherm nor contain any form of inorganic material, the usual methods of determining the loading were inadequate. Differential scanning calorimetry profiles of the freezing and melting behavior of the composites, performed on a TA Instruments Q-200, was instead used to determine microcapsule loading.

To collect freezing and melting profiles on the fibers and microcapsule powders, the samples were loaded into DSC pans, sealed, and placed within the DSC system. While multiple temperature ramps were used, in a typical experiment at sub-ambient conditions, the system was cooled to 0°C and allowed to soak for approximately 30 minutes. This step was added to be sure any sorbed water in polymer-µPCM composites was completely frozen before collecting the profile. The sample was then cooled to -50°C at 5°C/min, and soaked there for 5 minutes, collecting the freezing behavior of the PCM. The DSC then ramped the temperature back to 0°C at 5°C and soaked for 5 minutes. This process was completed for at least two cycles to be sure to isolate any history effects, though none were ever noted for these materials.

Collected DSC profiles allowed for the calculation of the latent heat of fusion of the phase change material or composite, via numerical integration of the profile within the analysis software. Determination of the weight loading of phase change materials within

fiber composites was calculated from the ratio of the composite fiber latent heat of fusion to the pure powder latent heat of fusion.

3.3.3.6   X-Ray Diffraction

X-Ray Diffraction patterns were collected on a Panalytical XPert Pro Alpha-1 X-Ray Diffractometer. Powder samples were collected through the pressing onto a zero background sample holder with a clean glass slide. Fiber samples were crushed mechanically using a mortar and pestle if brittle enough. In cases where they were not particularly brittle, fibers were mounted perpendicular to the incident beam direction on a zero background sample holder and scotch-taped down onto the holder to keep in place.

3.4   Dynamic Adsorption Performance Characterization

Dynamic adsorption performance characterization experiments (fixed bed breakthroughs, collection of thermal fronts, and fixed bed desorption profiles) were collected in a custom-built PSA-100 (L&C systems) shown in **Figure 3-9**. The system, built within a sub-ambient cabinet, allows for excellent temperature control when performing multi-component competitive adsorption experiments, pressure-swing-adsorption cycles, and collection of temperature profiles. Mass flow controllers (Parker Porter), located outside of the sub-ambient cabinet, were used to control the flow of purge and simulated flue gas throughout the experiments. System pressure is maintained using a custom programmed backpressure controller, where the transducer (Honeywell) is located inside the cabinet, and the flow controller (Parker Porter) is outside the cabinet. A Mass Spectrometer (MS), Pfeifer Omnistar, Pfeifer Vacuum. is installed downstream of the system to monitor the effluent of the system.
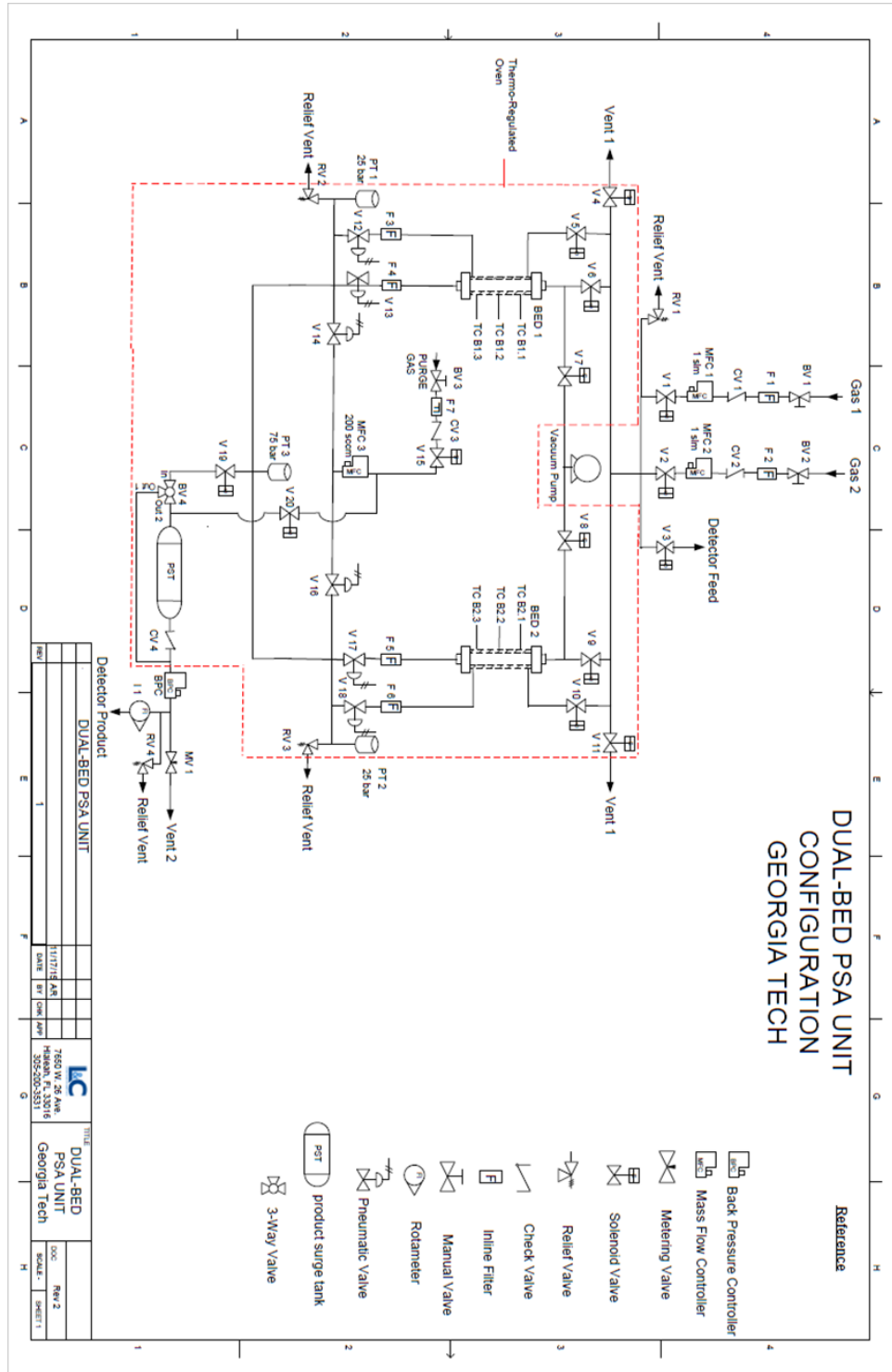
Figure 3-9. Process and Instrumentation Diagram for Dual Bed PSA unit used in this work

3.4.1.1 Fixed Bed Breakthrough Experiments

Competitive fixed bed breakthrough experiments were performed with the simulated dry flue gas (12.5% CO_2, 12.5% He, 75% N_2) at a variety of flow rates and temperatures to investigate sorption kinetics and the effects of temperature modulating phase change material. In all experiments, the fixed fiber beds were activated overnight at 50°C under flowing nitrogen to remove any adsorbed water. Once the beds were activated, they were pressurized to 16 bar under 100 sccm flow of dry nitrogen and cooled to the lowest target temperature.

A fixed volume (not used for the actual analysis) was installed parallel to the analysis bed, sealed off by multiple valves from the analysis flow path. This fixed volume was pressurized with N_2 to a pressure near the operating pressure of the experiment at the same time as the analysis bed and then isolated. At the start of the experiment, pure N_2 was allowed to flow over the analysis bed until the ion current readings of the downstream MS were stabilized. To start the breakthrough experiment, the N_2 flow was stopped to the system and switched to the fixed volume. The N_2 flow was then closed off, and the analysis gas switched on at the desired flow rate. Once the pressure in the fixed volume reached the operating pressure, the flow was redirected to the analysis bed and allowed to run until the breakthrough profile had been collected.

After the experiment was complete, the bed pressure was reduced to atmospheric pressure, then exposed to a dynamic vacuum ($\sim 10^{-4}$ bar) for at least 5 minutes to remove the majority of the adsorbed CO_2 from the bed. The bed was then re-pressurized to 1 bar, and dry N_2 was flowed as a purge gas over the bed for at least 5 minutes. The bed was then

pressurized to the operating pressure with N_2, and the effluent was sampled using mass spectrometry to confirm there was no remaining CO_2 or He. A new experiment was started once the effluent stream was found to contain the only N_2 for at least 5 minutes of operation

In this procedure, He acts as the inert tracer gas, N_2 as the carrier gas, and CO_2 as the adsorbate of interest.[19] Calculated breakthrough and pseudoequilibrium capacities were used to understand the performance of the fiber beds. As transport limitations like heat effects in adsorptive breakthroughs will broaden the breakthrough profile, so then more capacity at low adsorbate "leakage" can be indicative of heat being managed. Capacities were calculated using the area bound by the He and CO_2 concentration profiles from the effluent breakthrough curves collected by the mass spectrometer. As the Helium acts as an inert tracer, it captures the dead volume of the system, allowing for quick calculation of sorbent capacity. The product of area bound by the two curves at any time after He breakthrough and the inlet molar flow rate of the adsorbate species one can calculate the amount of CO_2 adsorbed at that given time[43]. For comparisons of capacity near breakthrough, where the effects of sorption enthalpy are most prevalent, we used the capacity at 5% leakage of CO_2. To confirm the loading of sorbent in the fibers was as expected, the capacity at 95% leakage or "pseudo-equilibrium" capacity, was used.

Calculation of breakthrough (5% leakage) and pseudoequilibrium (95% leakage) capacities using the inert tracer and CO_2 profiles were carried out, as discussed in previous work[20]. In short, profiles such as that shown in **Figure 3-10** were used to calculate capacity. The area bound by the He and CO_2 effluent profiles and the time, t = C/C_0 of CO_2 of interest, was calculated using the trapezoidal rule for each point collected. This area can then be combined with the inlet flow rate, the mole fraction of CO_2 in the

inlet gas, the dry weight of the fiber, and the fraction of the fiber mass, which is MOF to determine the amount sorbed.

$$CO_2 \ Sorbed \ \left(\frac{mmol \ CO2}{g \ sorbent - 66}\right)$$

$$= Inlet \ gas \ velocity \ \left(\frac{mmol}{sec}\right) * Mole \ fraction \ CO_2 \ \left(\frac{mmol \ CO2}{mmol}\right) \qquad (3\text{-}19)$$

$$* Area \ (sec) \Bigg(Dry \ Weight \ of \ fiber \ (g)$$

$$* Mass \ fraction \ sorbent \ in \ fiber \ \left(\frac{g}{g}\right)\Bigg)$$
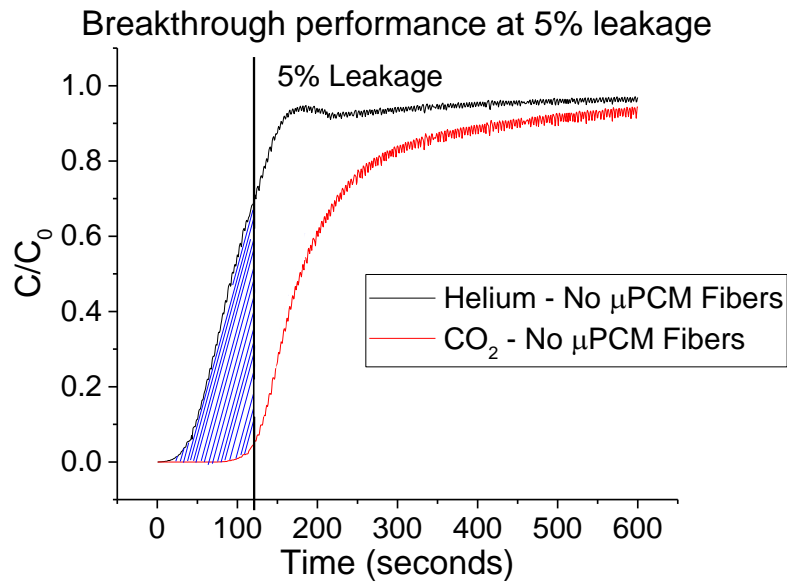
Figure 3-10. Example breakthrough profile used for calculating sorbent capacity in bed

3.4.1.2   Thermal Front Collection

Figure 3-11 provides a schematic and images of the module used for the "large" module breakthrough experiments. A 25.4 cm axial thermocouple probe (Type K, Omega Engineering) was sealed via compression fittings (Swagelok ®) to a 10 cm long 0.7 cm

126

diameter stainless steel tube. This tube contained the inactive length of the thermocouple

probe, so the interstitial region of the tube was filled with fast-drying epoxy. The end of

the tube was fit to a 3/8" Swagelok ® union T, and a second 10 cm long tube was fit to the

other end. This tube was filled with 32 fiber segments 12.7 cm long, and capped with

another 3/8" union T, which was capped with a tube plug. TC-1 and 3 were located at the

center of the union T inlet and outlet, while TC-2 was located at the center of the module.

Temperature profiles were collected simultaneous to breakthroughs on this system, with

the temperatures at all three points collected at a rate of 1 Hz by LabView © software

prepared by L&C systems.
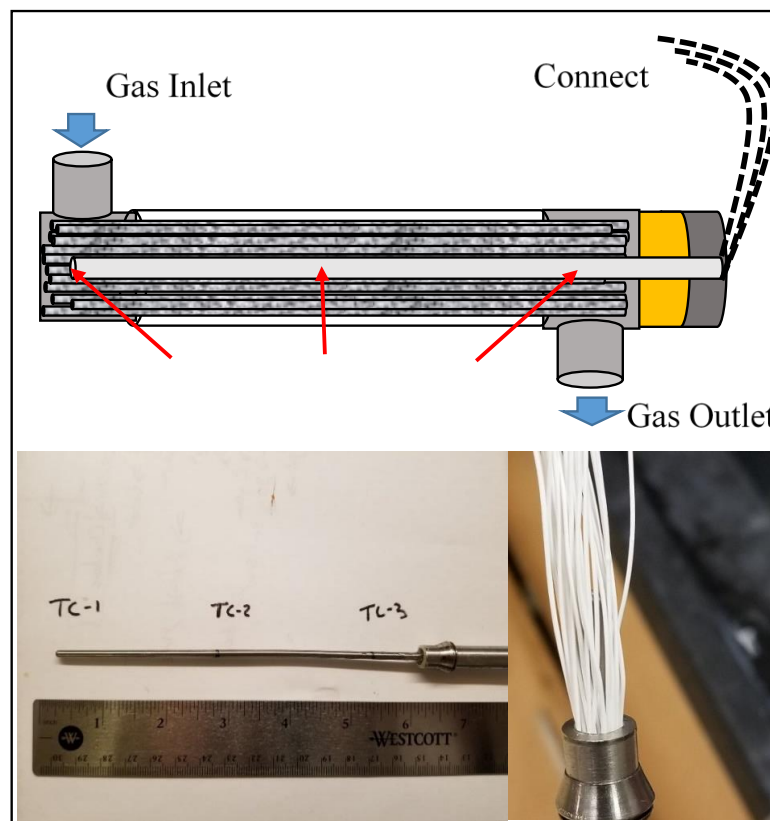
Figure 3-11. "Large" Module Schematic and photos. (top) Schematic of a large module with thermocouple needle installed down the middle (bottom-left) Photo of axial thermocouple probe, closed-end was sealed with adhesive. (bottom-right) photo of the module with fibers installed.

3.4.1.3 Fixed Bed Desorption Experiments

Fixed bed desorption profiles were collected using a similar preparation procedure to that described in fixed bed breakthroughs. Beds were prepared and activated using the same procedure, and the same cooling under pressurized flowing N_2 procedure was followed. Once the system was at the desired pressure and temperature, the gas flow to the analysis bed was switched to simulated flue gas (14.5% CO_2, 85.5% N_2) and fully saturated with the gas until the effluent of the bed reached the feed condition. One of two different desorption experiments, one at elevated pressure and one at ambient pressure, was then performed.

For high-pressure desorption, the analysis bed was isolated by closing the valves immediately up and downstream of the bed, and the dead volume of the entire system was exchanged with Helium via flow. Once the effluent of the system was reading a steady concentration of Helium, >99.9%, the gas flow path was adjusted to flow through the analysis bed, and the analysis bed was opened to the flow. The effluent profile for He, CO_2, and N_2 was monitored via MS, and the desorption profile was collected.

For ambient pressure desorption, a similar procedure was followed, except that before isolating the bed from the rest of the system, the analysis bed was first vented for 10 seconds to ambient pressure as confirmed by a downstream pressure transducer. The bed was then isolated, and the same He exchange of dead volumes and desorption procedure was followed, just at 1 bar pressure instead of elevated pressure. When analyzing desorption profiles, the concentrations of CO_2, N_2, and He were collected, and the relative ratio of CO_2 to N_2 was noted as the purity of the desorption product.

3.5 Fiber Sorbent Pressure Swing Adsorption

Single bed pressure swing adsorption experiments were carried out on MIL-101(Cr) fiber sorbent beds. In preparation for these experiments, the fiber beds were activated in the L&C PSA-100 system described in **Figure 3-9** using the same procedure outlined for breakthrough and desorption experiments. The system was also cooled and pressurized using the same approach described previously.

In preparation for running pressure swing adsorption experiments, the bed was first saturated with simulated flue gas. This "dirty" start to the experiment was maintained for the sake of consistency, and it has been noted elsewhere in the literature as one approach to get the system to a cyclic steady state faster, which is useful when trying to develop Pareto fronts rather than study start-up dynamics. In a similar vein, the downstream, high-pressure product storage tank was bypassed to reach a cyclic steady state more quickly

A four-step Skarstrom cycle (co-current Pressurization, co-current Feed, counter-current Blowdown, counter-current Evacuation) was performed on the beds. A typical cycle is illustrated in **Figure 3-12** below. In the first step, pressurization, the bed's pressure is increased through feeding simulated flue gas (13.5% CO_2, 85.5% N_2) to the bed with a valve downstream of the system closed to allow pressure to build (increasing pressure in **Figure 3-12**). Once the pressure set point is reached, the valve downstream of the fiber bed is opened, and gas is continuously fed at a given set point. During this feed step, a high pressure purified Nitrogen product is captured from the downstream, while the CO_2 is held up in the bed. At a predesignated time, the feed is halted, the bed is closed off, and a vent valve is opened, rapidly reducing the system pressure to near ambient pressure. Once a

blowdown pressure set point is reached (1.1 bar with a 0.1 bar tolerance), the vent valve is closed, and the vacuum valve is opened, and the bed's pressure is reduced to a given set point. Once that set point is reached, the system resets and begins the pressurization step anew.
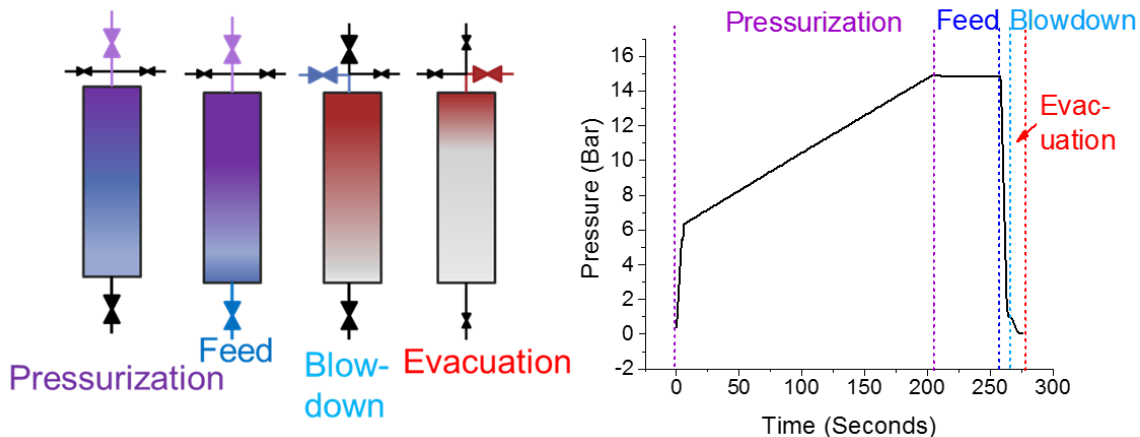
Figure 3-12. A four-step pressure swing adsorption cycle was used throughout this work, with pressure profiles similar to those pictured on the right.

The feed step product was monitored via MS to determine when a cyclic steady state had been reached. In most cases, a cyclic steady state was reached within ten cycles (maximum 15), and throughout all experiments, the system was allowed to run for at least 30 cycles monitoring the feed step effluent before switching to monitor the blowdown and evacuation products.

Once a cyclic steady state had been reached, the mass spectrometer inlet valve was switched to capture the blowdown and evacuation products, respectively. Due to the very short pulses of gas products produced in these steps, surge tanks were installed upstream of the MS inlet to allow for the capture of the transients experienced. The composition of these streams was monitored for at least five cycles to allow for the signal to stabilize. In a

few experiments, the vacuum product took longer to reach a steady composition than the five cycles, at which point the product was monitored for an additional 3-5 cycles during which the composition stabilized.

3.6   References

1.   James, R. Z., Alexander; Keairns, Dale; Turner, Marc; Woods, Mark; Kuehn, Norma *Cost and Performance Baseline for Fossil Energy Plants Volume 1: Bituminous Coal and Natural Gas to Electricity*; NETL: 2019.

2.   Boyce, M. P., 7 - Axial-Flow Compressors. In *Gas Turbine Engineering Handbook (Fourth Edition)*, Boyce, M. P., Ed. Butterworth-Heinemann: Oxford, 2012; pp 303-355.

3.   *Perry's Chemical engineers handbook*. Sixth edition / prepared by a staff of specialists under the editorial direction of late editor Robert H. Perry ; editor, Don W. Green ; assistant editor, James O. Maloney. New York : McGraw-Hill, [1984] ©1984: 1984.

4.   Services, T. B., Ohio State Term Schedule Discount Pricelist. Ohio.gov, Ed. 2012.

5.   Ng, K. C.; Chua, H. T.; Chung, C. Y.; Loke, C. H.; Kashiwagi, T.; Akisawa, A.; Saha, B. B., Experimental investigation of the silica gel–water adsorption isotherm characteristics. *Applied Thermal Engineering* **2001,** *21* (16), 1631-1642.

6.   Uzarevic, K.; Wang, T. C.; Moon, S. Y.; Fidelli, A. M.; Hupp, J. T.; Farha, O. K.; Friscic, T., Mechanochemical and solvent-free assembly of zirconium-based metal-organic frameworks. *Chemical Communications* **2016,** *52* (10), 2133-2136.

7.   Wang, K. K.; Li, C. F.; Liang, Y. X.; Han, T. T.; Huang, H. L.; Yang, Q. Y.; Liu, D. H.; Zhong, C. L., Rational construction of defects in a metal-organic framework for highly efficient adsorption and separation of dyes. *Chemical Engineering Journal* **2016,** *289*, 486-493.

8.   Jiao, Y.; Liu, Y.; Zhu, G.; Hungerford, J. T.; Bhattacharyya, S.; Lively, R. P.; Sholl, D. S.; Walton, K. S., Heat-Treatment of Defective UiO-66 from Modulated Synthesis: Adsorption and Stability Studies. *The Journal of Physical Chemistry C* **2017,** *121* (42), 23471-23479.

9.   Platero-Prats, A. E.; Mavrandonakis, A.; Gallington, L. C.; Liu, Y. Y.; Hupp, J. T.; Farha, O. K.; Cramer, C. J.; Chapmant, K. W., Structural Transitions of the Metal -Oxide Nodes within Metal- Organic Frameworks: On the Local Structures of NU-1000 and UiO-66. *Journal of the American Chemical Society* **2016,** *138* (12), 4178-4185.

10.   Chen, G.; Koros, W. J.; Jones, C. W., Hybrid Polymer/UiO-66(Zr) and Polymer/NaY Fiber Sorbents for Mercaptan Removal from Natural Gas. *Acs Applied Materials & Interfaces* **2016,** *8* (15), 9700-9709.

11.   Sinha, A.; Darunte, L. A.; Jones, C. W.; Realff, M. J.; Kawajiri, Y., Systems Design and Economic Analysis of Direct Air Capture of CO_2 through Temperature Vacuum Swing Adsorption Using MIL-101(Cr)-PEI-800 and mmen-Mg-2(dobpdc) MOF Adsorbents. *Ind. Eng. Chem. Res.* **2017,** *56* (3), 750-764.

12.   Llewellyn, P. L.; Bourrelly, S.; Serre, C.; Vimont, A.; Daturi, M.; Hamon, L.; De Weireld, G.; Chang, J. S.; Hong, D. Y.; Hwang, Y. K.; Jhung, S. H.; Ferey, G., High uptakes of CO_2 and CH_4 in mesoporous metal-organic frameworks MIL-100 and MIL-101. *Langmuir* **2008,** *24* (14), 7245-7250.

13.   Liu, Q.; Ning, L.; Zheng, S.; Tao, M.; Shi, Y.; He, Y., Adsorption of Carbon Dioxide by MIL-101(Cr): Regeneration Conditions and Influence of Flue Gas Contaminants. *Scientific Reports* **2013,** *3* (1), 2916.

14.   Khutia, A.; Rammelberg, H. U.; Schmidt, T.; Henninger, S.; Janiak, C., Water Sorption Cycle Measurements on Functionalized MIL-101Cr for Heat Transformation Application. *Chemistry of Materials* **2013,** *25* (5), 790-798.

15.   Bhattacharjee, S.; Chen, C.; Ahn, W.-S., Chromium terephthalate metal–organic framework MIL-101: synthesis, functionalization, and applications for adsorption and catalysis. *RSC Advances* **2014,** *4* (94), 52500-52525.

16.   Greeves, N., UiO-66 Metal Organic Framework. In *ChemTube 3D*, University of Liverpool: 2020.

17.   Férey, G.; Mellot-Draznieks, C.; Serre, C.; Millange, F.; Dutour, J.; Surblé, S.; Margiolaki, I., A Chromium Terephthalate-Based Solid with Unusually Large Pore Volumes and Surface Area. *Science* **2005,** *309* (5743), 2040-2042.

18.   Zhao, T.; Jeremias, F.; Boldog, I.; Nguyen, B.; Henninger, S. K.; Janiak, C., High-yield, fluoride-free and large-scale synthesis of MIL-101(Cr). *Dalton Transactions* **2015,** *44* (38), 16791-16801.

19.   Lively, R. P. Hollow Fiber Sorbents for Post-Combustion CO_2 Capture. Georgia Institute of Technology, 2011.

20.   Pimentel, B. Control of Diffusive Time Scales in Zeolite Imidazolate Frameworks for the Kinetic Separation of Light Hydrocarbons. Georgia Institute of Technology, Atlanta, GA, 2018.

CHAPTER 4.   TECHNOECONOMICS OF SUB-AMBIENT PSA

To guide future developments of materials, structures, and pressure swing adsorption cycles for sub-ambient CO_2 capture, it is important to have a good working understanding of the limitations and potential gains of this process design. To that end, this chapter focuses on developing a knowledge base of the proposed process. A baseline case for sub-ambient CO_2 capture via PSA is first presented highlighting some of the more important components of the process. The potential of adsorbent materials for pressure swing adsorption application is compared based on optimized cycles to help judge the actual potential of some possible materials and their role within the cost of the system. To dig deeper into what may be causing the changes in the cost of capture in the case studies, a sensitivity analysis is carried out to understand the role of individual process operating parameters when the PSA performance remains the same. This analysis helps to understand the key pieces of capital equipment and their effect on the economics of the process. Finally, the economics of thermally modulated fiber sorbents are analyzed and used to quantify the effects of adsorbent performance on the process economics.

4.1   Heat Integrated Multi-stage Sub-ambient CO_2 Capture

Inspired by the work of Haase et al. and others[1-5], who proposed a sub-ambient membrane process that required considerable pretreatment, the work discussed here focuses on the design of pretreatment systems for any separation process that relies on pressure driving forces (in particular, pressure swing adsorption). The critical consideration in any sub-ambient pressure-driven CO_2 capture process is the removal of heat from the feed. External refrigeration cycles are extremely expensive,[6] so the main portion of what makes the process proposed by Haase et al. economically viable is their ability to run the sub-ambient process without the need for any external cooling utility.

It is helpful to simplify the process considered into two distinct sub-processes: one that provides cooling through compression and expansion of flue gas components, and a second that produces the purified CO_2 to pipeline specifications (see **Figure 4-1**). The expansion of the nitrogen product provides cooling to both the feed after compression and the CO_2 product stream, as shown in **Figure 4-1**. The expansion of the nitrogen product is carried out on a stream that is already moderately cold through heat integration and removes the heat of compression. This also allows for the cooling of the CO_2 product before its liquefaction.
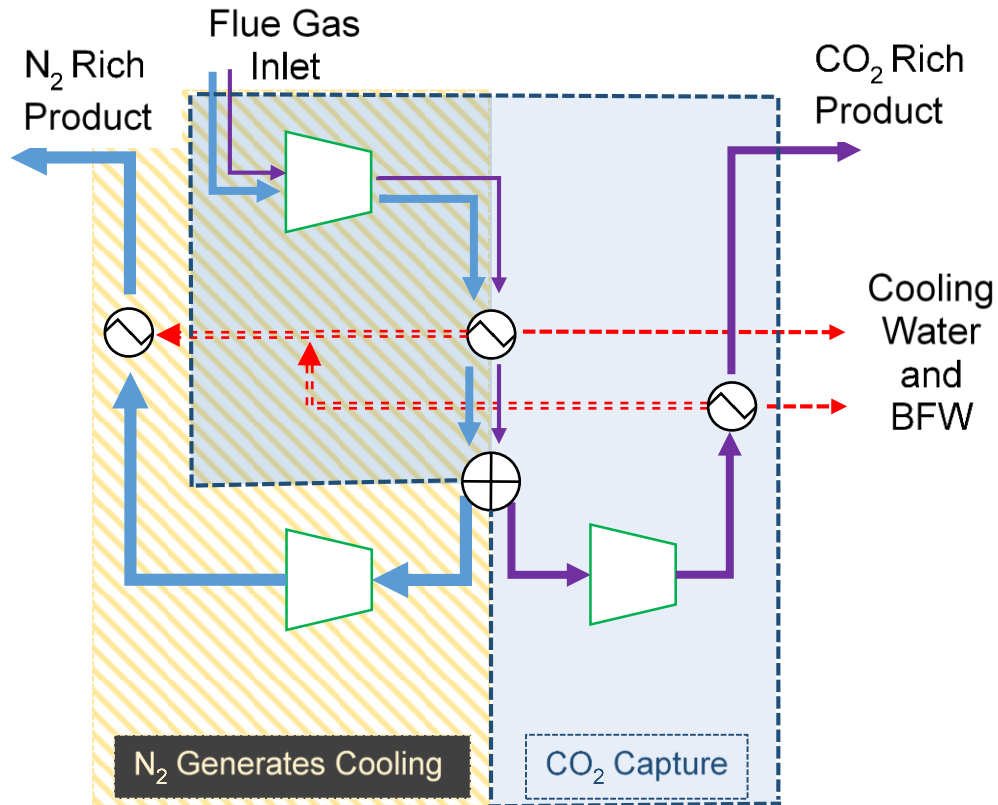
Figure 4-1. Simplified flowsheet for sub-ambient CO_2 capture. The Blue and purple arrows indicate N_2 rich and CO_2 rich products of separation. Red arrows indicate the flow of heat. The gold box refers to N_2 enriched Open *Refrigeration* Cycle. The navy box shows CO_2 separation and purification. Compressors and expanders are shown as one stage for clarity, and possible boiler feedwater (BFW) integration is noted to be supplemented with cooling water.

The process developed herein builds on this basic concept to enable the CO_2 capture process, with the additional downstream treatment of the CO_2 rich product. Liquefying the CO_2 rich product allows for the PSA unit to operate below the overall process purity specification, which hopefully will allow more materials to be competitive. This combined hybrid process is further explored in the following section.

4.1.1 Flowsheet Description

The overall process shown in **Figure 4-2** may be broken down into four subsections: 1. gas treatment and energy recovery, 2. sub-ambient heat exchange, 3.

pressure-driven CO_2 separation, and 4. product liquefaction. The second version of this flowsheet is reported in **Figure 4-3** for process configurations where the liquefaction pressure exceeds the separator operating pressure. In that configuration, one of the compressors (COMP4) is replaced with a turboexpander (TURB3), and its feed is passed through the sub-ambient heat exchanger network before expansion.

The complete flow sheet including all unit operations for the case shown in **Figure 4-2** is given in **Figure 4-6**, with its accompanying stream table reported in Table 4-1, at the end of this section. Specific values discussed throughout this section come from this flowsheet and accompanying stream tables.

An important feature of this design is the fact that it enables steady-state operation, including the secondary liquefaction-based separation without the need for any external cooling utility beyond cooling water. This is similar to the Linde cryogenic distillation case for air separations in this process, mechanical compression and expansion provide the cooling for the process and sufficient driving force to enable the separation.[7-11] Variation of process conditions to enable a reasonable minimum temperature approach and those subsequent effects on energetics and economics are considered in the following section. Due to the significant heat generated as a part of the compression train (Comp 1 in particular), there is the opportunity to explore heat integration with the coal plant to further drive down costs.
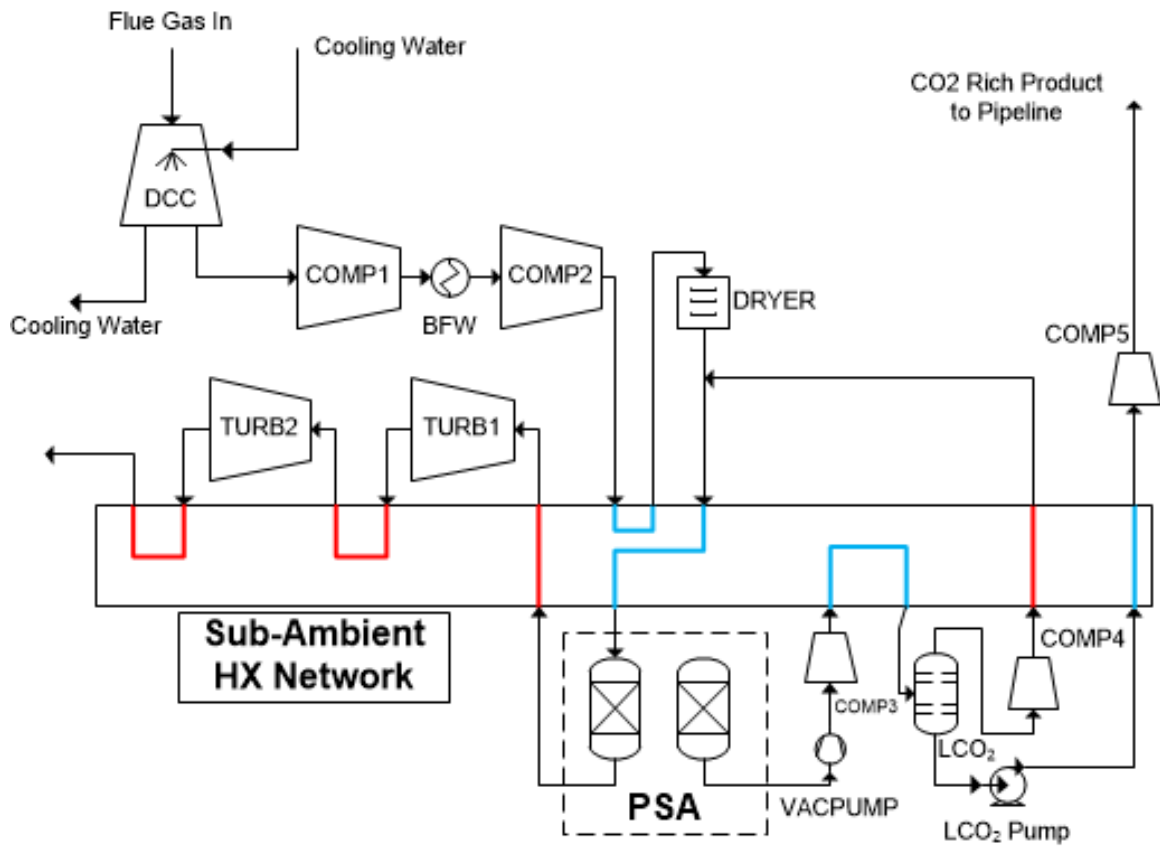
Figure 4-2. Simplified process flow diagram for a sub-ambient hybrid CO₂ capture process using pressure swing adsorption and product liquefaction. Intermediate heat exchangers on the primary compression train using cooling water are not included for the sake of simplicity. A direct contact chiller (DCC), utilizing plant cooling water is used for preliminary water removal. Blue lines in the sub-ambient heat exchanger network indicate streams that are being cooled, while red lines are those being heated.

Figure 4-3. Simplified process flowsheet for the case where the liquefaction column's (*LCO₂*) operating pressure exceeds the operating pressure of the PSA unit. *TURB3* replaces *COMP4* in Figure 4-2, and its feed passes through the sub-ambient HX network before expansion.

4.1.1.1 Gas Treatment and Energy Recovery

The flue gas treatment and energy recovery section of the flowsheet performs on water removal and compression of the flue gas and expansion of the N_2 enriched product of the separator. Ideally, these expansion and compression systems will share a joint driveshaft to reduce mechanical efficiency losses. The compression of the flue gas feed to the target condition is carried out via two-stage compression, with pressure ratios between 3 and 5. Multiple intercoolers are used to make the compression more efficient while also providing boiler feed-water (BFW) preheating for the plant. Further discussion of BFW integration can be found in Section 4.1.1.5. Using just the first stage of compression, the

heat for the first three boiler feed-water preheaters is provided as modeled in comparison to DOE Base Case 11a.[12] Cooling water can then be used to cool the feed gas. The compressed gas can be further cooled between compression stages using excess low quality (> 0 °C) cooling available from the product and byproduct gas. Following the second compression stage, the gas is cooled to 2 °C to further dehydrate the gas before the complete drying necessary to enter the sub-ambient heat exchange system.

The drying of flue gas for the post-combustion CO_2 capture process incurs high energy demands and is thus often considered impractical.[13-15] If flue gas can be dried, however, the options available for CO_2 capture broaden considerably. In our process, flue gas drying is carried out in three stages, first using cooling water from the plant, then taking advantage of Joule-Thomson cooling from the sub-ambient process, and finally, an adsorbent dryer bed. We expect the water from the first two drying stages to be recovered and sent to a cooling tower where it can be returned to the desired conditions. We assume that cooling water at 30 °C is used to remove the water before compression through the application of a direct contact chiller (DCC). The removal of as much water as possible before compression decreases the total volume of gas that must be compressed, which ultimately reduces the volume of gas to be compressed by ~10%. Removal of water is also vital when using axial compressors, as the condensation of water inside the compressor may damage the airfoils.

After the direct contact chiller, compression, and cooling the mole fraction of water in the flue gas stream is estimated in the Aspen model to be ~0.5%, as shown in **Table 4-1**. After the flue gas has been compressed to the target pressure, it is cooled to 2 °C using available cold N_2 enriched products as mentioned previously. This additional cooling

followed by a knock out decanter results in 528 ppm residual water left in the stream to be removed via the adsorbent. With such a low concentration of water in the flue gas, it is assumed an adsorption dryer will remain essentially isothermal during drying. If the heat integration were unavailable, the economic and energy penalty of the drying would be associated with the cost of drying 10-12 times as much water. Upon completion of its expansion to near atmospheric pressure, the N_2-rich product stream is used as a dry sweep gas for the regeneration of the dryer bed and then sent to the stack.

As noted above, compression of the feed and subsequent expansion of the high-pressure N_2 byproduct enables the cooling process. The process is therefore highly reliant on the ability to recover the maximum allowable energy via the expansion of this byproduct. In the base case considered, the energy demand for compression is 298.5 MW, a very significant parasitic load. With the inclusion of gas expansion that number is reduced to 207.1 MW. The compression work required is the dominant contribution to the parasitic energy demand on the coal plant. The energy required for the drying of the feed stream and the cooling throughout the process is provided through Joule-Thomson cooling and heat integration, allowing for no additional external energy requirement for the process outside of compression and pumping.

The flowsheet in **Figure 4-2** employs five compressors (two upstream for flue gas, three downstream for liquefaction, recycle, and reaching pipeline pressure specifications respectively), and two expanders (acting on the N_2 enriched product). The downstream compressors (COMP3, COMP4, and COMP5), along with the vacuum pump and the liquid CO_2 pump have no path for power recovery. Combined, they make up approximately 63.6 MW (21.3%) of the electrical demand of the process in the base case. The remaining 143.5

MW of energy is the balance of the compression work that could not be recovered via expansion of the N_2 product. Thus in the base case, ~39% of the work for compression of the flue gas was recovered via expansion.

4.1.1.2 Sub-Ambient Heat Exchange

Extensive heat integration throughout the process is critical to avoid an expensive external refrigeration utility. The compression of the flue gas upstream is primarily responsible for the process's ability to operate at a steady state with no external refrigeration, as conceptualized in **Figure 4-1**. The more the flue gas is compressed, the more high-quality heat removal becomes available from the multistage expansion of the N_2 rich byproduct. The base case considers two-stage expansion to produce the required heat removal so the N_2-rich product passes through the heat exchanger network three times as seen in **Figure 4-2.** This expansion-cooling train is responsible for the majority of the following steps: cooling the inlet gas entering the dryer unit, knocking out additional water, cooling the inlet gas to the separation unit, cooling the compressed CO_2 enriched product after recompression to the liquefaction condition, and liquefying the CO_2 enriched product.

4.1.1.3 Pressure Driven CO_2 Separation

The primary separation for the process is performed by a pressure difference driven separation unit (PSA) that pre-purifies at high recovery the flue gas to a CO_2 rich stream (>65% CO_2 Purity, >92% CO_2 recovery) that is then recovered at vacuum pressures (PSA vacuum product) to be sent to liquefaction. The minimum recovery of the primary separator was selected such that overall system recovery with the liquefaction step and recycle 90% overall system recovery consistently, as required by US DOE standards. This requirement

for process recovery was enforced through all analyses discussed herein. The CO_2 rich product from the separator is sent to the liquefaction process, which further purifies it to pipeline specification purities. The N_2 rich product, remaining at the high-pressure condition is sent to the heat and energy recovery system described previously.

4.1.1.4   Product Liquefaction

Hybrid CO_2 capture processes that perform the CO_2 purification in multiple stages have shown promise as a way to overcome the limitations of existing adsorbent or membrane materials.[13,16-18] While the baseline model assumes the primary separation unit can produce 95% pure CO_2 at 92% recovery, installation of a liquefaction column when the cooling is available may prove desirable to open up the selection of materials which may not be able to reach the final target conditions. The proposed process uses a CO_2 liquefaction column primarily to allow for more flexible decision making with materials and process design in the first separator.

Figure 4-4 shows the overall heat balance for the sub-ambient CO_2 capture process at the baseline condition. For the sake of clarity, the cooling water used in the process is not shown. In the base case, the minimum temperature approach (5 °C) occurs at the bubble point (T_B) liquefaction column. With 16 bar compression, this case resulted in an excess warming requirement of >21 MW in the 12-48 °C range. In this analysis, the excess warming of the product N_2 stream is unused and thus is vented to the environment via the stack.
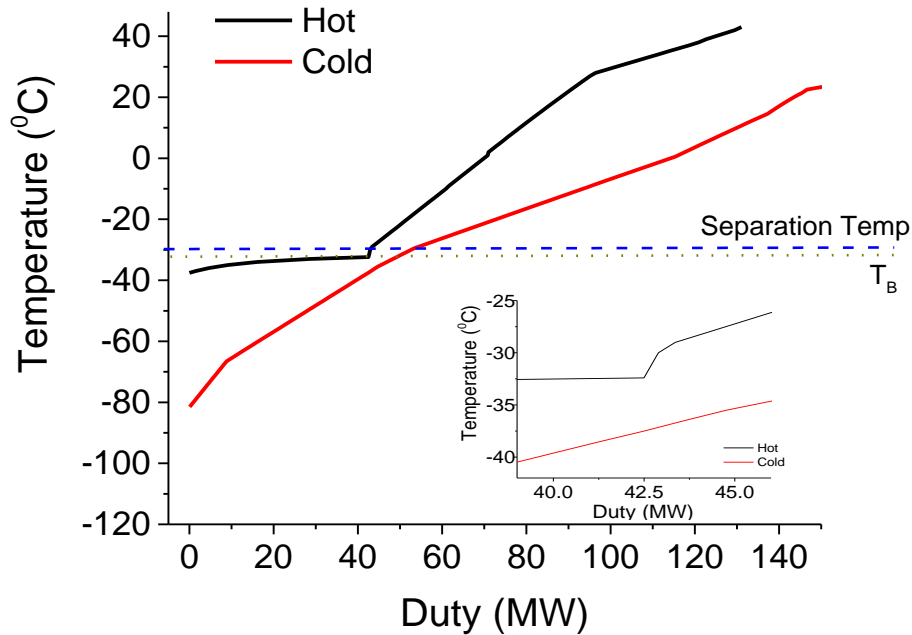
Figure 4-4. Temperature vs. heat duty requirement in the base case showing the temperature pinch is occurring at the bubble point of the liquefaction feed. Balancing the heat for the process at any desired separation operating conditions and product specifications will require tuning of the liquefaction pressure to shift the pinch. Inset, zoomed in on the temperature pinch, showing a 5°C temperature approach. The blue dashed line shows the operating temperature of the PSA system for this process. The Red dotted line is the boiling point of the purified CO_2 product in the liquefaction column

4.1.1.5   Boiler Feedwater Integration

The required intercooling between compression stages in the process offers the opportunity to provide additional heat to the coal plant via integration of the cooling of the compressed flue gas and the heating of boiler feedwater. Building off *Exhibit 4-26. Case B11A Energy and Mass Balance SubC steam cycle* from the Cost and Performance Baseline for Fossil Energy[12], it was found that the heat for the first three feedwater preheaters could be adequately replaced with the heat produced in the first compression stage of the CO_2 capture process. The flowsheet for this integration is given in **Figure 4-5**. In this approach, the steam that is normally removed at different stages throughout the LP turbine to provide the feedwater preheat is instead allowed to pass through the entire turbine. Post-

143

condensation in the *Water Cooled Condenser*, the condensate is split between the four streams: the feedwater and the three preheat steam conditions. Each of those three streams is then pumped up to the desired pressure (plus 2 psi to accommodate pressure drop), then reheated using the flue gas stream to provide the steam at the necessary conditions for plant operations. Comparing this approach with the traditional case shows an improvement exceeding 16 MW_e, which was taken as an energy credit to the CO_2 capture process throughout the economic analysis.
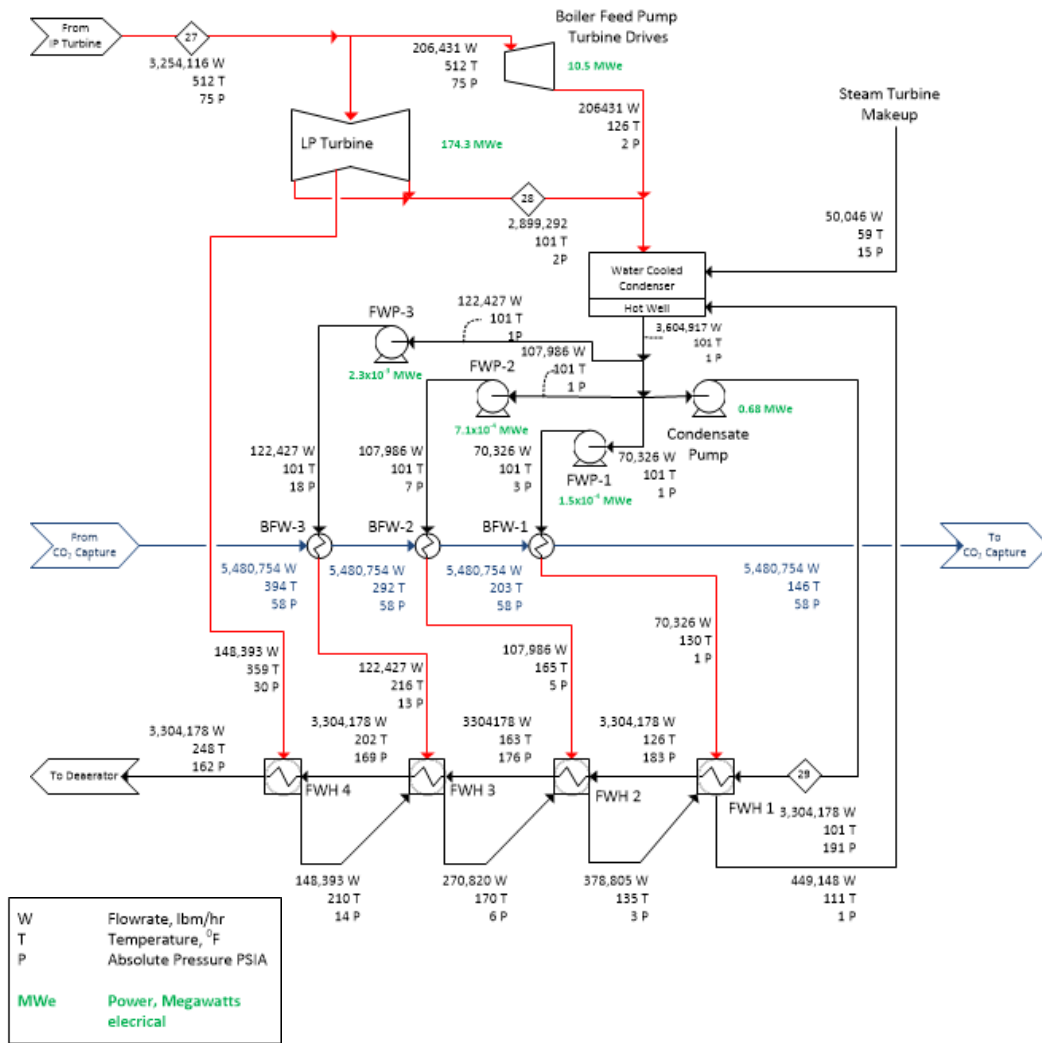
Figure 4-5. Proposed Boiler Feedwater pre-heat system with compressed flue gas providing heat for feedwater preheaters 1-3. The total energy produced from the LP turbine was estimated to be approximately 174.3 MWe and improvement of >16 MWe as compared to the baseline coal plant process.
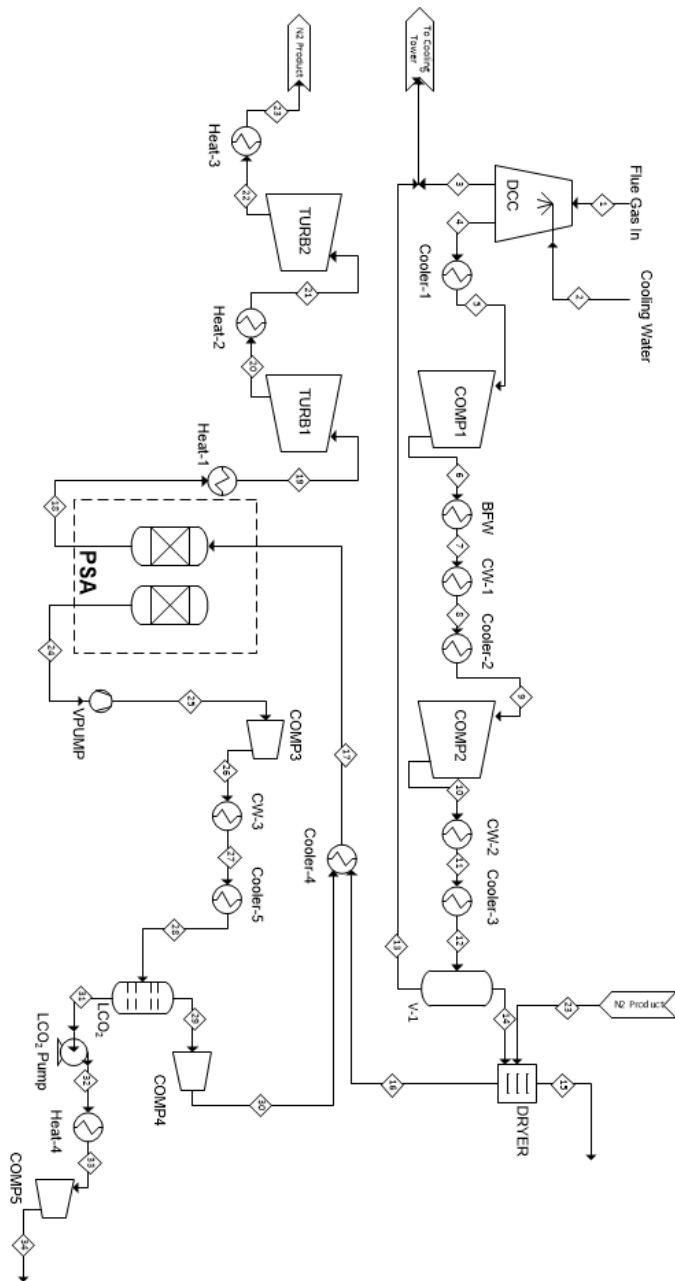
Figure 4-6. Extended process flowsheet showing all process streams and unit operations. Heat Exchangers labeled Cooler or Heat indicate heat exchangers which are a part of the sub-ambient heat exchanger network. Stream numbers (numbers within diamonds) correlate to the streams described in Table S1.

Table 4-1. Stream tables to accompany Figure 4-6. Numbers correlate to labels enclosed in diamonds in Figure 4-6. Continues on the next three pages.

Stream Number	Units	1	2	3	4	5	6	7	8	9
Condition										
Temperature	(°C)	57	30	43	43	28	201	63	42	28
Pressure	(bar)	1.0	1.0	1.0	1.0	0.9	4.1	4.0	4.0	3.9
Vapor Fraction	()	1	0	0	1	1	1	1	1	1
Molar Flow Rate	(kmol/hr)	96,040	602,544	616,536	82,048	82,048	82,048	82,048	82,048	82,048
Mass Flow Rate	(kg/hr)	2,738,090	10,855,000	11,107,062	2,486,028	2,486,028	2,486,028	2,486,028	2,486,028	2,486,028
Volumetric Flow Rate	(L/min)	43,866,538	170,188	186,806	35,970,543	38,028,869	13,156,256	9,540,593	8,942,464	8,758,268
Mole Fraction										
CO_2	(%)	12.5	0.0	0.0	14.6	14.6	14.6	14.6	14.6	14.6
N_2	(%)	72.6	0.0	0.0	84.9	84.9	84.9	84.9	84.9	84.9
H_2O	(%)	15.0	100.0	100.0	0.5	0.5	0.5	0.5	0.5	0.5
Total	(%)	100.0	100.0	100.0	100.0	100.0	100.0	100.0	100.0	100.0
Mass Fraction										
CO_2	(%)	19.2	0.0	0.0	21.2	21.2	21.2	21.2	21.2	21.2
N_2	(%)	71.3	0.0	0.0	78.5	78.5	78.5	78.5	78.5	78.5
H_2O	(%)	9.5	100.0	100.0	0.3	0.3	0.3	0.3	0.3	0.3

Stream Number	Units	10	11	12	13	14	15	16	17	18
Condition										
Temperature	(°C)	189	42	2	2	2	2	2	-30	-30
Pressure	(bar)	16.3	16.2	16.1	16.1	16.1	16.1	16.1	16.0	15.8
Vapor Fraction		1	1	1	0	1	0	1	1	1
Molar Flow Rate	(kmol/hr)	82,048	82,048	82,048	344	81,705	43	81,662	85,333	70,846
Mass Flow Rate	(kg/hr)	2,486,028	2,486,028	2,486,028	6,212	2,479,816	774	2,479,042	2,629,772	2,003,800
Volumetric Flow Rate	(L/min)	3,243,140	2,197,892	1,904,560	95	1,904,465	12	1,903,624	1,738,952	1,487,633
Mole Fraction										
CO_2	(%)	14.6	14.6	14.6	0.2	14.6	0.0	14.7	17.5	1.7
N_2	(%)	84.9	84.9	84.9	0.0	85.3	0.0	85.3	82.5	98.3
H_2O	(%)	0.5	0.5	0.5	99.7	0.1	100.0	0.0	0.0	0.0
Total	(%)	100.0	100.0	100.0	100.0	100.0	100.0	100.0	100.0	100.0
Mass Fraction										
CO_2	(%)	21.2	21.2	21.2	0.6	21.2	0.0	21.2	25.0	2.6
N_2	(%)	78.5	78.5	78.5	0.0	78.7	0.0	78.8	75.0	97.4
H_2O	(%)	0.3	0.3	0.3	99.4	0.0	100.0	0.0	0.0	0.0
Total	(%)	100.0	100.0	100.0	100.0	100.0	100.0	100.0	100.0	100.0

Stream Number	Units	19	20	21	22	23	24	25	26	27
Condition										
Temperature (°C)		0	-81	15	-67	48	-30	-30	206	42
Pressure (bar)		15.7	4.1	4.0	1.1	1.0	0.2	1.0	14.2	14.1
Vapor Fraction (0)		1	1	1	1	1	1	1	1	1
Molar Flow Rate (kmol/hr)		70,846	70,846	70,846	70,846	70,846	14,487	14,487	14,487	14,487
Mass Flow Rate (kg/hr)		2,003,800	2,003,800	2,003,800	2,003,800	2,003,800	625,972	625,972	625,972	625,972
Volumetric Flow Rate (L/min)		1,697,115	4,544,901	7,065,047	18,396,301	31,530,363	24,360,475	4,835,964	667,924	421,221
Mole Fraction										
CO_2 (%)		1.7	1.7	1.7	1.7	1.7	95.0	95.0	95.0	95.0
N_2 (%)		98.3	98.3	98.3	98.3	98.3	5.0	5.0	5.0	5.0
H_2O (%)		0.0	0.0	0.0	0.0	0.0	0.0	0.0	0.0	0.0
Total (%)		100.0	100.0	100.0	100.0	100.0	100.0	100.0	100.0	100.0
Mass Fraction										
CO_2 (%)		2.6	2.6	2.6	2.6	2.6	96.8	96.8	96.8	96.8
N_2 (%)		97.4	97.4	97.4	97.4	97.4	3.2	3.2	3.2	3.2
H_2O (%)		0.0	0.0	0.0	0.0	0.0	0.0	0.0	0.0	0.0
Total (%)		100.0	100.0	100.0	100.0	100.0	100.0	100.0	100.0	100.0

Stream Number		28	29	30	31	32	33	34
Condition	Units							
Temperature	(°C)	-10	-37	-26	-37	-35	35	112
Pressure	(bar)	14.0	14.0	16.3	14.0	63.4	63.3	152.7
Vapor Fraction	( )	1	1	1	0	0	1	1
Molar Flow Rate	(kmol/hr)	14,487	3,671	3,671	10,815	10,815	10,815	10,815
Mass Flow Rate	(kg/hr)	625,972	150,730	150,730	475,242	475,242	475,242	475,242
Volumetric Flow Rate	(L/min)	335,844	74,634	67,229	7,217	7,167	44,476	26,295
Mole Fraction								
CO$_2$	(%)	95.0	81.5	81.5	99.6	99.6	99.6	99.6
N$_2$	(%)	5.0	18.5	18.5	0.4	0.4	0.4	0.4
H$_2$O	(%)	0.0	0.0	0.0	0.0	0.0	0.0	0.0
Total	(%)	100.0	100.0	100.0	100.0	100.0	100.0	100.0
Mass Fraction								
CO$_2$	(%)	96.8	87.4	87.4	99.7	99.7	99.7	99.7
N$_2$	(%)	3.2	12.6	12.6	0.3	0.3	0.3	0.3
H$_2$O	(%)	0.0	0.0	0.0	0.0	0.0	0.0	0.0
Total	(%)	100.0	100.0	100.0	100.0	100.0	100.0	100.0

4.2   Sub-ambient Fiber Sorbent PSA

To understand the limitations of the sub-ambient PSA process with different adsorbents installed in the fiber morphology, the performance of each within a PSA unit was simulated. This section focuses on the performance of these adsorbents when multiple process parameters and fiber parameters are varied to optimize the material's performance.

UiO-66 and MIL-101(Cr) are two MOFs that show some promise for sub-ambient CO_2 capture.[19] Both materials are stable in liquid water, which is a prerequisite for their spinning into heat managed fiber sorbent structures. Both materials have shown the ability to be scaled up to the 10-1000 g batch scale[20]. The use of UiO-66 as a sorbent for sub-ambient CO_2 capture has been briefly discussed elsewhere, where an operating capacity of 4 mmol/g at 243 K was shown[21]. While MIL-101(Cr)'s sub-ambient performance has not been reported, its crystalline structure with very large pores (1.4 and 2.2 nm) makes it a promising material for having high working capacity.[22] Enabling these sorts of high working capacities is expected to be one of the key benefits to this sub-ambient process, enabling the very high productivities.

UiO-66 has been spun into fiber sorbents previously[21,23] while MIL-101(Cr) shows promise for such spinning, with its good aqueous and chemical stability.[24] Proof of concept sorbent spinning with microencapsulated phase change material (µPCM) was carried out with UiO-66 sorbents as part of this dissertation (discussed in detail in Chapter 6),[21] and the methods applied should be easily generalizable to other solid sorbent systems.[21]

The performance of these two MOF sorbents and zeolite 13X, a common sorbent considered for post-combustion CO_2 capture via PSA[15,25,26], for a sub-ambient PSA was

investigated using dynamic process simulations. To confirm the necessity of the downstream liquefaction, this was first carried out at feed conditions consistent with a process without downstream liquefaction and recycle (14:86 CO_2: N_2). The Pareto frontiers calculated for these materials at two temperatures (273 K and 298 K for 13X and 243 K and 273 K for the MOFs) are reported in **Figure 4-7** with the corresponding process and fiber parameters are reported in Appendix A. None of the sorbents considered were capable of reaching the overall performance goal of 95% purity and 90% recovery without liquefaction, so a hybrid system including liquefaction as a secondary purification step appears to be necessary for these sorbents.
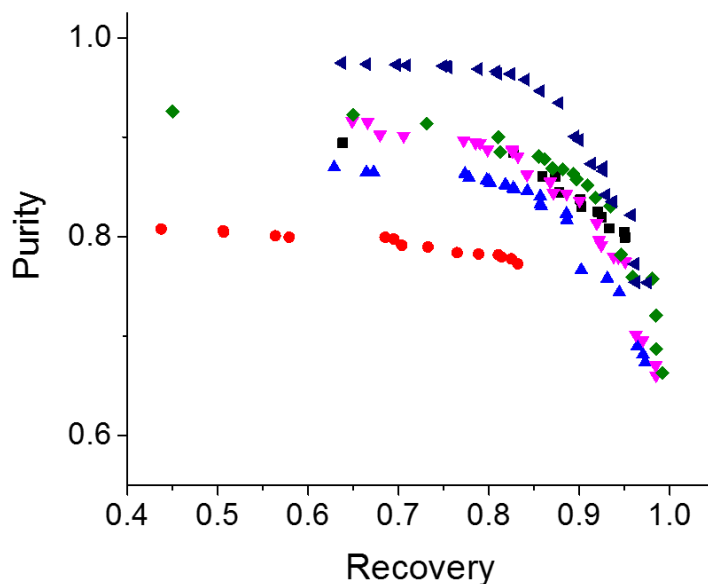
Figure 4-7. The Pareto frontier of Purity vs Recovery for a variety of thermally managed fiber sorbents at multiple temperatures for a feed of 14% CO_2, 86% N_2. (black) 13X at 298K, (red) 13X at 273K, (blue) UiO-66 at 273K (pink) UiO-66 at 243K, (green) MIL-101(Cr) at 273K, (navy) MIL-101(Cr) at 243K.

Zeolite 13X showed superior performance at 298 K (black) than at 273 K (red). The results at 273 K were unable to reach the required CO_2 product recovery for the PSA of

152

92% to enable the hybrid system to recycle CO_2 recovery of 90%, so this material may not be suitable for the sub-ambient PSA process. It is worth noting that at 298 K condition the productivities of the thermally managed 13X fiber sorbent PSA are expected to be 6-7 times higher than that of comparable pellet based systems[25,27,28]. With this performance improvement in mind, the flowsheet discussed throughout the prior sections of the manuscript was reconfigured to enable an ambient PSA process while still allowing for the removal of water and liquefaction of the CO_2 rich product via Joule-Thompson expansion. The relevant flowsheet and preliminary economic estimates for the best-case scenario are reported in Section 4.2.2.

4.2.1 Economics of Sub-ambient MOF Fiber Sorbents

Having established that liquefaction is required to reach the target delivery purity with the MOF sorbents considered, the Pareto frontiers were recomputed using a 17:83 CO_2: N_2 mixture to simulate the inlet to the PSA unit when liquefaction and recycle are employed. The complete Pareto front is given in **Figure 4-8** with all PSA operating conditions and fiber morphology parameters provided in appendix A. An inset in **Figure 4-8** shows the points with >65% purity and 92% recovery. MIL-101(Cr) shows a slightly more desirable Pareto frontier than UiO-66. Both sorbents have a clear tradeoff between the purity and recovery of the sub-ambient PSA unit. Ten separate PSA conditions, five for each sorbent, were used as case studies in the process model discussed in section 3. These conditions are indicated in **Figure 4-8** as starred points and their operating conditions, performance, and fiber compositions are listed in **Table 4-2**. For each case, the temperature, PSA pressure, PSA vacuum condition, and the PSA product purity and recovery were used as conditions within the process model. The heat exchanger system

was then optimized to include a 5 °C temperature approach by varying the liquefaction column pressure. The compressor before liquefaction was always kept as a single-stage, which in cases where the pressure ratio exceeded 10 may prove unrealistic and undesirable. In cases where the liquefaction pressure was greater than the PSA operating pressure, the same flowsheet adjustments were made as those described in Section 3 (the flowsheet in **Figure 4-3** was used instead of **Figure 4-2**). The T-H diagrams for each of the cases considered are given in **Figure 4-9** and **Figure 4-10**.
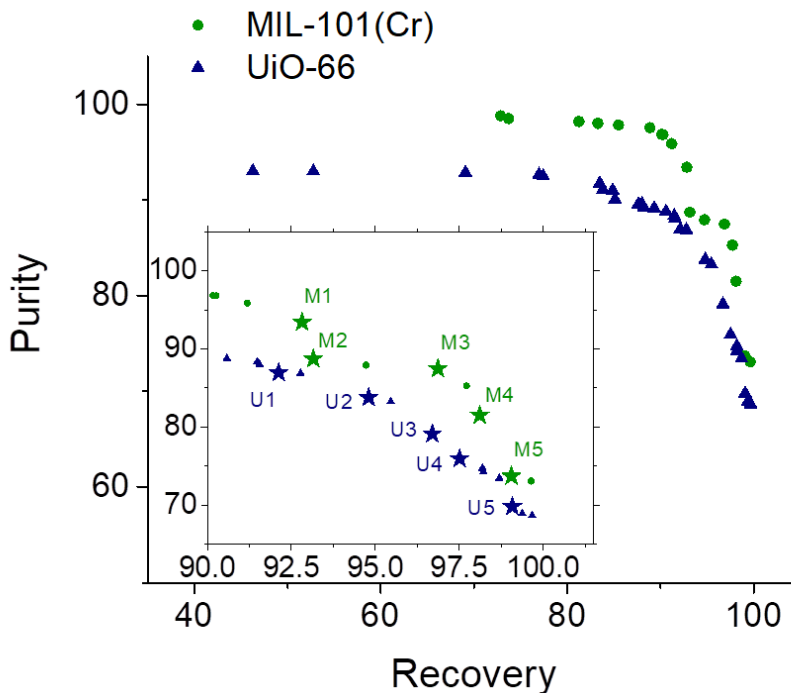
Figure 4-8. Optimized purity-recovery Pareto frontiers for UiO-66 (blue) and MIL-101(Cr) (green) fiber sorbents for sub-ambient PSA operation at 243 K. The inset shows points within the desired range of purity and recovery. Starred points indicate conditions used in separate case studies.

Table 4-2. Operating conditions, performance, and fiber compositions were used in the case studies with pressures in bar and productivity in mol kg^{-1} s^{-1}.

	U1	U2	U3	U4	U5	M1	M2	M3	M4	M5
PSA Operating Pressure	12.68	14.05	12.68	15.45	12.49	20.19	18.22	20.22	18.22	12.21
PSA Vacuum Pressure	0.10	0.10	0.10	0.12	0.11	0.10	0.10	0.10	0.10	0.10
% Recovery	92.12	94.80	96.70	97.51	99.08	93.00	93.00	97.00	98.00	99.00
% Purity	86.95	83.77	79.12	75.93	69.80	93.00	89.00	87.00	81.00	74.00
Productivity	0.019	0.017	0.016	0.015	0.013	0.033	0.025	0.027	0.020	0.017
Fiber MOF wt%	36.8	40.0	37.7	40.0	38.2	32.4	34.7	32.2	34.7	30.9
Fiber uPCM wt%	38.2	35.0	37.3	35.0	36.8	42.6	40.3	42.8	40.3	44.1

In all 10 cases considered, the optimizer yielded a result close to the specified lower bound value of the vacuum level for the PSA unit. This suggests there may be room for improvement in the performance of these fiber sorbents if the PSA process could be operated economically at even lower vacuum levels.

As a typical case, the simplified flowsheet for Case M1 is given in **Figure 4-11**. The flue gas enters the system and passes through the direct contact chiller, where 97.4% of water is removed, reducing the concentration of water in the stream to 0.47%. The partially dehumidified gas is then passed through a series of two compressors with intercoolers, where it reaches a target pressure of 20.49 bar. The stream is further cooled down to 2 °C in the sub-ambient heat exchanger network, where additional water is also removed. This high-pressure feed (1) at 20.29 bar contains only 437.6 ppm H_2O, which is removed in an adsorbent dryer. Leaving the adsorbent dryer, the now bone dry flue gas with composition 14.65% CO_2 and 85.35% N_2 is mixed with cold recycle (6) which is

81.5% CO_2. This mix (2), a CO_2 enriched feed of 18.9% CO_2, is then cooled to the -30°C operating condition of the PSA, entering the system at 20.19 bar.
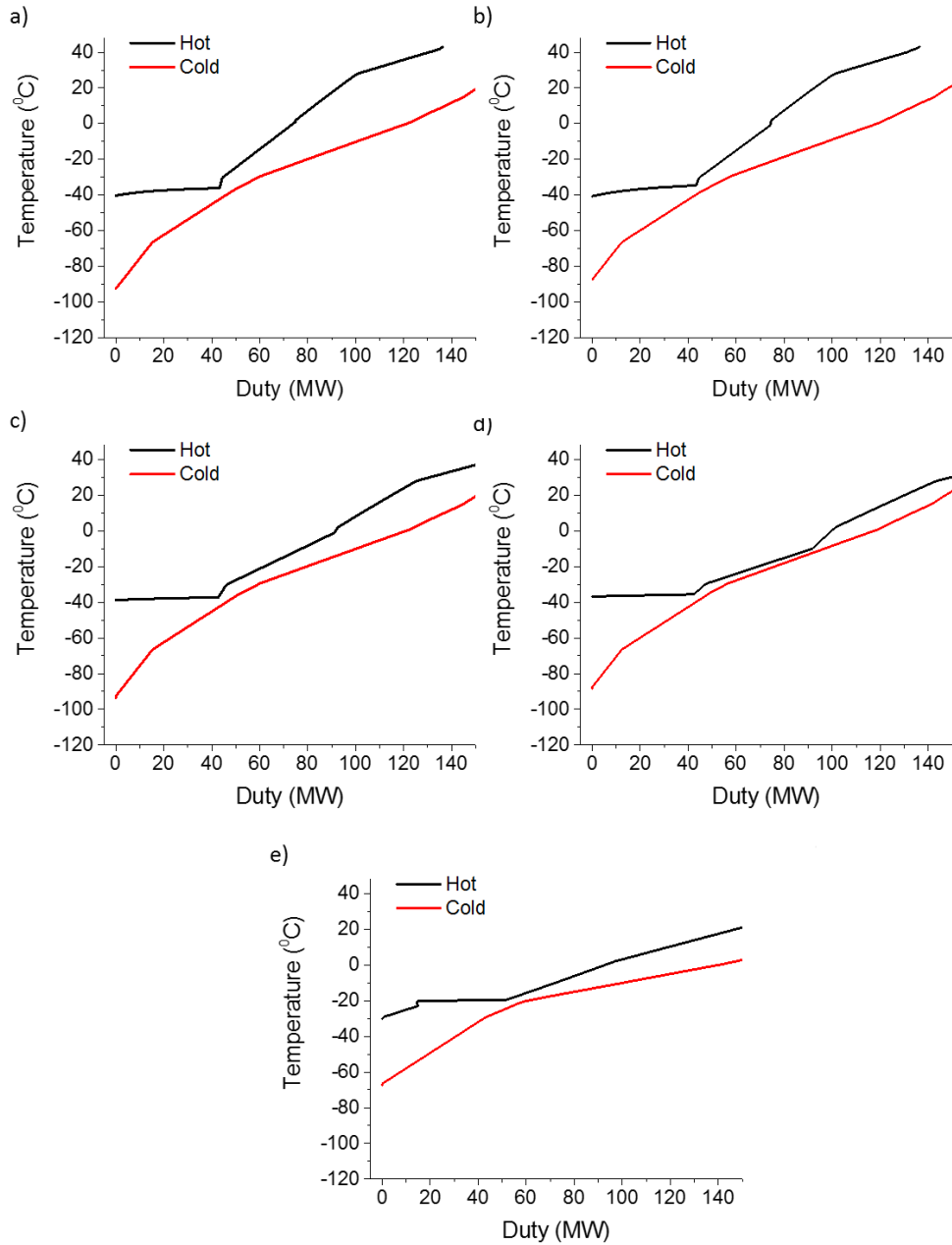
Figure 4-9. T-H profiles for Case Studies on MIL-101(Cr) thermally modulated fiber sorbents (a) M1, (b) M2, (c) M3, (d) M4, (e) M5.
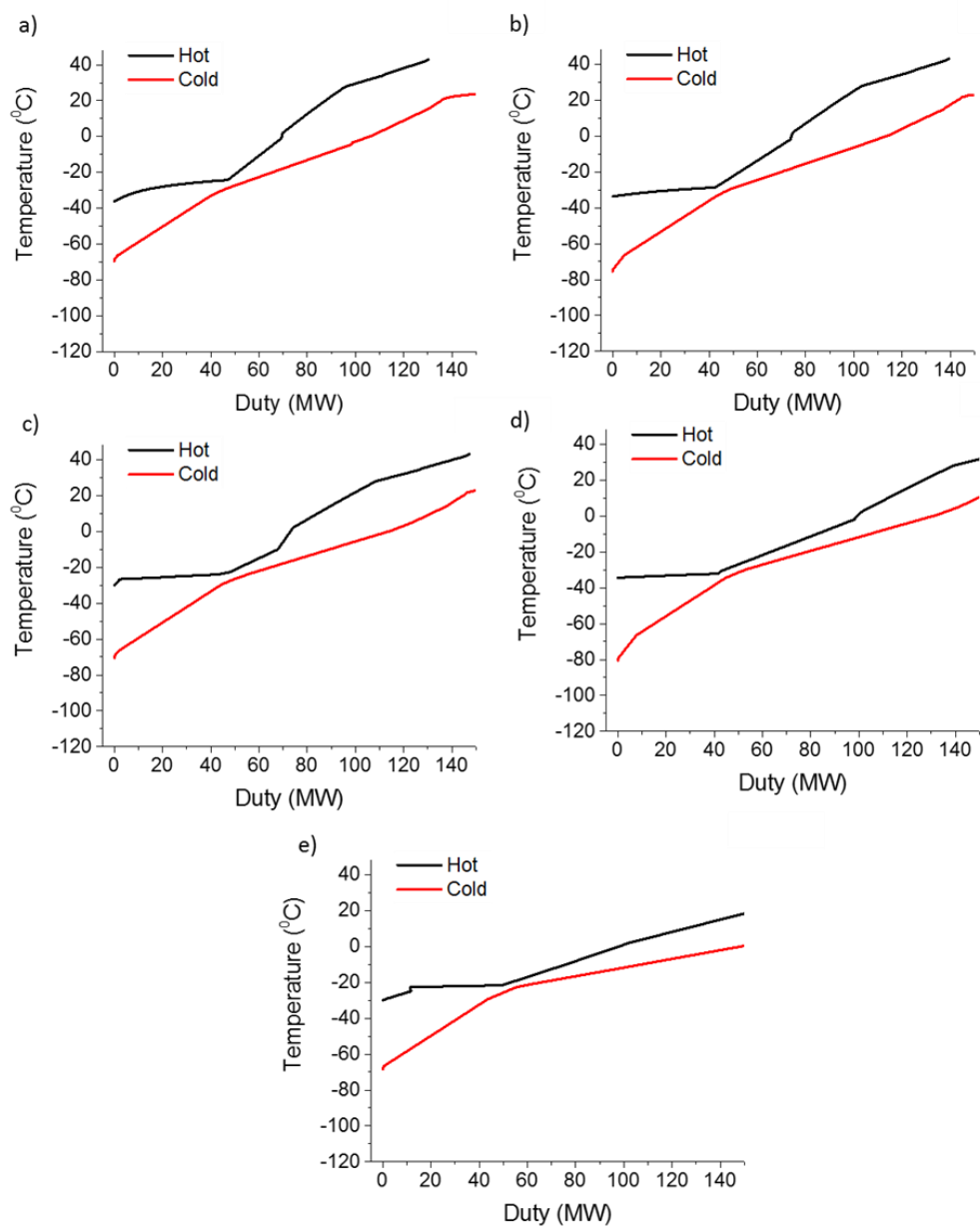
Figure 4-10. T-H profiles for Case Studies on UiO-66 thermally modulated fiber sorbents (a) U1, (b) U2, (c) U3, (d) U4, (e) U5.

The N_2 rich product in **Figure 4-11** (stream 3), still at a high-pressure condition of 19.99 bar, is then cooled and expanded repeatedly, generating streams at temperatures as low as -93 °C, while also recovering 97 MW of energy. The CO_2 enriched product is recovered at 0.103 bar vacuum pressure with a concentration of CO_2 of 93.4%. From the vacuum pump, it is recompressed to a moderate 12.5 bar pressure before being sent back to the sub-ambient heat exchange network as the feed to the liquefaction column. Operating at -40.4 °C, the top stream from the liquefaction column is recompressed from the 12.5 bar liquefaction pressure to 20.29 bar where the cold recycle (stream 6) enriches the feed. The liquid CO_2 product (stream 7), now 99.6% CO_2, is pumped to the feed condition of the 5th stage of the multistage compression (63.4 bar) and heated to provide heat removal to the rest of the system from -38 °C to 35 °C. It can then be compressed to the pipeline condition of 152.7 bar, where it can be transported to storage or sequestration.
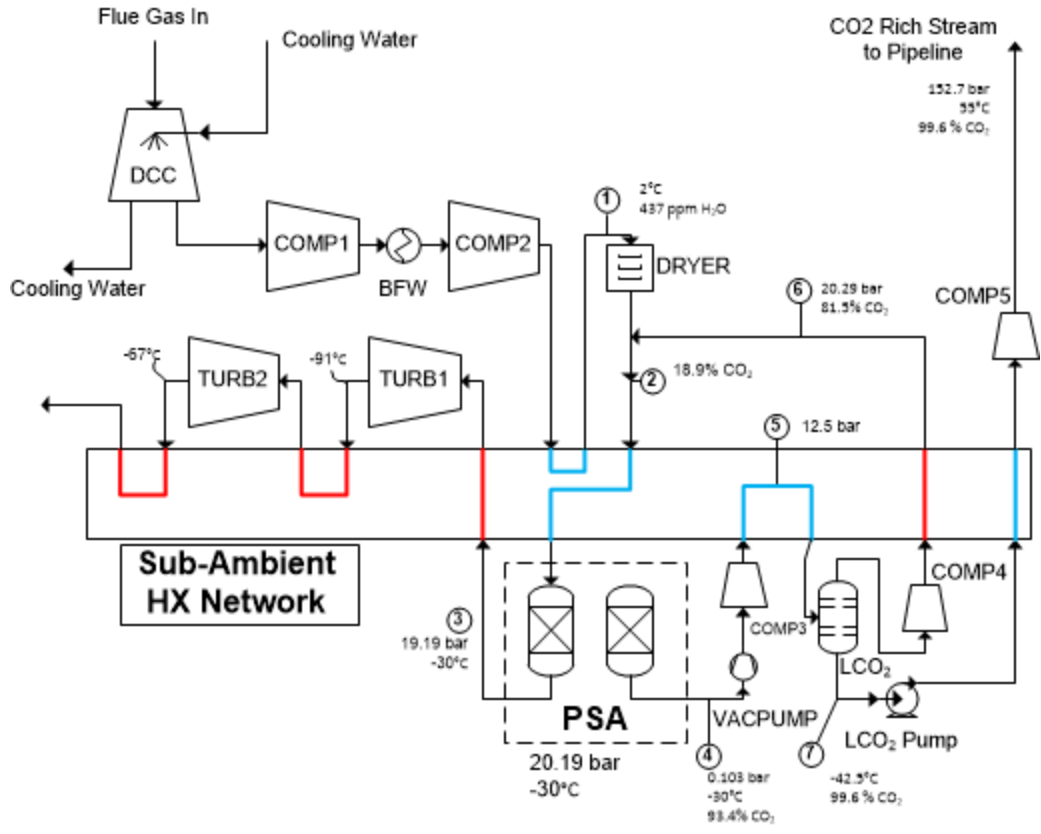
Figure 4-11 Simplified flow diagram for Case M1. Selected streams are labeled with circled numbers are discussed further in the text.

Figure 4-12 shows the cost of capture as a function of the recovery of the PSA unit for the two MOF sorbents. There is a clear positive correlation between the recovery of the system and the cost of the CO_2 capture system. As the recovery goes up so too does the size of the downstream liquefaction and recycle systems. This effect is primarily driven by the amount of gas that has to be compressed during liquefaction but it is also impacted by the CO_2 purity from the liquefaction column since higher recoveries are often associated with lower purities.
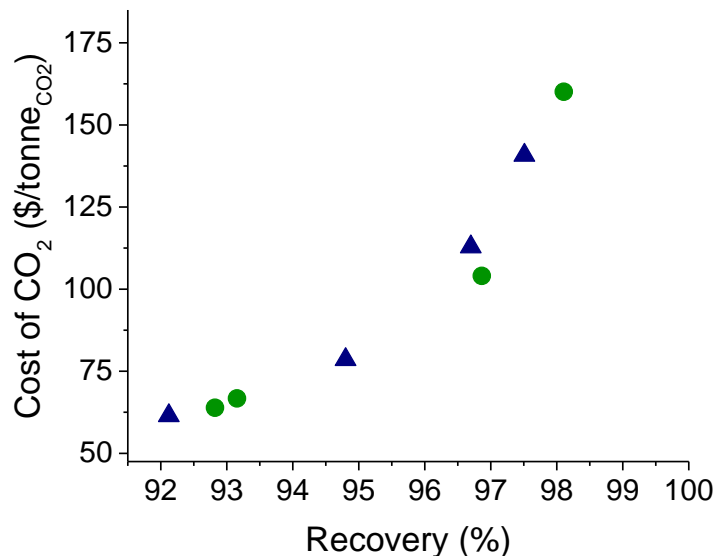
Figure 4-12. Cost of CO$_2$ capture of 8 different cases studied (case M1-4) MIL-101(Cr), green circles, (Case U1-U4) UiO-66, navy triangle as compared to CO$_2$ recovery of the PSA unit. Case M5 and U5 were not included to make the Figure clear.

Cost as a function of other PSA performance parameters productivity and purity are shown in **Figure 4-13**. Unlike recovery, the trends are a bit less pronounced, particularly comparing between sorbents. In **Figure 4-12** regardless of the sorbent chosen all the values could probably be fit to the same best fit with little disagreement between adsorbents. In the case of productivity, it appears as though UiO-66's operation at lower productivities results in a similar cost of capture overall. This makes sense if recovery is the actual variable dominating the economics between the cases, as the UiO-66 cases with lower costs and lower productivities also have lower recovery. This behavior is similar for purity as well, where there appears to be a negative correlation between cost and purity. Since the tradeoff between purity and recovery is well documented (and seen clearly in **Figure 4-7** and **Figure 4-8**), it appears that having lower recovery and higher purity combined results in the most cost-effective CO$_2$ capture. The MIL-101(Cr) fiber sorbents show some increases in price with productivity between 0.025 and 0.035 mol/kg*sec. This

160

result comes about because of the lower purity and higher recovery in that case, the result of which is increased cost due to the increase in size of the secondary separation system.
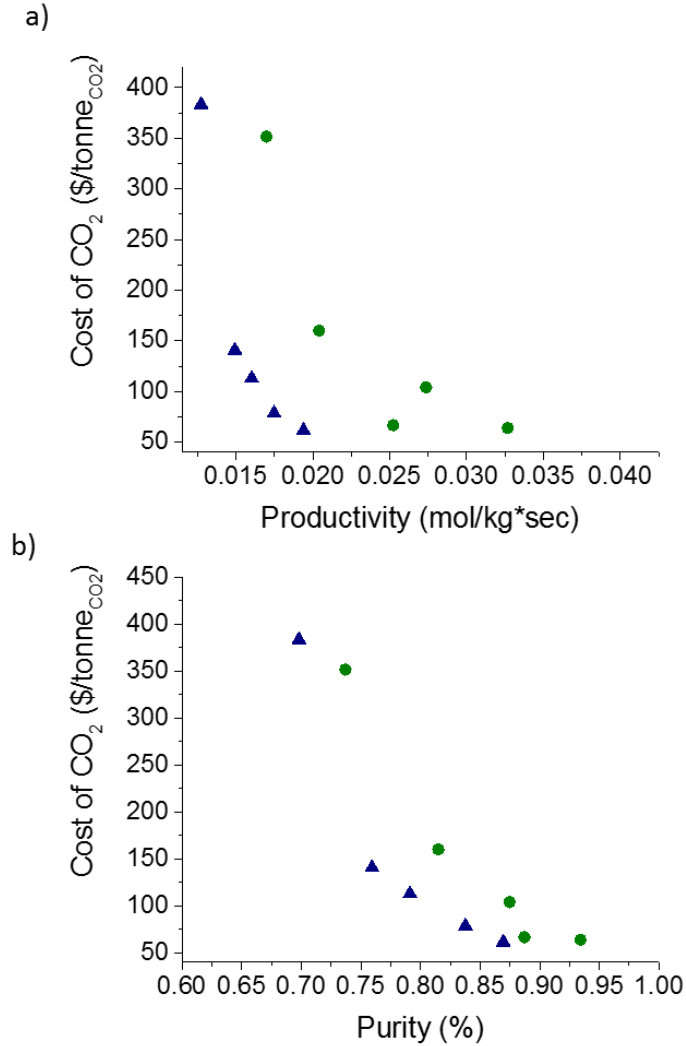
Figure 4-13. Cost of capture ($/tonne$_{CO2}$) for case studies as it relates to (a) PSA productivity (b) CO₂ product off PSA purity. (blue triangles) UiO-66 at 243 K, (green circles) MIL-101(Cr) at 243 K.

Figure 4-14 shows the cost ($/tonne CO_2) comparison for the ten MOF sorbent cases, with each case's cost broken down into its constituent costs (capital and energy). As the recovery increases and the purity decreases (left to right on each plot), the energy, rotating equipment, and PSA units' costs all increase significantly. The increase in energy and rotating equipment cost mainly comes from the increased amount of gas in the

liquefaction process, which drives up the size and energy demand of COMP3 in **Figure 4-2** and **Figure 4-3**. In cases M5 and U5, the energy demand of that single compressor is greater than the amount of energy produced by the base case plant. The increase in PSA cost relates both to recovery and productivity. With increasing recovery more CO_2 must be captured by the PSA, along with slight increases in the amount of CO_2 held up in the recycling of the system. Cases M5, U4, and U5 also suffer from 20-30% reductions in PSA productivity as compared to the lower recovery cases, which will also play a role in the increased price of the PSA unit.
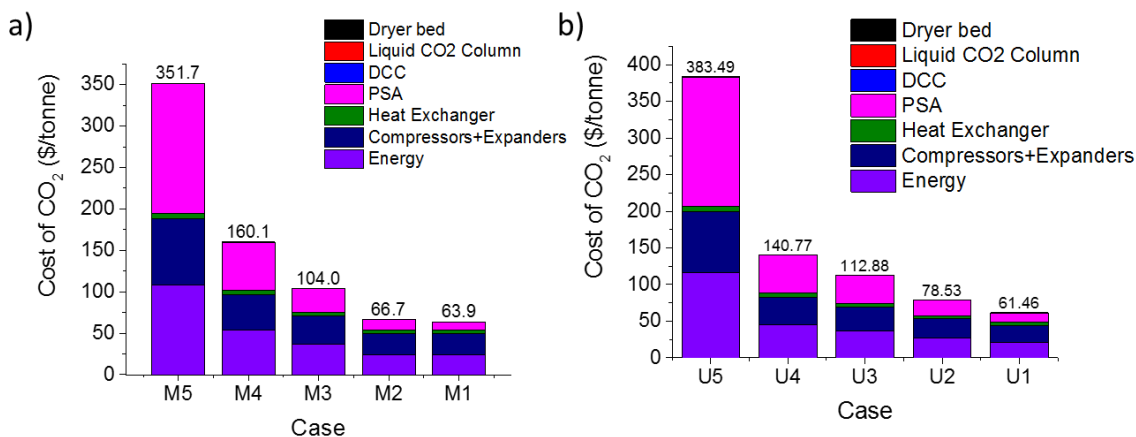
Figure 4-14. (a) Cost of capture for the five MIL-101(Cr) cases, broken down into capital and energy costs. (b) Cost of capture breakdown for UiO-66 thermally modulated fiber sorbents.

Considering sorbents on the whole for this sub-ambient PSA process, it appears that the main room for improvement will come about by increasing the purity of the CO_2 produced from the PSA without sacrificing recovery and still showing high productivities. This goal may be reached in a variety of ways, including sorbent design/selection or an improved PSA cycle design. Increasing the selectivity of the sorbent while not sacrificing too much of its capacity for CO_2 at sub-ambient conditions would drive the Pareto frontier in **Figure 4-8** to more desirable conditions. Sorbents which could reach the desired purities,

162

recoveries, and productivities shown for MIL-101(Cr) and UiO-66, but not requiring as low a vacuum condition may also be able to drive down the cost, which will be explored in the following section. The PSA cycle considered here did not consider any pressure equalization between beds. The inclusion of this feature and similar degrees of freedom for the PSA cycle design may result in further improvements in PSA performance, driving up recovery and purity, at some cost of productivity.

4.2.2   Ambient Thermally Modulated Zeolite 13X Fiber Sorbent PSA

Thermally modulated fiber sorbents containing Zeolite 13X do not appear to be able to reach the required recovery (exceeding 90%) at sub-ambient conditions to make it a desirable adsorbent material for this hybrid CO_2 capture process. With that said, the productivities estimated for those Pareto frontiers are still very high (many exceeding 0.01 mol*kg^{-1}*sec^{-1}), so an attempt was made to adapt the main flowsheets discussed in this work for ambient PSA operation.

While Zeolite 13X does not take advantage of all of the benefits of sub-ambient operation (particularly on PSA performance), it can still take advantage of the Joule Thompson cooling made available through operating at elevated pressures. This cooling is necessary for the proposed water removal strategy, as well as allowing for less than 95% purity of the CO_2 rich product of the PSA. Zeolite 13X has well-documented issues with humid feeds, so this process scheme may enable its use for post-combustion CO_2 capture where water removal is a real challenge.

The proposed adaptation of the process flowsheet for ambient PSA operation is shown in **Figure 4-15**. The only major difference between it and the process proposed in

Figure 4-3 is the feed to the PSA unit is heated in the heat exchanger network, as opposed

to cool. This results in a slight reduction in the required heat exchanger area of the system.

Another major impact of operating the PSA at ambient conditions is the N_2 rich product

also leaves at ambient conditions. This results in the first expansion of the N_2 rich product

reaching a ~50 °C warmer temperature as compared to the sub-ambient process. This has

a significant effect on the downstream liquefaction process, requiring the liquefaction to

operate at a higher temperature and pressure, which increases the size of COMP 3.
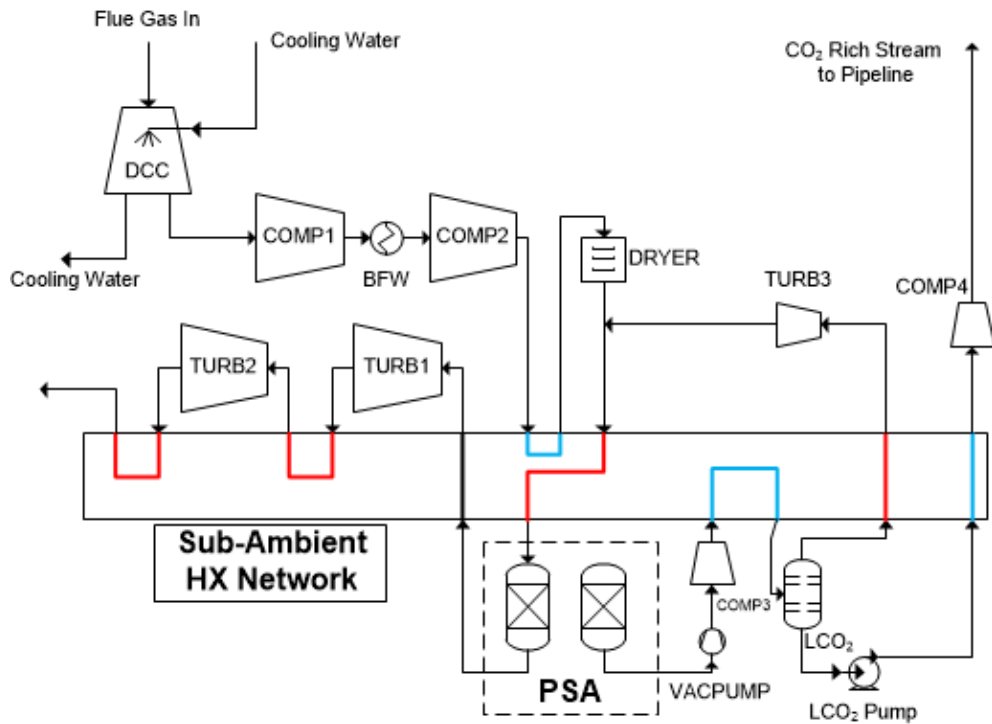
Figure 4-15. Simplified process flowsheet for the ambient PSA operation. The sub-ambient heat exchanger network is still required for the removal of water and operation of the liquefaction system.

To understand the possible lower limits of operating the ambient PSA process for

Zeolite 13X thermally modulated fiber sorbents, the Pareto Frontiers were calculated for a

17% CO_2 83% N_2 feed at an operating temperature of 298 K, which are reported in **Table 4-3**. As this analysis was preliminary to see the potential of such a process, the expected

"best" Pareto condition, given the work with the MOFs, was selected as informed by the

work performed on the MOFs at sub-ambient conditions. That is the point whose recovery

exceeded 92% most closely, the values of which are highlighted in light blue in **Table 4-3**.

Table 4-3. Pareto conditions for 13X fibers at 298 K for a feed of 17% CO_2, 83% N_2.

Recovery	()	0.254	0.617	0.739	0.815	0.833	0.845	0.850	0.869
Purity	()	0.900	0.900	0.898	0.894	0.892	0.890	0.889	0.885
Productivity	(mol kg^{-1} sec^{-1})	0.0107	0.0124	0.0131	0.0134	0.0133	0.0133	0.0136	0.0131
Cycle Time	(sec)	104.3	91.6	84.7	80.9	80.8	79.9	78.3	80.9
Pressure	(bar)	16.2	13.0	16.1	16.1	16.1	16.1	16.1	13.1
Vacuum	(bar)	0.102	0.102	0.106	0.110	0.110	0.110	0.109	0.107
Zeolite Fraction	(%)	40.0	39.9	40.0	40.0	40.0	40.0	39.9	39.6
µPCM Fraction	(%)	35.0	35.1	35.0	35.0	35.0	35.0	35.1	35.4
Polymer Fraction	(%)	25	25	25	25	25	25	25	25

Recovery	()	0.879	0.892	0.898	0.919	0.919	0.927	0.933
Purity	()	0.880	0.880	0.873	0.868	0.862	0.862	0.856
Productivity	(mol kg^{-1} sec^{-1})	0.0129	0.0133	0.0129	0.0127	0.0129	0.0124	0.0124
Cycle Time	(sec)	79.8	79.4	79.2	78.4	75.6	77.7	77.4
Pressure	(bar)	13.1	13.0	13.0	13.1	13.1	13.1	13.0
Vacuum	(bar)	0.107	0.102	0.103	0.103	0.102	0.102	0.102
Zeolite Fraction	(%)	39.7	39.4	39.1	39.5	39.1	39.8	39.3
µPCM Fraction	(%)	35.3	35.6	35.9	35.5	35.9	35.2	35.7
Polymer Fraction	(%)	25	25	25	25	25	25	25

Figure 4-16 reports the performance of the "best case" for zeolite 13X as compared to the MOF sorbents as a function of PSA purity, recovery, and productivity. Two Zeolite 13X cases are plotted at varying sorbent cost ($1 and $30/kg) for all conditions as zeolite fiber sorbents may cost less due to the reduced cost of the sorbent materials. In-fact, the effect of reducing the price is rather small (<$1.50/tonne$_{CO2}$ captured). In general, the ambient 13X fiber sorbent PSA appears to be less cost-effective at CO_2 capture when the PSA is operating at similar purities and recoveries, likely due to reduced productivity as compared to the MOF materials.
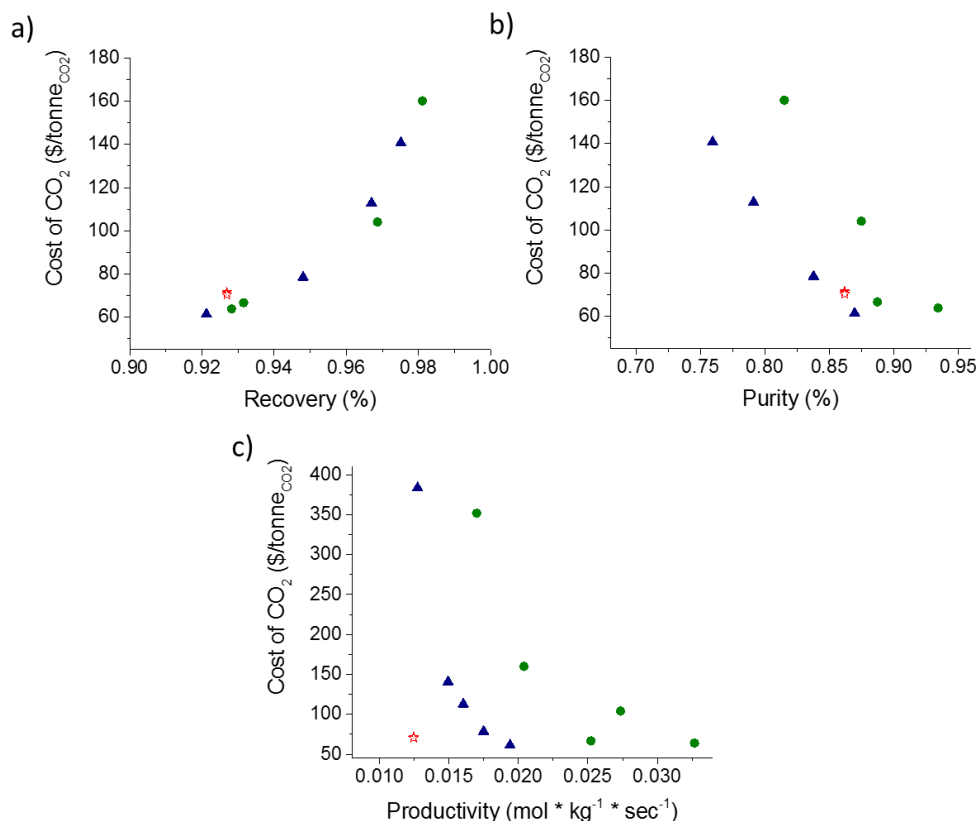
Figure 4-16. Cost of CO_2 capture as a function of (a) Recovery, (b) Purity, and (c) Productivity, for MOF fiber sorbents operating at sub-ambient conditions as reported in Figure 4-12 and Figure 4-13 and Zeolite 13X fiber sorbents operating at ambient conditions $30/kg sorbent cost (red filled in star) and $1/kg sorbent cost (red empty star). Cases U5 and M5 were left off (a) and (b) for clarity

Figure 4-17 compares the cost of capture broken down categorically of the ambient 13X fibers vs the sub-ambient MOF fibers. The 13X ambient PSA process has a very similar cost profile, with a small reduction in the heat exchanger cost being offset by slight increases in the PSA and energy costs.
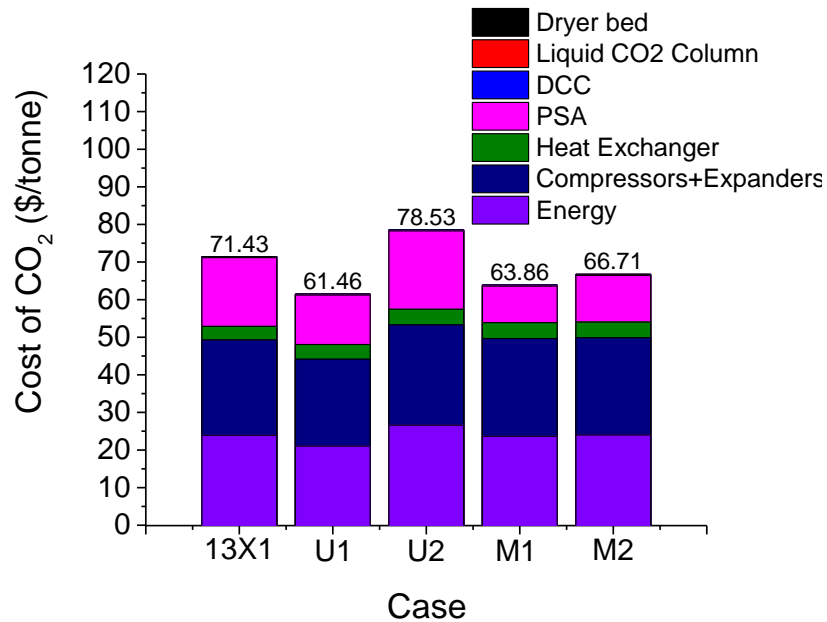
Figure 4-17. Cost of CO₂ capture for Zeolite 13X thermally managed fiber sorbents operating at 298 K (13X1) as compared to the best cases for the two MOFs considered at sub-ambient conditions.

While the ambient PSA process does not show a significant increase in performance as compared to the sub-ambient MOF process, it still performs surprisingly well. This points to the possibility with further sorbent optimization, either the sub-ambient or ambient process may prove to be competitive.

4.3 Sensitivity Analysis

Hybrid separations, using multiple separations in series, like the one considered here (PSA and liquefaction) have a variety of operating conditions that may be varied to boost the performance of the separation. Operating a PSA at higher pressures, lower levels

of vacuum, or different temperatures can have wide-ranging effects on the performance of the separation. This section focuses on the direct effects of changing these parameters on the economics and energetics of the process assuming the separation performance is held constant. The overall process flowsheet is first described in some detail, after which, the sensitivity of the CO_2 capture process energetics are discussed in detail as they relate to four important operating conditions: 1. primary separator high-pressure condition, 2. primary separator vacuum condition, 3. primary separator temperature, and 4. liquefaction pressure. The first three variables play a major role in the size and performance of the primary separator. The liquefaction pressure is the key parameter controlling the system temperature profile when overall system recovery is held constant.

Four important operating conditions that will affect material selection and performance were identified: the primary separator feed pressure, the primary separator vacuum pressure, the primary separator operating temperature, and the liquefaction pressure. Exploring the effects of varying these process parameters gives insight into the desired properties of the separation unit as well as performance tradeoffs that exist. The effects of the primary separator performance when operating conditions are held constant are considered in detail in Section 4.

The sensitivity of these four process conditions was examined with the other three held constant at the baseline levels listed in **Table 4-4**. The heat balance of the plant and pinch analysis were not optimized in this analysis except for the baseline case, as these considerations are best meant for optimization cases requiring knowledge regarding the specific separation modality. The effects of purity as it related to the cost of the separation

unit itself are discussed for the baseline case in Section 4.4, but **Table 4-4** also gives the relevant performance parameters of the primary separator.

Table 4-4. Base case parameters used in the sensitivity analysis

Base Case Condition	Value
Separator Operating Pressure	16 bar
Operating Temperature	-30 °C
Separator Vacuum Pressure	0.2 bar
Liquefaction Column Pressure	14 bar
Separator CO_2 Product Purity	95%
Separator CO_2 Recovery	92%
System CO_2 Recovery	90%

4.3.1 Primary Separator Pressure

The level of flue gas compression before the separation affects two main performance metrics. First and most importantly, higher compression requires more energy. **Figure 4-18a** shows the relationship between compression and process energy requirement (kWh/tonneCO_2) on the capture process. As more compression is required from the process, the compressors become larger and require more energy, resulting in an expected increase in energy cost per tonne of CO_2. The trend, normalized to the baseline power requirement of 403.1 kWh/tonneCO_2, appears fairly linear, which may be expected. However, depending on the separation process and materials, additional compression may allow for a more effective separation (higher CO_2 purity, recovery, and productivity/fluxes) at the cost of this additional energy demand but an ultimately lower cost of CO_2 capture.
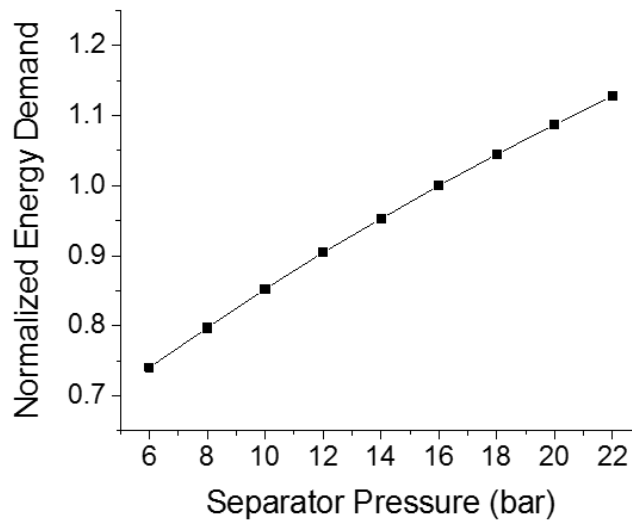
Figure 4-18. Effects on overall energy demand for CO_2 capture (kWh/tonneCO$_2$ normalized, where base case 403.1 kWh/tonneCO$_2$) varying separator operating pressure

Increases in the required compression also necessitate an increase in the size of three of the four compressors in the system resulting in a higher capital cost (**Figure 4-19a**). This cost may be partially offset with the size reduction of other system components, like piping, whose size is in part determined by the volumetric flow rate; this is not accounted for in this preliminary cost study. The effects of purity follow as might have been expected, as the PSA produces a lower purity product at the same recovery, the cost goes up. This will likely be true in all cases simply because the liquefaction compressor will need to compress more volume of gas (thus increase in energy requirement and size) regardless of how the process condition is being changed.

170
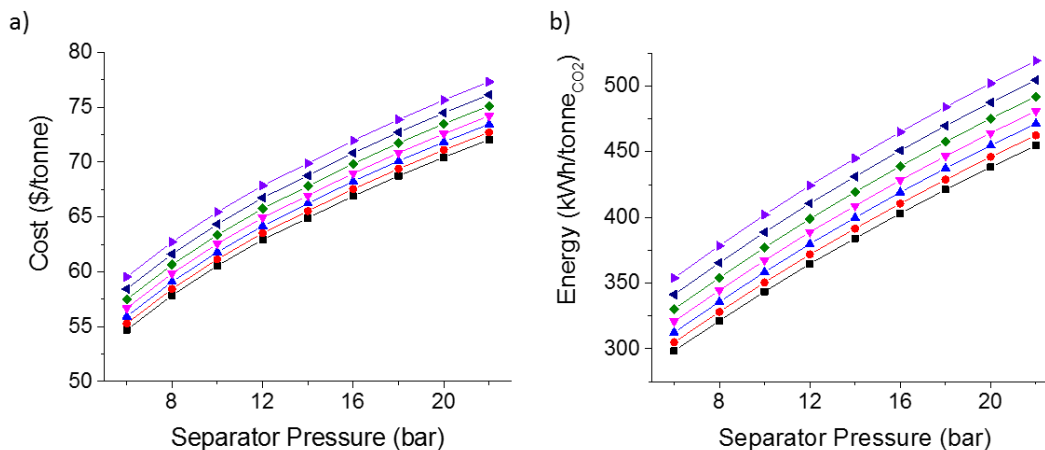
Figure 4-19. (a) Cost of capture as a function of primary separator pressure, (b) Energy demand of process as a function of primary separator pressure. (black) 95% CO₂ purity in the product of the separator, (red) 90% CO₂ purity, (blue) 85% CO₂ purity, (pink) 80% CO₂ purity, (green) 75% CO₂ purity, (navy) 70% CO₂ purity, (purple) 65% CO₂ purity.

Compression is a vital part of the ability of the process to operate without an external cooling utility, as previously discussed. Beyond a certain level of compression, the amount of cooling available via Joule-Thomson cooling cannot provide the required heat removal. In this scenario, there is no simple way to adjust the process design (e.g., changing the expander pressure ratio will not allow for more cooling to become available) to provide more cooling to the process. While we do not observe this in cases where the operating pressure is 6 bar or above it is conceivable such situations may arise.

4.3.2 Operating Temperature

Figure 4-20 shows the effect of decreasing the operating temperature of the separator on the overall energy demand of the process. As the operating temperature decreases the overall system energy requirements decrease, while the total amount of heat removal required increases. This increase in required cooling ultimately does not impact the energy demand of the process on the plant due to the significant levels of heat integration and recovery. Across all separation system temperatures considered we

171

estimated that there were at least 18.5 MW of excess heat removal capabilities available at low qualities (-5 to 30°C). The decrease in energy instead is due to a slight reduction in the required energy of the liquefaction compressor (in COMP3 in **Figure 4-2**) as the compressor receives a lower temperature inlet gas.
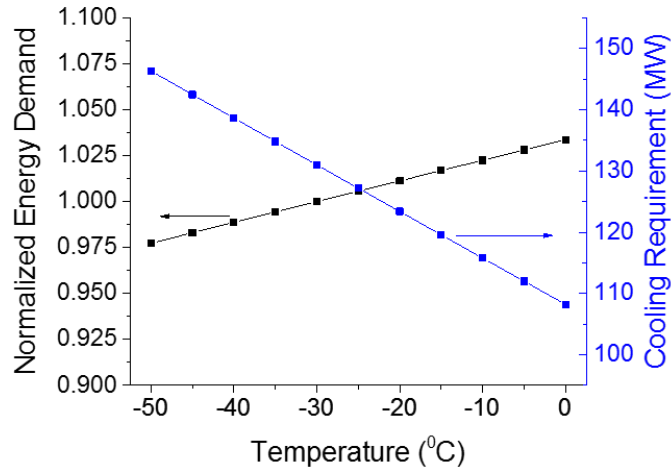
Figure 4-20. Effects on overall energy demand (black) for CO$_2$ capture (kWh/tonneCO$_2$ normalized, where base case 403.1 kWh/tonneCO$_2$) and (blue) net heat removal process requirements varying separator operating temperature

The economic analysis for the process shows a similarly small reduction in the cost of capture with lower temperatures (**Figure 4-21a**). This tradeoff is true across all PSA purities, though seems to become slightly more pronounced at lower purities (larger slope in lower purities compared to higher purities.
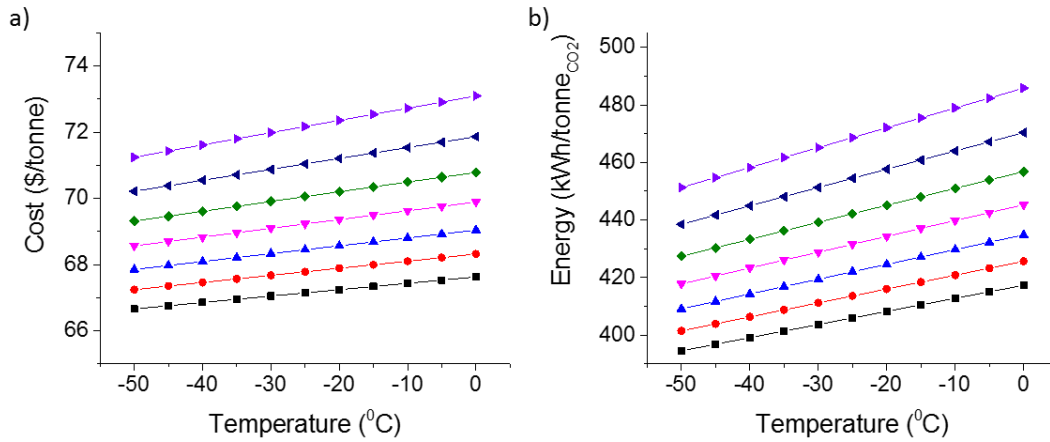
Figure 4-21. (a) Cost of capture as a function of primary separator operating temperature, (b) Energy demand of process as a function of primary separator operating temperature. Caption colors signify purities as in Figure 4-19

Looking deeper into the economics, the cost of the additional heat exchanger area (**Figure 4-22a**) is offset almost entirely by the reduction in monetized energy demand on the plant and compressor capital costs(**Figure 4-22b**). This makes some sense, as at colder operating temperatures COMP3's size decreases slightly, but at the cost of the heat exchanger area increasing.
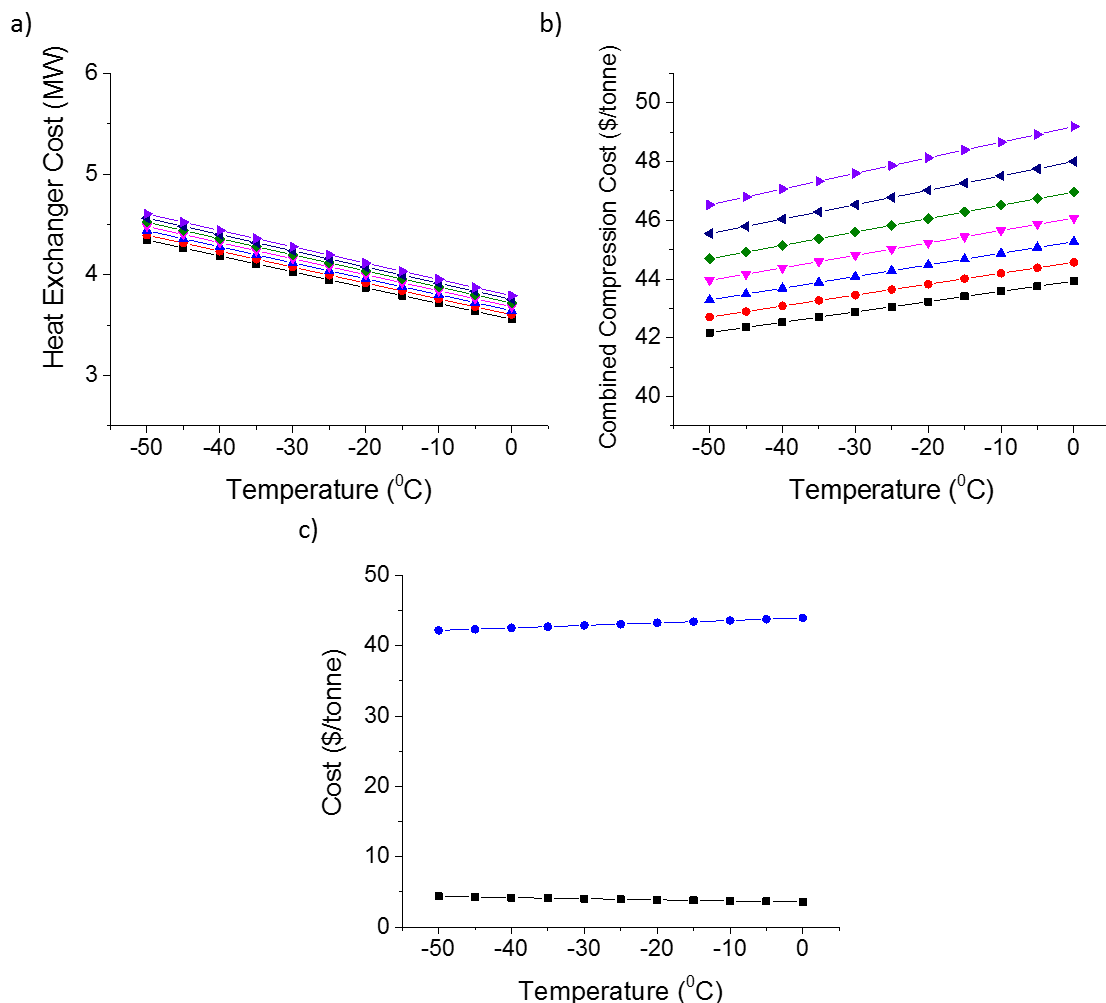
Figure 4-22. (a) Contribution of heat exchangers to cost of capture as a function of operating temperature, (b) Contribution of rotating equipment (compressors, expanders, pumps) combined with the energy to cost of capture as a function of operating temperature. Caption colors signify purities as in Figure 4-19 (c) Comparison of the contribution of rotating equipment and energy (blue) and heat exchangers (black) for the case of 95% purity off separator on a common axis.

4.3.3   Vacuum Pressure

The vacuum pressure used to recover the CO_2-rich product leaving the separator was varied from 0.05 to 0.3 bar. With these moderate levels of vacuum, we assumed a vacuum efficiency of 0.8 for an isothermal vacuum pump. Since the vacuum pump is somewhat isolated from the rest of the process, a variation of the vacuum pressure results follows a logarithmic profile for energy as shown in **Figure 4-23**. It's interesting just how

much of an impact pulling lower levels of vacuum has on the energy of the baseline system as compared to some of the other variables considered. Just comparing the size of equipment like the compression/expansion train or the heat exchanger network as compared to the vacuum system, the range of energy demand's produced here shows just how important the decision of vacuum pressure can be.
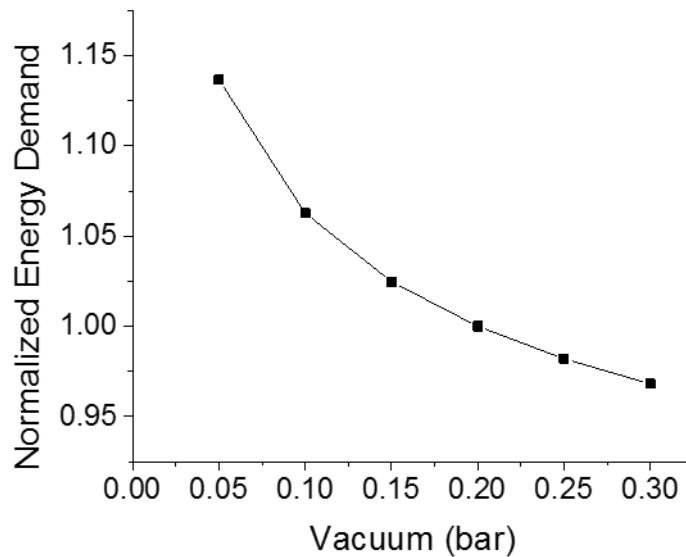
Figure 4-23. Effects on overall energy demand for CO_2 capture (kWh/tonneCO₂ normalized, where base case 403.1 kWh/tonneCO₂) varying PSA vacuum pressure

The lower the purity at the designated recovery, the more the volume of gas that needs to be removed via the vacuum, resulting in higher cost and energy (see **Figure 4-24**). The purity is therefore going to be a key variable when it comes to sizing the vacuum pump, and this is clear to see when examining the range of costs (almost $10 cost increase when moving from 95% purity to 65% purity). This cost would be exacerbated if the recovery was also increasing, a tradeoff that is often seen in pressure swing adsorption systems.
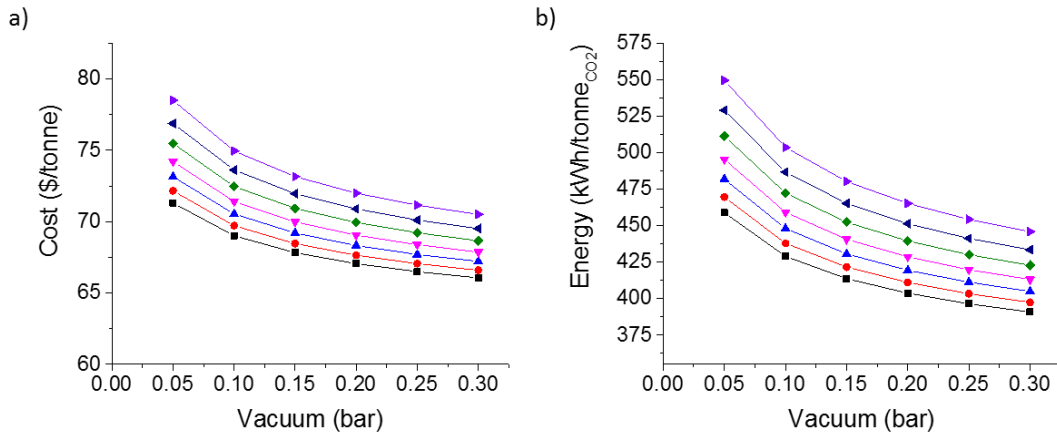
Figure 4-24. (a) Cost of capture as a function of primary separator vacuum condition, (b) Energy demand of process as a function of primary separator vacuum pressure. Caption colors signify purities as in Figure 4-19

4.3.4 Liquefaction Pressure

From an electrical energy and cost perspective, there is a moderate effect on increasing the liquefaction pressure, as shown in **Figure 4-25** and **Figure 4-26a,** respectively. This increase is primarily due to the increase in the size of the compressor used for liquefaction. The increase is slightly reduced as the liquefaction pressure approaches the separator operating pressure due to the necessity for less work in the recycle compressor. The primary effect of the choice of liquefaction pressure is on the temperature the liquefaction column requires for the 90% CO_2 recovery condition set as a requirement for the process, so this variable has wide-ranging effects on the heat profile of the system, something which is not accounted for in this sensitivity analysis.
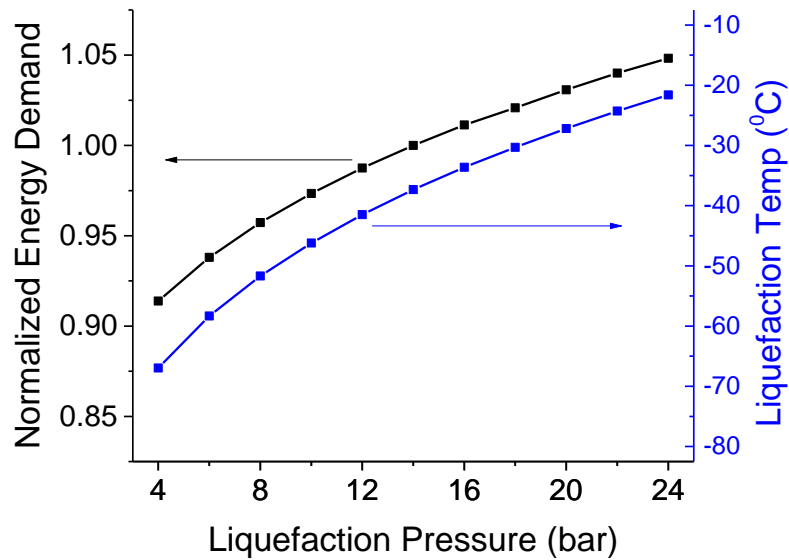
Figure 4-25. Effects on overall energy demand (black) for CO_2 capture (kWh/tonneCO_2 normalized, where base case 403.1 kWh/tonneCO_2) and (blue) Liquefaction Column operating temperature varying liquefaction pressure

This point can be clarified further looking at the temperature effects across a wide range of separation performance (purity) conditions given in **Figure 4-26c**. Again, we see that as purity goes down the liquefaction temperature required to reach the 90% recovery system must be colder. Thus this tradeoff between energy for liquefaction, and the lowest temperature the liquefaction column can operate at given the cooling produced by the Joule Thompson Expansion has considerable effects on the design of the final heat exchanger network. The ability of the plant to utilize the process' available heat removal with a reasonable temperature approach and to do so without external cooling, will be key.
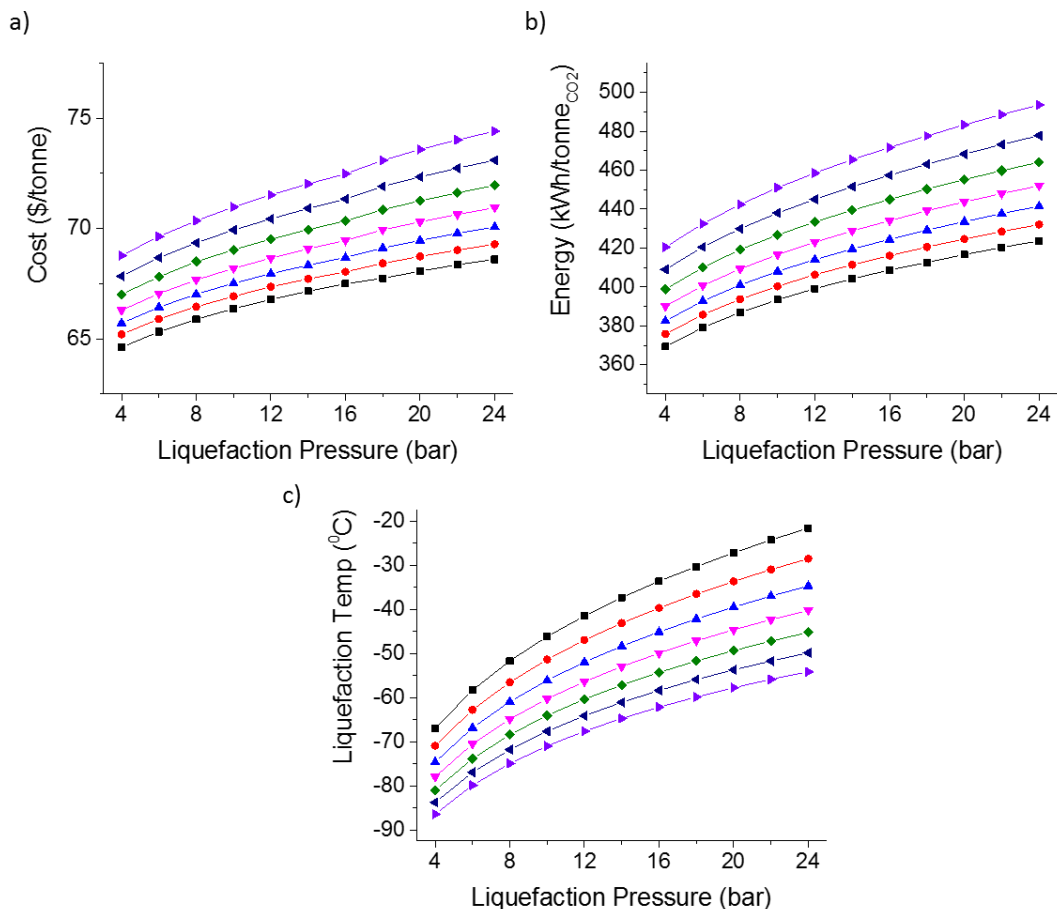
Figure 4-26. Cost of capture as a function of liquefaction pressure, (b) Energy demand of process as a function of liquefaction pressure, (c) Liquefaction temperature as a function of liquefaction pressure. Caption colors signify purities as in Figure 4-19

4.4 Fiber Performance Impacts and Manufacturing Costs

The cost of manufacturing the PSA unit out of fiber sorbents was investigated to better understand the cost of fibers with thermal management installed in the model of the high productivity fibers from the simulation results in Section 4.2. As the economics of a membrane-based process have already been considered in some detail in the work of Haase et al[2,3],[2,3] it is interesting to explore the performance of a PSA separation in the sub-ambient capture process. First analyzed in this section was the effect of different fiber manufacturing variables and costs on the overall cost of the PSA unit. To keep the analysis

consistent with the economics in the prior section, the cost includes not only raw material costs but also the associated costs of the actual beds and expected valves and fittings.

4.4.1 Fiber Manufacturing Parameter Costs

A simple four-step cycle for heavy-product recovery (pressurization, feed, blowdown, and evacuation) was considered for baseline performance. For preliminary analysis of the economics of CO_2 capture, we assumed a 2-bed system with a 360 s cycle time (180 s on pressurization and feed, 180 s on blowdown and evacuation), and PSA productivity of 0.0138 mol $kg_{sorbent}^{-1}$ sec^{-1}.

The cost of fiber sorbent contactors containing phase change materials[21] has not previously been considered in detail. Fiber beds were estimated to be made up of a multitude of individual fibers (diameter 650 μm, length 1 m). The weight ratio of phase change material to sorbent was taken at 1.25:1. The cost of the fibers was broken down into three parts, the price of the sorbent (base case economics take this value as $30/kg), the price of microencapsulated phase change material ($10/kg, based on an estimate from an industrial manufacturer), and the cost of the manufacture of the fibers and fixing them in flow modules ($20/$m^2$ fiber external surface area). The manufacturing cost was estimated from the price of industrial hollow fiber membranes, which are also produced using dry-jet wet-quench techniques. **Figure 4-27** shows the estimated breakdown in the cost of manufacturing the PSA unit containing fibers with phase change materials for our baseline case as a function of sorbent price. Across all considered sorbent costs, the price of manufacturing the fibers and potting them in modules dominates. Even in cases where

the sorbent price is high ($100/kg), the device manufacturing costs rather than the material

costs still make up the majority of the total cost.
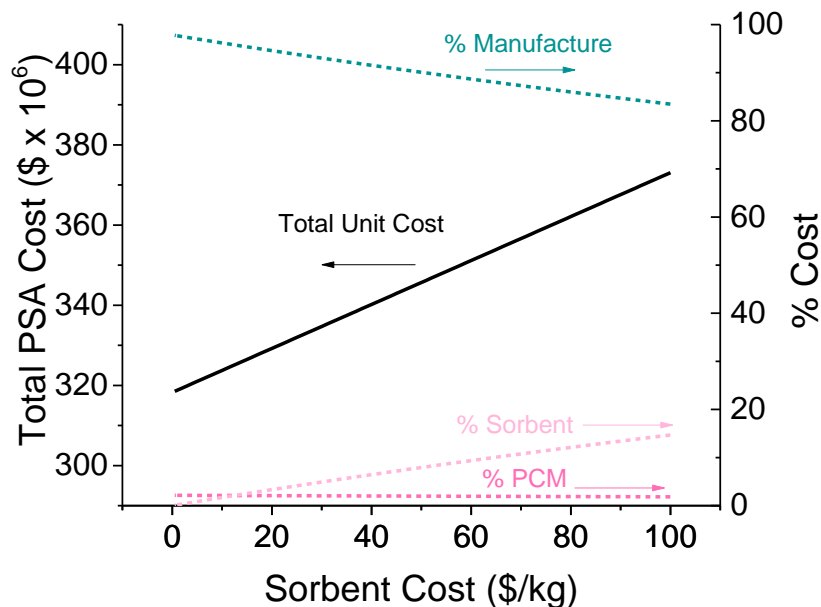
Figure 4-27. Cost breakdown of PSA fiber module manufacturing for a MOF-µPCM-polymer fiber sorbent module with 75 wt. % solids loading and a 1:1.25 mass ratio of MOF:µPCM at varying cost of the sorbent

While sorbent cost is expected to play a significant role in the price of the PSA unit,

many other manufacturing variables can also play a role in the price of the system[29,30].

Changes in the fiber diameter will play a significant role in the total number of fibers that

need to be potted in each PSA unit module. Smaller fibers would be expected to reduce

any potential intra-fiber diffusion limitations not related to the crystal structure of the

sorbent itself. With smaller diameters, the adsorbate needs to travel a shorter distance

through the porous polymer matrix to reach the further adsorbent particle in the fiber. The

effect on the unit cost of varying the diameter is given in **Figure 4-28**. Note, in this analysis,

we are purely considering the manufacturing cost, with the productivity fixed, so none of

the potential performance improvements discussed earlier will be shown in this plot. The

cost behavior is as one might expect, smaller fibers make the module manufacture more expensive, while the sorbent and heat management become more of a share of cost as manufacture drops.
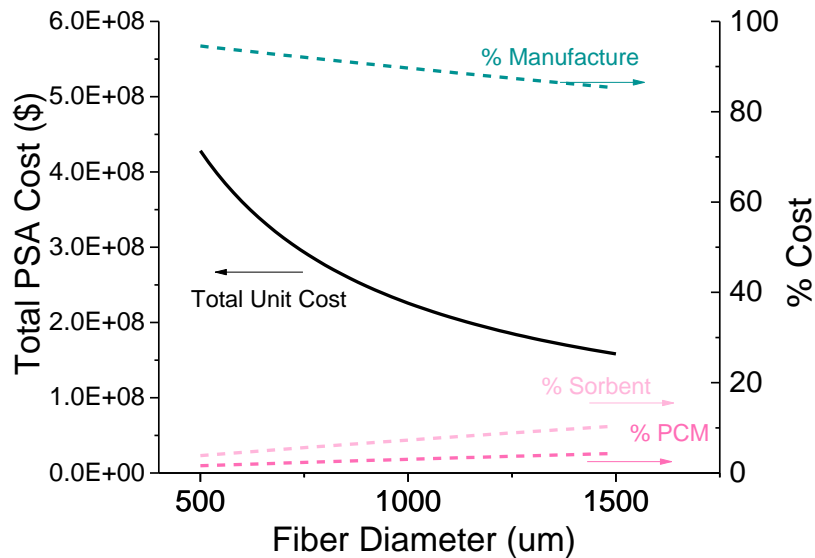
Figure 4-28. PSA cost and share of the cost of thermally managed fiber sorbents as a function of fiber diameter.

Another key parameter affecting the cost of the PSA unit will be the total solids loading (how much weight of sorbent and thermal management can be fit within the fiber). A plot showing those effects is given in **Figure 4-29**, where lower solids loadings lead to significant increases in the cost of the PSA unit. At the same productivity, the same amount of adsorbent is going to be necessary to capture the CO_2, so the less sorbent which can be fit within a single fiber means more total fibers (and more PSA modules) must be manufactured. While a maximum loading of 75-80% [23,31] have been noted for fiber sorbents in the literature, several cases have come along where the nature of the adsorbent filler limits the weight loading in the fiber to significantly lower values [30,32,33].
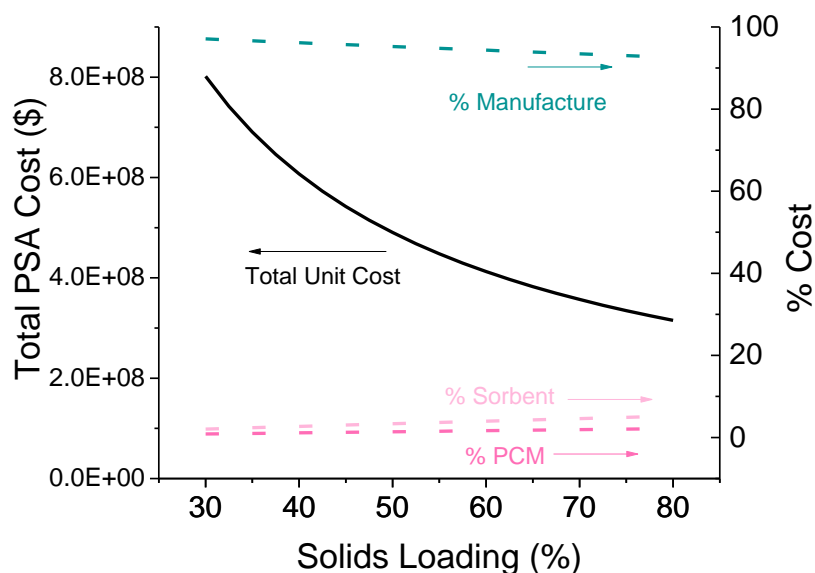
Figure 4-29. Cost breakdown of PSA fiber module manufacturing for a MOF-µPCM-polymer fiber sorbent module with a 1:1.25 mass ratio of MOF:µPCM at varying total solids content of the fibers

Finally, for the case of thermally managed fibers, it would be useful to understand the manufacturing cost impacts of putting more phase change material into a fiber, instead of putting more adsorbent in there. While it has not yet been investigated whether there is a 1:1 replacement ratio between microcapsules and sorbents in the fiber sorbent structure, it is still useful to get an idea of the cost implications of that replacement[21,29]. As with the prior discussion, the productivity is held constant in **Figure 4-30**, which is likely not the reality, as heat management should help to boost the productivity of the fiber sorbents. Still, replacing sorbent with µPCM follows a similar trend to that of solids loading, as one may expect. The less sorbent inside each fiber increases the total number of fibers required at constant productivity. In this case though, along with the sorbent cost-share decreasing due to the increase in the manufacture, we also observe a small increase in the cost-share of the phase change materials.
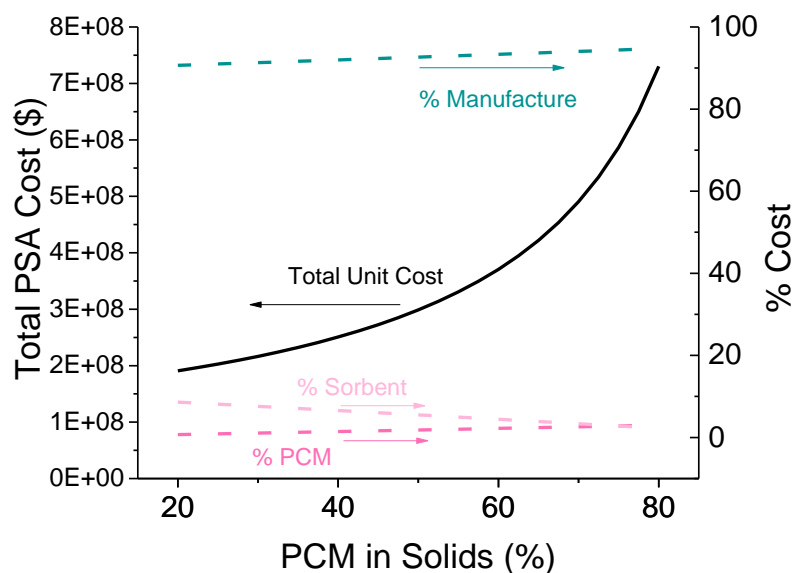
Figure 4-30. Cost breakdown of PSA fiber module manufacturing for a MOF-μPCM-polymer fiber sorbent module with 75 wt. % solids loading and varying the mass ratio of PCM to sorbent particles.

4.4.2 PSA Productivity's Role in Cost of Capture

Using an idealized cycle design (360 s cycle time) we estimated the cost of CO_2 capture using a sub-ambient sorbent for a wide range of sorbent productivities and CO_2 purities leaving the PSA unit.

Figure 4-31 shows the effect of sorbent productivity and CO_2 on the overall cost of capture. The cost of capture is significantly less sensitive to sorbent productivity at productivities greater than 0.015 mol kg^{-1} s^{-1}. Around this value, the cost of the PSA unit is less than 25% of the total capital cost so the capital cost is dominated by the energy demand of the process and the other capital equipment. Overall, regardless of the adsorbent performance this analysis also showed that the cost of the rest of the capital and energy for the sub-ambient CO_2 capture would come to slightly more than \$47/tonne$_{CO2}$ for the base case.

183

An interesting implication of **Figure 4-31** is that varying the rich product purity from the PSA unit leads to only minor variation in the total cost of CO_2 capture. Reducing the CO_2 rich product purity from the PSA unit to values from 85% to 75% CO_2 showed a $1.00-$1.20/tonne increase in total capture cost. This change stems from an increase in the size and energy requirement of the liquefaction system for the reduced purity case. Reducing purity also leads to increased energy demand due to a reduction in the amount of expansion energy that can be recaptured. This analysis can offer some insights into the economic tradeoffs of slight improvements in productivity at the cost of purity. As an example, using PSA for a given sorbent with PSA purity of 95% and productivities of 6.66×10^{-3} mol kg^{-1} sec^{-1} is estimated to cost $88/tonne. A different sorbent, which could only produce 75% purity, would require productivities to improve about 1.25 times (to 8.33×10^{-3} mol kg^{-1} sec^{-1}) to have a similar overall cost of capture.
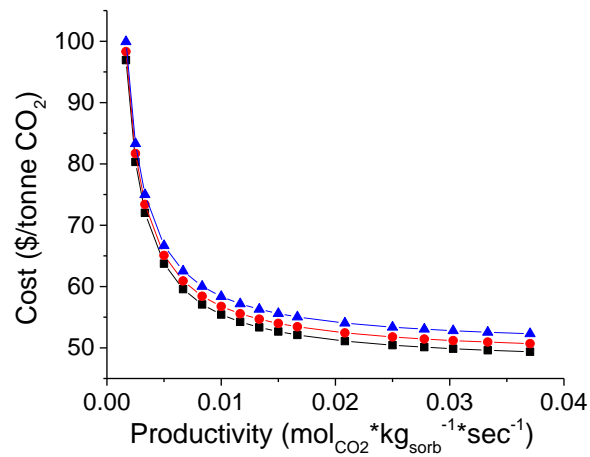
Figure 4-31. The effect of sorbent productivity (molCO$_2$ kg$_{sorb}^{-1}$ s^{-1}) on the overall cost of capture at baseline operating conditions (Table 1) with 95%, 85%, and 75% CO$_2$ purity resulting from the PSA unit. The cost of capture approaches $47.12 asymptotically to increasing productivity

4.5 Summary

The main objective of this chapter was to build a knowledge base for the economics and energy considerations that must be made when considering a sub-ambient CO_2 capture process using pressure swing adsorption. The sub-ambient CO_2 capture process considered was extremely capital intensive, but is operating at the capital intensive conditions the fiber sorbent platform showed extremely high productivities (which are necessary to be competitive with other approaches.). The PSA productivity, PSA unit operating pressure, and purity-recovery tradeoffs of the PSA unit appear to be the key parameters to be considered to understand the costs of capture.

Overall, regardless of the adsorbent performance, the analysis in Section 4.4 showed that the cost of the rest of the capital and energy for the sub-ambient CO_2 capture would come to slightly more than $47/tonne$_{CO2}$, for operation at the baseline conditions. This cost of capture is made up of just the supporting capital equipment and energy required for compression. The analysis in Sensitivity Analysis did show there was some potential for cost reduction with lower pressures and higher vacuum conditions, but the work in Sub-ambient Fiber Sorbent PSA showed that real adsorbents would most optimally be operated at the more expensive conditions. Much of the impact on capital cost increases in the real adsorbent system showed the downstream liquefaction was playing a major role in the cost. Future sorbent development for sub-ambient CO_2 capture may look to focus on reaching the DOE goals for purity and recovery without the need for the liquefaction and recycle to assist in reaching cost goals.

4.6   References

1.   Liu L, Sanders ES, Kulkarni SS, Hasse DJ, Koros WJ. Sub-ambient temperature flue gas carbon dioxide capture via Matrimid (R) hollow fiber membranes. *J. Membr. Sci.* Sep 2014;465:49-55.

2.   Hasse D, Ma JF, Kulkarni S, et al. CO_2 Capture by Cold Membrane Operation. In: Dixon T, Herzog H, Twinning S, eds. *12th International Conference on Greenhouse Gas Control Technologies, Ghgt-12.* Vol 63. Amsterdam: Elsevier Science Bv; 2014:186-193.

3.   Hasse D, Kulkarni S, Sanders E, Corson E, Tranier JP. CO_2 capture by sub-ambient membrane operation. In: Dixon T, Yamaji K, eds. *Ghgt-11.* Vol 37. Amsterdam: Elsevier Science Bv; 2013:993-1003.

4.   Song C, Liu Q, Ji N, et al. Reducing the energy consumption of membrane-cryogenic hybrid CO_2 capture by process optimization. *Energy.* 2017/04/01/ 2017;124:29-39.

5.   Lee S, Kim J-K. Process-integrated design of a sub-ambient membrane process for CO_2 removal from natural gas power plants. *Applied Energy.* 2020/02/15/ 2020;260:114255.

6.   Luyben WL. Estimating refrigeration costs at cryogenic temperatures. *Computers & Chemical Engineering.* 2017/08/04/ 2017;103:144-150.

7.   Castle WF. Fifty-Years' Development of Cryogenic Liquefaction Processes. In: Timmerhaus KD, Reed RP, eds. *Cryogenic Engineering.* New York, NY: Springer New York; 2007:146-160.

8.   Agrawal R. Synthesis of Distillation Column Configurations for a Multicomponent Separation. *Ind. Eng. Chem. Res.* 1996/01/01 1996;35(4):1059-1071.

9.   Castle WF. Air separation and liquefaction: recent developments and prospects for the beginning of the new millennium. *International Journal of Refrigeration.* 2002/01/01/ 2002;25(1):158-172.

10.   Li Y, Wang X, Ding Y. An optimal design methodology for large-scale gas liquefaction. *Applied Energy.* 2012/11/01/ 2012;99:484-490.

11.   Latimer RE. Distillation of Air. *Chemical Engineering Progress.* 1967;63(2):35-59.

12.   James RZ, Alexander; Keairns, Dale; Turner, Marc; Woods, Mark; Kuehn, Norma. *Cost and Performance Baseline for Fossil Energy Plants Volume 1: Bituminous Coal and Natural Gas to Electricity*: NETL;2019.

13. Joss L, Gazzani M, Mazzotti M. Rational design of temperature swing adsorption cycles for post-combustion CO_2 capture. *Chemical Engineering Science.* 2017/02/02/ 2017;158:381-394.

14. Zanco SE, Joss L, Hefti M, Gazzani M, Mazzotti M. Addressing the Criticalities for the Deployment of Adsorption-based CO_2 Capture Processes. *Energy Procedia.* 2017/07/01/ 2017;114:2497-2505.

15. Bui M, Adjiman CS, Bardow A, et al. Carbon capture and storage (CCS): the way forward. *Energy Environ. Sci.* 2018;11(5):1062-1176.

16. Anantharaman R, Berstad D, Roussanaly S. Techno-economic Performance of a Hybrid Membrane – Liquefaction Process for Post-combustion CO_2 Capture. *Energy Procedia.* 2014/01/01/ 2014;61:1244-1247.

17. Wetenhall B, Aghajani H, Chalmers H, et al. Impact of CO_2 impurity on CO_2 compression, liquefaction and transportation. *Energy Procedia.* 2014/01/01/ 2014;63:2764-2778.

18. Yoo B-Y, Lee S-G, Rhee K-p, Na H-S, Park J-M. New CCS system integration with CO_2 carrier and liquefaction process. *Energy Procedia.* 2011/01/01/ 2011;4:2308-2314.

19. Park J, Rubiera Landa H, Kawajiri Y, Realff M, Lively R, Sholl D. How Well Do Approximate Models of Adsorption-Based CO_2 Capture Processes Predict Results of Detailed Process Models? *Ind. Eng. Chem. Res.* 04/15 2020;59:7097-7108.

20. Zhao T, Jeremias F, Boldog I, Nguyen B, Henninger SK, Janiak C. High-yield, fluoride-free and large-scale synthesis of MIL-101(Cr). *Dalton Transactions.* 2015;44(38):16791-16801.

21. DeWitt SJA, Rubiera Landa HO, Kawajiri Y, Realff M, Lively RP. Development of Phase-Change-Based Thermally Modulated Fiber Sorbents. *Ind. Eng. Chem. Res.* 2018/12/13 2018.

22. Ye S, Jiang X, Ruan L-W, et al. Post-combustion CO_2 capture with the HKUST-1 and MIL-101(Cr) metal–organic frameworks: Adsorption, separation and regeneration investigations. *Microporous and Mesoporous Materials.* 2013/09/15/ 2013;179:191-197.

23. Chen G, Koros WJ, Jones CW. Hybrid Polymer/UiO-66(Zr) and Polymer/NaY Fiber Sorbents for Mercaptan Removal from Natural Gas. *ACS Applied Materials & Interfaces.* Apr 2016;8(15):9700-9709.

24. Liu Q, Ning L, Zheng S, Tao M, Shi Y, He Y. Adsorption of Carbon Dioxide by MIL-101(Cr): Regeneration Conditions and Influence of Flue Gas Contaminants. *Scientific Reports.* 2013/10/10 2013;3(1):2916.

25.   Xu M, Chen S, Seo D-K, Deng S. Evaluation and optimization of VPSA processes with nanostructured zeolite NaX for post-combustion CO_2 capture. *Chemical Engineering Journal.* 2019/09/01/ 2019;371:693-705.

26.   Akhtar F, Ogunwumi S, Bergström L. Thin zeolite laminates for rapid and energy-efficient carbon capture. *Scientific Reports.* 2017/09/08 2017;7(1):10988.

27.   Haghpanah R, Majumder A, Nilam R, et al. Multiobjective Optimization of a Four-Step Adsorption Process for Post-combustion CO_2 Capture Via Finite Volume Simulation. *Ind. Eng. Chem. Res.* 2013/03/20 2013;52(11):4249-4265.

28.   Haghpanah R, Nilam R, Rajendran A, Farooq S, Karimi IA. Cycle synthesis and optimization of a VSA process for post-combustion CO_2 capture. *AIChE Journal.* 2013;59(12):4735-4748.

29.   Lee YH, Jeong J, Kim K, Hyun T, Jamal A, Koh D-Y. Microporous Materials in Scalable Shapes: Fiber Sorbents. *Chemistry of Materials.* 2020/09/08 2020;32(17):7081-7104.

30.   DeWitt SJA, Sinha A, Kalyanaraman J, Zhang F, Realff MJ, Lively RP. Critical Comparison of Structured Contactors for Adsorption-Based Gas Separations. *Annual Review of Chemical and Biomolecular Engineering.* 2018;9(1):129-152.

31.   Pimentel BR, Fultz AW, Presnell KV, Lively RP. Synthesis of Water-Sensitive Metal-Organic Frameworks within Fiber Sorbent Modules. *Ind. Eng. Chem. Res.* May 2017;56(17):5070-5077.

32.   Fan YF, Liyely RP, Labreche Y, Rezaei F, Koros WJ, Jones CW. Evaluation of CO_2 adsorption dynamics of polymer/silica-supported poly(ethylenimine) hollow fiber sorbents in rapid temperature swing adsorption. *International Journal of Greenhouse Gas Control.* Feb 2014;21:61-71.

33.   Fan YF, Labreche Y, Lively RP, Jones CW, Koros WJ. Dynamic CO_2 Adsorption Performance of Internally Cooled Silica-Supported Poly(ethylenimine) Hollow Fiber Sorbents. *Aiche Journal.* Nov 2014;60(11):3878-3887.

CHAPTER 5.   SPINNING OF HIGH CAPACITY FIBER SORBENTS

One of the key outcomes of the work discussed in Chapter 4 was that there was a significant need for high productivity fiber sorbents to enable the most economically-feasible version of the sub-ambient pressure swing adsorption process. The following three chapters focus on the manufacture of materials to enable these high productivities. The work in this chapter focuses on the manufacture of fiber adsorbents with the high swing capacity adsorbent MIL-101(Cr), whose structure was considered in Section 4.2.

The first step in developing MIL-101(Cr) adsorbents was to develop a method for scaling up the synthesis to allow for full-scale fiber spinning (total mass of adsorbent at a minimum of 100 grams), discussed in detail in Chapter 3. Once the material could be repeatedly synthesized at a reasonable scale, a dope composition for the spinning of MIL-101(Cr) was developed. Challenges were experienced with sorbent mass loss during the spinning process, and two methods of overcoming this problem were postulated and carried out. This was the first definitive recorded instance of adsorbent leaching in the fiber spinning process according to the reported literature at the time. As a result of this work, it was determined that polyvinylpyrrolidone, a commonly used additive in fiber adsorbent spinning, combined with the small particle size of the synthesized MIL-101(Cr) was leading to leaching of adsorbent material from the fiber structure during the post-spinning solvent exchange process. Once fibers were able to be spun without sorbent leaching their dynamic adsorption performance was characterized via fixed bed breakthroughs and Helium-assisted desorption experiments. The fibers developed in the work described in

this chapter were then used for bench-scale sub-ambient PSA testing discussed in Chapter 7.

5.1   Scale-up Synthesis of MIL-101(Cr) Sorbents

As the main focus of this work has been to develop scalable materials suitable for the economic operation of the sub-ambient CO_2 capture process, a significant challenge to address was the spinning of an adsorbent material that would be greatly advantaged by operating within the process framework. The exploratory work of Park et al.[1] focused on determining the characteristics of adsorbents which would best produce high swing capacities, identified a number of promising materials for sub-ambient CO_2 capture. Unfortunately, of the 70+ adsorbent materials found as a part of that analysis, none of them displayed the two characteristics that would be necessary for the manufacture of fiber sorbents: 1. Stability in liquid water to survive the numerous solvent exchange steps involved in fiber manufacturing, and 2. Some path to procure the more than 100 grams of adsorbent (synthesis or purchase) that would be necessary to develop a dope composition and spin fiber sorbents for testing. One sorbent of those listed was water-stable (Ni-BDP), but the synthesis proved extremely challenging at the 250 mg scale; moreover, it was not available for purchase.

MIL-101(Cr), a metal-organic framework with chromium-oxo nodes and terephthalic acid linkers was found to be an especially promising candidate for sub-ambient PSA, due to its high recorded BET surface areas (2800-3100 m^2/g experimental, >4000 m^2/g simulated), and moderate isosteric heat of adsorption for CO_2(between 22-23 kJ/mol)[2-5]. A graphical representation of its crystal structure is given in **Figure 5-1,**

showing its two large pore cavities, 2.9 and 3.4 nm in diameter, which is linked by

pentagonal and hexagonal pore windows. These large pore cavities lead to its large surface

area and pore volume, which was linked to its high capacities for CO_2. Moreover, the two

relatively large pore windows are desirable for equilibrium driven post-combustion CO_2

pressure swing adsorption, as it should allow for rapid mass transfer inside the crystal.
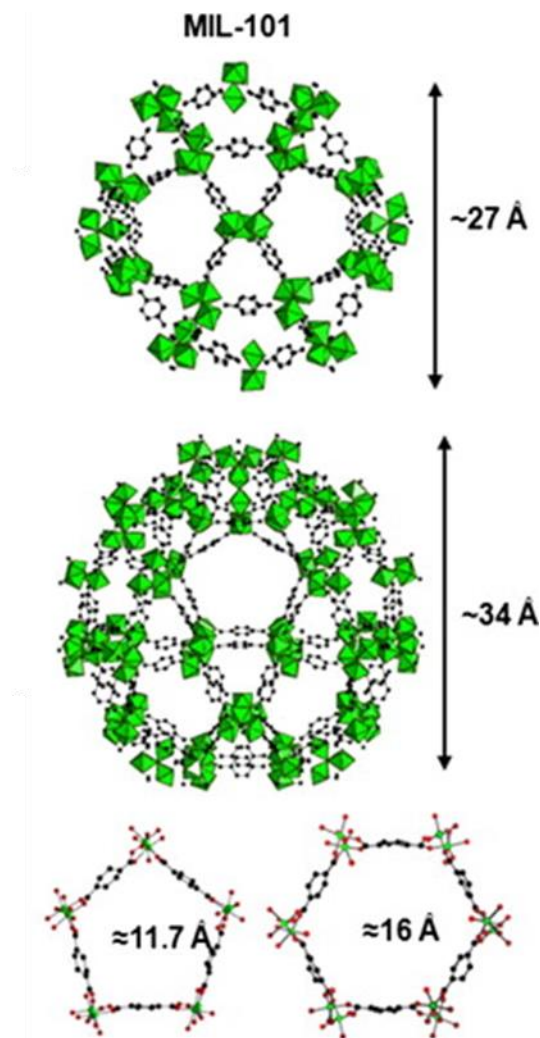
Figure 5-1. MIL-101(Cr) crystal structure showing the geometry of its two component cages and the pore windows connecting them. Adapted with permission[6] Copyright © 2010 Elsevier Inc. All rights reserved.

Outside of these expected advantages for capturing CO_2, from a manufacturing

perspective MIL-101(Cr) was also promising. MIL-101(Cr) had been previously scaled up

to ~ 20-gram batch scale in the literature, making it one of a choice few adsorbents which could conceivably be manufactured into fibers at meaningful scales.[7-8] Additionally, it had been reportedly stable in boiling water for prolonged periods, allowing it to potentially be spun using the scalable direct spinning methods which have been developed in the literature. These two factors made MIL-101(Cr) an excellent candidate for manufacture into fiber sorbents.

One potential challenge noted in the literature was MIL-101(Cr)'s a significant loss in permanent porosity (surface area and pore volume) when it was pelletized. Raj and co-workers[9] found pellets manufactured both with and without binder resulted in a reduction of permanent porosity and surface area of the sample of as much as 60% (the best pellet lost about 40% of its surface area). We repeated this analysis independently on our synthesized MIL-101(Cr) sample with the assistance of a pellet press, and found a similar loss in capacity (~ 45%), as shown in **Figure 5-2**. This loss in capacity is a significant hindrance to the application of MIL-101(Cr) to adsorption or catalysis, as its very low crystalline density (0.4 g/cc)[10], will lead to a very large device volumes.
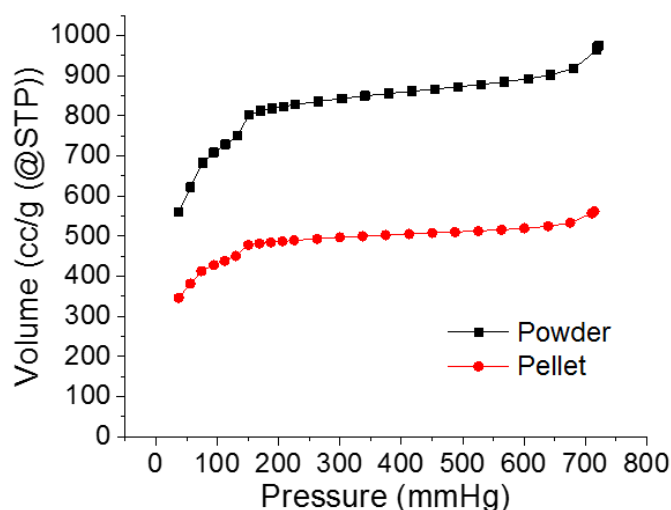
Figure 5-2. MIL-101(Cr) N_2 physisorption isotherm at 77 K, (black) powder and (red) pellet

The effects of low mechanical stability of an adsorbent particle on fiber sorbent spinning have not been considered in much detail in prior literature, so the spinning of MIL-101(Cr) offers some opportunity to probe possible advantages of fiber spinning over pelletization for forming scalable structured contactors. The fiber sorbent manufacturing process does not induce significant mechanical stresses when compared to the ton scales used in pelletization. Only two portions of the manufacturing process where the MOF is put under any notable mechanical stress are the repeated sonication to break up sorbent agglomerates, and the unidirectional stress that forms in the pump and line of the spinneret during spinning, which generally amounts to no more than 500 pounds per square inch. This tradeoff between the mechanical stability limitations of pelletization of some sorbents and chemical stability limitations of fiber manufacturing of other sorbents may prove to be an advantage that has not been explored with earlier adsorbent materials. Especially with sorbents such as MOFs, which are expected to be expensive relative to the current industrial standard adsorbents, having a method to manufacture structures that do not lead to losses

in the sorbent's thermodynamic performance could be key to the application to real systems.

MIL-101(Cr) was scaled up to 12-15g scales using the procedure outlined in Chapter 3, which was adapted from the literature. The product was characterized using a variety of techniques. To test the repeatability of the synthesis, N_2 physisorption at 77K was performed on the batches, two of the collected isotherms are given in **Figure 5-3.** The two isotherms show good repeatability, each resulting in BET surface areas between 2900 m^2/g and 3100 m^2/g. Batches which showed poor N_2 physisorption were put through the washing procedure a second time until the surface area of the batch was determined to be within the range expected. The MIL-101(Cr) powders were also thermally decomposed in an air atmosphere using a TGA to collect weight change differences. The TGA profile for one such batch is given in **Figure 5-4.** The PXRD pattern of one batch is given in **Figure 5-5**, accompanied by the simulated pattern. All relevant reflections appear in the powder pattern, with similar intensities to that of the simulated pattern.
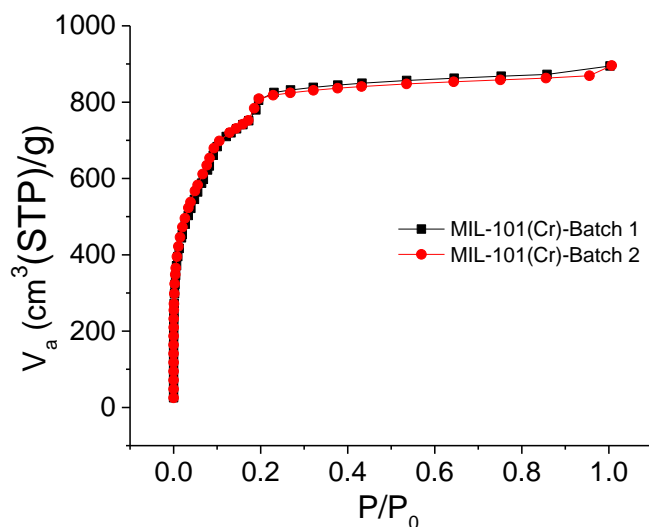
Figure 5-3. Nitrogen physisorption at 77K performed on multiple batches of MIL-101(Cr) showed good agreement in uptake.

The particle size of the scaled-up synthesis was qualitatively determined through the analysis of SEM images collected on the powders. **Figure 5-6** shows two such images of the powders, zoomed in at different levels. The particles appear rhombic in shape with a range of particle sizes, the majority of which are less than 1μm. A few larger particles (1-5μm) were noted throughout the powder. With the design and size of the batch, it makes some sense that the particle size would vary to some extent. This particle size tends to be on the lower end of the range of particles typically spun into fiber sorbents. With that said, the ability to work with smaller particle sizes is a possible advantage of fiber sorbents over other sorbent structures, as the porous polymer matrix should contain the particles during cycling. Small particle sizes are typically avoided when possible when working with pellets, as without proper adhesion cycling of small particle-containing pellets may result in fluidization of the particles if any attrition occurs.
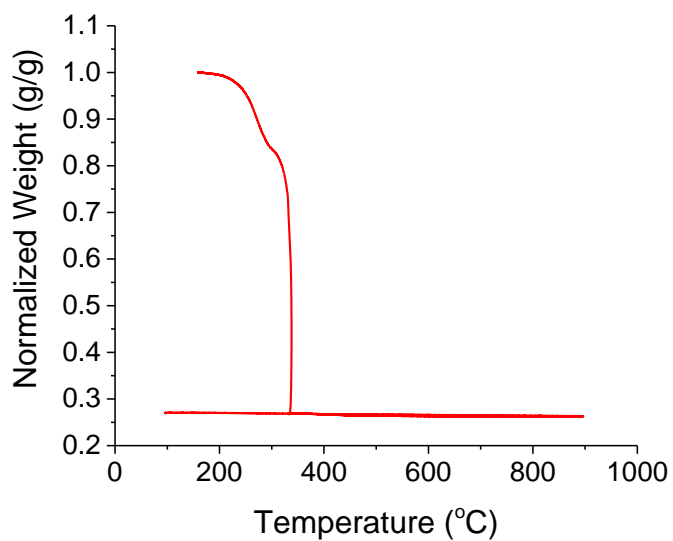
Figure 5-4. TGA burnup in an air atmosphere of scale-up synthesis of MIL-101(Cr). Typical batch to batch variation in "dry weight" varied 1-2% of the normalized mass
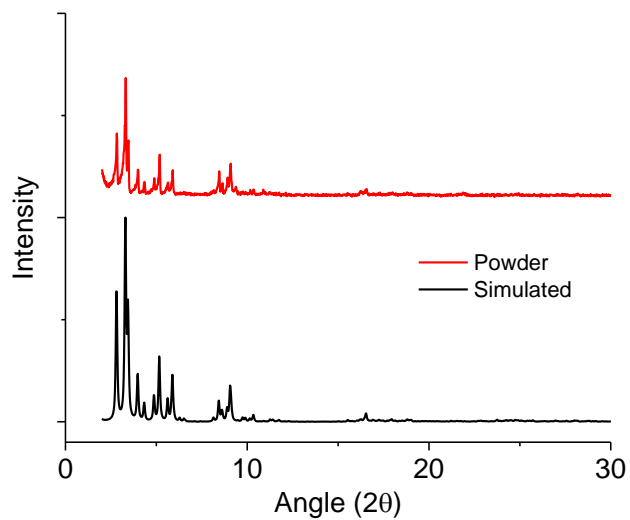
Figure 5-5. PXRD patterns for (red) scaled up MIL-101(Cr) batch compared to (black) simulated pattern
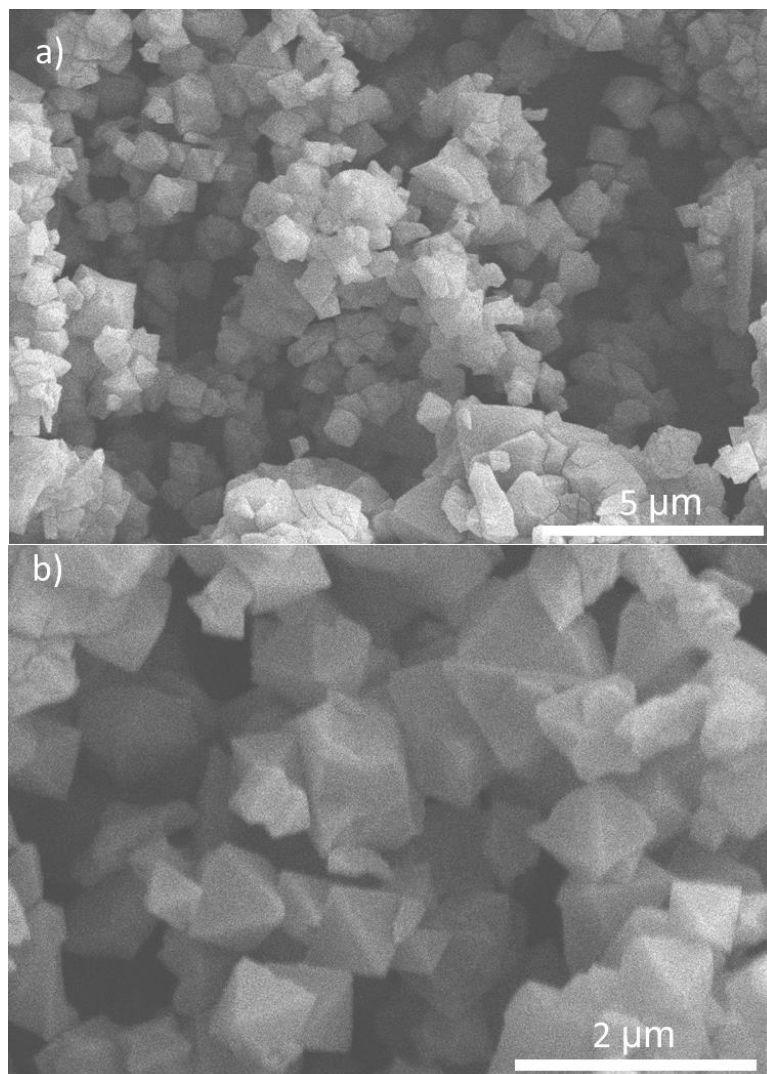
Figure 5-6. SEM images of powder MIL-101(Cr) produced using the scale-up synthesis.

With the scale-up synthesis complete, sub-ambient pure gas isotherms for carbon dioxide and nitrogen were collected using the as-synthesized samples, given in **Figure 5-7** and **Figure 5-8**. The MIL-101(Cr) CO_2 sorption isotherm shows significant increases as the temperature gets colder, culminating at a capacity of nearly 30 $mmol_{CO2}$/gram at 4.75 bar and 223K. MIL-101(Cr)'s CO_2 sorption isotherm appears to be relatively linear, not reaching saturation at any of the temperatures and pressures we considered. Its nearly 8 $mmol_{CO2}$/gram capacity at 243K and ~2 bar (which is near the pressures we would expect

our PSA system to be operating) exceeds the state of the art MOF (Mg-MOF-74) and Zeolite (13X) capacity for ambient PSA by 3 and 5 $mmol_{CO2}$/gram respectively, allowing for the significant productivity increases we observed in the simulated Pareto's reported in Chapter 4. The nitrogen isotherms in **Figure 5-8** show that MIL-101(Cr) does have a reasonably high capacity for N_2 at sub-ambient conditions, which may result in low purities from the PSA system. Nevertheless, MIL-101(Cr)'s large CO_2 swing capacity at sub-ambient conditions makes it an ideal adsorbent for proof of concept sub-ambient CO_2 capture via PSA.
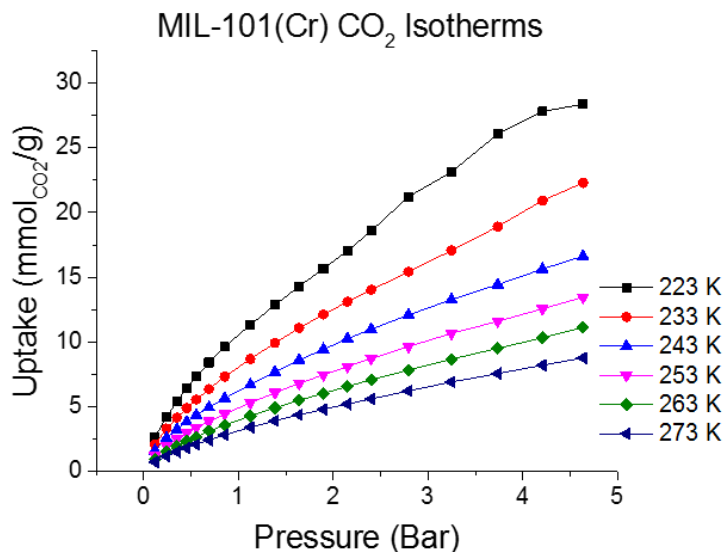
Figure 5-7. MIL-101(Cr) CO_2 Sorption Isotherm at sub-ambient temperatures ranging from 223-273K

One interesting behavior observed in the MIL-101(Cr) CO_2 isotherm at 223 K in **Figure 5-7** was the small inflection noted between 2.5 and 4 bar partial pressure. We postulate this inflection is a pore filling phenomenon, a behavior rarely observed in CO_2 isotherms though oftentimes observed in H_2O and N_2 isotherms. The CO_2 sorption isotherm at 195 K, shown in **Figure 5-9**, collected many points within the range of the step in the isotherm and was able to confirm this behavior in the isotherm was not due to some

experimental error. Indeed, there is a second step in **Figure 5-9** between 700 and 800 mbar.[11]
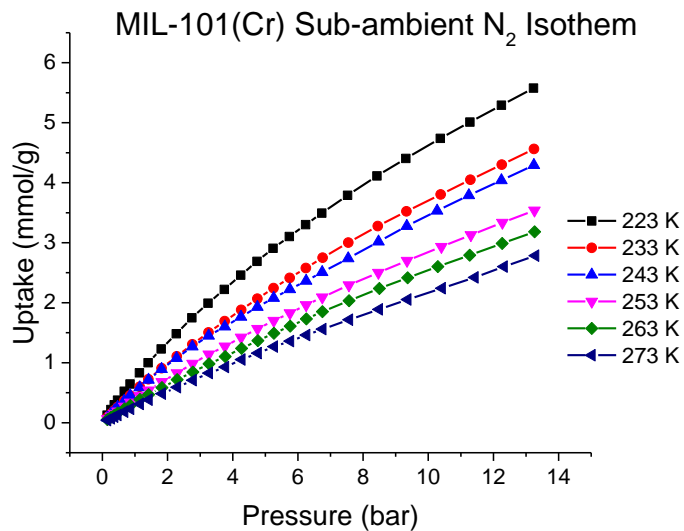
Figure 5-8. MIL-101(Cr) N2 Sorption Isotherm at sub-ambient temperatures ranging from 223-273K
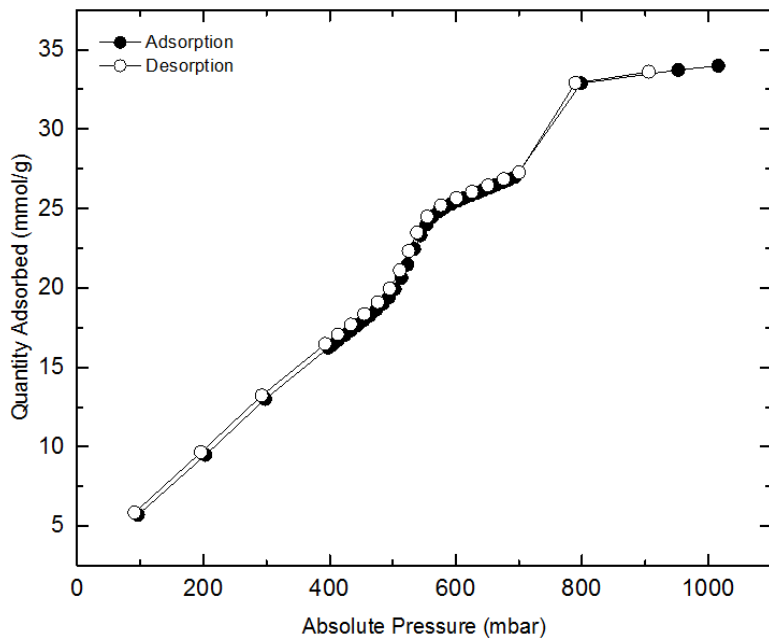
Figure 5-9. MIL-101(Cr) CO₂ Sorption Isotherm at 195K, collected by collaborators in the Walton Lab[11]

5.2 Spinning MIL-101(Cr) Fiber Sorbents

5.2.1 Syringe Extrusions of MIL-101(Cr)-Cellulose Acetate Fibers

Preliminary syringe extrusions were carried out to probe the spinnability and survivability of MIL-101(Cr) to the fiber spinning process. The dope composition used for the first syringe extrusions is given in **Table 5-1**, modeled after the dope composition used for MOF spinning developed in prior work.[12] Extrusion of the polymer dope was straightforward, with the dope's viscosity falling well within the spinnable range and the fibers being relatively easily drawn. Post-solvent exchange, the fibers were observed to be relatively brittle, but this is generally expected from syringe extrusions as they usually have larger diameters than what is normally produced in fiber spinning (**Figure 5-10a.**).

Table 5-1. Preliminary dope composition and spinning conditions for MIL-101(Cr) spinning where sorbent leaching was noted

Component	Weight Percent in Dope
NMP	64.68
H$_2$O	7.06
CA	10.59
PVP	7.05
MIL-101(Cr)	10.62
Spinning Characteristics	
Flow Rate (mL/hr)	200, 300
Air Gap (cm)	3
Spinneret temp (°C)	50
Bath Temp (°C)	50
Take-up rate (m/min)	10, 20

The syringe extrusions were then imaged using SEM to examine the substructure and dispersion of sorbent particles within the polymeric dope. **Figure 5-10a** shows a low magnification image of the fibers, showing a relatively large (~1.5 mm) diameter. The structure at this level appears fairly consistent with most other cellulose acetate fibers (the most common polymer support in the fiber sorbent literature), though a few macro voids

do appear around the edges of the fiber, indicating perhaps imperfect phase inversion. Next, observing the substructure of the fibers in **Figure 5-10b** and **Figure 5-10c**, the structure of the fibers does appear porous, though the walls of the pores do not appear to be made of polymer, but rather appear to be made up of the MIL-101(Cr) particles. **Figure 5-10b** appears to have a 40-50μm region that is particularly dense with MOF particles located near the center of the image, which may be a cause for slightly slower mass transfer if there are no gas transport pathways in pores below the agglomerate. The majority of the polymer structure appears more like that of **Figure 5-10c**, where there are pores throughout the polymer matrix, but the polymer itself appears rough as compared to other fiber sorbents reported in the literature. Investigating the nature of that rough surface is shown in **Figure 5-10d**. The polymer backbone is not apparent when looking at that very close image, instead, it appears as though the fiber is made up of walls of sorbent particles.
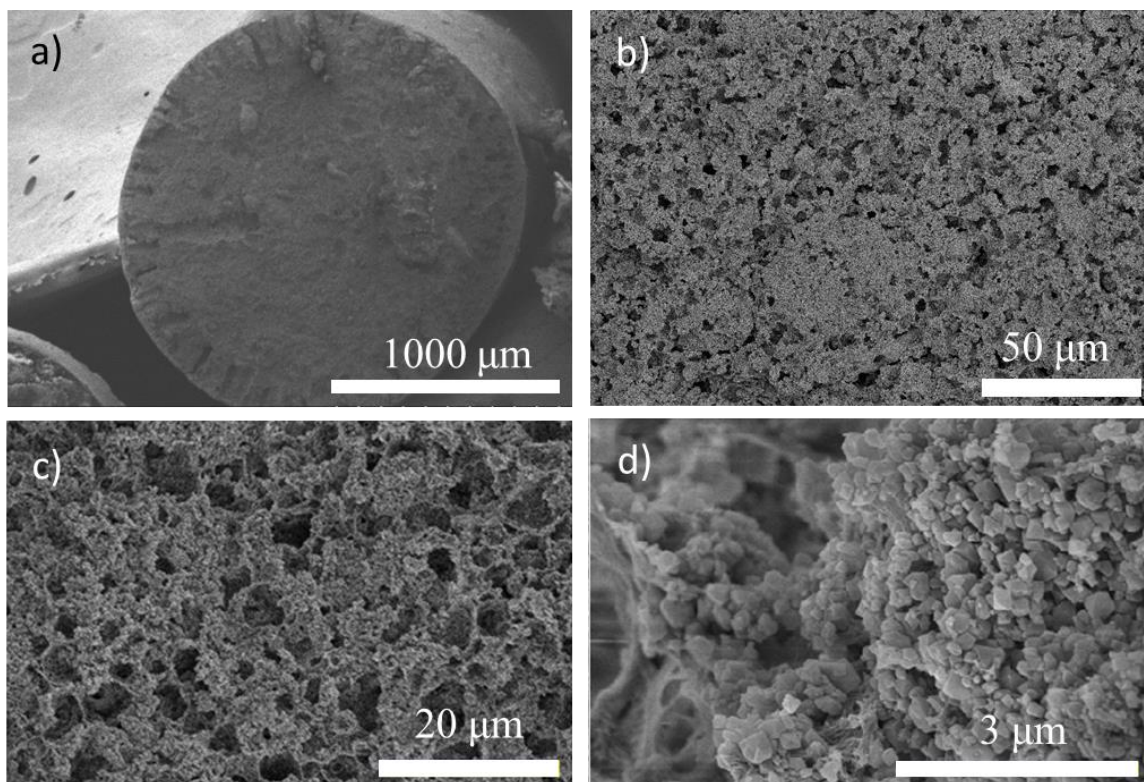
Figure 5-10. SEM Images of preliminary MIL-101(Cr) syringe extrusions

This substructure is fairly surprising, as it has not been reported for other MOF or zeolite fiber sorbents. We postulate this structure is formed as a result of the nanoscopic MIL-101(Cr) particles. In prior fiber sorbent structures, the larger adsorbent particles seemed to settle within the pores of the polymer matrix, forming a "sieve in a cage" morphology. With these much smaller particles, it seems likely many particles would be stuck together within the pores, and since the particles cannot simply float in space they must eventually settle onto the walls of the porous polymer matrix.

X-ray diffraction was carried out on crushed syringe fibers, shown in **Figure 5-11a**, comparing both to the simulated pattern and the powder pattern for the scaled-up MIL-101(Cr) (previously shown in **Figure 5-5**). All the major reflections appear to be retained in the fiber XRD, though the signal is considerably noisier and lower intensity (note

intensities in **Figure 5-11** are normalized to the highest intensity reflection), due to the relative abundance of polymer and the voids within the polymer matrix. There are some differences in the relative intensity of the individual reflections, which can be ascribed to the differences in sample preparation in the case of the fibers.

Nitrogen physisorption at 77 K was performed on the syringe extrudates (**Figure 5-11b**)to determine the relative loading of the MIL-101(Cr) in the polymer, with the dope composition leading to an expected loading of 50%. Comparing the N_2 uptakes at P/P_0 of 0.5, the MOF loading was found to be only about 36% MIL-101(Cr), far below the expected value. Thermogravimetric analysis performed on the syringe extrudate showed a more moderate weight loss, with inorganic loading pointing to a MOF loading of 44% in the fibers.
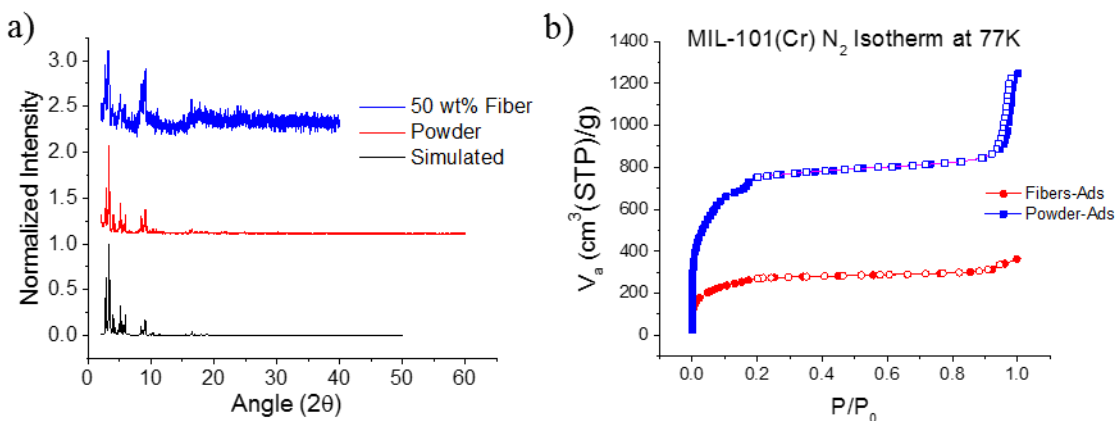
Figure 5-11. (a) PXRD patterns for MIL-101(Cr) (black) simulated pattern, (red) powder from synthesis, and (blue) 50 wt% expected MIL-101(Cr)-Cellulose acetate syringe fiber. (b) N_2 physisorption isotherm at 77K comparison between MIL-101(Cr) powder and 50 wt% expected fiber.

The difference between the loadings calculated based on sorption and TGA may have been due to the same phenomena that led to the wall coating of the polymer phase within the fiber in **Figure 5-10**. Some fraction of the MOF particles could get "stuck"

within the polymer-rich phase (rather than being rejected to the polymer lean phase where the pores eventually form). This densified polymer phase surrounding the particle is desired in some other applications of fiber spinning (mixed matrix membranes), where small particle size is desired to accomplish this exact morphology. With that said, the loss of sorbent responsible for the 6% reduction in weight loading (going from 50 wt% to 44 wt% means losing approximately 200 mg on a 1 gram of material added basis, or 20% loss of material) needs to be accounted within the manufacturing process for both environmental and economic reasons.

The usual reason for the calculated loss of loaded sorbent mass in fiber manufacturing has been due to not accounting for adsorbed water on the sorbent. The usual method employed to overcome this issue is to "pre-saturate" the adsorbent with a known amount of water (100% RH) ahead of dope preparation.[13-14] This turned out to not be possible with MIL-101(Cr), as it sorbed nearly its mass in additional water when pre-saturated at 100% RH, which was more water than was needed in the dope composition even if no other water were added. With this in mind, the water content of MIL-101(Cr) during storage in the lab was determined via drying in the TGA and added to the dope (removing any water necessary to balance out the dope). TGA on that sample resulted in nearly the same amount of missing material.

With the mass balance confirmed during dope preparation, the next possibility was that the sorbent was leaving the fiber during the extrusion and phase inversion process. With this in mind, a syringe dope was extruded into a 1L beaker of deionized water, allowed to solvent exchange as typical for syringe extrusions. When the fibers were removed, instead of disposing of the water, the water solution was placed in a rotary

evaporator and the majority of its volume evaporated off. The final solution turned green in color, as pictured in **Figure 5-12**.
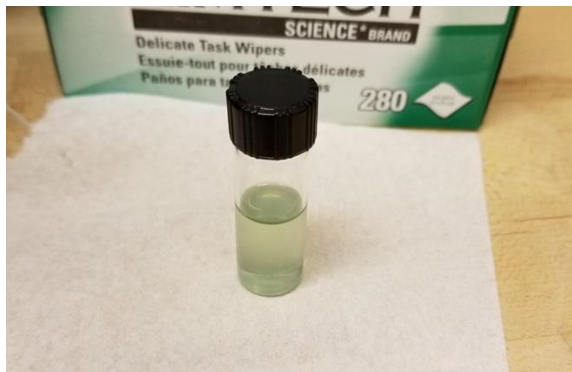
Figure 5-12. Water exchange solution (2 mL) after rotary evaporation from the 1L solution

Trying to understand the nature of the leaching further, new polymer dopes, with the same polymer-solvent-nonsolvent dope compositions, and different MOF loading, were prepared and subsequently syringe extruded. The resulting TGA profiles of those syringe extrusions are given in **Figure 5-13**, with the calculated MOF weight percentages noted next to the residual masses.
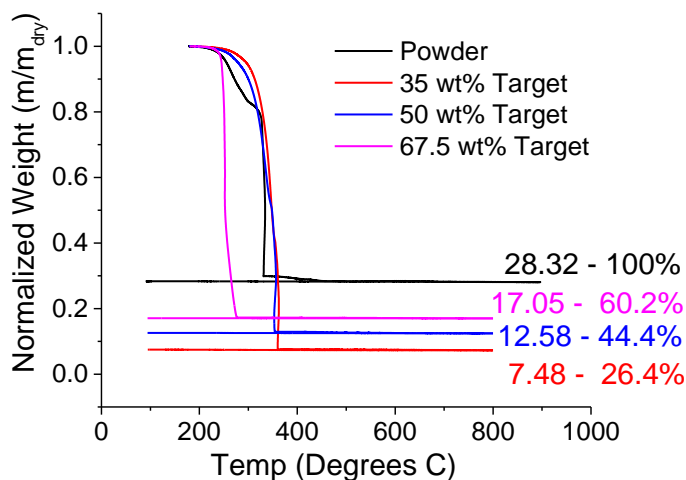
Figure 5-13. TGA profiles of MIL-101(Cr) Syringe Extrusions at different expected weight loadings.

205

To minimize or eliminate the sorbent leaching two hypotheses were considered, shown in **Figure 5-14** below: 1. The small particle size was enabling leaching during the solvent exchange process, and 2. The dope composition's high polyvinylpyrrolidone fraction as compared to some other cellulose acetate fiber sorbent dopes was leading to sorbent leaching.

In the first hypothesis, the particles get caught up in the polymer lean phase during solvent exchange and due to their small size relative to the size of the polymer domains they pass through the polymer rich sieve and leach out. Extrusion of fibers with larger particles then would result in less leaching. The second hypothesis focuses less on the particles and more on the polymer lean phase. If the elevated PVP fraction (light blue colors polymer lean phase) in these dopes allows for more rapid removal of the polymer lean phase (dark blue arrows), possibly via expanding the size of the polymer lean domains. More rapid transfer could be result in the very small MIL-101(Cr) particle leaching. Reducing the PVP fraction then would result in less of a driving force for the removal of the particles in the polymer lean phase during phase inversion.
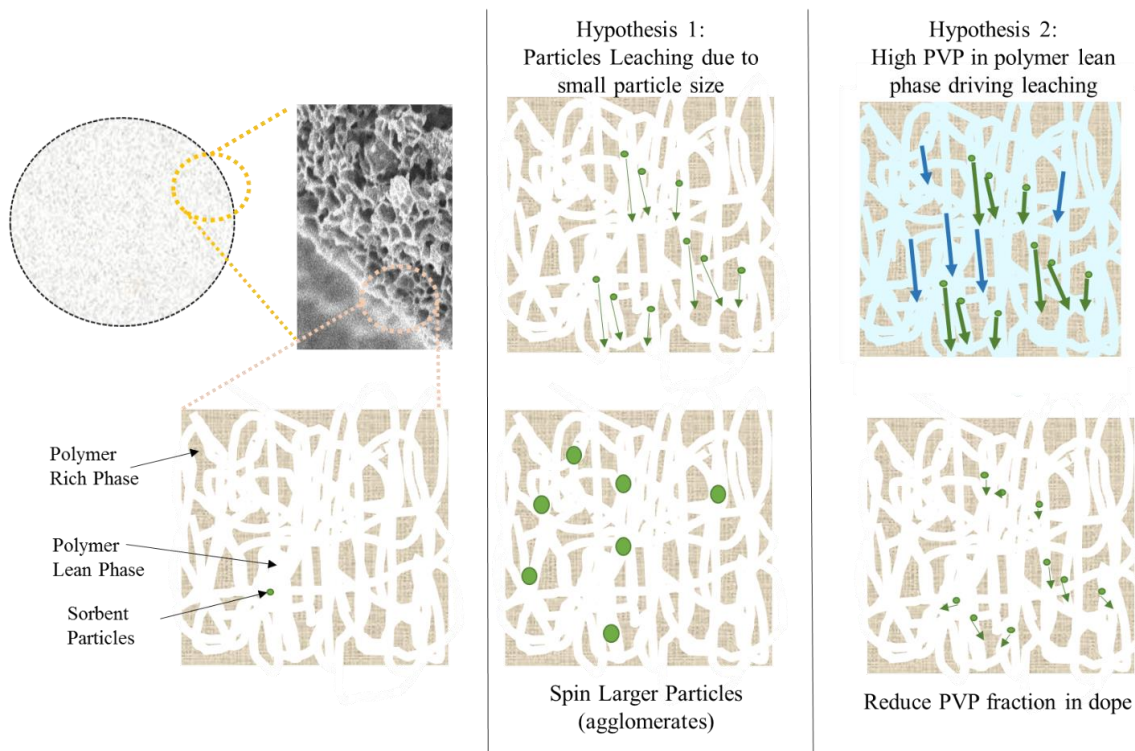
Figure 5-14. Possible explanations of sorbent leaching explored in the following sections. In hypothesis one, the very small particle size enables leaching during solvent exchange. In hypothesis two, the elevated PVP fraction, light blue color, in polymer lean phase enables the leaching via expanded domain size of the polymer lean phase.

5.2.2 Spinning of Sorbent Agglomerates

The first hypothesis was that the sorbent was leaching from the fibers due to their very small particle sizes. The morphology of the fibers shown in **Figure 5-10** has particles coating the walls. If the MOF particles size makes them more mobile, leading to coating the walls, increasing the particle size would eliminate this issue. An alternative synthesis was tested at small (20mL) scales using an excess of acetic acid modulator instead of nitric acid, resulting in larger particle sizes (800 nm rod-shaped crystals, shown in **Figure 5-15**). Unfortunately, the use of the modulator diminished the yield to such an extent it would no longer be suitable for fiber spinning (>50 mg).
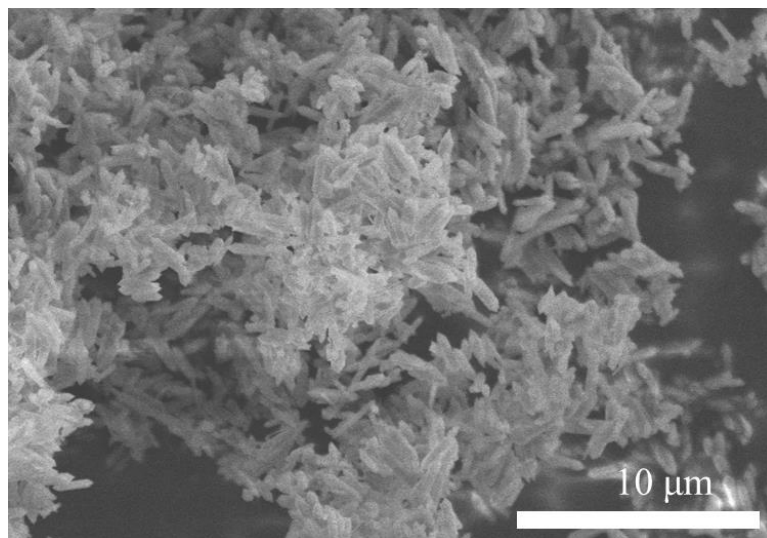
Figure 5-15. Large MIL-101(Cr) crystals produced via alternative

Lacking larger particles available at spinning scales, an alternative approach was proposed to the dope preparation step, where the sorbent agglomerates would not be broken up via sonication. In this approach, the majority of the particles, having formed agglomerates in the drying and activation step of the synthesis process, would remain as agglomerates through the fiber manufacturing process. Syringe extrusions at 33% and 50% target fiber weight were carried out. N_2 physisorption (**Figure 5-16**), thermogravimetric analysis, and SEM were carried out on these fibers, to determine if the alternative approach to dope preparation resulted in fibers with less leaching. Looking at the N_2 physisorption results for the 50 wt% expected fiber composition in **Figure 5-16**, the weight loading in these fibers is estimated to be just over 47%, a marked improvement over the 36% found for sorbent fibers where sonication was used.
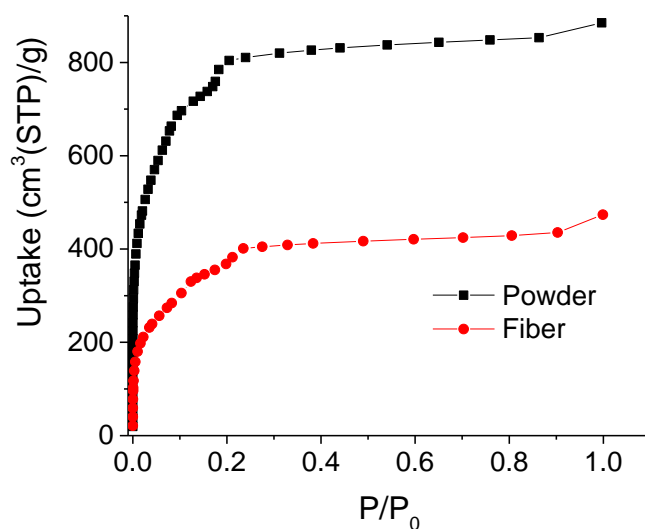
Figure 5-16. N$_2$ Phsysisorption isotherms at 77K of MIL-101(Cr) powder (black) and syringe extruded fiber (red) produced without sonication

Residual mass analysis was carried out on the syringe fibers produced without sonication to determine the weight loading of MOF within the fiber. The results of that analysis are plotted versus the expected loading given the dope composition in **Figure 5-17**. The equivalent values of loading determined for the fibers where leaching was present and sonication was used are also shown on the parity plot in **Figure 5-17**. At low weight loading (33%), the residual mass analysis points to no leaching behavior, though at comparable relative loadings non-agglomerate extrusion resulted in notable leaching. While some leaching is still found at the 50 wt% target extrusion without sonication, the value is improved compared to the traditional dope preparation approach and is confirmed by N$_2$ physisorption (**Figure 5-16**) versus the significant discrepancy in those values for the traditional dope preparation approach.
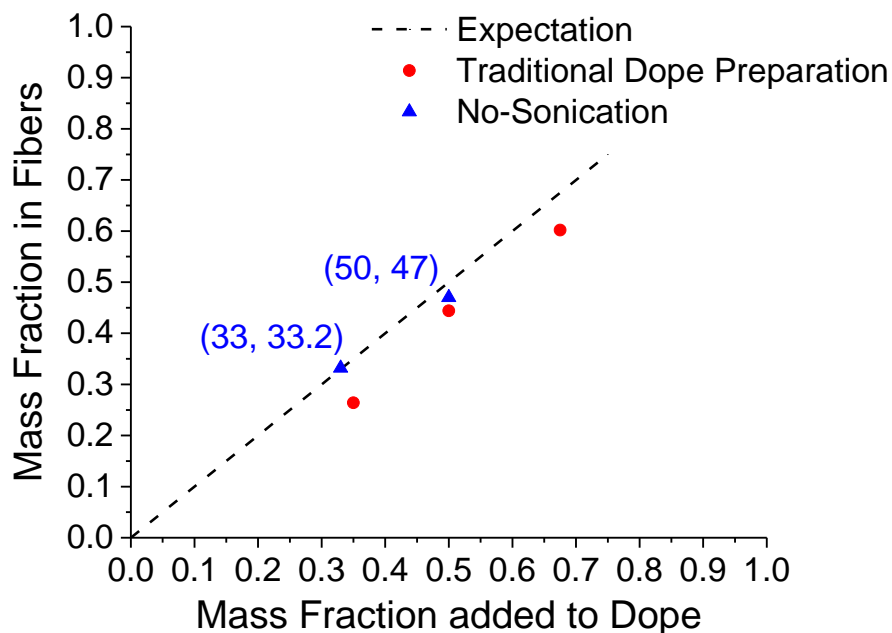
Figure 5-17. Parity plot comparing the expected mass fraction in the fibers given the dope composition (x-axis) and the estimated mass fraction of MIL-101(Cr) from residual mass analysis from TGA. (red circles) traditional dope preparation where sonication was used, (blue triangles) syringe extrusions without sonication

SEM images taken of the no-sonication syringe extruded fibers showed several large agglomerate structures, an example of which is given in **Figure 5-18**. These syringe extrusions still had numerous individual particles scattered throughout the structure, which likely led to the small amount of leaching determined by the follow-up analysis. Still, the results showed promise as an approach to overcome leaching, so full-scale fiber spinning was attempted.
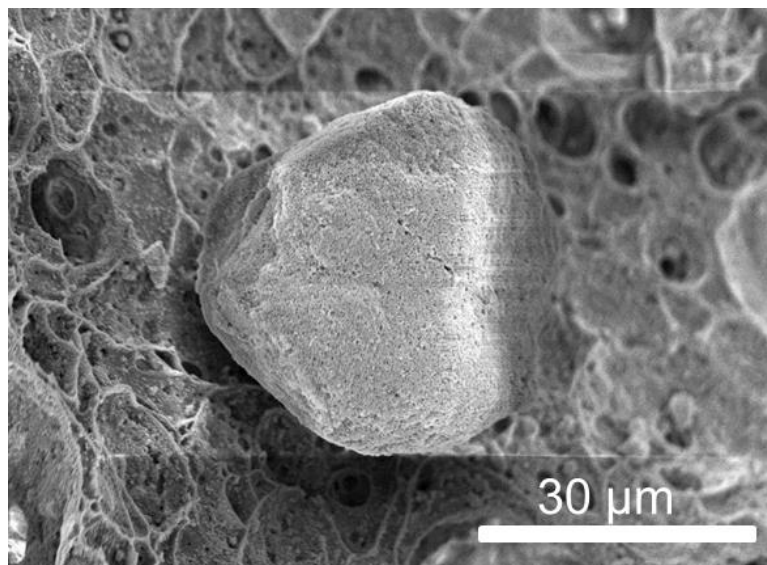
Figure 5-18. SEM image of agglomerate within the porous polymer matrix of syringe extrusion where sonication was removed from dope preparation.

The dope composition for fiber manufacturing with no sonication used is given in **Table 5-2**. The dope composition is effectively the same as the composition reported in **Table 5-1**, so the only major difference in the two approaches was the elimination of the sonication step. The spin itself was challenging, exhibiting an unusually high number of line breaks and irregularities in the flow, like filament pulsing and filament winding leaving the extruder. This was due to factors beyond just the spinning of agglomerates, including the use of a Swagelok adapter in place of the spinneret due to concerns of clogging.

Table 5-2. Dope composition and spinning parameters for MIL-101(Cr) agglomerate spin

Component	Weight Percent in Dope
NMP	64.61
H_2O	7.14
CA	10.58
PVP	7.07
MIL-101(Cr)	10.59
Spinning Characteristics	
Flow Rate (mL/hr)	200
Air Gap (cm)	5
Spinneret temp (°C)	25
Bath Temp (°C)	50
Take-up rate (m/min)	10

Figure 5-19 shows the N_2 physisorption isotherm collected at 77K on the fiber sorbents spun without sonication. Interestingly, the N_2 physisorption result of the large scale spin shows significant (~41 wt% estimated based on isotherm values) leaching still occurred. SEM images of the agglomerate spun fibers show several agglomerates packed within a spiderweb of polymer that is coated much like what was seen in **Figure 5-10**.
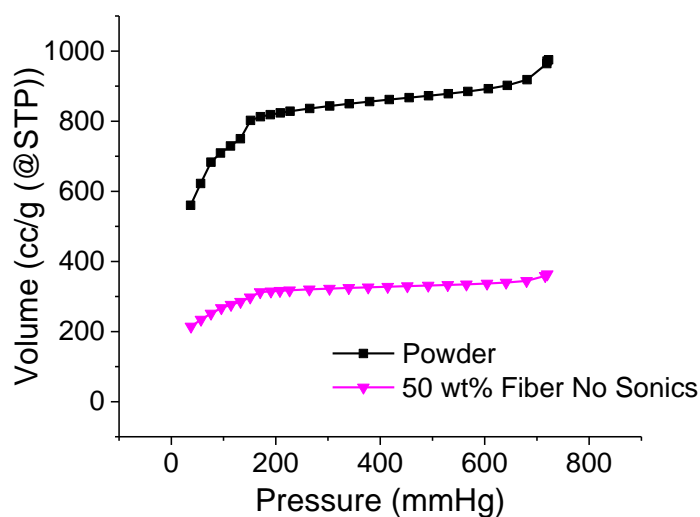
Figure 5-19. Nitrogen physisorption isotherm for MIL-101(Cr) agglomerate fibers

We postulate the extensive mixing of the impeller used to create the larger dope resulted in the breaking up of many of the agglomerates. Unlike the syringe extrusions, which were vortex mixed for about a minute before polymer was added, in the case of the larger scale dopes the sorbent dispersion was allowed to mix for 2-3 hours to allow the very large agglomerates (>100μm as observed by the eye) to break up. This was done out of concern over the spinnability of the dope, as very large agglomerates can (and did) introduce abnormal flow occurrences in the extruder and filament, but also was likely responsible for some of the agglomerate formation. In terms of optimization, pre-screening the adsorbent agglomerates through one or more sieves to have a consistent agglomerate size reducing the risk to the spinneret may be appropriate. The challenge then is having enough adsorbent agglomerates of the appropriate size to do a full-scale spin.

5.2.3   The Role of PVP in Sorbent Leaching

The second plausible reason for the sorbent leaching experienced in the first dope formulation was the possibility the ratio of polyvinylpyrrolidone to cellulose acetate polymer in the solution was enabling the leaching of the sorbent. PVP is added to fiber dopes primarily as a viscosity enhancer and pore former. Since PVP is water-soluble, adding it to dope allows for some reduction in the amount of cellulose acetate polymer included in the dope, but upon solvent exchange PVP dissolves during the water soak portion of the solvent exchange. For fiber sorbents, the addition of more PVP can be advantageous, as it allows the "solids loading" of the final fiber (**Figure 4-29**) to increase without requiring additional adsorbent particles.

PVP's exact role in the fiber formation process has been probed in the hollow fiber membrane literature, but its effect on solid particles dispersion has yet to be studied (an area of future work discussed in greater detail in Chapter 8.) If the majority of the PVP joins the polymer lean phase, it likely increases the viscosity of that phase, possibly slowing its rate of solvent exchange. We postulate that high PVP/CA fractions in the polymer dope introduce some change in the solvent exchange of the polymer lean phase, which in turn enables the leaching of some fraction of the sorbent particles, illustrated in hypothesis 2 in **Figure 5-14**. Based on the work with sorbent agglomerates (with high PVP fraction) it would also seem that particle size plays some role in the leaching, which helps explain why the elevated PVP fraction was still successful for spinning of UiO-66. Interestingly, in that work, visible sorbent loss was found for MIL-53(Al) particles purchased from Sigma Aldrich. The sorbent loss, in that case, was attributed to poor solvent/water stability of the

adsorbent, but this very well could have been due to the PVP fraction used in the dope preparation.

Syringe extrusions were carried out for fibers with lower PVP fractions, with an example dope composition given in **Table 5-3**. The resulting TGA and N_2 physisorption characterization showed no significant loss of sorbent mass based on the preliminary dope compositions. In syringe extrusions, a maximum sorbent loading of 65% was reached before the gel point was reached in this dope composition. This value is slightly lower than the maximum loading reached in the high PVP dopes (~68%), but the 65% loading was retained in the fiber when the dope contained a reduced fraction of PVP.

Table 5-3. Dope composition and spinning parameters for MIL-101(Cr)-Cellulose Acetate fiber spin with low PVP fraction

Component	Weight Percent in Dope
NMP	65.42
H_2O	8.89
CA	10.68
PVP	4.26
MIL-101(Cr)	10.74
Spinning Characteristics	
Flow Rate (mL/hr)	200
Air Gap (cm)	5
Spinneret temp (°C)	50
Bath Temp (°C)	50
Take-up rate (m/min)	10

Full-scale fiber spinning was carried out using the reduced PVP fraction polymer dope composition given in **Table 5-3**. Scanning Electron Microscopy performed on the resulting MIL-101(Cr)-Cellulose Acetate fibers showed the fibers spun were approximately 600 μm in diameter (**Figure 5-20a**), showing some of the smaller macro voids noted in the higher PVP dope (**Figure 5-10a**). In the low magnification image, a few

20-30 µm sorbent agglomerates were noted in the substructure, and smaller 3-10 µm agglomerates were noted within the sub-structure when zoomed in further (**Figure 5-20b**).
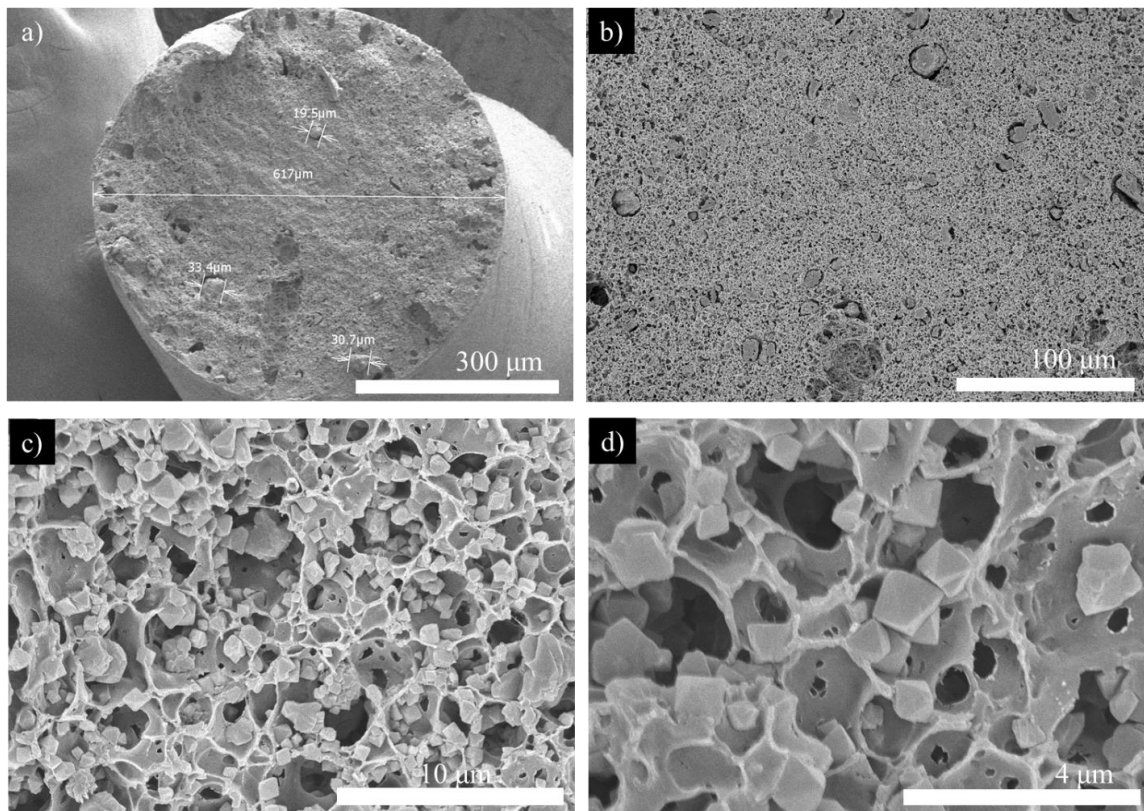
Figure 5-20. SEM images of reduced PVP fraction MIL-101(Cr) fiber sorbents

Further magnifying the images the porous polymer backbone appears to be well-formed in the dope, shown in **Figure 5-20c** and **d**. This is in drastic contrast to the substructure noted in the high PVP fraction dopes (**Figure 5-10b** and **c**), which showed the polymer walls had been decorated to such an extent that the polymer was barely visible. Since the dope compositions had the same ratio of MIL-101(Cr) to cellulose acetate in both cases, it appears as though the reduced PVP fraction in this dope had a significant effect on the kinetics of the formation of pores within the polymer backbone, which seems to have limited the sorbent leaching.

Residual mass analysis and N_2 physisorption, shown in **Figure 5-21**, both confirmed the spun fibers were approximately 50 wt% MIL-101(Cr). Small variations in the loading were noted between states, which may be indicative of some particle agglomerate settling in the dope during the degas step, as the numbering of states corresponded to what time within the spin the fibers were extruded (state 1 was extruded from the top of the syringe pump drum, state 2 further down the pump, etc.). As the TGA and N_2 physisorption do not necessarily agree on this point (State 1's loading per TGA is ~53%, while N_2 comes to 45%), we are confident the fiber did not leach any sorbent.
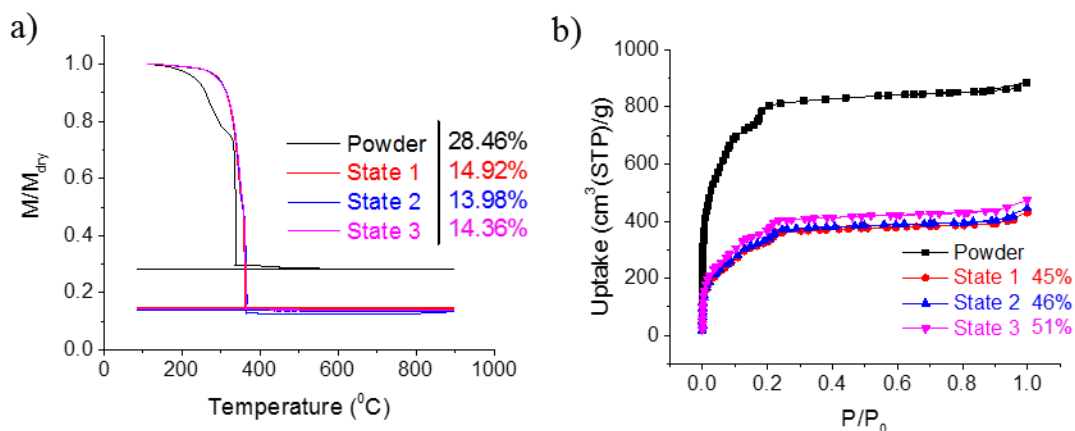
Figure 5-21. Characterization of MIL-101(Cr)- Cellulose Acetate fibers spun with dope composition noted in Table 3. (a)Thermogravimetric analysis (b) N_2 physisorption at 77 K

CO$_2$ physisorption at 243K was performed on the fiber samples as a final check of sorbent performance (**Figure 5-22**). Interpolating the weight loading using the two CO$_2$ sorption isotherms gives an expected MOF loading of 55%, which exceeds slightly the values estimated from residual mass analysis and N_2 physisorption. This overestimation can be accounted for by including the sorption of CO$_2$ onto the surface of the polymer backbone, which, while small, does have a minimal additive effect on the adsorption in the fibers.
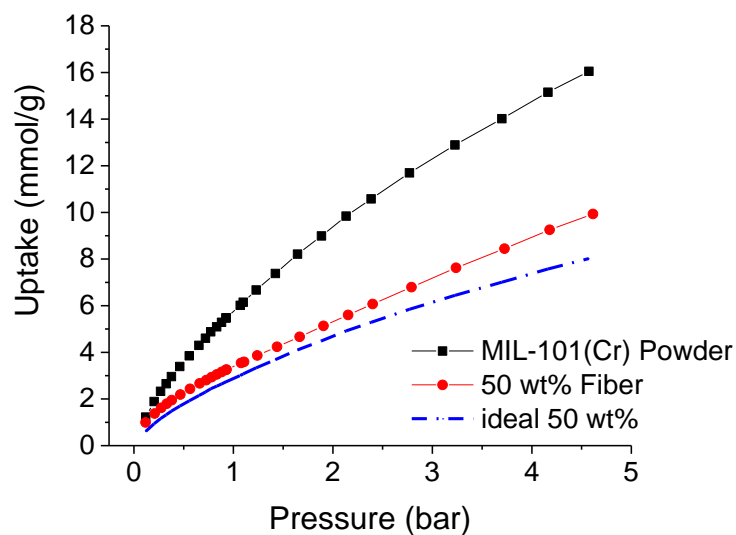
Figure 5-22. CO$_2$ sorption isotherms at 243K for MIL-101(Cr) powder and MIL-101(Cr) fibers produced as part of this work

The fibers manufactured as part of this spin were applied for the work in the remainder of the chapter, and for the preliminary CO$_2$ cycling examined in Chapter 7.

5.3   Dynamic Adsorption Characterization

Fixed bed breakthrough experiments and helium-assisted desorption experiments were performed on the MIL-101(Cr)-Cellulose Acetate fiber sorbents begin to understand the dynamic adsorption performance of the fibers. Within our sub-ambient PSA unit, a variety of operating conditions for adsorptive breakthroughs were considered to provide some insights into the adsorption dynamics within the bed that may be expected before performing actual pressure swing adsorption cycles. Operating pressure, temperature, and flow rate were all varied to observe changes in adsorption dynamics. Helium assisted desorption profiles on fully saturated beds were collected to benchmark an upper ceiling on CO$_2$ capture performance of a PSA unit containing these fibers. Experiments reported in the following section were performed on a 16 inch (40.6 cm long) and 10 inch fixed beds

(0.455 cm in inner diameter) loaded with 28 MIL-101(Cr)-cellulose acetate fibers of average diameter 620μm (~52% fiber packing fraction). The fibers are the same 50-wt% MIL-101(Cr) fibers reported in section 5.2.3.

5.3.1   Fixed Bed Breakthroughs

In performing fixed bed breakthroughs many relevant parameters can be calculated which are useful for beginning to understand the performance of the beds being considered. Two key adsorbent properties are the breakthrough and pseudoequilibrium capacities, approximate values of the amount of gas adsorbed at different points in the experiment. The pseudoequilibrium capacity will ideally match the expected single component or mixed gas uptake of the adsorbate on the adsorbent, while the breakthrough capacity can be used as a proxy for studying the dynamics of the bed. Several other values can be calculated from either single or groups of breakthrough profiles, including values like the front velocity, and degree of spreading of the front.

To ensure accurate comparisons of fixed bed breakthroughs, it is important to confirm that the mass transfer front through the bed is fully developed. If the front has not reached a fully developed state the mass transfer front will appear sharper for the longer of the two beds, as when the bed is near isothermal the typical final kinetic action holding up the front development will be the so-called "self-sharpening" behavior[15-16]. **Figure 5-23** shows the fixed bed breakthroughs of two beds of different lengths, performed at identical flow rates, pressure, and temperatures. In **Figure 5-23a** we first can observe the Helium tracer breakthroughs nearly perfectly overlap until the onset of roll-up. This typically is a good sign that the mass transfer front is fully developed, as Helium will capture most of

the mass transfer development, except for sorbent specific development (like self-sharpening).[13] The two CO_2 fronts follow the expected trend in breakthrough time, with the longer bed which contains more sorbent mass breaking through later than the shorter bed. In **Figure 5-23b** the CO_2 fronts are re-plotted normalizing the time axis at the stoichiometric breakthrough time (the time where $C/C_0 = 0.5$, which should indicate the square wave breakthrough time), and we see the two bed's CO_2 breakthrough fronts are nearly identical. The longer beds appear just slightly broader than the shorter beds, which is likely due to a bit of non-isothermal broadening.[17] With the confirmation of fully developed flow in the 10" beds, comparisons of dynamic breakthrough quantities like pseudoequilibrium capacity, front velocity, and degree of front spreading at a variety of conditions could be compared in the 16" beds.
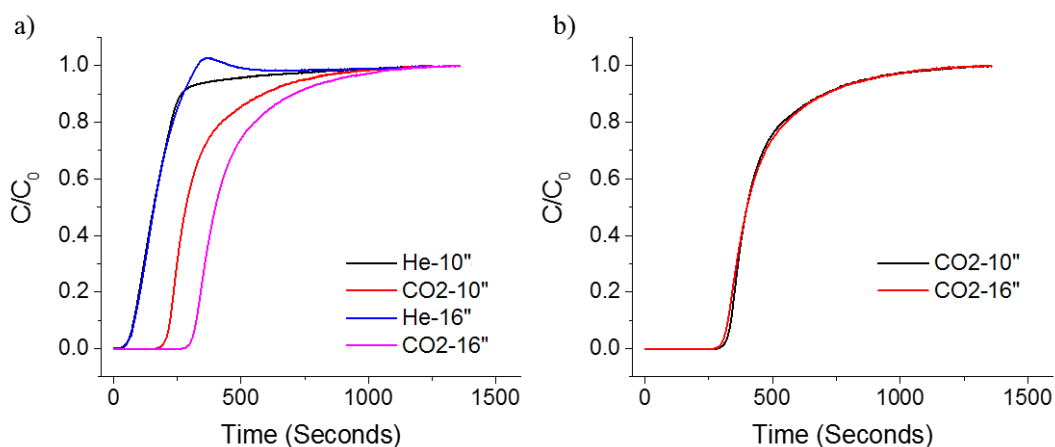
Figure 5-23. Fixed bed breakthrough results of MIL-101(Cr) fiber sorbents, collected at 253 K, 100 sccm flow, 16 bar pressure (a)Comparing breakthrough curves of 10" and 16" long beds, time=0 is taken at the first signal of Helium breakthrough (b) Overlaying CO_2 breakthrough curves of both bed lengths normalizing by stoichiometric time

Breakthroughs collected at progressively cooler temperatures, from 273 K to 243K, are reported in **Figure 5-24**, with only the helium tracer at 273 K included for the sake clarity. The three other helium tracers appeared nearly identical, with a very small amount

220

of broadening occurring between profiles, likely due to a combination of small reductions in fluid velocity and small increases in axial spreading phenomena. The breakthrough times observed in the **Figure** follow the expected trend of more adsorption occurring (later breakthrough) at lower temperatures, corroborated by the breakthrough capacities and pseudoequilibrium capacity trends noted in **Table 4**.
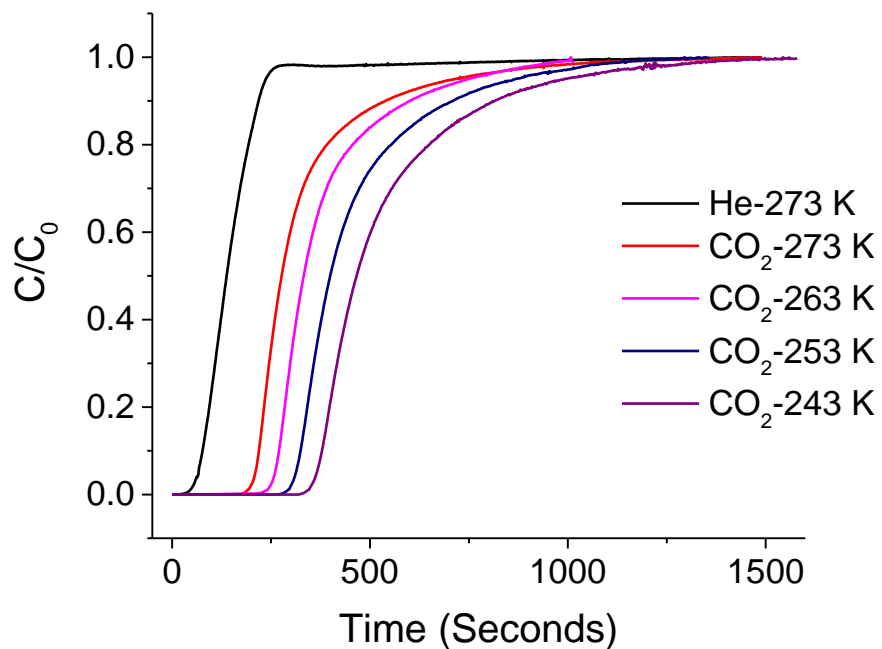
Figure 5-24. Fixed bed breakthrough curves for 16" long beds operating at 16 bar and 100 sccm, varying the operating temperature.

The CO_2 breakthroughs can be replotted normalizing to stoichiometric time and zoomed in to observe the differences formed in the fronts, as shown in **Figure 5-25**.[15] When observing this profile, it is clear that the colder CO_2 fronts result in slightly broader profiles, particularly at 243 K and 253K. With that noted, the calculated degree of spreading of the bed changes decreases only slightly as the breakthrough is operated at different temperatures, indicating the broadening observed in the fronts in **Figure 5-25** is most likely

being driven by the increase in capacity of the sorbent, rather than an increase in the mass

transfer limitations.

Table 5-4. Breakthrough and pseudo-equilibrium capacities, and other breakthrough performance factors of MIL-101(Cr)-Cellulose Acetate fiber beds, at a variety of different operating conditions

Pressure	Temperature	Flow Rate	Breakthrough capacity	Pseudo-equilibrium capacity	CO$_2$ Front Velocity	Degree of spreading
(bar)	(K)	(sccm)	(mmol/ g$_{MIL-101(Cr)}$)	(mmol/ g$_{MIL-101(Cr)}$)	cm/s	(cm)
16	**243**	100	4.25	7.522	0.075	1.86
	253	100	2.22	4.769	0.084	1.73
	263	100	1.68	3.602	0.105	1.73
	273	100	1.16	2.740	0.123	1.74
16	243	**50**	4.23	8.450	0.037	2.22
		100	4.25	7.522	0.075	1.86
		150	4.08	7.757	0.112	1.83
		200	4.10	8.227	0.144	1.77
		250	4.08	7.859	0.189	1.82
		300	3.92	8.446	0.214	1.75
		400	3.71	7.502	0.293	1.73
12	243	100	4.22	6.901	0.094	1.62
16		100	4.25	7.522	0.075	1.86
20		100	4.42	8.184	0.064	2.01
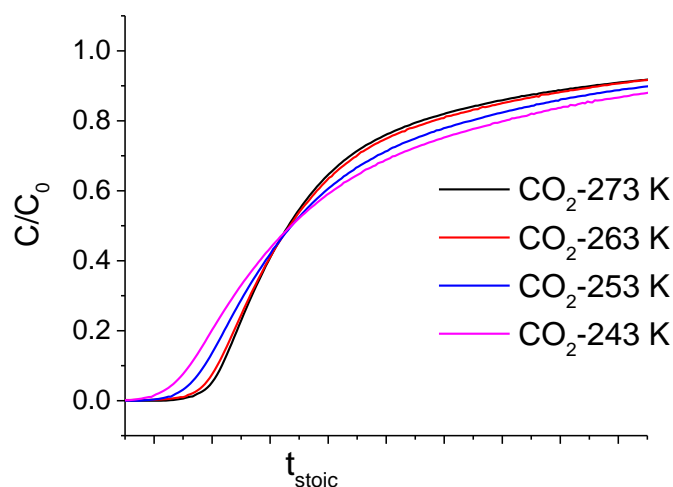
Figure 5-25. CO_2 breakthrough profiles for 16" long beds (16 bar, 100 sccm), showing different temperature results normalized to stoichiometric time

Varying the flow rate of simulated flue gas in the bed can be informative as to the modes of mass transfer present. If fronts are especially spread at low velocities it may indicate some form of external diffusion limitation related to the magnitude of the mass transfer boundary layer. Similarly, reductions in the breakthrough capacity at higher flow rates may indicate the non-isothermal nature in the bed as the heat generation rate in the adsorbent bed will relate directly to the rate at which moles of adsorbent is added to the bed. **Figure 5-26** shows the CO_2 effluent profiles of breakthroughs run at feed rates ranging from 50-400 sccm. As expected, the slower the gas feed rate the longer it takes to break through the bed. By calculating the breakthrough capacities (**Table 4**), we can normalize this effect away and observe how the adsorbent is performing. The breakthrough capacities remained effectively the same regardless of the flow rate, with all capacities falling within 5% of each other, until the fastest flow rate where the breakthrough capacity drops.
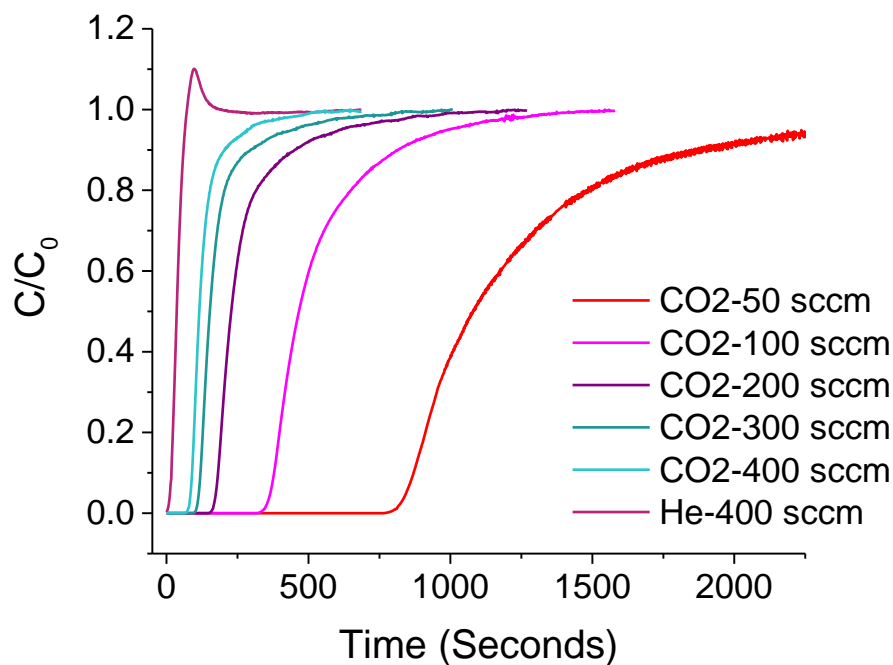
Figure 5-26. Fixed bed breakthrough profiles for MIL-101(Cr) fiber sorbents in 16" beds (243 K, 16 bar), varying the flow rate from 50-400 sccm.

Finally, comparing the breakthroughs across different pressures can offer insight into the effects of varying the superficial velocity over the bed and sorption capacity (**Figure 5-27**). Given a constant volume feed, reducing the operating pressure of the system will result in a more rapid superficial velocity in the bed, similar to changing the feed rate directly as in **Figure 5-26**. Increasing the pressure will also increase the equilibrium uptake of CO_2 within the sorbent, reflected in the pseudoequilibrium capacities noted in **Table 4**. Interestingly, the front spreading increases over a greater range than seen when comparing flow rates or temperatures, though all the degree of spreading values when normalized by the 40.6 cm length of bed show little variation regardless of the parameter changes made.
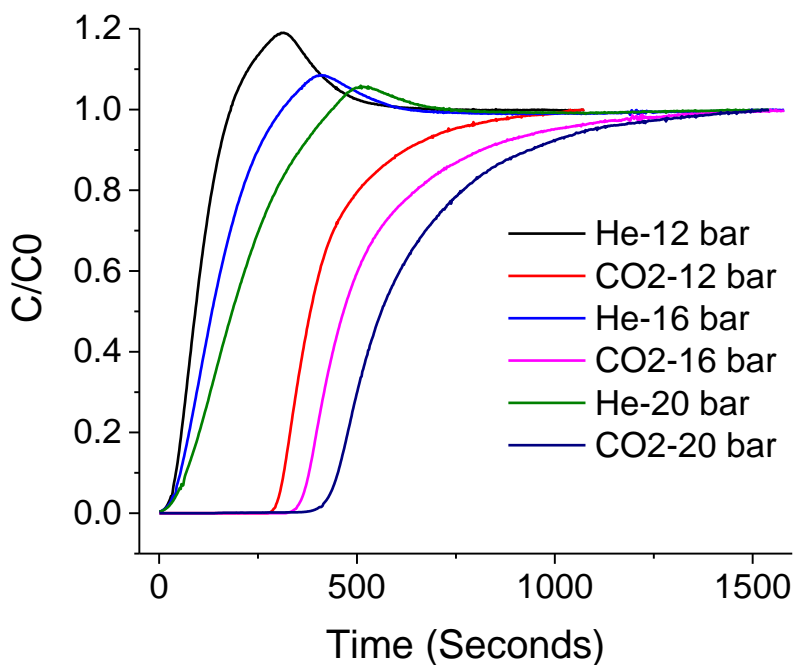
Figure 5-27. Fixed bed breakthrough profiles for MIL-101(Cr) fiber sorbents in 16" beds (243K, 100 sccm), for operating pressures of 12, 16, and 20 bar.

The breakthrough results collected on the MIL-101(Cr) fibers show it is possible to spin these fibers and have dynamic CO_2 capacities that are very large. All breakthrough capacities reported at the 243 K temperature condition exceed the maximum loading of CO_2 possible in Zeolite 13X at equilibrium. From that perspective, these materials show good promise for producing high CO_2 capture productivities, as even when operating in a regime where only 60-70% of the sorbent particles are saturated with CO_2 they are still holding more CO_2 than we would expect at the equilibrium of another state of the art sorbents for CO_2 capture.

5.3.2   MIL-101(Cr) Desorption Performance

Understanding how simulated flue gas desorbs from the bed is equally important to how it adsorbs when considering the design of a pressure swing adsorption cycle. While

performing the cycle is the ultimate experiment, it is possible to probe the composition of the gas in the bed via the collection of desorption profiles. In the pressure swing adsorption process considered for sub-ambient post-combustion CO_2 capture, there are two steps where desorption will occur, first, the blowdown from the operating pressure to near ambient pressure, and second the evacuation of the bed. Both of these steps will be very rapid at bench scale (the blowdown is usually very fast regardless of process scale, as it is effectively a free expansion), but studying each step's desorption in a more controlled approach can be equally insightful.

Helium-assisted desorption experiments were also performed on the same 40.6 cm bed to probe the expected performance of the desorption in the blowdown and evacuation steps. Through sweeping the bed at the feed and ambient pressure (2 bar partial pressure CO_2 and 1 bar overall pressure respectively), it is possible to observe what may be the upper ceiling of purity of the products of the PSA system. In the real PSA, it is likely the bed would not have broken through completely in pursuance of high CO_2 recoveries, but observing what that gas composition could look like in both the blowdown and evacuation products may offer some insight into actual cycle design.

The collection of the desorption profiles in this experiment resulted in an affluent profile containing a plug of the CO_2 and Nitrogen displaced and desorbed by the helium. The effluent profile of the desorption experiment carried out at elevated pressure is given in **Figure 5-28**, with the helium concentrations removed **Figure 5-28a** and the CO_2 and N_2 profiles normalized to observe the apparent purity of the plug **Figure 5-28b**. The fully saturated fiber bed at 14.8 bar will also contain approximately 14.8-bed void volumes of the feed gas (13.5% CO_2, 86.5% N_2), which is the gas that should be removed during the

blowdown step, leaving the higher purity CO_2 behind. This desorption experiment should capture all the gas which leaves the bed during both the blowdown and evacuation steps. Looking at the effluent profiles we note a large plug of CO_2/N_2 mix exiting the bed in the first 150 seconds, which is expected to be made up of primarily this feed composition. Since the sweep rate is relatively slow, the sorbed CO_2 does still desorb, which is observed from about 30 seconds to 400 seconds in the profile. If we assume the gas flow rate out of the bed is the same as the flow into the bed, we can approximate the composition of the blowdown and evacuation products combined by calculating the integrals of their respective effluent profiles, and then taking the ratio of the two. Calculating for the first 600 seconds of the plugs exit from the bed the purity of the blowdown and evacuation of the fully saturated bed is found to be about 31% CO_2. This value seems fairly reasonable, as the blowdown will be a fair amount of volume of gas at basically a slightly purified feed condition (due to any very rapid desorption of CO_2), and the rest of the product should be higher purity CO_2 captured during the evacuation step.
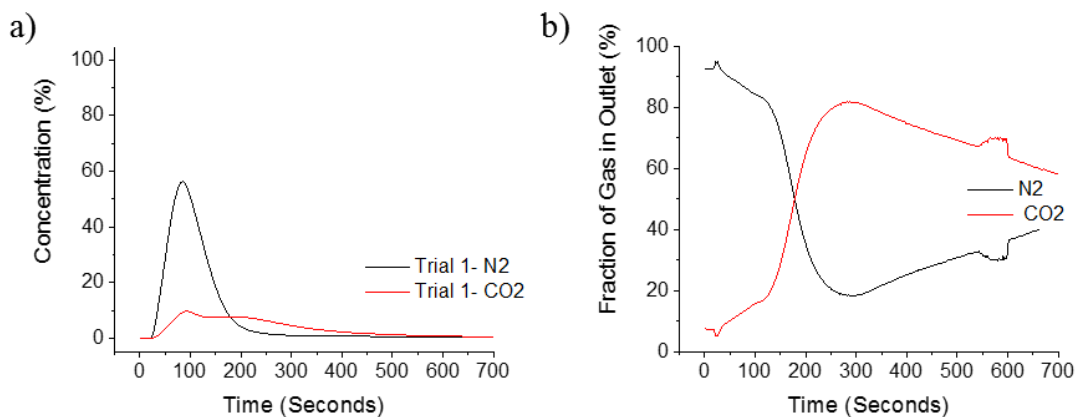
Figure 5-28. Helium-assisted desorption profile for co-current blowdown at 200 sccm, 243K, and 14.8 bar pressure (a) Mole fraction of effluent as a function of time with Helium profile removed (b) Mole fraction of blowdown effluent versus time profile after normalizing away the Helium.

The behavior of the evacuation step alone can be probed similarly if the countercurrent blowdown step is carried out via the venting of the bed before starting the desorption experiment. The effluent profiles of this helium assisted desorption at ambient pressures are given in **Figure 5-29**. What stands out immediately when observing the profiles is the significantly larger area of the CO_2 adsorbate profile. Calculating the area similar to that done on the blowdown desorption (using the first 200 seconds), the effluent of the helium assisted desorption was found to be ~75% CO_2 25% N_2. Like the blowdown, this step will be significantly faster in the PSA unit, but reaching purities of 75% in this helium assisted evacuation does show the MIL-101(Cr) is selectively capturing CO_2 from the gas.
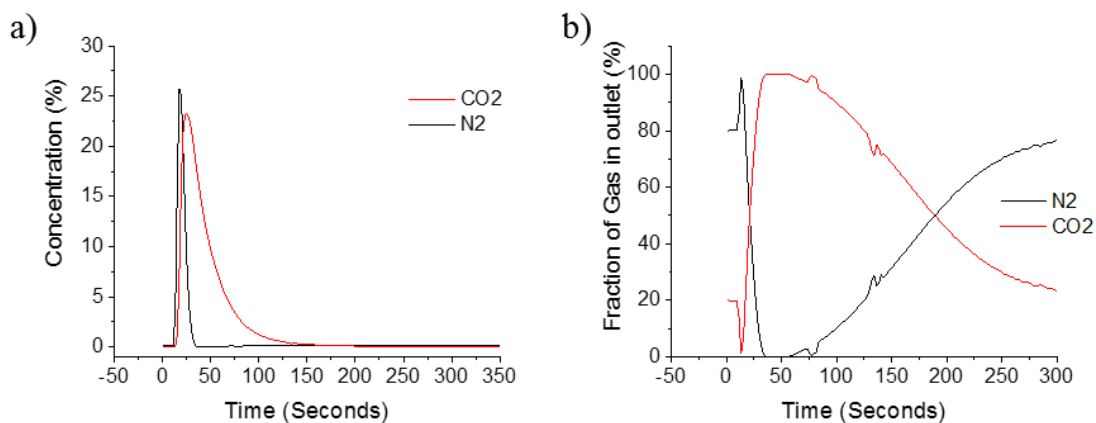
Figure 5-29. Helium-assisted desorption profile for co-current evacuation 200 sccm, 243K, and 1 bar pressure (a) Mole fraction of effluent as a function of time with Helium profile removed (b) Mole fraction of blowdown effluent versus time profile after normalizing away the Helium

Comparing the areas of the CO_2 effluents between the two profiles may offer some insight into the apparent recovery we may expect of the CO_2 which does not pass through the beds. Looking at these two values, the CO_2 effluent profile area was approximately 33% of the CO_2 effluent in the simulated blowdown. This is an exceptionally low recovery for CO_2 capture and may indicate the kinetics of desorption of CO_2 is so fast that much of the CO_2 is being lost in the blowdown product. Improvements in recovery will come about with more complex cycle designs, to be discussed in more detail in Chapter 7, in general, rapid desorption kinetics are desired in PSA units to allow for faster cycling.

5.4   Summary

This chapter presented two methods of spinning fiber sorbents when there are concerns over sorbent leaching due to small particle sizes, culminating in the manufacture of 50 weight percent MIL-101(Cr)-Cellulose Acetate fiber sorbents showing the high capacity for CO_2 at sub-ambient conditions. High polyvinylpyrrolidone concentrations in the polymer dope were determined to be enabling the leaching of MIL-101(Cr) sorbent

particles into the solvent exchange bath during fiber spinning. The role of PVP in the phase

inversion process of fiber sorbent materials remains an area for further study. The spinning

of agglomerates in dopes with high PVP fraction showed promise at smaller scales, but the

full-scale spinning of sorbent agglomerates remains an area requiring further optimization,

particularly in the management of agglomerates during dope preparation. Produced fibers

showed no leaching, and very high breakthrough and pseudo-equilibrium capacities, as

anticipated of MIL-101(Cr)'s a large capacity for CO_2 at sub-ambient conditions. Probing

the desorption of CO_2 from fully saturated beds showed CO_2 purities as high as 75% could

be attained in fiber beds, but concerns exist over the amount of CO_2 desorbing as part of

the blowdown step as compared to the evacuation step.

5.5   References

1.   Park, J.; Lively, R. P.; Sholl, D. S., Establishing Upper Bounds on CO_2 Swing Capacity in Sub-Ambient Pressure Swing Adsorption via Molecular Simulation of Metal-Organic Frameworks. *Journal of Materials Chemistry A* **2017**.

2.   Férey, G.; Mellot-Draznieks, C.; Serre, C.; Millange, F.; Dutour, J.; Surblé, S.; Margiolaki, I., A Chromium Terephthalate-Based Solid with Unusually Large Pore Volumes and Surface Area. *Science* **2005,** *309* (5743), 2040-2042.

3.   Bhattacharjee, S.; Chen, C.; Ahn, W.-S., Chromium terephthalate metal–organic framework MIL-101: synthesis, functionalization, and applications for adsorption and catalysis. *RSC Advances* **2014,** *4* (94), 52500-52525.

4.   Hong, W. Y.; Perera, S. P.; Burrows, A. D., Manufacturing of metal-organic framework monoliths and their application in CO_2 adsorption. *Microporous and Mesoporous Materials* **2015,** *214*, 149-155.

5.   Llewellyn, P. L.; Bourrelly, S.; Serre, C.; Vimont, A.; Daturi, M.; Hamon, L.; De Weireld, G.; Chang, J. S.; Hong, D. Y.; Hwang, Y. K.; Jhung, S. H.; Ferey, G., High uptakes of CO_2 and CH_4 in mesoporous metal-organic frameworks MIL-100 and MIL-101. *Langmuir* **2008,** *24* (14), 7245-7250.

6.   Trung, T. K.; Ramsahye, N. A.; Trens, P.; Tanchoux, N.; Serre, C.; Fajula, F.; Férey, G., Adsorption of C5–C9 hydrocarbons in microporous MOFs MIL-100(Cr) and

MIL-101(Cr): A manometric study. *Microporous and Mesoporous Materials* **2010,** *134* (1), 134-140.

7.   Zhao, T.; Jeremias, F.; Boldog, I.; Nguyen, B.; Henninger, S. K.; Janiak, C., High-yield, fluoride-free and large-scale synthesis of MIL-101(Cr). *Dalton Transactions* **2015,** *44* (38), 16791-16801.

8.   Ye, S.; Jiang, X.; Ruan, L.-W.; Liu, B.; Wang, Y.-M.; Zhu, J.-F.; Qiu, L.-G., Post-combustion CO_2 capture with the HKUST-1 and MIL-101(Cr) metal–organic frameworks: Adsorption, separation and regeneration investigations. *Microporous and Mesoporous Materials* **2013,** *179*, 191-197.

9.   Raj, M. C.; Senthilkumar, S.; Somani, R. S.; Bajaj, H. C., Preparation, characterization and hydrogen sorption study of MIL-101(Cr) pellets. *International Journal of Environmental Studies* **2016,** *73* (3), 357-368.

10.   Furukawa, H.; Cordova, K. E.; O'Keeffe, M.; Yaghi, O. M., The Chemistry and Applications of Metal-Organic Frameworks. *Science* **2013,** *341* (6149), 1230444.

11.   Carter, E., Stability of MIL-101(Cr) in Acid Gas Environments. 2020.

12.   Chen, G.; Koros, W. J.; Jones, C. W., Hybrid Polymer/UiO-66(Zr) and Polymer/NaY Fiber Sorbents for Mercaptan Removal from Natural Gas. *Acs Applied Materials & Interfaces* **2016,** *8* (15), 9700-9709.

13.   Lively, R. P. Hollow Fiber Sorbents for Post-Combustion CO_2 Capture. Georgia Institute of Technology, 2011.

14.   Lively, R. P.; Chance, R. R.; Kelley, B. T.; Deckman, H. W.; Drese, J. H.; Jones, C. W.; Koros, W. J., Hollow Fiber Adsorbents for CO_2 Removal from Flue Gas. *Ind. Eng. Chem. Res.* **2009,** *48* (15), 7314-7324.

15.   Ruthven, D. M., *Principles of Adsorption and Adsorption Processes*. Wiley: New York, 1984.

16.   Ruthven, D. M.; Farooq, S.; Knaebel, K. S., *Pressure Swing Adsorption*. VCH Publishers Inc: New York, NY, 1994.

17.   Ruthven, D. M.; Rojo, J. C., A simple model for a nonisothemral adsorption column. *Canadian Journal of Chemical Engineering* **1990,** *68* (5), 795-798.

CHAPTER 6.   MANUFACTURE OF THERMALLY

MODULATED FIBER SORBENTS

A significant challenge facing the application of adsorbents to sub-ambient CO_2 capture will be minimizing and managing the deleterious effects of sorption enthalpy on the performance of the system. Managing heat will be especially necessary when working at the high productivities desired, as the flow rates required will lead to significant thermal swings. While work has been done to allow for heat management in the fiber morphology through augmentation or utilization of the fiber bore, an alternative which simplifies the manufacturing process considerably would be desirable. The work described here details the first of a kind production of novel fiber sorbents containing both sorbent particles and microencapsulated phase change material within a fiber. The intimate contact between the phase change material and sorbent particles inside the fiber should allow for internal, passive control of the sorption enthalpy released during the adsorption-desorption process, making for more efficient sorption dynamics. The reduced effect of heat generation on the breakthrough profiles will lead to more sorption occurring prior to breakthroughs. After proof-of-concept spinning of composite fibers, dynamic column CO_2 breakthrough experiments operating at sub-ambient conditions and elevated pressures reveal the effects of heat management on the sorbent's dynamic performance. Dynamic column breakthrough capacities at low sorbate leakage are compared between fibers with and without temperature relevant phase change material included to demonstrate the effect of thermal management. The benefits of the intimate contact between the sorbent and phase change material are probed in near-isothermal small diameter beds, while larger diameter

beds illustrate how the microcapsules can manage effectively heat generation in conditions closer to an adiabatic regime, typically found in industrial-scale adsorption-based processes, e.g., PSA/VSA.

6.1   Characterization of Sorbents and μPCM

Sub-ambient CO_2 isotherms of UiO-66 were collected using a high-pressure volumetric analyzer at a variety of temperatures, shown in **Figure 6-1**. Isotherm collection was carried out between 0.2 and 5 bar using pure CO_2 at the desired temperature. After each isotherm was collected, the sample was reactivated at 200 °C for 6 hours under dynamic vacuum to remove adsorbed CO_2.
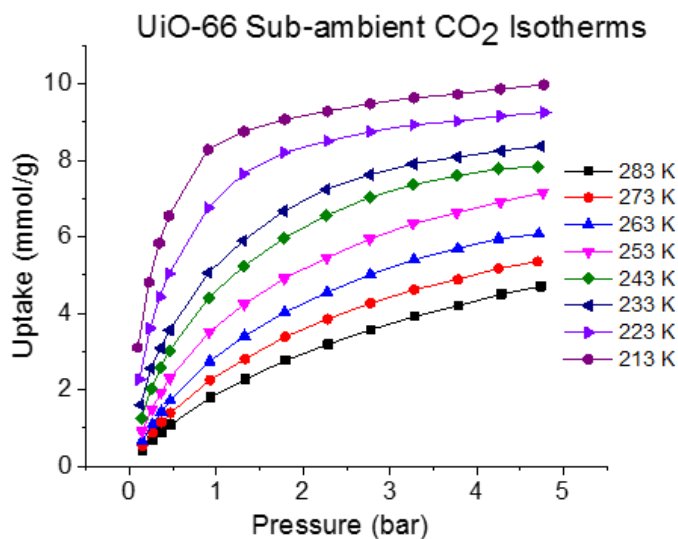
Figure 6-1. UiO-66 Sub-ambient CO₂ Isotherms

The as-delivered μPCM particles were spherical with a polydisperse size distribution and a maximum diameter of ~20μm, as illustrated in **Figure 6-2**. This size is on the high end of the desirable size of insoluble additives for fiber spinning, as much

larger sizes has been known to lead to some clogging of the spinneret. In the long run the polydispersity may be desired, as it could allow for more efficient packing of the spherical particles within the polymer matrix at high loadings.

20 µm
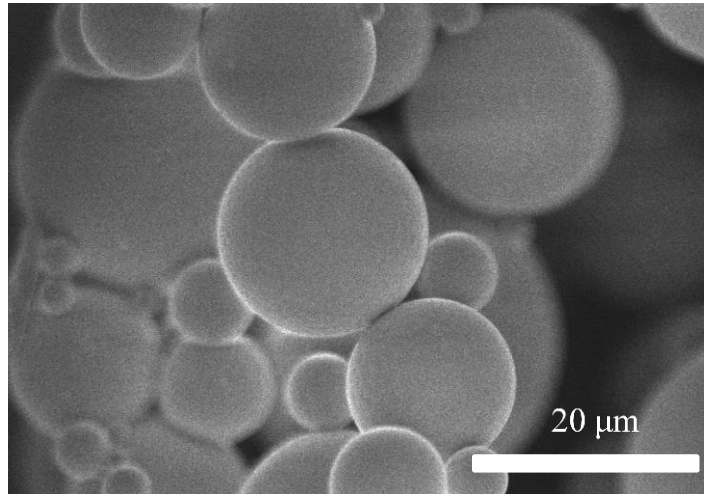
Figure 6-2 SEM image of microencapsulated phase change material

DSC analysis on the as-delivered sub-ambient µPCM allowed for calculation of a heat of fusion of 148±5 J/g, as shown in **Figure 6-3a** (error estimate is the range of values determined by different DSC experiments). This value is near the expected value of 150 J/g reported by the distributor, and was deemed appropriate for the experiments to follow. While the melting performance itself is suitable, it is interesting to note the freezing and melting behavior are a bit more complex than one might expect. Typically freezing and melting temperatures are believed to occur at a single, consistent temperature, but in the case of these microencapsulated phase change materials the freezing (upper curve, read from left to right) appears more complex, with a humped sort of profile.[1] The melting profile, meanwhile, appears to occur more in a single step. Since the mixture is not a single pure component, the freezing and melting behavior becomes more complex, similar to what

we are observing. Alternatively, this behavior could be an artifact for the DSC profile, as heat transfer limitations of the sample pan will also impact the shape of the profile.

In an effort to limit those transport limitations, a second profile was collected on the as delivered sample, this time with a significantly slower ramp rate (0.1 C/min), shown in **Figure 6-3b**. From this profile it is clear there are multiple distinct freezing points of the material (one around -30°C, one around -33°C, and one around -37°C, while the melting profile remains a single portion, with a temperature onset around -32°C, and peak around -29.5°C. As finding a perfect pure material with the exact correct melting point for an application will be rare, this behavior, while not desired, was not expected to greatly impact the ability of the material to modulate performance.

a)

b)
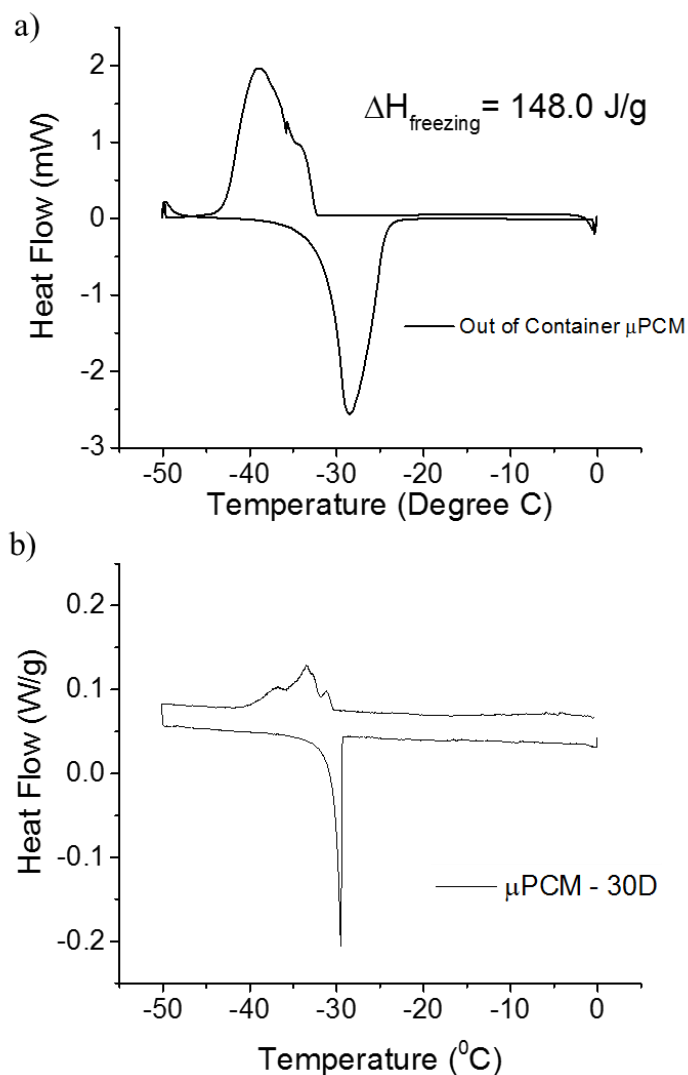
Figure 6-3. Differential Scanning Calorimetry Profiles for microencapsulated PCM used in this work a) 5 C/min ramp. (b) DSC run at 0.1 C/min to diminish conduction resistance for determining optimal breakthrough operating conditions.

A second microencapsulated phase change material, μPCM 28D, was used for control experiments as it had a melting point well above the expected operating conditions of our phase change material. This near-ambient temperature μPCM's DSC profile, shown in **Figure 6-4** shows the same complex freezing behavior as the sub-ambient μPCM, with multiple *peaks* in the freezing behavior, but a very defined single melting point. As this

material was going to be used as a control, the most important parameter we were worried about was the fact it's melting and freezing at temperatures far warmer than our system should ever reach.
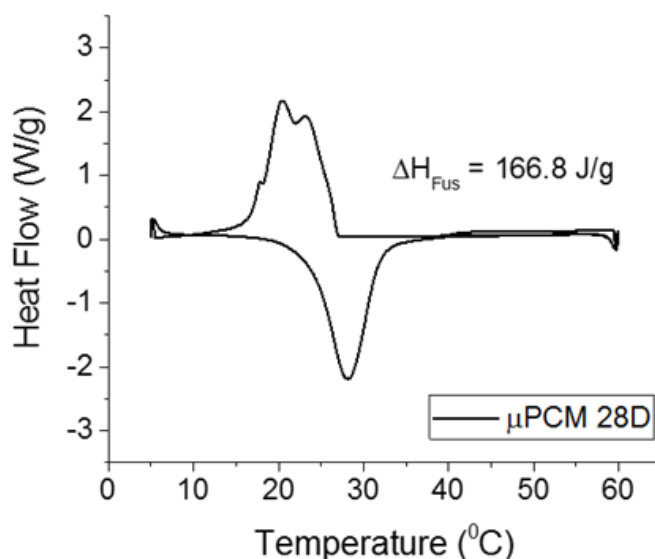
Figure 6-4. DSC profile for MPCM 28D, used as "unmodulating" PCM in large module experiments

6.2 Solvent Stability of μPCM

To spin microencapsulated phase change material into a fiber sorbent contactor, the stability of the μPCM in the spinning solvents had to be confirmed.[2] Microcapsules were exposed to water, NMP, hexanes, and methanol as these solvents would be key to the spinning of the materials. For all solvents, except methanol, differential scanning calorimetry showed no significant loss in capacity indicating the μPCM has good solvent stability. For the methanol exposed samples the heat of freezing remained about the same, though the shape of the profile changed slightly, shown in **Figure 6-5**. The shape of the freezing profile after methanol exposure no longer showed a double humped profile, but rather a single freezing behavior. Since the melting profile remains effectively the same,

just with more spread out heat flow, this is likely an artifact of the packing of the methanol exposed sample in the sample pan, rather than a chemical change of the phase change material. Methanol freezes at -97.6°C, so any methanol left in the system post solvent exchange to water and drying would probably not impact the freezing behavior.
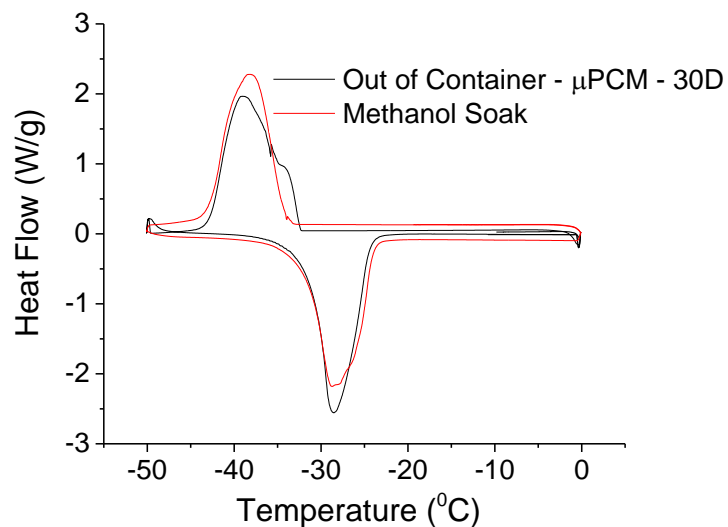
Figure 6-5. DSC analysis comparing methanol soaked MPCM to out of container, both show heat of fusion of approximately 150J/g

SEM analysis on the solvent treated µPCM showed no noticeable structural change due to treatment, A number of the examined microcapsules of the methanol treated µPCM showed structural collapse (**Figure 6-6**). Although the DSC signaled phase change performance was retained, we removed the relatively standard methanol solvent exchange step from the fiber fabrication process (this step is typically included to prevent the collapse of small pores beneath the skin layers of asymmetric hollow fiber membranes). This step appears to be unnecessary for fiber sorbents of cellulose acetate, as the fibers produced in this work exhibit none of the usual signs of collapsed pore structures as a result of avoiding the methanol exchange.
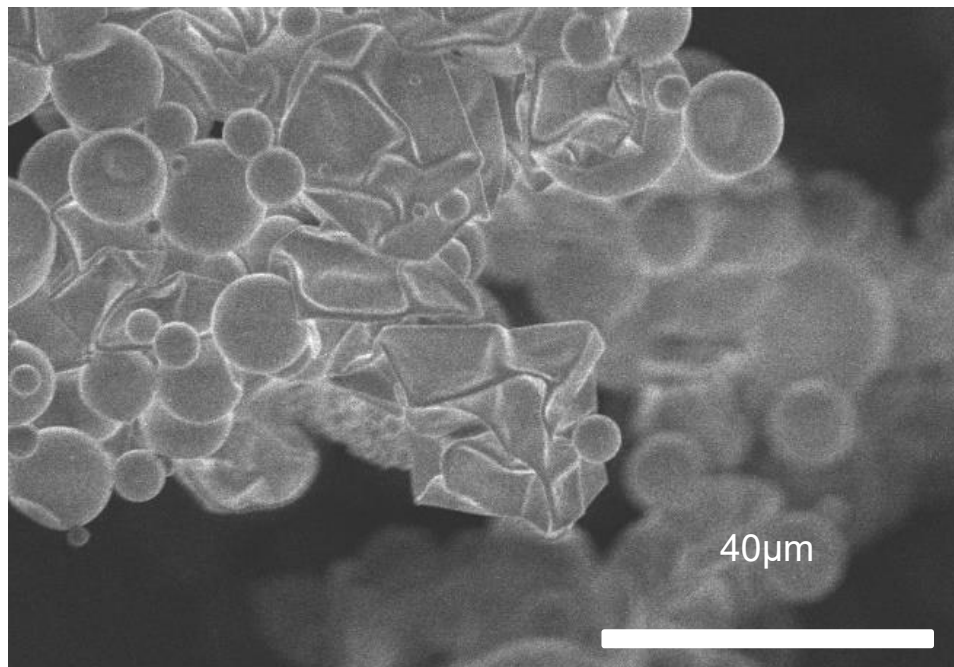
Figure 6-6. SEM image of physical degredation of MPCM-30D when exposed to methanol

6.3 Fiber Spinning

6.3.1 μPCM-Cellulose Acetate Fiber Spinning

In order to confirm the μPCM could be spun into fibers with sorbent, it was first important to confirm the μPCM would survive the spinning process, in the absence of sorbent.[2] Small-scale extrusions of μPCM-loaded spin dopes through a 16-gauge needle were carried out to confirm the survival of the microcapsule under simulated stresses of spinning. SEM micrographs of the fibers produced are shown in the **Figure 6-7a-d**, showing the microcapsule spheres survive the spinning process with little to no change in physical structure of the microcapsules. When targeting 50 weight percent (wt%) μPCM in the fibers (**Figure 6-7a**) the syringe fibers had notable macrovoids, which do not appear in the case of the 75 wt% μPCM fibers. Macrovoids typically can be eliminated from a

dope via increasing the dope's viscosity, so it would make sense that they may be eliminated when moving to higher weight loadings of μPCM. The microstructure of the porous polymer matrix of the 50 wt% fibers, shown in **Figure 6-7c**, appears very porous as compared to that of the 75 wt% fibers (**Figure 6-7**). This is an interest artifact of spinning at very high weight (and volume fractions of non-porous solids).
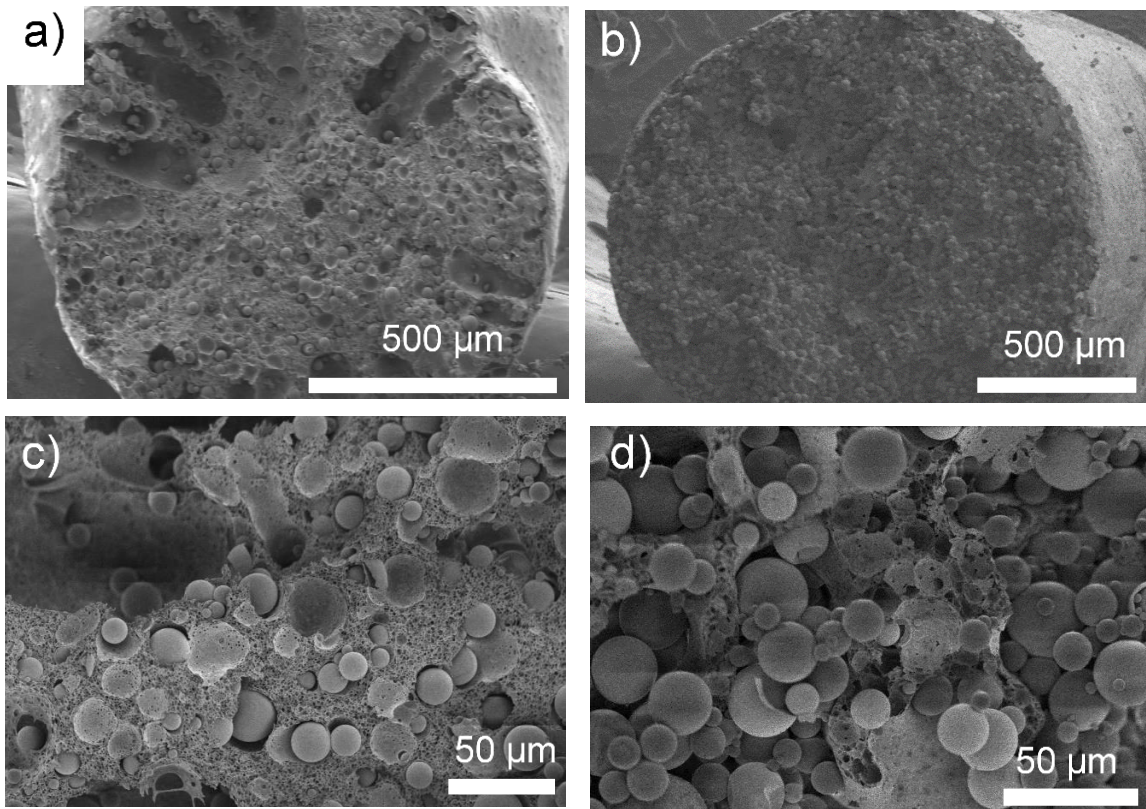
Figure 6-7. SEM images and DSC profiles of Microencapulsated PCM Fibers. (a) Low magnification image of 50 wt% fiber (b) Low magnification image of 75 wt% fiber (c) SEM image of 50 wt% fiber substructure (d) SEM image of 75 wt% fiber substructure

DSC analysis was used to determine the weight loading of the μPCM within the fiber. By taking the fraction of the heat of fusion (determined by integrating the fiber-μPCM DSC curve) relative to the heat of fusion of the neat μPCM. The DSC results for 50 and 75 weight % μPCM syringe fibers are shown in **Figure 6-8** and compare well with the target loadings (i.e., observed loadings of 51.8 wt% and 78 wt% were estimated via DSC).

In both cases the onset temperatures of freezing and melting lag behind that of the neat μPCM. This lag is expected as the fiber has additional thermal resistance due to the polymer matrix, as compared to a pure powder sample.
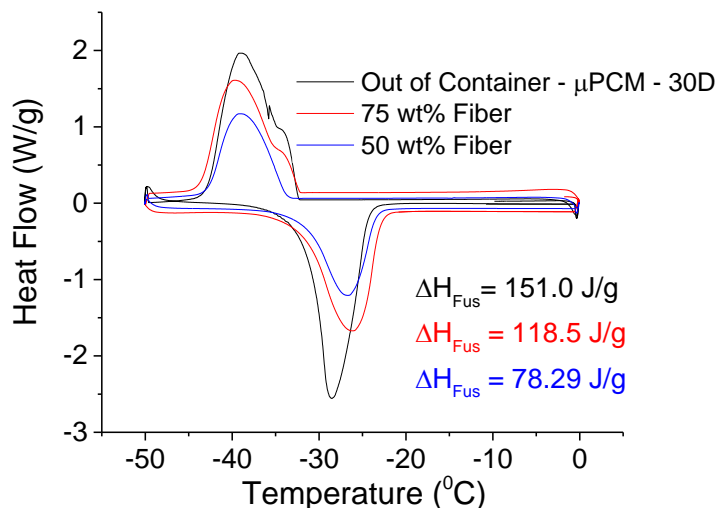
Figure 6-8. DSC profiles comparing out of container uPCM to uPCM fibers (exotherm is up)

6.3.2   Composite μPCM-UiO-66-Cellulose Acetate Fiber Spinning

The μPCM particles were co-spun with UiO-66 to create composite fiber sorbents with localized thermal modulation, with the dope compositions reported in **Table 6-1**.[3] By varying the flow rate of the dope as well as the take-up rate (Table 6-2) fiber diameters ranging from 500-1200 μm were produced. The desired weight fraction of UiO-66 and μPCM in the fiber matrix was set such that all of the heat released upon CO_2 adsorption into UiO-66 at -30 °C (the onset temperature for freezing and melting of the μPCM) could be captured by the heat of fusion of the μPCM. **Figure 6-9** shows the morphological structure of the μPCM-UiO-66-CA fibers spun using the conditions noted in **Table 6-1** and **Table 6-2**. **Figure 6-9a** shows the microcapsules are well distributed throughout the fiber,

241

and the fiber appears to be highly porous. **Figure 6-9b** presents a magnified view of the composite structures, revealing that the MOF crystals are distributed throughout the fiber matrix and importantly adjacent to the phase change material particles. This adjacency is critical for improving heat transfer performance, as it suggests that significant decreases in the thermal resistance of the system relative to other arrangements that would place the sorbent relatively far (i.e., >100 µm) from the PCM.
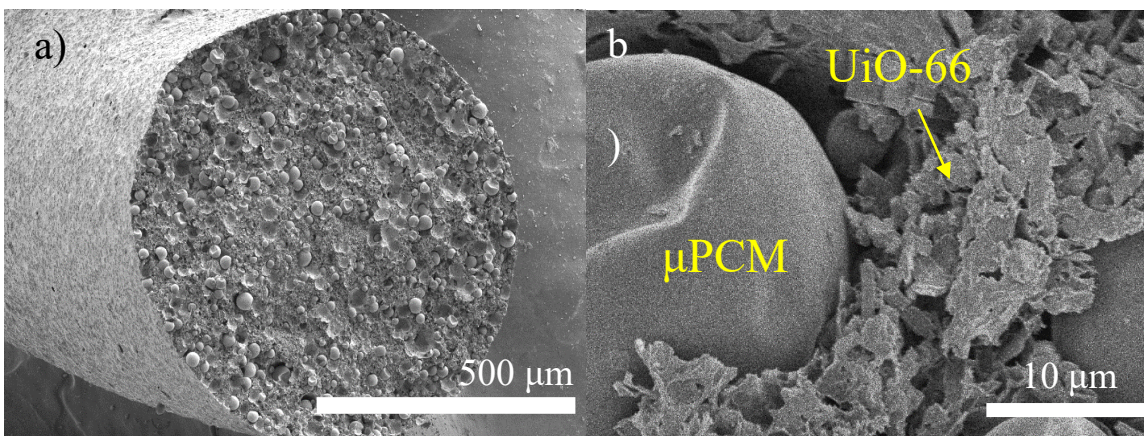
Figure 6-9. SEM images of cellulose acetate fibers containing both µPCM and the MOF UiO-66. (a) low magnification image showing the distribution of µPCM throughout the fiber. (b) magnified image showing the relative location of the two fillers.

Confirmation of fiber sorbent loading was carried out via residual mass analysis performed on the TGA reported in **Figure 6-10a**. Three fiber spin's are compared in **Figure 6-10a**, Unmodulated-noµPCM Fibers (discussed in more detail in section 6.3.3) are fibers loaded with 75 wt% UiO-66 sorbent. The two other states, Modulated and Unmodulated-µPCM Fibers are the two composite fiber states spun containing µPCM -30D and µPCM 28D respectively. The residual mass analysis shows the sorbent loading to be approximately 36% as compared to the pure UiO-66 sorbent, which is very close to the 37.5% expected given the dope composition reported in **Table 6-1**. In both fiber states we

would expect three distinct decompositions, the PCM, the cellulose acetate, and the UiO-66. Interestingly, in the case of the Unmodulated- µPCM fibers, the cellulose acetate and PCM appear to burn off around the same temperature, such that it is difficult to differentiate between the two.

Table 6-1. Dope compositions of fibers spun in this work

Dope Component	Unmodulated -no µPCM (Wt%)	Modulated (Wt%)	Unmodulated -µPCM (Wt%)
CA	7.5	7.7	7.5
PVP	6.0	6.1	6.0
NMP	56.4	57.8	56.6
H2O	7.5	7.6	7.5
UiO-66	22.6	10.4	11.2
µPCM -30C	0	10.4	0
µPCM 28C	0	0	11.2

Table 6-2. Spinning Parameters used in current work

Spinning Characteristics	
Flow Rate (mL/hr)	200-1000
Air Gap (cm)	5
Spinneret temp (°C)	50
Bath Temp (°C)	50
Take-up rate (m/min)	10-30

The weight loading of µPCM in the modulated fibers was confirmed using DSC analysis, shown in **Figure 6-10b**. Like the fibers without any UiO-66 (**Figure 6-8**), there is a reduction in the amplitude of the heat flow peak during freezing and melting, as well as a reduction in the amount of heat required to fully freeze/melt the fibers. The calculated latent heat of fusion of the composite fibers was found to be ~51.2 kJ/mol, slightly lower than the 55 kJ/mol that was expected given the dope composition, though fairly close. Like the µPCM-Cellulose acetate fibers the heat flow throughout the profile ramp at temperatures not within the phase change actually exceeded that of pure material. This is likely due to a combination of factors including the temperature ramp rate and the

differences between the heat capacity and relevant modes of heat transfer of the porous composite fiber and the μPCM powder. As with the μPCM-Cellulose acetate fibers, there is a slight delay in the onset of freezing and melting in the fibers as compared to the powders, due to those same heat transfer differences.
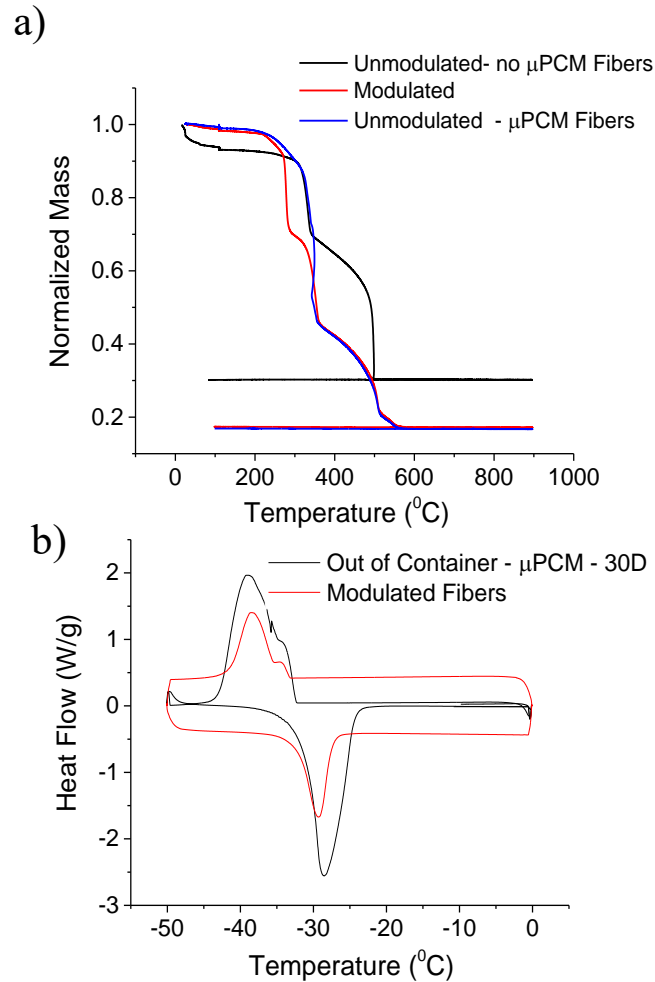
Figure 6-10. Thermogravimetric Analysis performed on different fibers manufactured as part of this work(b) DSC profile of out of container μPCM (black) and Modulated composite fiber

6.3.3   UiO-66-Cellulose Acetate Fiber Spinning

UiO-66-Cellulose acetate fiber sorbents at high (75 wt%) loadings were spun to compare the performance of the "best" adsorbent fiber without thermal modulation to fibers with the microcapsules installed for thermal modulation. SEM images of the UiO-66-Cellulose Acetate fibers are given in **Figure 6-11**. Looking at the fibers, there is good dispersion of the UiO-66 particles, though a number of agglomerates can be noted in **Figure 6-11b** and **c**. These agglomerates were noted in the pure powder as well, and proved very difficult to break up in the polymer dopes. Interestingly, among the particles of UiO-66 there were also a few needle like structures notable. These needles are likely a small fraction of the terephthalic acid linkers which were not completely washed away post-synthesis even with the post-delivery additional washing steps initiated in this work. Fortunately these excess linkers appeared to be negligible in the residual mass analysis reported in **Figure 6-10**, which gives an estimated weight loading of UiO-66 in the fibers of 74.5 wt%, very close to the expected loading based on the dope composition of 75 wt%.
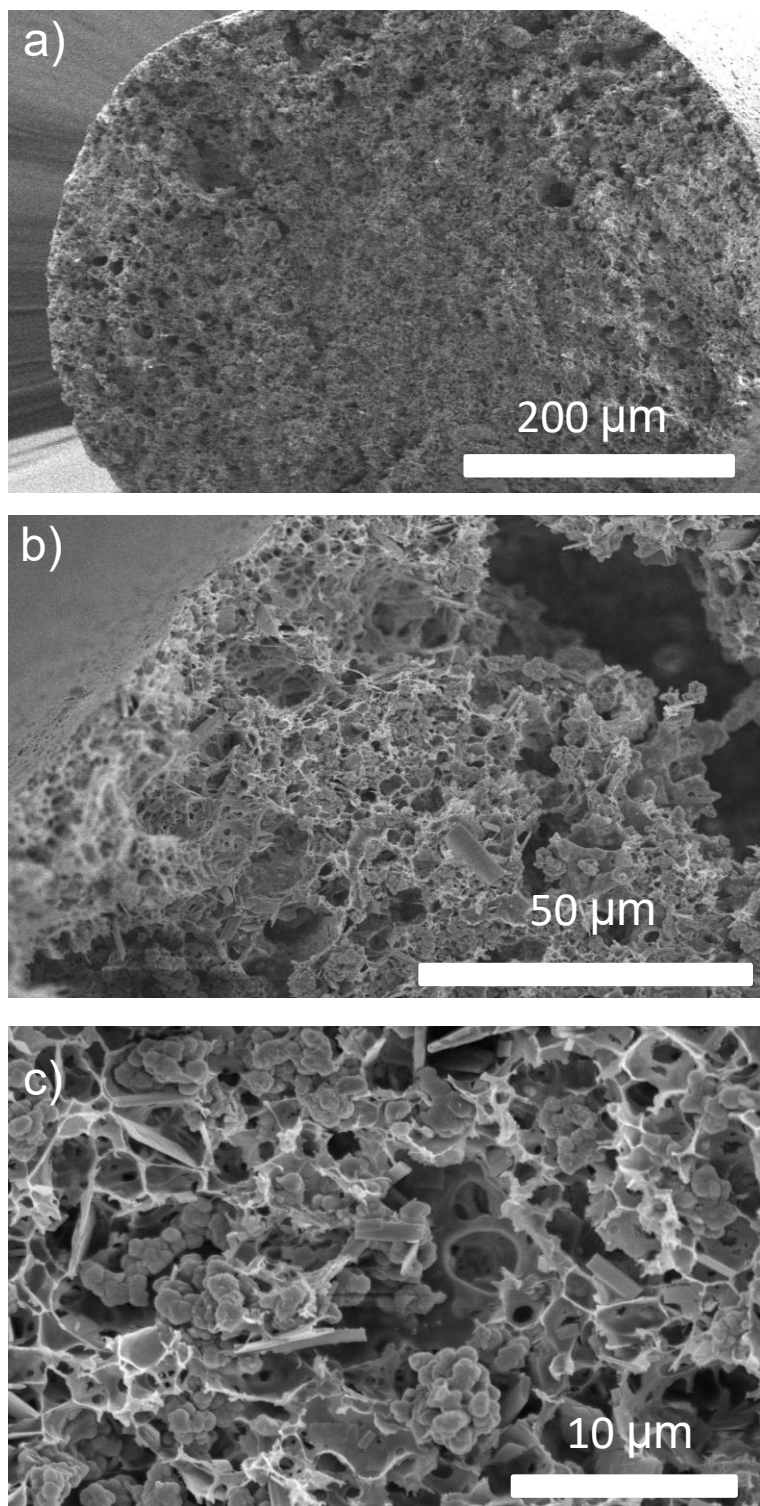
Figure 6-11. SEM images of Unmodulated-no uPCM Fibers (a) Low magnification image of fiber (b) Porous fiber substructure (c) UiO-66 sorbent particles dispersed in polymer substructure

6.4 Fixed Bed Breakthrough Analysis

In the 0.455 cm inner diameter modules fixed bed dynamic breakthroughs were performed and analyzed to probe the effects of phase change material incorporation on sorption dynamics. In these smaller diameter modules, the effects of heat dissipation through module walls tends to dominate the heat effects, thus dampening the magnitude of adsorption-induced thermal excursions in the bed. the heat is rapidly removed from the system through the metal walls of the module, so there is intrinsic global thermal modulation due to the small scales of the experiment. While this effect's importance is greatly diminished at the scales where post-combustion CO_2 capture would require, it does allow for insights to be drawn about more local (internal to the contactor) thermal management. While managing the thermal excursion could be possible with external solutions (like flowing water through a fiber bore), the ability to manage heat locally inside the fiber could be an advantage of working with µPCMs. Study of the µPCM's ability to manage heat fronts within the bed are discussed in more detail in larger beds in Section 6.5.

The CO_2 breakthrough profiles for the "Modulated" and "Unmodulated-no µPCM" fiber sorbents are shown in **Figure 6-12**. As mentioned previously, the "Modulated" fibers were cellulose acetate fibers containing sub-ambient µPCM along with UiO-66 sorbent, while the" Unmodulated-no µPCM" fibers were high weight loading UiO-66-Cellulose acetate fibers. An example breakthrough operated at 16 bar, 200 sccm, and 238 K; is illustrated in **Figure 6-12**. The pseudoequilibrium capacities of the sorbent in the two fiber states were calculated to be ~5.5 $mmol_{CO2}/g_{UiO-66}$, which matches well with the sorption isotherms for UiO-66 at these conditions (**Figure 6-1**). The temperature was selected based

on differential scanning calorimetry of the microencapsulated PCM at a low ramp rate shown in **Figure 6-3b**)**,** where the majority of the freezing behavior occurs prior to 238 K, while the onset of melting behavior occurred around 243 K.

The breakthrough time for the modulated fibers is shorter than that of the unmodulated fibers. Shorter breakthrough time is expected, since the amount of available sorbent in the modulated fibers is only half the amount in the unmodulated fibers, as per the discussion in Section 6.4.[4-5] In fact, if no heat were being managed we would expect the breakthrough time of the modulated fibers to be approximately half the breakthrough time of the unmodulated fibers. Instead the modulated fiber break through at 78 seconds after the appearance of the helium tracer, while the unmodulated fibers break through at ~95 seconds. The influence of the phase change material on sorption dynamics can be confirmed by analyzing the shape of the breakthrough profiles, which will be sharpened by local containment of sorption enthalpy. We confirmed an 80% sharper CO_2 breakthrough (slope of CO_2 breakthrough calculated at $C/C_0=0.5$, where C is the effluent concentration and C_0 is the inlet concentration respectively) in the case of the modulated fibers.[4]
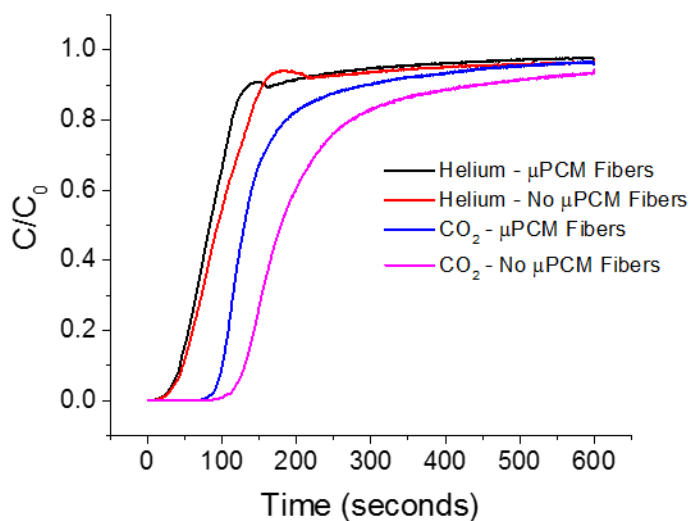
Figure 6-12. CO₂ breakthrough profiles collected for "Modulated" and Unmodulated-no µPCM" UiO-66 fiber sorbents. Profiles were collected at 238K, 16 bar total pressure, and 200 sccm (mL/min) flow rate. Profiles were smoothed using a 5 point Savitzky-Golay method in Origin Pro 2016

Similar breakthrough profile comparisons collected at other flow rates and temperatures were collected. As the heat generation rate within the adsorbent bed scales directly with the flow rate (more moles of CO_2 enter second at higher flow. The differences in CO_2 breakthrough capacities in the modulated and unmodulated cases at 5% leakage ($C/C_0=0.05$) are a useful probe to capture the dynamic performance of the adsorption bed. **Figure 6-13** highlights the breakthrough capacities calculated at 5% CO_2 leakage for both modulated and unmodulated without PCM fibers normalized by the MOF loading over the range of tested flow rates at two temperatures: one near the melting point of the µPCM, and the other away from it.

When operating at 228 K—a temperature requiring large local thermal excursions to reach the melting conditions of the phase change material—no increase in sorbent CO_2 capacity at 5% leakage is noted (Fig. 5a). In these small diameter beds, the similar capacities are indicative that rapid heat dissipation through the walls is not allowing the

fibers to reach the elevated temperatures required to melt the PCM (15K heating locally would be necessary). With the heat being removed before the phase transition temperature of the µPCM can be reached locally, the two beds operate approximately the same when normalized by the amount of MOF, even with double the amount of adsorbent being present in the no-µPCM case. Also of interest are the effects of varying the flow rate. Flow rates from 100-250 sccm show very similar breakthrough confirming the heat generation rate increases over that range are likely leaving thorough the walls, as there is little to no effect on the actual sorption performance. At 300 sccm there is a slight difference (around 10% improvement in the modulated case) between the two cases, which could indicate some heat management is occurring. The trend does not continue when the heat generation rate is increased to 400 or 800 sccm, where there is again good agreement between the modulated and unmodulated fiber breakthrough capacities.

At 238 K, where the PCM is active with only small local thermal excursions, the breakthrough capacity of the sorbent at 5% gas leakage increases by at least 20% across all flow rates investigated (**Figure 6-13b**). Interestingly the improvement is fairly consistent across all flow rates, where we were originally expecting some effect of heat generation rate changes due to increased flow would lead to more drastic improvements.[4, 6] The same reduction in breakthrough capacity was experienced in the 238 K case as was experienced in the 228 K case. This reduction being consistent across multiple temperatures indicates some other transport effect is leading to front broadening. Most likely the bed is not long enough in this case to reach a fully developed flow condition, so what we are seeing is the *self-sharpening* behavior we would expect given the positive slope of the isotherm has not completely developed in our beds prior to breakthrough[7].

a) Sorbent Capacity at 228 K

b) Sorbent capacity at 238 K
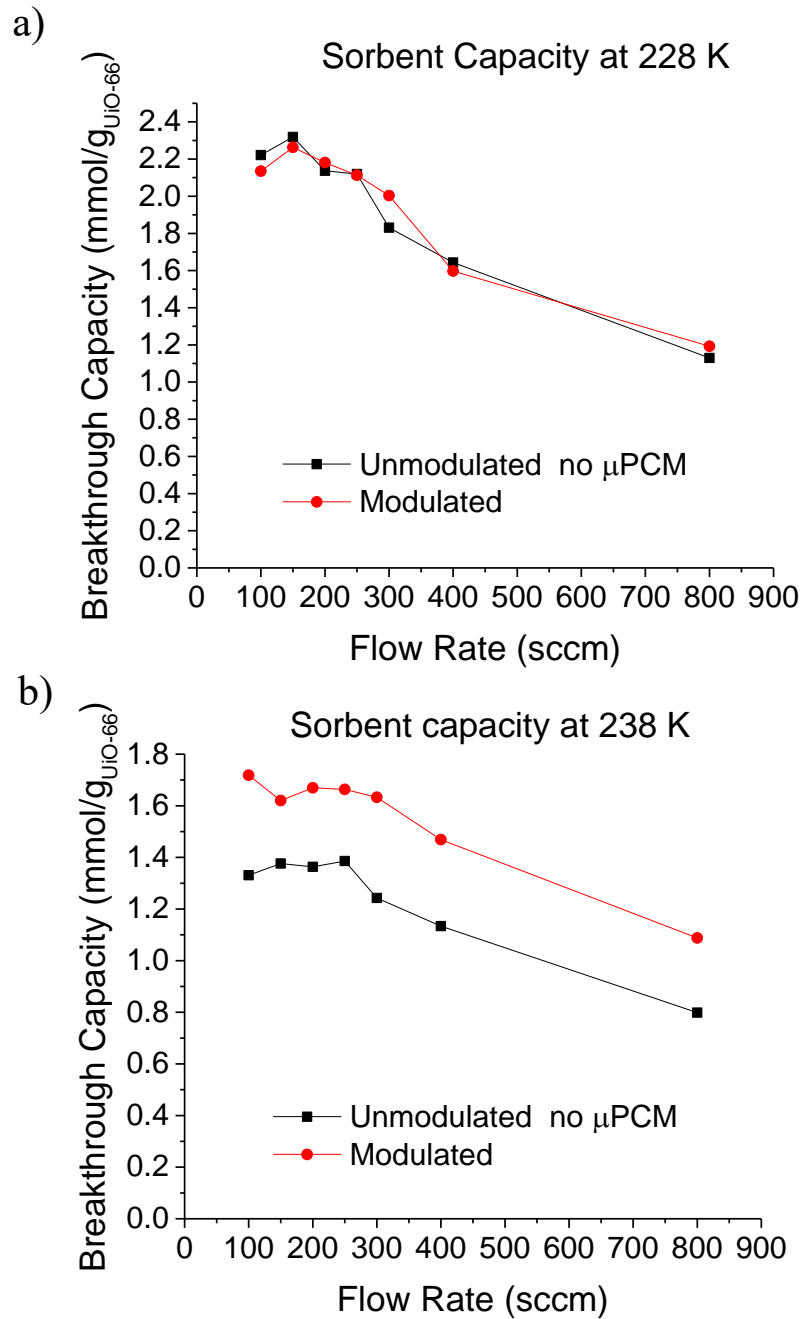
Figure 6-13. Sorbent capacity at 5% adsorbate leakage of fibers containing μPCM as compared to those fully loaded with UiO-66 over a range of flow rates, capacities are normalized per gram of sorbent (a) 228 K, significantly below point (b) 238K, near phase transition temperature

The increase in sorbent capacity at low leakage in the modulated fibers near the phase change temperature, but not at lower temperatures, indicates that the μPCM is capable of capturing locally released heat, improving the sorption dynamics of the system. As the operating temperature moves further from the phase change temperature, the heat of adsorption can be removed effectively via heat dissipation through the module wall, so the phase change material never has the opportunity to be effective. This effect would only be present when the heat transfer distances between the phase change material and sorbent are very short.

6.5   The role of μPCM in Managing Thermal Fronts

6.5.1   Generated Thermal Fronts in beds

The incorporation of phase change material into the fiber sorbent contactor should reduce the amount of heat transferred to the gas phase in the adsorption process. Through the incorporation of an axial thermocouple (**Figure 3-11**) in a larger diameter bed (0.7 cm ID), the temperature profile of different breakthroughs may be collected. Working with the larger diameter was necessary for insertion of the thermocouple. It also helps to reduce the effect of heat leakage through the walls, although it is unlikely with these still small beds we will approach adiabatic like conditions experienced in industrial beds.

The two fiber states used in the large bed operation (Modulated-μPCM and Unmodulated-μPCM) contain approximately the same weight loading of UiO-66 sorbent, but different kinds of μPCM materials, i.e., different phase-transition temperatures. This additional degree of control for comparison was desired in the case further from isothermal

operation of larger diameter modules to isolate the effects of the μPCM more effectively. The use of ambient temperature μPCM in the "unmodulated" case kept the sensible heat of the fibers close to constant in both samples, and the similar loading of sorbent kept the expected equilibrium heat generated by breakthroughs consistent.

Similar experiments to those described in the previous section were carried out with the larger diameter modules, with internal data logging software used to monitor the temperature in the bed. Different velocities and operating temperatures were used to vary the heat generation rate and amount of heat required to trigger the onset of the phase change material.

Example thermal profiles for all three thermocouple points, for modulated and unmodulated fibers, at 100 sccm and 238 K are given in **Figure 6-14**. TC-1 and TC-3, monitoring the temperature at the inlet and exit of the module respectively, while the midpoint of the bed was monitored at TC-2. Comparing the fronts in the modulated and unmodulated cases it appears as though the most heat is generated at the entrance of the bed (TC-1), but is dissipated as the front propagates the bed with TC-2 and TC-3 showing smaller intensity thermal fronts[6-7]. This heat dissipation is more pronounced in the modulated fiber system, where the combination of phase change material and wall leakage effects lead to smaller thermal excursions.
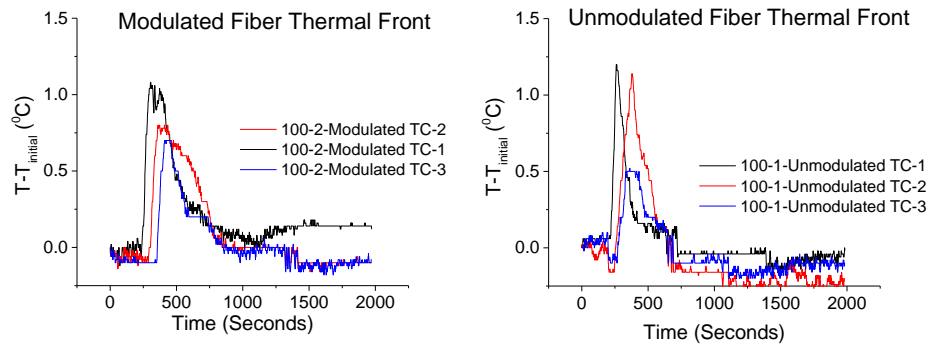
Figure 6-14. Example Thermal responses to breakthroughs in large modules for modulated and unmodulated fibers. TC-1 is at the inlet, TC-2 is at the center, and TC-3 is at the exit of the bed

The temperature at the center of the bed (TC-2) during breakthrough of both the modulated PCM fibers and the unmodulated PCM fibers across five flow rates (100, 200, 300, 400, and 800 sccm) are given in **Figure 6-15**. As the flow rate of gas through the bed increased from 100 sccm to 800 sccm the peak temperature of the gas increased and the thermal wave propagates through the bed more quickly. This behavior was consistent for both Modulated-μPCM and Unmodulated-μPCM fibers, showing the microencapsulated phase change material at current loading was not capable of containing all of the sorption enthalpy produced. Comparing the modulated fibers to those unmodulated at the fastest feed condition, 800 sccm, (**Figure 6-15** inset) the peak amplitude of the thermal wave is approximately 40% in the unmodulated fiber case as compared to the modulated case. Higher peak amplitudes were found across all flow conditions. With near equal weight loading of UiO-66 in both fiber states, "Modulated" and Unmodulated-no μPCM," under identical conditions, if no thermal modulation were present, it would be expected that the thermal profiles.

254
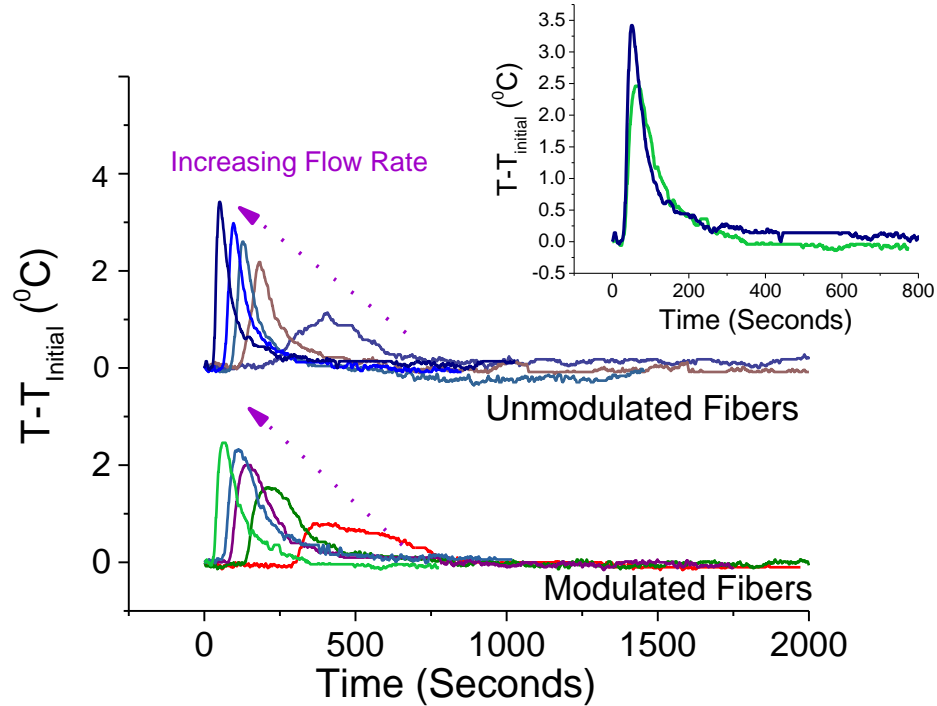
Figure 6-15. Temperature profiles collected at different flow rates from 100-800 sccm, comparing modulated fibers (bottom) and Unmodulated fibers (top). (inset) overlaid comparison of 800sccm flow rate thermal profiles for fibers with (green) and without (blue) thermal modulation.

6.5.2   *Breakthrough Capacity of beds operating further from isothermal*

Since the thermal fronts were collected during the operation of breakthrough experiments, with the only difference being the thermocouple's insertion axially down the center of the bed, we were able to collect and analyze breakthrough profiles to accompany the thermal fronts. The pseudoequilibrium and breakthrough capacities were calculated to see if the same or better improvement in performance would be realized in the less isothermal case. Unlike the case of the small modules, there is a 3-5x improvement in breakthrough capacity in the modulated fibers as compared to the unmodulated fibers (**Figure 6-16b** and **Figure 6-17b**) at both operating temperatures. The pseudoequilibrium capacity per gram of sorbent of the fibers at 228 K remains near identical, indicating, as in

the case of the 238 K experiments, that the sorbent loadings are consistent with expectation. There was significantly more variability in the calculated pseudoequilibrium capacities of the experiments run at 238K, as high as 15% change at different flow rates. We believe this variability comes primarily from the drift in the helium and CO_2 profiles on the mass spectrometer. This drift happened when breakthroughs were run for a prolonged period of time (>2 hours), and resulted in areas (and therefore capacities) being added to the profile which were likely in error.
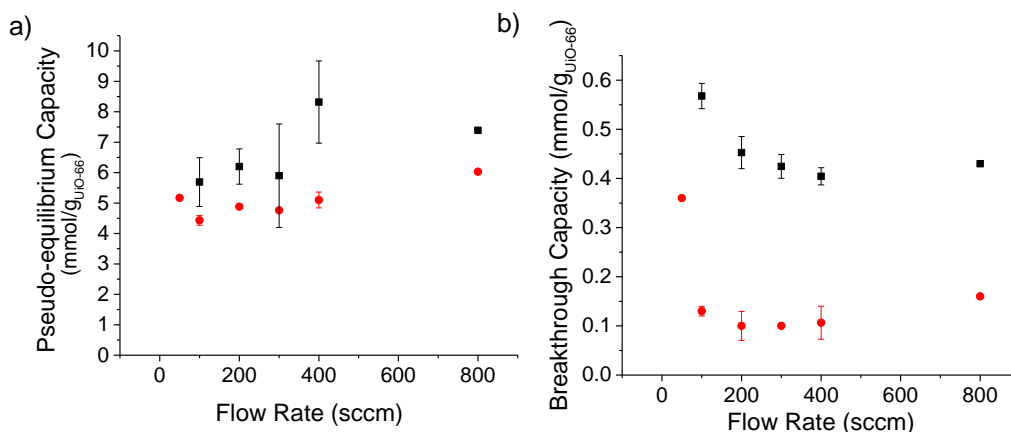
Figure 6-16. Breakthrough and pseudoequilibrium capacities for Modulated- and Unmodulated-μPCM fiber sorbents, normalized by weight loading of UiO-66 in the fiber, at 238 K. (a) pseduoequilibrium capacities calculated at 95% CO_2 breakthrough, (b) breakthrough capacities calculated at 5% adsorbate leakage. Red points are the unmodulated fibers, while black points are the modulated fibers. Error bars are two standard deviations from the mean for experiments repeated at least 3 times.
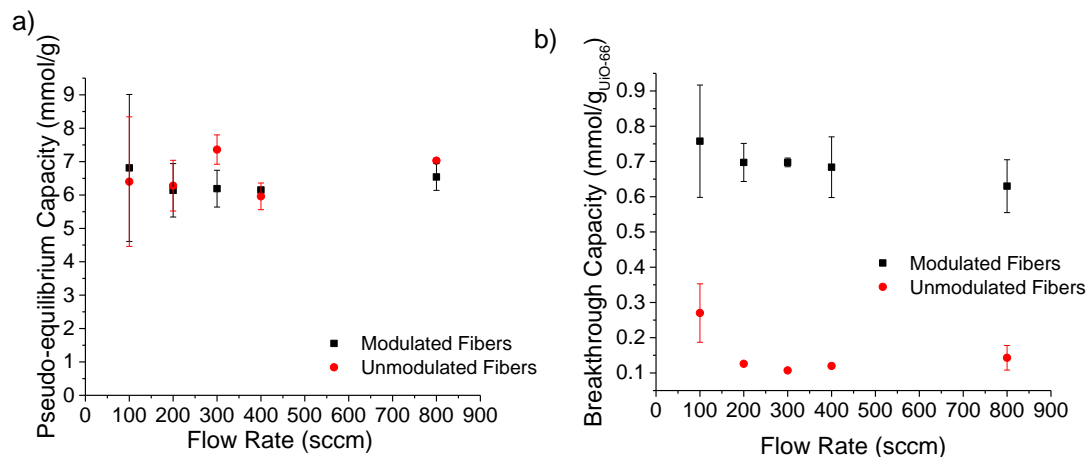
Figure 6-17. Breakthrough and pseudoequilibrium capacities of large modules when experiments are performed at 228 K. . (a) pseduoequilibrium capacities calculated at 95% CO₂ breakthrough, (b) breakthrough capacities calculated at 5% adsorbate leakage. Red points are the unmodulated fibers, while black points are the modulated fibers. Error bars are two standard deviations from the mean for experiments repeated at least 3 times.

It was unexpected to see the 3-5x improvement in breakthrough capacities at both operating temperatures, but perhaps more surprising was the lower breakthrough capacities in general as compared to the values found in the experiments without the thermocouple needle in the module (**Figure 6-13b**). A part of this could be due to the larger heat generation relative to heat leakage through the walls, which we were hoping to study. With that said, the expectation in that case would be to see more improvement in the 238K case, where the beds should be modulating a lot of heat. In the 228K case, the beds would still need to warm more than 10K to begin to see the effects of thermal modulation, so it would be expected to see less improvement.

While heat management is convincingly occurring, as shown in the heat front comparison, additional experiments were designed to see if this behavior was repeatable in similarly sized beds without the thermocouple installed. Two reasons for the drastic performance enhancement were considered most likely to be responsible and so additional

experiments were performed. The first possible reason for the drastically low breakthrough capacities of the unmodulated fibers was that there was some fluid channeling effect occurring in the unmodulated fiber case. If gas were able to bypass the fibers the breakthrough would occur considerably earlier as a fraction of the gas was not interacting with the fiber adsorbent. This would lead to low breakthrough capacities, but similar pseudoequilibrium capacities, as eventually all the fibers would still be saturated. The second possibility was that the concentration front within the bed was not fully developed, leading to a broader than expected front. With this in mind, additional breakthroughs were performed in a 25.4 cm long 0.7 diameter module without the thermocouple installed, which would have similar relative heat effects, but no longer suffer from the possible channeling effects of the thermocouple. The additional length allowed for testing as to whether the concentration front was fully developed.

Figure 6-18 shows the CO_2 breakthroughs at 100 sccm, 238K, and 16 bar of the 15.2 and 25.4 cm long beds, normalized such that time = 0 occurs at $C/C_0 = 0.5$, a method commonly used for determining whether fully developed flow has been reached. Looking at **Figure 6-18**, It can be seen that the longer beds show broader breakthrough profiles, indicating some combination of channeling effects and/or underdeveloped fronts are occurring in the shorter bed.

Direct comparison based on breakthrough capacities between different sorbents when the flow is underdeveloped may cause overestimation of the improvement of heat management in the two beds. Looking to confirm we have a fully developed flow regime, an additional bed, 20.3 cm long was constructed with the same fibers used in the 25.4 cm bed, cutting off the ends of the bed, with the fibers remaining inside the bed. In this case,

258

nearly identical breakthrough profiles after normalizing time were found, indicating those comparisons would be fair to make.

CO$_2$ Breakthrough Profile Comparison
100 sccm flow rate, 238 K, Modulated Fibers

Legend:
CO$_2$ - 15.2 cm
CO$_2$ - 25.4 cm
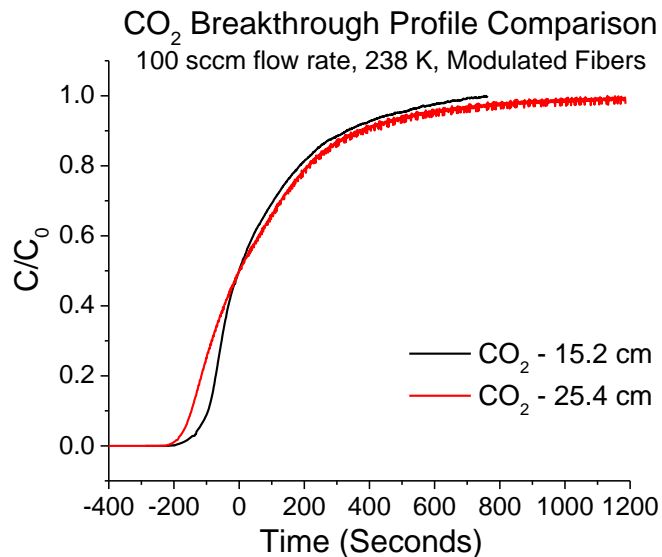
Figure 6-18 CO$_2$ Breakthrough Front comparison between two 0.7 cm diameter beds, (black) 15.2 cm long beds with thermocouple installed (red) 25.4 cm long bed with no thermocouple.

Figure 6-19 compares the pseudoequilibrium and breakthrough capacities across the reported flow rates for these longer beds. While they do not show the very large increase in capacity experienced in the shorter beds, they still show a 20-30% increase in capacity across all flow rates. Pseudo-equilibrium capacities (**Figure 6-19a**) show the relative loadings of UiO-66 sorbent are similar across the two modules, and are far closer than those seen in **Figure 6-16a**) when the thermocouple was installed. Breakthrough capacities show a similar 20-30% improvement to those seen in the smaller diameter beds, with capacity values significantly higher than what was seen in the beds with thermocouples. While there is still the question as to whether the mass transfer front is fully developed in the samples with the thermocouple installed, eliminating the thermocouple and being sure to have. Fully developed flow shows the same sorts of improvements..
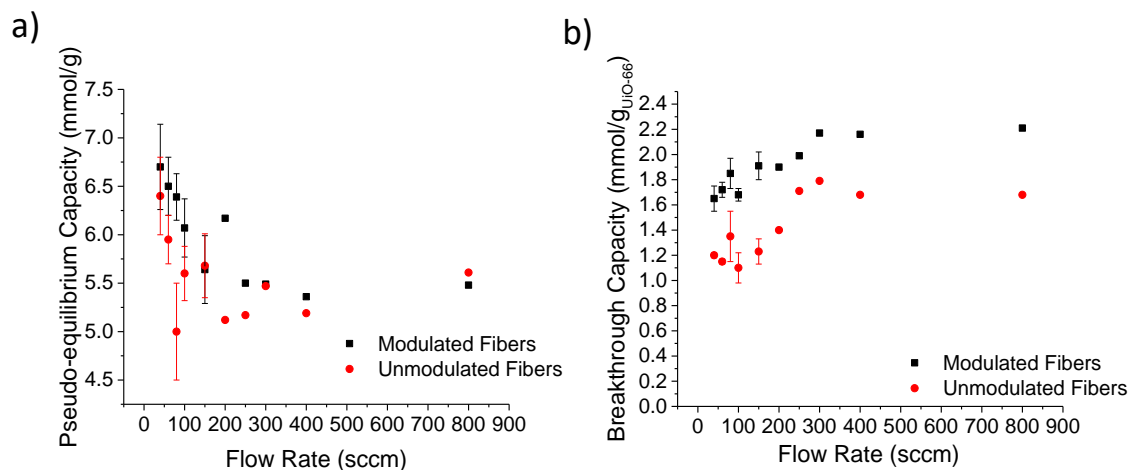
Figure 6-19. a)Pseudo-equilibrium and (b) Breakthrough capacities of 25.4 cm long 0.7 cm diameter modules loaded with "Modulated" and "Unmodulated-µPCM" Fibers at a variety of flow rates. Experiments performed at 238K and 16 bar.

6.6   Summary

Incorporation of phase change material into fiber sorbent systems has been shown to be possible with the incorporation of phase change materials directly into the spinning dope. µPCM-UiO-66 composite fiber sorbents were produced, the first instance of phase change material and sorbent being incorporated simultaneously into a single structured contactor. In this work, the applicability of microencapsulated phase change materials for thermal front modulation was explored and subsequently applied to fiber sorbent contactors for use in the sub-ambient CO_2 capture. µPCM were found to have desirable freezing and melting behavior and required chemical and thermal stability for spinning into fiber sorbent contactors. Dynamic gas breakthrough experiments show an increase in breakthrough time per sorbent mass loading and sharpening of CO_2 breakthrough profiles, as characterized by the sorbent capacity at five percent adsorbate leakage. An improvement of 20-25% CO_2 capacity per gram of UiO-66 was noted. Thermal fronts observed in this study show a reduction in heat released to the flowing gas and peak intensity of thermal fronts when

microencapsulated phase change materials are incorporated into the fiber bed and operate at temperatures near its melting point.

6.7   References

1.   Smith, J. M.; Van Ness, H. C.; Abbott, M. M., Introduction to chemical engineering thermodynamics. 7th ed. / ed.; McGraw-Hill: Boston, 2005.

2.   DeWitt, S. J. A.; Sinha, A.; Kalyanaraman, J.; Zhang, F.; Realff, M. J.; Lively, R. P., Critical Comparison of Structured Contactors for Adsorption-Based Gas Separations. Annual Review of Chemical and Biomolecular Engineering 2018, 9 (1), 129-152.

3.   Chen, G.; Koros, W. J.; Jones, C. W., Hybrid Polymer/UiO-66(Zr) and Polymer/NaY Fiber Sorbents for Mercaptan Removal from Natural Gas. Acs Applied Materials & Interfaces 2016, 8 (15), 9700-9709.

4.   Lively, R. P. Hollow Fiber Sorbents for Post-Combustion CO_2 Capture. Georgia Institute of Technology, 2011.

5.   Pimentel, B. R.; Fultz, A. W.; Presnell, K. V.; Lively, R. P., Synthesis of Water-Sensitive Metal-Organic Frameworks within Fiber Sorbent Modules. Ind. Eng. Chem. Res. 2017, 56 (17), 5070-5077.

6.   Farooq, S.; Hassan, M. M.; Ruthven, D. M., Heat-Effects in Pressure Swing Adsorption Systems. Chemical Engineering Science 1988, 43 (5), 1017-1031.

7.   Ruthven, D. M., Principles of Adsorption and Adsorption Processes. Wiley: New York, 1984.

CHAPTER 7.   SUB-AMBIENT PSA USING FIBER SORBENTS

The manufacturing process for the new MOF fiber sorbents exhibiting high operating capacities enables the next step in process development for the proof of concept sub-ambient pressure swing adsorption process for CO_2 capture. The work described in this chapter focuses on developing methods for determining the performance of the fiber sorbent sub-ambient pressure swing adsorption system and its proof of concept operation for the purification of CO_2. Preceding chapters have discussed the need for the pressure swing adsorption system to operate at very high productivities, so four-step single bed PSA cycles using simulated flue gas feed were performed. So long as reasonable purities and recoveries can be achieved, single bed pressure swing adsorption cycles maximize the productivity capable within the system. The single bed PSA cycles performed as part of this work were capable of reaching moderate purities of >50% but with low recoveries (< 45%) in the evacuation product. This low recovery drives down the CO_2 capture productivities to 0.008 mol kg^{-1}sec^{-1}, still a very high number, but one which will clearly be improved via improvements in recovery. Preliminary PSA results working with microencapsulated phase change material containing MIL-101(Cr) fiber sorbents are also presented, although challenges in fiber spinning and bed preparation make a comparison between structured contactors extremely challenging. Still, operating at temperatures below the freezing point of the microencapsulated phase change material results in some improvement in the CO_2 product purity as compared to similar experiments located just at the freezing point. The thermally modulated fiber beds do not show better performance

than the best performance of the non-modulated case, though, at comparable recoveries, the heat managed cases show better purities and productivities. There is an excellent opportunity for improvement in both recovery and productivity moving forward via the operation of multi-bed cycles incorporating one or more pressure equalization steps and possibly a light product pressurization step.

7.1   Fixed Bed Breakthroughs

Fixed bed breakthrough experiments were performed to provide baseline estimates for some of the relevant adsorption step operating parameters. Fixed bed breakthrough experiments, by design, are effectively "clean bed" control experiments of the feed or *adsorption* step of a pressure swing adsorption cycle. The main difference between these experiments and the lab-scale PSA experiments (besides scale the real operation) will be the nature of the gas the bed is pressurized with prior to the beginning of the adsorption step. In the breakthrough experiments, the bed is pressurized with Nitrogen gas, while in the real PSA experiment, the bed will be "dirty" with any CO_2 that was not removed from the bed in the regeneration steps of the prior cycle as well as the simulated flue gas used to pressurize the system.[1,2] The information gathered in the fixed bed breakthrough experiments offers information that can be used to estimate cycle parameters for the real PSA analysis.

A significant concern of any lab-scale dynamic adsorption experiments or cycle testing is overcoming some of the issues that come about due to the small amount of sorbent mass used in the system relative to the volumes of the rest of the system[3]. Initial PSA cycles performed using the fiber beds used in Chapter 5 showed the effects of the system dead

volumes to be significant in suppressing the effects of different operating parameters. Changing the breakthrough time from 1 minute to 5 minutes resulted in zero change in the CO_2 product purity (which remained steady at ~35 mol%). To help overcome the issue of large dead volumes, experiments in this chapter were performed in sixteen-inch long 3/8" tube diameter Swagelok ® beds containing 88 fibers of 50 weight percent MIL-101(Cr)-cellulose acetate (~3 g fiber, 1.5 g MIL-101(Cr)).

The resulting breakthrough and pseudo-equilibrium capacities for these fiber sorbent beds are reported in Table 7-1 below, with experiments run in duplicate. Values calculated for all experiments are given in **Figure 7-2**. In general, the breakthrough and pseudoequilibrium capacities exceed the values of the fiber beds reported in Chapter 5, particularly those performed at very low flow rates. Part of the reason for this is the small amount of heat expected to be generated at the very low flow rates in these larger diameter beds. Even with similar packing fraction, and a higher sorbent loading per surface area (which could possibly result in more significant heat effects), the lower superficial velocities of the gas phase mean there is more time for the heat to be dissipated in the larger beds. The slight "improvement" in pseudo-equilibrium capacities at the low flow rates is mostly due to the nature of how the calculation is performed and may be observed in **Figure 7-1**.
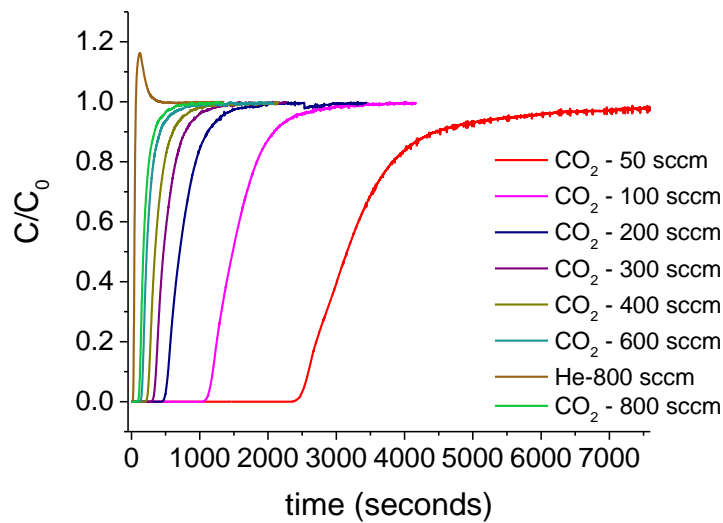
Figure 7-1. CO₂ breakthrough curves collected on 3/8'' MIL-101(Cr)-Cellulose acetate beds at 243K and 16 bar.

At lower flow rates, the *tails* on the breakthroughs approach equilibrium more slowly, allowing for many more seconds of calculation of the small area's bound by the helium and CO_2 profiles. In a perfect calculation of capacity and not pseudo-equilibrium capacity, where there is less variability in the tails of the breakthrough, this experimental error would not be present. This can also be illustrated by comparing the error bars of the breakthrough capacity and the pseudo-equilibrium capacities noted in Figure 7-2. The pseudo-equilibrium capacities errors exhibit higher error across all flow rates as compared to their respective breakthrough capacities. In Figure 7-2, the breakthrough capacity of the MIL-101(Cr) fiber bed begins to fall by about 10% between 600 and 800 sccm, likely due to more prevalent heat effects broadening the mass transfer front.
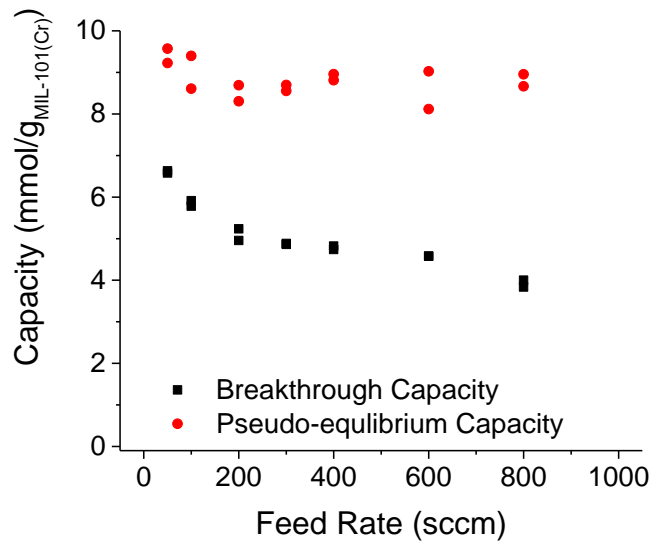
Figure 7-2. Breakthrough and pseudo-equilibrium capacities as a function of feed rate. Experiments were run in duplicate, with both experiments values plotted

Table 7-1. Breakthrough and pseudo-equilibrium capacities for duplicate runs

Flow Rate	Temperature	Pressure	Breakthrough Capacity		Pseudo-Equilibrium Capacity	
sccm	K	bar	mmol/g		mmol/g	
50			6.58	6.63	9.57	9.23
100			5.78	5.91	8.61	9.40
200			4.96	5.24	8.31	8.69
300	243	16	4.88	4.86	8.70	8.55
400			4.74	4.82	8.81	8.96
600			4.58	4.58	9.03	8.12
800			3.84	4.00	8.67	8.95
	233		6.47	6.60	10.95	10.93
200	243	16	4.96	5.24	8.31	8.69
	253		3.90	7.03	7.03	6.80
	273		2.07	4.21	4.21	4.33
		12	4.77	5.19	7.25	7.95
200	243	16	4.96	5.24	8.31	8.69
		20	5.05	5.13	10.18	10.51

266

Similar experiments to those in Chapter 5, varying both temperature and flow rate were carried out in these larger beds, and the same sort of relationships were noted. As the temperature was reduced, the beds broke through later, indicating more CO_2 being adsorbed, as noted in **Figure 7-3** and **Table 7-1**. As within Chapter 5's smaller bed results, there is a small amount of front broadening observable if the CO_2 breakthrough curves are normalized to the stoichiometric breakthrough time. The front spreading is likely due to a combination of heat effects, temperature effects on diffusion playing a role in axial spreading, and small reductions in the superficial velocity of the gas in the bed.
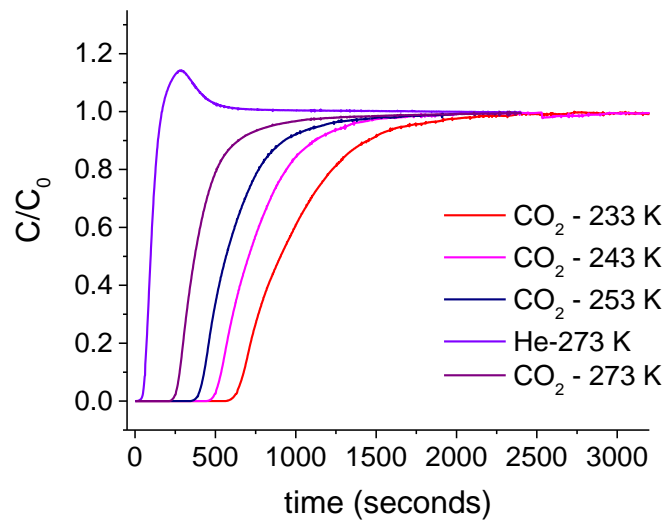
Figure 7-3. CO_2 breakthrough profiles at 200 sccm, 16 bar in 3/8" diameter beds at a variety of operating temperatures.

Figure 7-4 shows the effects of varying the pressure between 12 and 20 bar on the CO_2 and helium breakthrough curves. Higher pressure does lead to slight increases in breakthrough time, though in the 20 bar case, it appears as though the breakthrough capacity does not increase. This is most likely due to the small amount of broadening observed in the helium breakthrough profile, resulting in most part from the reduction in

the average gas velocity through the bed at higher pressures and the same inlet molar flow rate.
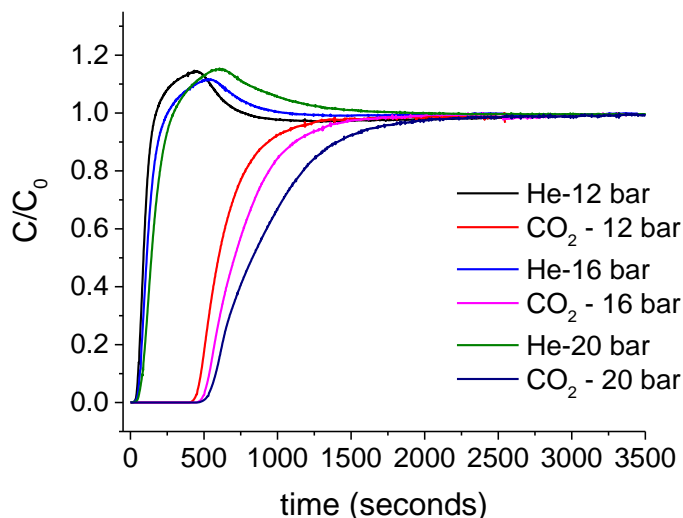
Figure 7-4. Helium and CO₂ breakthrough profiles at 200sccm and 243K in 3/8" diameter beds

7.2 Lab Scale PSA

Having collected breakthrough curves to help to determine the location of some of the ideal operating parameters of the PSA process, lab-scale sub-ambient PSA experiments were carried out on the 3/8" fiber beds. Beds were installed in the PSA system, leak checked, and activated under vacuum at 60°C to remove any adsorbed water. Leak checking of beds involved the pressurization of the beds to ~4 bar, then leaving the bed isolated with one of the installed pressure transducers. If a leak rate of less than 0.005 bar/min was observed over a period of 10 minutes the beds were determined to have no leak.

A typical four-step pressure swing adsorption cycle was performed: 1. Pressurization, 2. Feed, 3. Blowdown, and 4. Evacuation.[2] A graphic showing the valve scheduling of the system during each step, as well as an example pressure profile, is given in **Figure 7-5**

268

Figure 7-5. In the pressurization step, the bed is filled with feed gas (simulated flue gas CO_2: N_2), at a given feed rate controlled by an upstream mass flow controller. Once the bed reaches the pressure set point, a downstream valve connected to a back pressure controller is opened, and a Nitrogen enriched product is produced. During the feed step, the bed becomes progressively saturated with sorbed CO_2, which will later be recovered as a product. Once the feed step has completed, the bed is closed and blown down to the atmosphere via an upstream vent valve (blowdown step). When the bed reaches a given target pressure near ambient pressure (1.1 bar in all experiments), the vent is closed, and the system is exposed to a vacuum pump, which reduces the pressure to a given vacuum condition. Depending on the goals of the process, purified *heavy product* (CO_2 for this application) can be recovered in both the blowdown and evacuation steps. If high purity is required, as is the case in post-combustion CO_2 capture, the evacuation product alone may be used as the product, as the blowdown step tends to be relatively low purity CO_2, particularly if the bed has not been fully saturated with the feed.
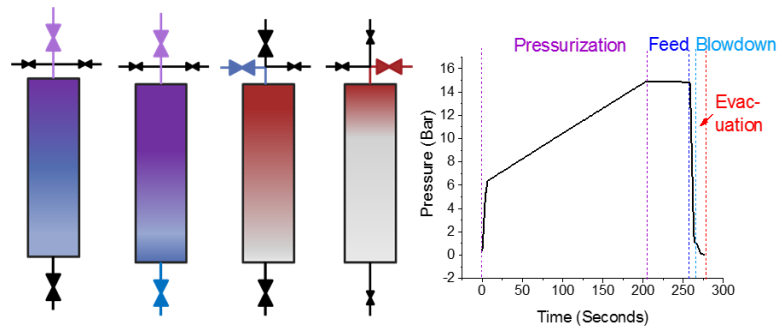
Figure 7-5. (Left) Schematic of 4 step PSA process used throughout this chapter, where blue is purified light product, red is purified heavy product, and purple is feed. (right) bed pressure profile for an example cycle.

7.2.1 *Performance Parameter Estimation*

In pressure swing adsorption processes, four variables are typically defined to be used to judge the relative performance of one cycle design against another. These four variables are purity, recovery, productivity, and specific energy. The purity of a product is the mole fraction of the desired product in that product stream, usually reported as a percentage. The recovery of the product is the ratio of the number of moles of the product species leaving in that product stream versus the total number of moles which entered the cycle as fresh feed, again, given as a percentage. Purity and recovery of a PSA process when operating at reasonable process conditions will exhibit a trade-off, improvements in product purity resulting when less overall product is recovered. The productivity is the number of moles of product produced in its respective stream normalized by the cycle time and the mass of adsorbent (or volume of bed). Depending on the audience, the productivity value will sometimes be inverted and referred to as the bed size factor. The choice of one or another is mostly semantical, where when discussing in terms of productivity, larger numbers are better, where bed size factor is the reverse. Specific energy, a variable not considered in the rest of the discussion (as the actual process energy was covered extensively in Chapter 4), is the amount of energy expended to run the process normalized by the number of moles of product produced per second of cycle time. The three parameters considered in the following discussion are defined below for the CO_2 enriched product.[2]

$$Purity = \frac{n_{CO2}^{Evac}}{n_{CO2}^{Evac} + n_{N2}^{Evac}} \tag{7-1}$$

$$Recovery = \frac{n_{CO2}^{Evac}}{n_{CO2}^{P} + n_{CO2}^{F-in}} \tag{7-2}$$

$$Productivity = \frac{n_{CO2}^{Evac}}{t_{cycle} \times m_{MIL-101(Cr)}} \qquad (7\text{-}3)$$

For this dissertation, we expect the closest we will get to the required CO_2 purities will be if only the evacuation product is used for the CO_2 rich product. This will sacrifice recovery considerably, as a non-negligible amount of CO_2 will be lost in the blowdown step.

PSA experiments performed allowed for the collection of the purities of all three significant products (feed, blowdown, and evacuation) via mass spectrometry. The feed composition could be monitored continuously, as the feed step results in the effluent for a prolonged period of time. For this reason, the feed was monitored at the start of each experiment to determine the approach to the cyclic steady state of the experiment. For nearly all experiments, a cyclic steady state was reached within ten cycles, and all experiments were allowed to run for a minimum of 30 cycles to be sure cyclic steady state had been reached. In the case of the blowdown and evacuation product's molar compositions, these steps resulted in rapid (>10 sec in most cases) pulses of large volumes of product. This pulse resulted in the mass spectrometer typically only recording 4-5 readings of the composition of these respective products. The volumetric flow rates of these steps proved challenging to determine proved challenging, so it was estimated via a mass balance (**eq 7-4 - 7-6**). The flow rates of the pressurization step inlet and the feed inlet and outlet could be monitored by the PSA. The feed step's product flow rate was controlled via a back pressure controller, which recorded flow rates assuming the product was at STP. As the MFC is acting to control the pressure it is expected the individual readings will show

some error, calculations therefore assumed the moles of gas that entered the feed step was equivalent to the moles of gas in the outlet. This assumption is common in many of the experiments we have discussed already, including all breakthrough experiments. The mass balances used to determine the total moles of gas leaving in the blowdown and evacuation steps are given as follows at cyclic steady state

$$n^{in} = n^{out} \tag{7-4}$$

$$n^P + n^{F-in} = n^{F-out} + n^{BD} + n^{Evac} \tag{7-5}$$

Where n^{in} and n^{out} are the total moles which enter and leave the adsorbent bed each cycle. Each term can be further decomposed, with the inlet moles made up of the moles which enter during pressurization (n^P) and feed (n^{F-in}), while the oulet is made up of the moles which leave during the feed (n^{F-out}), blowdown (n^{BD}) and evacuation steps (n^{Evac}) respectively.

This mass balance can be solved simultaneously with the following CO_2 balance, where y^i_{CO2} is the mole fraction of CO_2 in the ith step of the PSA cycle:

$$y^{F-in}_{CO2} \bullet (n^P + n^{F-in})$$
$$= y^{F-out}_{CO2} \bullet n^{F-out} + y^{BD}_{CO2} \bullet n^{BD} + y^{Evac}_{CO2} \bullet n^{Evac} \tag{7-6}$$

The feed inlet composition and total moles in the inlet and in the outlet of the feed step are known and mass spectrometry can be used to esimtate the feed, blowdown, and evacuation step product compositions. This leaves two equations and two unknowns

n^{BD} and n^{Evac}, which can be estimated. This analysis will not be perfect, as every variable above is actually a function of time (except y_{CO2}^{F-in}), but it will allow us to begin exploring the performance of the PSA unit.

There is one other confounding variable in the analysis related to the flow of gas during the pressurization step. At the very beginning of each pressurization step, as highlighted in green on the plot in **Figure 7-6**, the system first exhibits very rapid pressurization. This occurs during the transition from evacuation to pressurization as V10 (in the image in **Figure 7-6**) is closed, and V1 and V5 are opened. During this time, all of the gas trapped between V1 and V5, which at that point is at the operating pressure of the system, immediately fills the volume of the bed in a rapid pressure equalization. This volume of gas is part of the pressurization, which cannot be accounted for via monitoring the mass flow controller. For the purposes of this analysis, this volume was estimated using the change in pressure of the next 20 seconds of the pressurization step as a basis for the number of moles introduced to the system as part of the rapid pressurization.
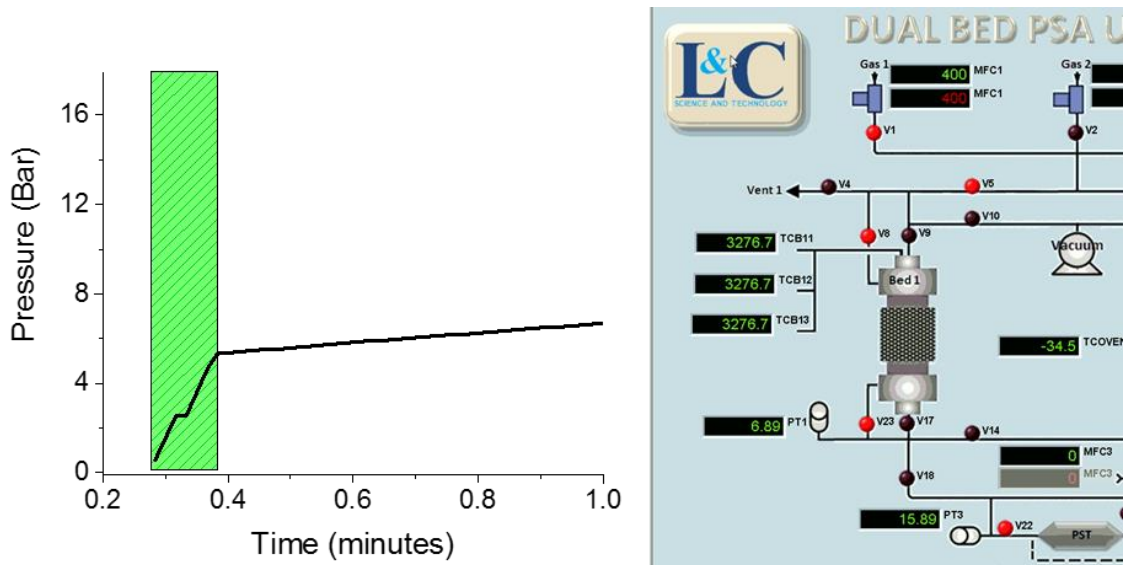
Figure 7-6. Rapid pressurization of the bed occurs as a result of upstream dead volumes pressure-equalizing with the bed upon the start of the pressurization step. (Left) recorded pressure profile for Bed 1 during pressurization, with rapid pressurization highlighted in green (Right) Valve position of PSA during pressurization

7.2.2 Single Bed Four-Step PSA Performance

As the design goal of these experiments was to collect information about the performance of the sub-ambient PSA's operation for CO_2 capture, the decision was made to perform the cycles on a single bed, which is the most straightforward process configuration. Industrial PSA units will virtually never run this way, as significant gains in recovery and energy (and in some cases purity) can be made through the application of more complex dual bed cycles employing additional steps connecting multiple beds like pressure equalizations or light product pressurization. These steps are valuable for boosting the performance of an adsorbent bed, but all of these steps come at the cost of additional capital and potentially at the cost of recovery. The losses in productivity when utilizing pressure equalization(s) come about for two reasons.

First, during the pressure equalization step, the *already treated* gas is transferred between the partially saturated bed and the evacuated bed. This will almost always improve recovery, as less product gas will be lost to the blowdown since a fraction of the gas is being retained within the multi-bed system. However, that also means less feed gas enters the system as a part of the pressurization step, meaning per unit time the bed is actually treating less gas.

The second reason pressure equalization steps will lead to reduced productivity is the required built-in dead time for the two beds to reach the same time in the cycle. In **Figure 7-5**, we can see for that cycle, the pressurization and feed steps take approximately 255 seconds, while the blowdown and evacuation steps take a combined 20 seconds. This cycle, in a two-bed system, would require the second bed to rest for ~235 seconds, while awaiting the first bed finishing its pressurization and feed step. Based on that estimate, the effective cycle time of the process would *double* due to the implementation of the pressure equalization step. That doubling of cycle time would then effectively half the productivity of the system, not including the fact that less total gas was being fed to the system each cycle. While at an industrial scale, this effect would be less pronounced, these experiments are being performed in a lab-scale piece of equipment, with only two beds. With these reasons in mind, the experiments performed throughout the remainder of this chapter were all performed as single bed cycles, with the four steps shown in **Figure 7-5**.

The resulting experiments produced effluent profiles similar to those shown in **Figure 7-7**. The experiment begins by monitoring the light product of the feed step and is allowed to run until a cyclic steady state is reached. At that point, the mass spectrometer inlet port is closed, transferred to the blowdown product storage tank, and reopened. At

least five cycles are collected at the blowdown condition; then, the same procedure is repeated moving from the blowdown to the evacuation storage tank. Once at least five cycles had been collected, the mass spec inlet was shifted to the light product inlet port, and the experiment was halted. Prior to the completion of the experiment, the mass spec also collected the feed composition for at least 10 minutes so that any variation in the recorded inlet composition as compared to the documented purity of the gas cylinder could be corrected for in the final analysis.
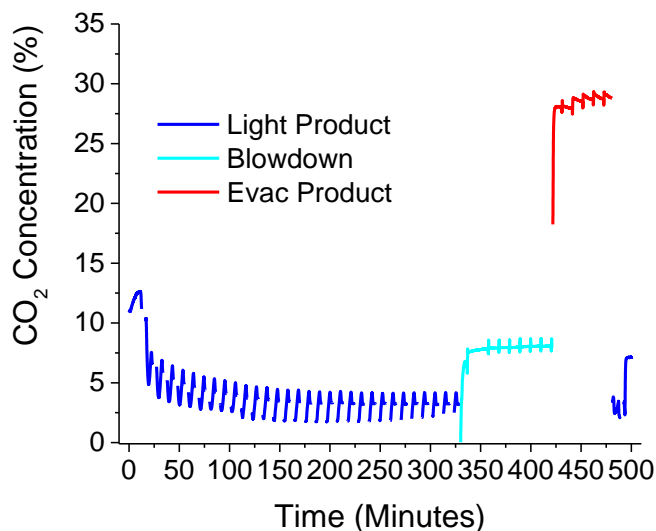
Figure 7-7. Mass spectrometer reading of the effluent of one PSA experiment performed on the MIL-101(Cr)-cellulose acetate fiber sorbent bed used in Chapter 5 (smaller bed diameter)

The results of the PSA experiments at a variety of different operating conditions performed on the 50 wt% MIL-101(Cr)-Cellulose acetate 88 fiber module is reported in **Table 7-2**.

Table 7-2. Pressure Swing Adsorption Operating Conditions and Results for 88 fiber module at 243K. Units are: Pressures (bar), Rates (mL/min), times (seconds), purity and recovery (%), productivity mol kg^{-1} sec^{-1}

PSA Pressure	PSA Vacuum Pressure	Pressure Rate	Feed Rate	Feed time	Cycle Time	Vacuum			Blowdown and Vacuum	
						CO$_2$ Purity	CO$_2$ Recovery	CO$_2$ Productivity	CO$_2$ Purity	CO$_2$ Recovery
18	0.084	192	192	720	1126	55.1	21.6	0.0031	22.7	73.5
	0.102		384	360	1074	59.7	43.3	0.0065	26.0	86.4
	0.008	384	384	120	352	49.2	23.3	0.0067	18.2	94.9
	0.09			180	416	49	30.5	0.0086	20.1	91.5
	0.084			30	513	41.5	13.1	0.0020	14.7	98.8
	0.094			300	536	56.6	24.5	0.0067	22.2	80.1
16	0.298	96	96	480	1153	38.9	22.8	0.0018	18.6	93.4
	0.23		192	240	915	38.1	26.3	0.0027	18.5	92.8
	0.212	192	192	240	600	36.4	25.1	0.0039	18.4	92.2
	0.295			360	737	40.5	23.9	0.0035	19.9	85.8
	0.1			600	1030	55.1	41.3	0.0056	25.7	87.9
	0.298			720	1097	44.3	16.9	0.0023	21.7	66.2
	0.26			1080	1427	42.2	15.1	0.0021	22.6	52.9
	0.1		384	360	778	60.1	23.9	0.0047	25.3	78.0
	0.186	384	192	240	435	38.3	21.7	0.0046	18.3	91.4
	0.2			360	550	39.1	28.8	0.0056	19.8	85.2
	0.274			540	727	41.8	24.5	0.0044	21.3	76.0
	0.28			720	910	42.8	18.5	0.0031	21.8	66.1
	0.16		384	120	318	40	21.9	0.0064	18.3	92.3
	0.088			120	324	45.6	25.4	0.0073	19.0	95.8
	0.098			150	366	45	38.9	0.0108	20.4	95.5
	0.094			150	369	46.5	30.8	0.0085	20.2	94.3
	0.092			180	384	45.8	33.4	0.0094	21.0	91.2
	0.1			180	394	49.8	29.9	0.0083	21.1	91.9
	0.096			240	450	49.8	33.3	0.0091	22.5	86.0
	0.1			180	513	52.7	40.2	0.0086	22.4	98.0
	0.1			300	532	50.1	32.7	0.0086	24.1	82.9
	0.1			300	542	52.5	35.8	0.0092	24.8	85.2
	0.1			360	588	54.4	32.7	0.0086	25.2	77.7
	0.192	576	192	240	375	40.8	13.6	0.0034	18.3	92.2
	0.276		384	120	265	41	31.5	0.0112	18.5	93.1
	0.258	768	192	240	345	41.1	19.7	0.0053	18.3	92.3
	0.282		192	240	347	38.2	26.6	0.0072	18.3	92.3
	0.27		384	120	238	42.6	18.1	0.0070	18.5	93.0

PSA Pressure	PSA Vacuum Pressure	Pressure Rate	Feed Rate	Feed time	Cycle Time	Vacuum			Blowdown and Vacuum	
						CO_2 Purity	CO_2 Recovery	CO_2 Productivity	CO_2 Purity	CO_2 Recovery
14	0.012	192	192	720	1041	49.7	33.9	0.0047	25.6	71.2
	0.01			108	290	49.2	25.0	0.0071	19.0	95.0
	0.104	384	384	120	431	44.9	48.0	0.0095	20.4	98.1
	0.012			300	480	47.5	30.5	0.0082	23.8	74.8

A total of 38 different conditions were examined as part of this analysis, varying high-pressure conditions, vacuum, feed rate, feed time, and pressurization rate. Cycle time with feed time and pressurization rate as expected, though the time to reach the blowdown and vacuum set points did vary between experiments. As an example, two experiments were run at 16 bar, 768 sccm pressurization rate, 192 sccm feed rate, feeding for the same 240 second period, but the evacuation and blowdown time took approximately 2 seconds more extended in one case as compared to the other. The resulting purity, recovery, and productivity (41.1% vs. 38.2%, 19.7% vs. 26.6%, and 0.0053 vs. 0.0072 mol kg^{-1} sec^{-1}) do indicate that the estimates presented for PSA performance in this work have some run-to-run variation. We attribute much of this variation to the propagation of the errors estimating the purity of the evacuation product and blowdown product using the mass spectrometer as those estimates will experience significant fluctuations over the 2-second sampling delay of the mass spectrometer. We can confirm this is the majority of the source of the error by lumping the calculated moles of evacuation and blowdown products (and compositions) of the mass balance together, as shown in the final two columns of **Table 7-2**. This lumped term is the PSA performance as could be calculated with only the feed step effluent and the relevant known flow rates and shows good agreement between experiments with the same operating conditions (to 3 decimal places 18.291% vs. 18.293% purity, 92.290% vs. 92.269%). While acknowledging the error in the experiment due to the mass spectrometer,

it is still worthwhile to analyze the results of the experiments for more general trends in performance as a function of different operating conditions.

As the primary goal of operating the PSA unit at sub-ambient conditions with these materials was to boost productivity, it is worthwhile to see how some of the estimated purities and recoveries relate to the calculated productivities. **Figure 7-8** shows the relationship between the estimated productivities and the cycle's respective recovery and purity. There is an observable positive correlation between both product purity and product recovery and the respective cycles' productivity, though the correlation appears stronger relative to recovery. Based on the definitions of these terms, this makes is reasonable, as high productivity in a given bed is directly proportional to the number of moles of CO_2 in the product stream, which influences the calculated recovery and purity as well. The strong positive correlation between recovery and productivity would also indicate there is likely not that strong a negative correlation between the cycle time and the productivity, as the cycle time is the other major component of the productivity that can be varied experimentally in the same adsorbent bed.
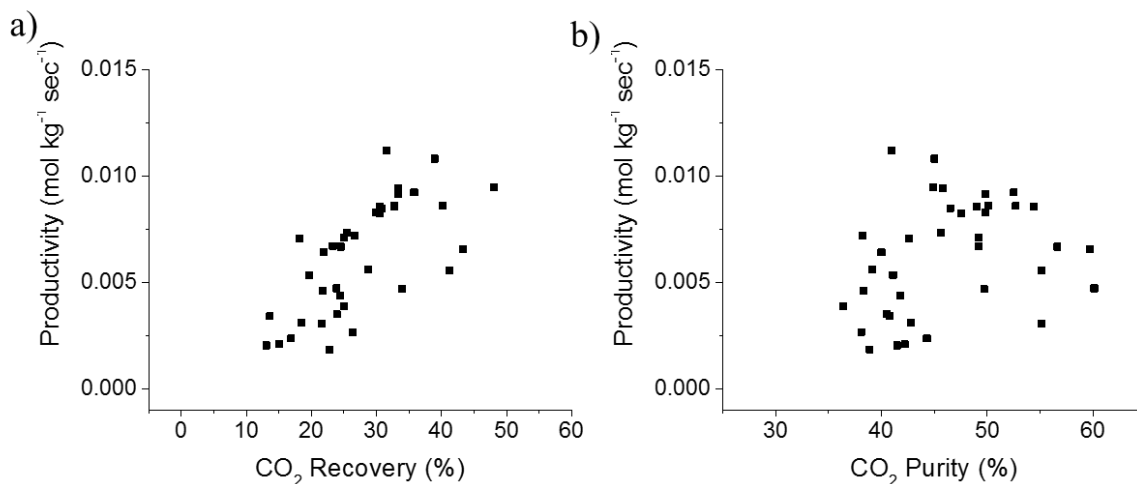
Figure 7-8. Productivity (mol kg^{-1} sec^{-1}) of the sub-ambient PSA unit with 50 wt% MIL-101(Cr)-cellulose acetate fibers as a function of (a) Recovery and (b) Purity

The relationship between productivity and cycle time is given in **Figure 7-9a**, showing the expected weak negative correlation between the two variables. Since productivity is normalized per second of cycle time, it makes sense that shorter cycle times should lead to higher productivities. Something similar is observed in **Figure 7-9b**, where the time the feed step is running is compared to productivity. Since the longer the time of the feed step, at a given inlet flow, the more the bed is saturated, the amount of CO_2 captured should increase with the feed time. In terms of productivity, though, there is some offsetting effect on productivity, as the cycle time increases with the feed time.
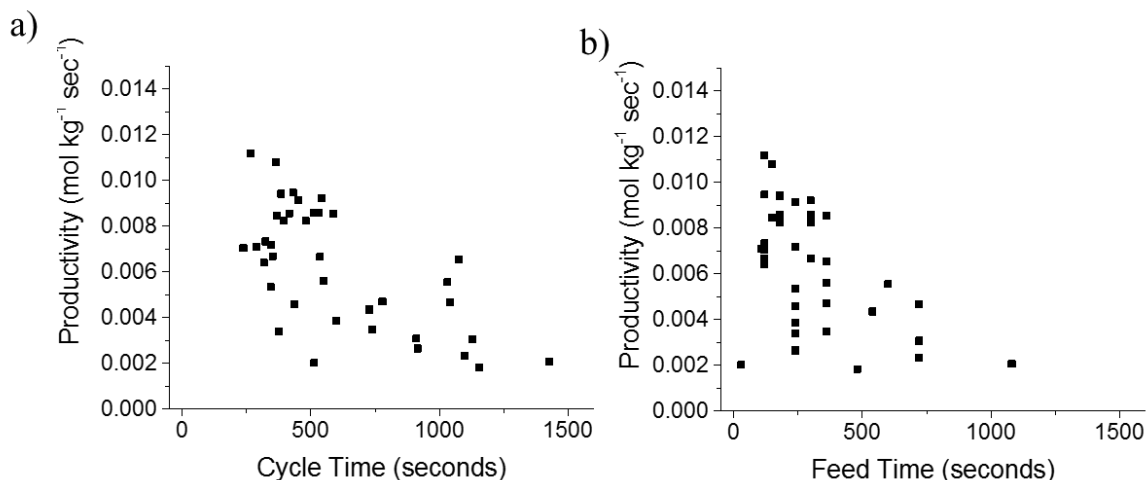
Figure 7-9. Productivity (mol kg^{-1} sec^{-1}) of the sub-ambient PSA unit with 50 wt% MIL-101(Cr)-cellulose acetate fibers as a function of (a) Cycle time and (b) Feed time

Both trends in **Figure 7-9** show what may be considered an upper ceiling on productivity with this particular PSA system as the cycle time approaches zero at about 0.14 mol kg^{-1} sec^{-1}. As the cycle time approaches zero, so too would the feed time, and an effectively zero feed time would expectedly lead to the lowest possible purity and recovery. The shortest experimental feed step was only about 30 seconds (although the pressurization was carried out at a relatively slow rate, leading to a total cycle time of 513 seconds), which resulted in the lowest productivity of all the examined cases. Even with this limitation in mind, it is interesting to observe the possible limits on productivity in this bed in **Figure 7-9**, though many more experiments would be necessary to be sure of a maximum.

While the final vacuum pressure in our system varied slightly from experiment to experiment, two preset experimental conditions were considered in the experiments performed at 16 bar operating pressure. The first, the moderate vacuum condition, was reached by setting the vacuum setpoint to 0.7 bar, though valve delay led to the actual vacuum condition reaching near 0.2 bar. The lower vacuum condition considered was

reached using a set point of 0.1 bar, though again, valve delay led to some further reduction in vacuum pressure at some tested conditions. The relationships between purity, recovery, and productivity for these two vacuum conditions are shown in **Figure 7-10**. Clearly, across all other tested conditions at 16 bar and 243K, the pulling of deeper vacuum resulted in higher purities and recoveries. Pulling deeper vacuum both recovers more of the CO_2 rich adsorbed phase and cleans the bed further. Increased recovery of the CO_2 rich phase results in higher purities, as the adsorbed phase is CO_2 rich. Recovering more adsorbed CO_2, and better bed regeneration results in higher recoveries, as the bed being more fully regenerated should lead to better purification of the feed, so less CO_2 should be lost in that step. Looking at the productivities compared to the recovery, higher purity and recovery of the lower vacuum cases results in higher productivities. While deeper vacuum conditions may be desired to increase PSA performance, as noted in Chapter 4, this does come at a high cost. One outlier is noted comparing the productivity to the collected purities and recoveries; this outlier appears to be due to an especially low estimated blowdown purity, leading to significantly more moles of CO_2 produced in the evacuation as compared to the other moderate vacuum cases.
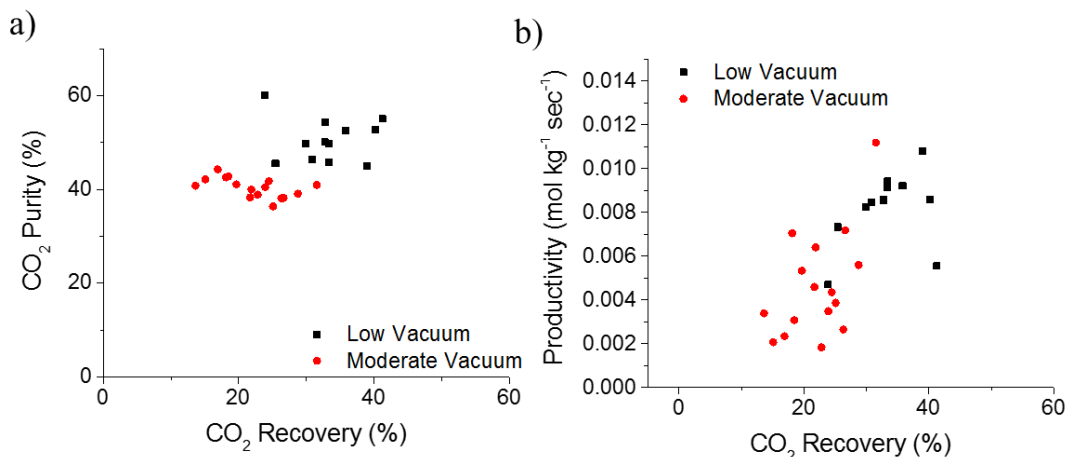
Figure 7-10. Effects of minimum vacuum condition on purity, recovery, and productivity. (red) moderate (>0.2 bar) vacuum condition, (black) low (~0.1 bar) vacuum condition. All experiments were performed at 16 bar operating pressure and 243K.

Three pressure conditions were probed as a part of the analysis, and their respective purities and recoveries are plotted in **Figure 7-11**. It is worth noting that the 14 bar conditions were run at another order of magnitude lower vacuum condition as compared to the 16 and 18 bar conditions, thus enabling investigation of lower vacuum levels. Still, little improvement or losses are noted as the pressure is varied to the 14 or 16 bar condition as it comes to purity or recovery. We postulate that any trend in the purity-recovery of the PSA process that may have occurred as the pressure was changed was probably lost due to the very low pressure at the 14 bar condition boosting its performance (as would be expected based on Figure 7-10), so additional experiments will be necessary to confirm any sort of correlation. As with the vacuum, if there is an improvement in performance with pressure, it would be partially offset in the economics by the energy requirements of reaching that higher pressure condition.
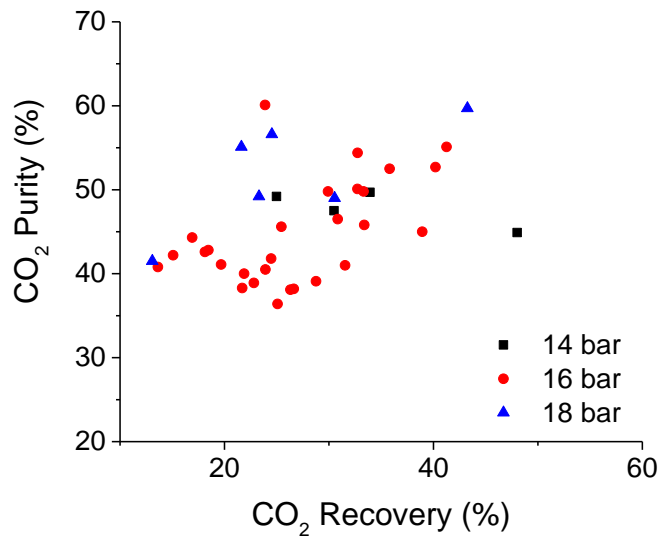
Figure 7-11. Effect of operating pressure on the CO₂ purity and recovery of the PSA system. Note: the 14 bar condition was at significantly lower vacuum condition than the 16 and 18 bar conditions.

The purity-recovery Pareto curve for the PSA conditions considered is given for in **Figure 7-12**, including for referencing the same Pareto curve for the case where the blowdown and evacuation steps are combined as an alternative for CO_2 purification. Clearly, the sub-ambient PSA unit is not currently reaching the required 75% purity, and 90% recovery condition noted in Chapter 4 for the sub-ambient CO_2 capture process to approach economic viability. Neither purity nor recovery exceeds 60% in this particular series of PSA experiments, so there is a great deal of room for improvement in the PSA equipment. Typically, when performing these variations in PSA operating conditions, the goal is to have a clearly defined Pareto frontier, where changes in operating conditions cannot reach beyond a series of purity-recovery values due to the limitations of the process. The "evacuation product only" Pareto does not show a clear Pareto front, due to a number of factors. It is likely that if many more experiments were performed, a clear frontier would present itself. With that said, the noted variability in our estimate of purities of the evacuation and blowdown product is likely clouding the real Pareto frontier of the process,

at least to some extent. For comparison, the combined evacuation and blowdown values, where the variability in the mass spectrometer reading is significantly reduced, show a clear Pareto frontier, with an upper purity ceiling of about 26%, and recoveries reaching nearly 99%. The combined blowdown-evacuation product is not expected to ever reach the required purity, due to the voids within the bed being full of 10+ bed volumes of feed gas.
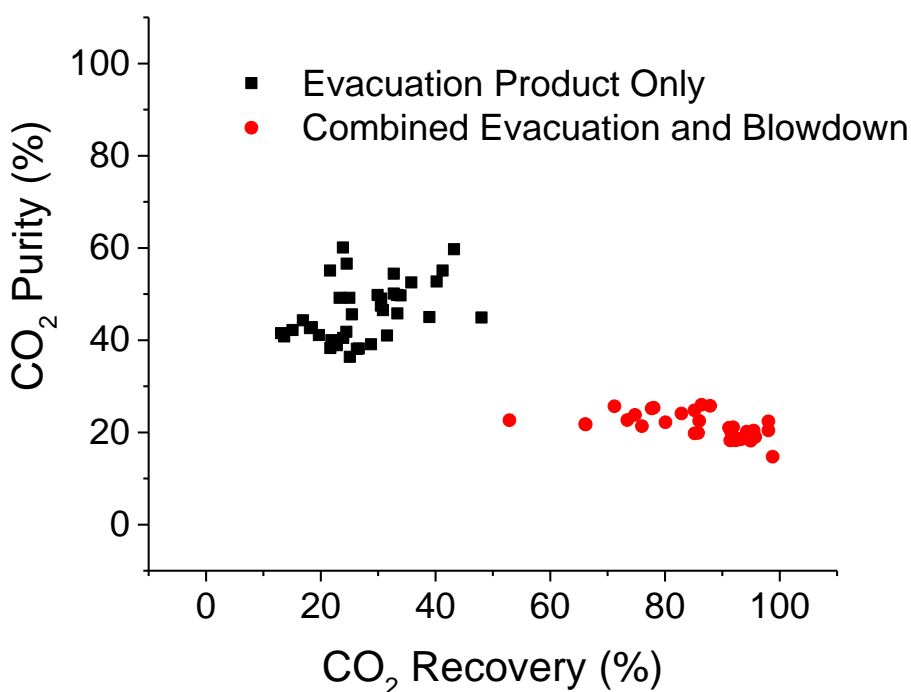
Figure 7-12. Purity-Recovery Pareto for 50 wt% MIL-101(Cr)-cellulose acetate fibers. (black) Evacuation Product estimated performance (red) performance of the PSA system if blowdown and evacuation products are both used as the CO_2 rich product

The productivities noted for the evacuation product across all cases, shown in **Figure 7-8** and **Figure 7-9**, are very high values as compared to those reported elsewhere in the literature for pressure swing adsorption[4-7], approaching the values reported for amine loaded silica fiber sorbent RTSA[8]. At the same time, there is a clear need for improved

purity and recovery; the productivities calculated in this work point for a real opportunity for sub-ambient CO_2 capture using high CO_2 capacity fiber adsorbents.

A variety of options both in bed construction and cycle design are available in the future to help to push the evacuation product's purity and recovery closer to the values where the sub-ambient CO_2 capture process may approach economic viability.[2] These improvements can be done in addition to upgrading the PSA equipment (e.g., valves, controllers). The first will be to load more fibers into the module. The fiber module used as a part of this study was about 48% void fraction, but the theoretical packing of cylindrical fibers within a cylinder should allow for void fractions as low as 22%. As has been noted elsewhere, the packing of polymeric fiber sorbents is somewhat challenging at high weight loadings, mainly when performed by hand in the lab, but the development of better bed manufacturing methods should allow for more fibers, and therefore more adsorbent to be fit within the bed. More adsorbent should allow for higher purities to be reached, as more CO_2 will be in the adsorbed phase to be recovered in the evacuation step. Additionally, reducing the void fraction of the bed will help to boost the purity, as less interstitial gas will be recovered in the evacuation step.

As mentioned at the beginning of this section, single bed cycles enable very high productivities. Sacrificing some productivity for the recovery of more CO_2 from the blowdown, as would occur in a pressure equalization step, will almost definitely be required to reach the required recoveries of the sub-ambient PSA. Exploring these additional steps to the cycle would be a significant point of emphasis for future work in trying to enable the sub-ambient PSA process.

One other way to boost the recovery, at the cost of purity, but not necessarily the productivity, which was not considered in this parametric study, would be varying the pressure where the PSA unit switches from the blowdown step to the evacuation step. This was not considered in this work out of fear of damaging the laboratory vacuum pump attached to the system, but halting the blowdown sooner would mean less CO_2 has the opportunity to desorb during the blowdown, and can therefore be recovered as a part of the evacuation process.

7.3 Testing Thermally modulated fiber sorbent beds

MIL-101(Cr)-µPCM-cellulose acetate fiber adsorbents offer a good opportunity for the comparison of the performance of the sub-ambient PSA process. In Chapter 6, it was shown that sorption enthalpy could be managed, resulting in a sharper breakthrough performance, even in relatively small diameter beds, using UiO-66 as a sorbent for comparison. With this knowledge in mind, the goal of this section was to see if the performance of the MIL-101(Cr) fiber adsorbents could be realized in the same way, now testing the performance in the sub-ambient PSA unit, as the ultimate application of the materials.

7.3.1 *Manufacturing Thermally modulated fiber sorbents*

The fiber spinning of MIL-101(Cr)-µPCM-cellulose acetate fiber adsorbents was attempted, first targetting for 75 weight% combined solids fraction equally distributed between MIL-101(Cr) and µPCM. Syringe extrusions showed the fibers could be extruded, though with a minimal draw, and so a polymer dope containing cellulose acetate, PVP, MIL-101(Cr), µPCM-30D, NMP, and deionized water was prepared. The estimated dope

287

composition is given the best estimate of the remaining dope of the first spin, and the additional prime is given in **Table 7-3**. While spinning the fibers, it proved virtually impossible to draw the fibers onto the drum, as the filament would immediately break in the first quench bath when draw beyond the dropping of the guide was applied.

Table 7-3. Estimated Dope composition for the MIL-101(Cr)- μPCM-Cellulose acetate fiber segments

Dope Component	Estimated Dope Composition at time of spin (%)	Estimated Dope Composition based on TGA (%)
CA	11.21	10.88
PVP	4.53	4.39
NMP	54.78	53.18
H2O	7.5	7.28
MIL-101(Cr)	10.98	12.12
μPCM -30C	10.98	12.12

This spin also turned out to be unable to handle the draw required to produce continuous fibers. Still, in the interest of probing the effects of heat management on PSA performance, *fiber segments* were extruded into the water bath without a draw and recovered into the water bath. Without any draw applied, these fiber segments had inconsistent diameters both in each extruded length as well as between extruded lengths. Residual mass analysis on the fiber segments resulted in an average MIL-101(Cr) content in the fibers of ~ 35 wt%, which is slightly more than would be estimated based on the dope composition estimate at the time of spin. It is possible to estimate the dope composition, which would have been required to produce that loading, which is also given in **Table 7-3**.

SEM images of the fiber structure are given in **Figure 7-13**. Due to the inherent variability of extruding fibers without a draw on the phase inversion behavior between fiber states, it is difficult to draw any significant conclusions based on SEM, as one fiber segment

may have experienced vastly different phase inversion phenomena as compared to any other fiber. Still, the images show the µPCM survived the spinning process with good dispersion. The divets in **Figure 7-13a** regularly appear in µPCM containing fibers, as the fracture of the fibers leads to some capsules being entrapped on one fracture or the other (or lost in the fracture itself if not adhering to either). Still, the divets and microcapsules show good dispersion throughout the fiber cross-section.
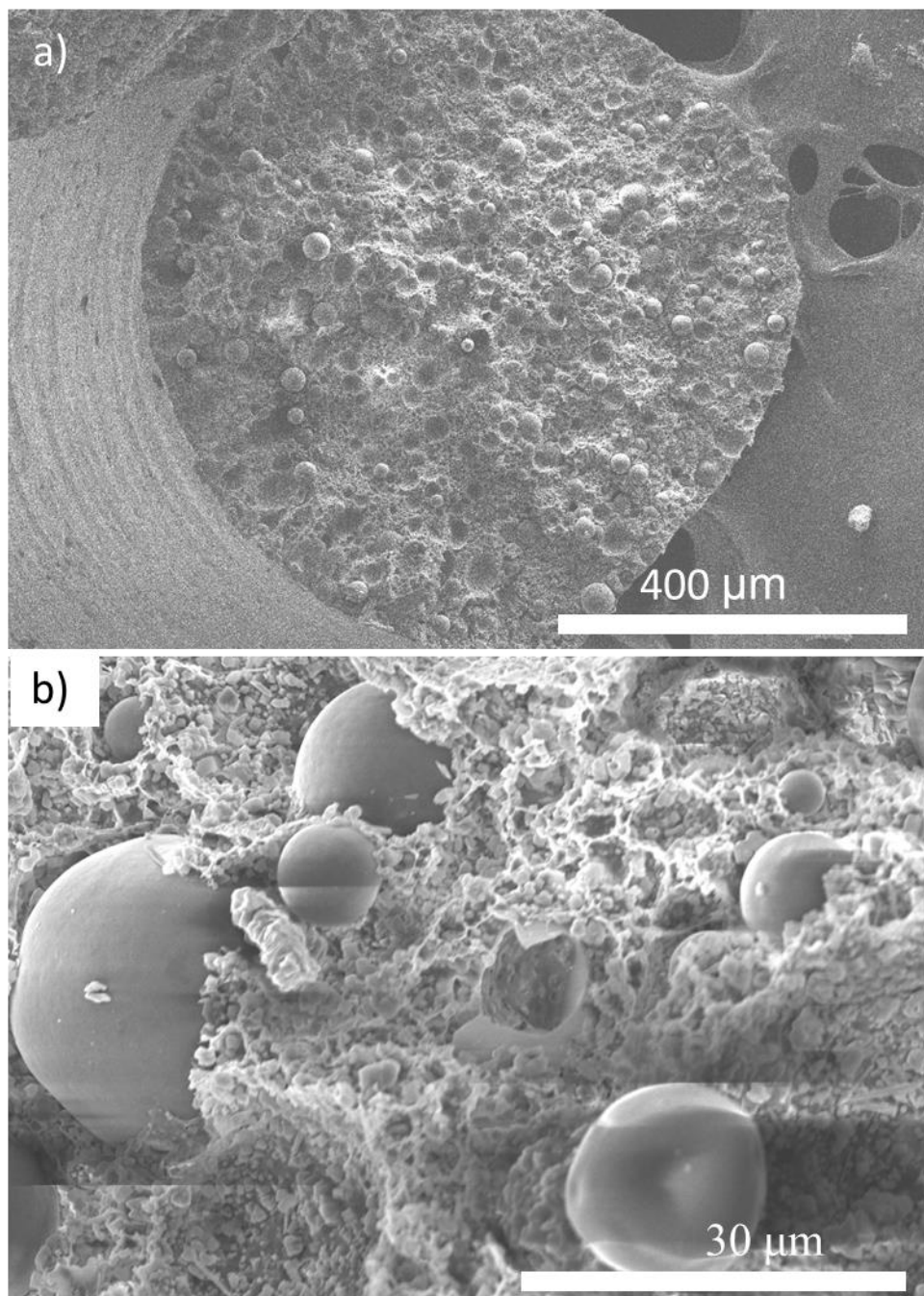
Figure 7-13. SEM images of MIL-101(Cr)- µPCM –Cellulose acetate fiber segment cross-sections (a) Low resolution SEM, (b) zoomed in on sub-structure of fiber

The microstructure in **Figure 7-13b** shows the MIL-101(Cr) particles well distributed throughout the structure, with many effectively *touching* the µPCM particles in the polymer matrix. The polymer matrix is challenging to make out in the image, though a

few pores and general polymer structure is visible. The microstructure does appear less porous than other fibers manufactured as part of this work.

7.3.2   *Thermally Modulated MIL-101(Cr) Fiber PSA Performance*

While the spin was not successful in producing continuous fibers, which would have been most desirable for bed construction, a single fixed bed of fiber segments was prepared. The bed (16" long, 3/8" Swagelok tube) was packed with fiber segments until no more fibers could possibly be packed. Due to the variable diameters and lengths of the fibers, it is challenging to determine the exact volume fraction of the bed, but the total fiber mass was recorded as 3.557 grams of fiber (estimated 1.245 grams of MIL-101(Cr)).

Fixed bed breakthrough experiments were first performed on the beds at 243K to help to determine potential PSA operating parameters and confirm the loading of MOF in the bed. A comparison of the breakthrough profiles of the μPCM-MIL-101(Cr)-cellulose acetate bed and the 50 wt% MIL-101(Cr)-Cellulose acetate beds used in the previous section is shown in **Figure 7-14**. As expected, given the relatively lower MIL-101(Cr) loading in the thermally modulated fiber bed, it breaks through earlier than the unmodulated fibers. The thermally modulated fiber bed appears to have a sharper breakthrough, with a ~40% increase in the derivative at $C/C_0=0.5$, though operating at 243K, the breakthrough and pseudoequilibrium capacities normalized to the MOF loading have good agreement with the 50 wt% MIL-101(Cr)-Cellulose acetate fibers.
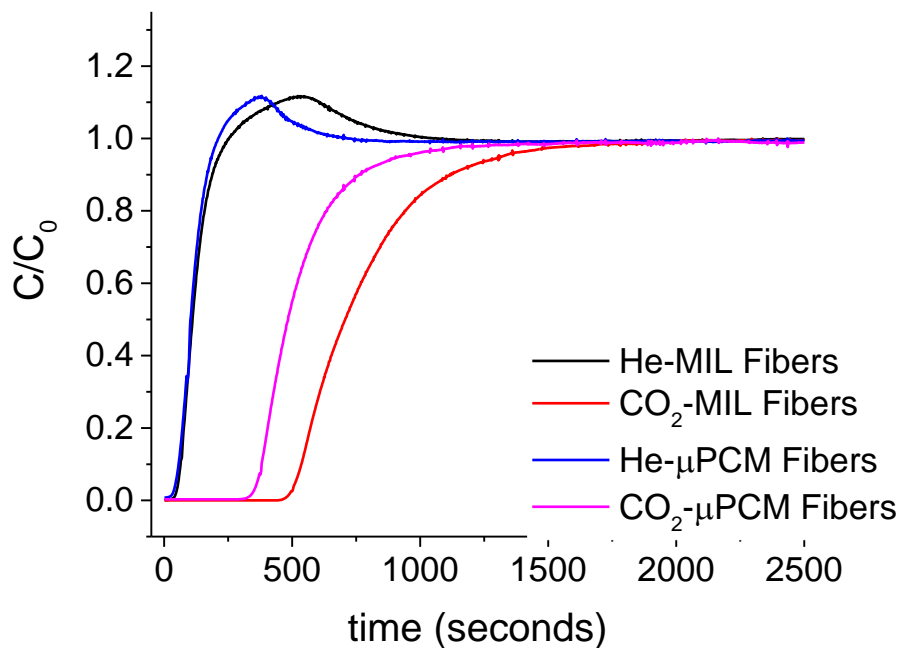
Figure 7-14. CO₂ Breakthrough profile comparison between 50 wt% MIL-101(Cr)-Cellulose acetate fibers and thermally modulated fiber sorbents operating at 243K, 200 sccm, and 16 bar pressure.

With the shorter breakthrough times noted, relatively shorter feed times were used to offer some opportunity for comparison between the modulated and unmodulated fiber beds. The results of the PSA experiments (all at 16 bar) operating pressure are given in **Table 7-4** below. The main objective of these experiments was to test the effects of the μPCM's potential heat management performance on the PSA's overall performance. With this goal in mind, experiments were run at two operating temperatures, 243 K and 238 K. The μPCM could conceivably be active at both operating temperatures as 243 K is the location of the onset of the freezing behavior, but the hypothesis of these experiments is that the μPCM will be more effective at the 238K condition where it is starting from a fully frozen state. Over the course of a cycle, in either case, the μPCM is expected to freeze and melt, coupled to the adsorption and desorption enthalpy effects within the bed. At 238 K, though, the μPCM should swing between a nearly entirely frozen state and a partially

melted state, while at 243 K, we expect it to begin at that partially melted state and reach a

near completely melted state.

Table 7-4. PSA operating parameters and resulting performance

Temper-ature	Vacuum Pressure	Pressure Rate	Feed Rate	Feed Time	Cycle Time	Vacuum			Blowdown and Vacuum	
						CO_2 Purity	CO_2 Recovery	CO_2 Product-ivity	CO_2 Purity	CO_2 Recovery
	0.074	192	192	120	469	41.3	21.8	0.0044	16.3	97.4
	0.068	192	192	600	944	47.2	15.2	0.0027	19.9	66.3
	0.082			30	221	40.2	22.4	0.0088	14.9	98.7
243	0.1			60	270	40.8	24.1	0.0086	16.4	97.9
	0.01	384	384	90	282	46.0	15.4	0.0057	17.7	96.0
	0.09			120	316	46.3	23.2	0.0084	18.6	93.1
	0.052			150	338	51.1	9.5	0.0035	19.3	89.3
	0.09			30	227	43.2	11.2	0.0043	15.0	99.0
	0.92			60	266	46.9	22.0	0.0080	16.4	98.1
	0.1			90	296	49.7	24.4	0.0087	17.9	97.3
238	0.092	384	384	120	316	48.6	23.9	0.0087	18.9	94.9
	0.058			150	341	49.8	18.9	0.0069	19.5	90.4
	0.068			180	371	53.4	18.9	0.0068	19.9	85.9
	0.06			360	555	53.2	19.3	0.0066	21.7	66.1

The resulting estimated purities and recovery for the cycles are plotted in **Figure 7-15**, and the productivities are compared in **Figure 7-16**. Besides the experiments run with very long feed time (performed to try to probe the maximum purity which could be reached, the experiments performed at 238 K show higher purity and comparable recoveries as compared to the experiments performed at 243 K. Since the MOF will also have slightly higher capacity at 238 K as compared to 243 K, it is difficult to conclusively say that the phase change material's performance is the only factor at play.
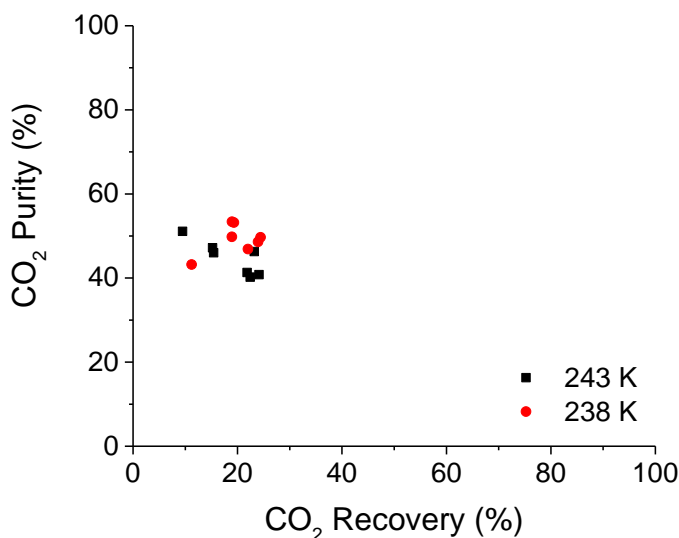
Figure 7-15. CO_2 Purity-Recovery Pareto for MIL-101(Cr)-µPCM-cellulose acetate fiber segments at two operating temperatures.

The relationship between recovery and productivity falls in line with the same behavior observed in **Figure 7-8a**, where the two appear directly related. Interestingly, the productivity-recovery relationship in **Figure 7-16** does not appear to be affected by the operating temperature of the thermally modulated fibers, perhaps indicating the potentially increased performance of the thermally modulated fibers at lower temperatures on purity is not leading to significant gains overall.
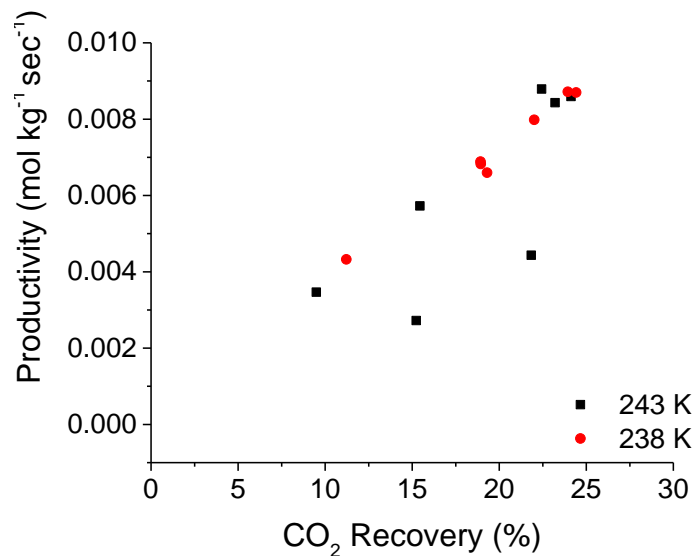
Figure 7-16. Thermally modulated fiber sorbent productivity-recovery relationship at different operating temperatures

The purity-recovery and productivity-recovery relationships with both the thermally modulated and 50 wt% cellulose acetate fiber sorbents operating at 16 bar pressure are given in **Figure 7-17**. The 50 wt% fibers are capable of reaching higher purities, recoveries, and productivities as compared to the thermally modulated fibers, though comparing at the same recovery values, as in **Figure 7-18** shows the thermally modulated fibers operating at 238 K comparable or higher productivities and purities than the fibers without heat management. Interestingly, while the 243K operating temperature thermally modulated fibers show approximately the same purities as the 50 wt% fibers, the heat management does appear to improve productivity, at the same recovery values.
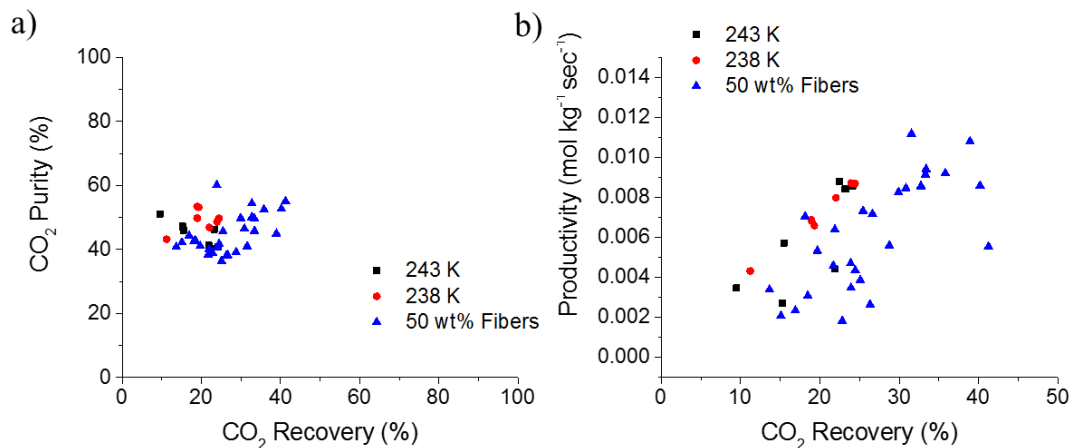
Figure 7-17. Purity-Recovery and Productivity-Recovery of the sub-ambient PSA process comparing thermally modulated and 50 wt% MIL-101(Cr)-Cellulose acetate fiber sorbents.

Many more experiments would be required to fully develop enough understanding to say conclusively whether the thermal modulation is improving the PSA performance in these smaller diameter beds. To better probe the effects of heat management, different temperatures, flow rates, and other operating conditions will offer greater insight. Additionally, working in a more massive diameter bed, where heat effects will be more prevalent in the system, could lead to more dramatic effects becoming apparent comparing between thermally modulated cases.
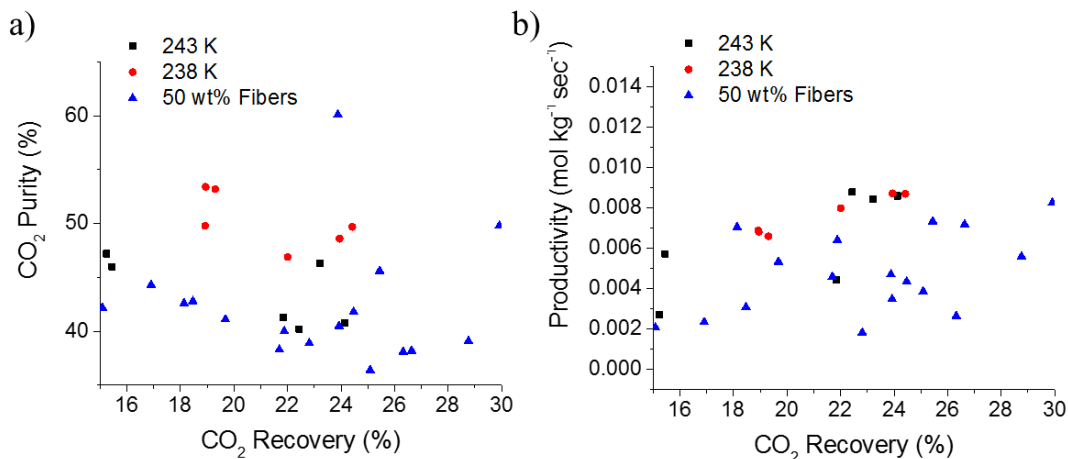
Figure 7-18. Purity-Recovery and Productivity-Recovery of the sub-ambient PSA process comparing thermally modulated and 50 wt% MIL-101(Cr)-Cellulose acetate fiber sorbents, with recovery rescaled to compare comparable values

7.4   Summary

This chapter presented the lab-scale pressure swing adsorption performance of MIL-101(Cr)-cellulose acetate fiber sorbents operating at sub-ambient conditions. Maximum CO_2 purity of 60.1 % was achieved in the 50 wt% MIL-101(Cr) fiber sorbents prepared in the work of Chapter 5, but this purity is still not close to the 70-80% required for the sub-ambient PSA process. CO_2 recoveries in the PSA were relatively low, only once exceeding 45%, in cases where very deep vacuums (~0.01 bar) was used. While these purities and recoveries come nowhere near the required performance for the sub-ambient PSA process, the estimated productivities of the system are too high, offering some guidance for future work with these materials. There is significant room for improvement in the performance of MIL-101(Cr)-cellulose acetate fiber sorbents with more complex cycle designs, as this work used the simplest possible cycle design in an effort to probe the maximum possible productivity in this lab scale experiment. More complex cycles may offer the opportunity to boost recoveries significantly, as upwards of 50% of the CO_2 at

nearly all operating conditions was lost in the blowdown step, an issue that could be partially offset via operation of the cycle with one or more pressure equalization steps.

Thermally modulated MIL-101(Cr) fiber sorbent spinning proved unsuccessful in first attempts, but fiber segments extruded under no draw allowed for some comparison between thermally modulated fibers and fibers without thermal modulation. In these lab-scale experiments, the thermal modulation proved to be limited in its ability to improve performance, though some improvements in purity and productivity were noted when compared to the non-modulated fiber sorbents at constant recovery. Across all cases, the MIL-101(Cr) containing fiber sorbents showed exceptional productivities, with limited purities and recoveries, an issue which may be overcome with proper cycle design.

7.5   References

1.   Ruthven DM. *Principles of Adsorption and Adsorption Processes*. New York: Wiley; 1984.

2.   Ruthven DM, Farooq S, Knaebel KS. *Pressure Swing Adsorption*. New York, NY: VCH Publishers Inc; 1994.

3.   Pimentel B. *Control of Diffusive Time Scales in Zeolite Imidazolate Frameworks for the Kinetic Separation of Light Hydrocarbons*. Atlanta, GA: School of Chemical and Biomolecular Engineering, Georgia Institute of Technology; 2018.

4.   Ho MT, Allinson GW, Wiley DE. Reducing the cost of CO_2 capture from flue gases using pressure swing adsorption. *Ind. Eng. Chem. Res.* Jul 2008;47(14):4883-4890.

5.   Kikkinides ES, Yang R, Cho S. Concentration and recovery of carbon dioxide from flue gas by pressure swing adsorption. *Ind. Eng. Chem. Res.* 1993;32(11):2714-2720.

6.   Kopaygorodsky EM, Guliants VV, Krantz WB. Predictive dynamic model of single-stage Ultra-Rapid Pressure Swing Adsorption. *Aiche Journal.* May 2004;50(5):953-962.

7.   Reynolds SP, Ebner AD, Ritter JA. New Pressure Swing Adsorption Cycles for Carbon Dioxide Sequestration. *Adsorption.* July 01 2005;11(1):531-536.

8.	Labreche Y, Fan YF, Rezaei F, Lively RP, Jones CW, Koros WJ. Poly(amide-imide)/Silica Supported PEI Hollow Fiber Sorbents for Postcombustion CO_2 Capture by RTSA. *Acs Applied Materials & Interfaces.* Nov 2014;6(21):19336-19346.

CHAPTER 8.   DISSERTATION CONCLUSIONS, SUMMARY, AND FUTURE WORK

This dissertation developed an understanding of the potential of sub-ambient CO_2 capture from post-combustion flue gas using pressure swing adsorption, including the development of new materials and strategies to improve PSA performance. The research presented in this dissertation has five main conclusions

1) Sub-ambient pressure swing adsorption has potential for CO_2 capture, but its application will be extremely capital intensive. At the baseline conditions considered in this process the cost of capture, excluding the cost of the actual separation process comes to $47/tonne, with the best case adsorbent based on simulation of a thermally modulated fiber sorbent resulting in costs of capture north of $60/tonne. The development of better adsorbent materials capable of reaching the DOE goals of 95% purity and 90% recovery without additional downstream processing (liquefaction) may lead to cost reductions to make this process competitive.

2) Sorbent leaching during fiber extrusion and solvent exchange, a phenomenon not previously experienced in fiber sorbent manufacturing is both possible and may be overcome through the tuning of the dope composition. The phenomena appear to be due in large part to the spinning of a very small adsorbent particle, small enough to wash out of the porous polymer matrix during the solvent

exchange. The reduction in the fraction of water-soluble polymer additive (PVP) within the polymer dope effectively eliminated the leaching phenomena.

3) The fiber sorbent platform, while currently limited in the number of suitable adsorbents appropriate for the traditional manufacturing process due to solvent and water stability limitations, offers a non-destructive forming approach for adsorbents with limited mechanical stability. Pelletization of MIL-101(Cr) has been shown to result in a 40-60% reduction in the capacity of the adsorbent per gram due to poor stability under very high pressure. Manufacturing of MIL-101(Cr) fiber sorbents meanwhile results in complete retention of the adsorbent properties of the material, due to the manufacturing process not putting the material under high compression stress.

4) Internal, passive thermal management is possible in fiber sorbents via the incorporation of microencapsulated phase change materials. Spinning of microencapsulated phase change material-adsorbent fibers can be performed from a single spinning dope, with both adsorbent and microcapsule surviving with good dispersion throughout the fiber. Indeed this approach allows for the adsorbent particles (heat source) to be located only a few microns from the microcapsule (heat sink). Fibers produced containing microencapsulated phase change materials show a 20-30% improvement in dynamic adsorbent performance metrics while reducing the size of the thermal front generated during adsorption.

5) Sub-ambient pressure swing adsorption using high capacity fiber sorbents was demonstrated at the lab scale using a single bed cycle. CO_2 purities 45% were achieved in the cycle, but with rather low recoveries bed cycles. Preliminary thermally modulated fiber sorbent performance was demonstrated, but low sorbent loading in the fiber combined with large dead volumes in the system resulted in relatively poorer performance than that of the non-modulated case. In both sets of fibers, productivities far exceeded the current state of the art pellet PSA system at ambient conditions.

8.1 Dissertation Overview

This dissertation explored a new process approach to post-combustion CO_2 capture via sub-ambient pressure swing adsorption. The process relies on a significant energy and heat integration to enable enhancement in adsorbent performance and suffers high capital cost in making that possible. Methods of spinning off a new MOF material, MIL-101(Cr), into fiber adsorbents was developed, overcoming the effects of adsorbent leaching experienced due in part to the synthesized adsorbent's small particle size. A novel heat management approach for pressure swing adsorption, incorporation of microencapsulated phase change material within the structured sorbent, was developed and proven effective at managing generated heat. Structured adsorbent materials, MIL-101(Cr)-cellulose acetate fiber sorbents, produced as a part of this work exhibit capacities for CO_2 2-3x higher than the current state of the art adsorbents, and their performance for sub-ambient post-combustion CO_2 capture was probed.

8.2 Summary

After Chapter 1 for objectives were laid out to guide the research plan of this dissertation.

8.2.1 Objective 1

Development of a process model for sub-ambient pressure-driven separation and exploration of its economic and energetic potential for post-combustion CO_2 capture from coal combustion derived flue gas.

Chapter Four presented a process model that enables sub-ambient CO_2 capture via pressure-driven separation (pressure swing adsorption) combined with CO_2 rich product liquefaction to reach pipeline specifications. The feasibility of the process is strongly coupled to the application of Joule-Thompson cooling to allow the sub-ambient operation, water removal, and liquefaction of the CO_2 enriched product, without requiring an external refrigeration cycle. Sub-ambient CO_2 capture via pressure swing adsorption is a capital-intensive approach to post-combustion CO_2 capture, such that even if the adsorbent material were free the cost of capture would exceed $40/tonne$_{CO2}$. Once adsorbents achieve productivities exceeding 0.015 mol kg^{-1} sec^{-1} the cost savings of additional productivity reaches diminishing returns, such that other PSA operating parameters like CO_2 product purity and recovery become more important in the economics of capture. Looking at the energetics of the process, the upstream compression is key to enabling the sub-ambient process, with a minimum pressure of 6 bar required such that all heat can be removed. The temperature pinch point of the process occurs at the boiling point reached in the

liquefaction column, so the liquefaction pressure becomes an important tuning parameter to enable sub-optimal PSA purities.

8.2.2   Objective 2

Scale-up and manufacture of MIL-101(Cr) fiber sorbents for sub-ambient CO_2 Capture

Chapter Five presented the process of scaling up and spinning an adsorbent material, MIL-101(Cr), capable of extremely high operating capacities for sub-ambient CO_2 capture. MIL-101(Cr) fiber sorbents were shown to have good performance for separating CO_2 from simulated flue gas, with helium assisted desorption experiments showing purities as high as 75% CO_2 achievable. Besides its high capacity for CO_2 and ideal stability for adsorbent spinning, MIL-101(Cr) proved an interesting adsorbent to spin due to its incompatibility with pelletization. Its poor mechanical stability under tons of compressive force leads to 40-60% reductions in its adsorption performance when structured into pellets, but in fibers, it never experiences those sorts of stresses. The successful spinning of MIL-101(Cr) proved a new benefit to the fiber adsorbent platform, the ability to non-destructively manufacture a scalable structured adsorbent contactor that suffered in its manufacture into alternate structures.

The small particle sizes produced as a part of the scale-up synthesis were believed to lead to a significant amount of sorbent loss, or *leaching*, during the spinning process. Two approaches to overcoming the challenge of sorbent leaching were presented, agglomerate spinning and PVP reduction in the adsorbent dope. Agglomerate spinning proved to be a workable solution in syringe extrusions, but significant leaching was still

experienced during the full-scale spin, coupled with an extremely challenging manufacturing process. Optimization of the preparation of agglomerate dopes and alternative spinneret dimensions would be necessary to prove this method achievable at the necessary scale. PVP reduction in the dope composition proved to be the key parameter to the spinning of MIL-101(Cr) nanoparticles. The exact role PVP plays in the leaching process will need to be studied further, but with reductions in PVP fraction in the dope MIL-101(Cr) fibers were successfully spun.

8.2.3   Objective 3

Development of internal passive thermal management solutions for fiber sorbent contactors

Chapter 6 focused on the development of fiber adsorbents capable of managing thermal swings internally, without the need for external heat management systems. Microencapsulated phase change materials, materials which freeze and melt over small temperature ranges near a desired operating condition were considered for this application. Their application could simplify the manufacturing process cutting out multiple challenging steps while offering very short mass transfer distances between the thermal source (adsorbent particles) and thermal sink (μPCM). The μPCM proved to be spinnable, and weight loadings of pure μPCM-cellulose acetate fibers were found to reach as high as 75wt%. Once spinnability was confirmed, UiO-66 – μPCM – Cellulose acetate fiber sorbents of equal loading were manufactured, showing co-dispersion of both materials throughout the fiber substructure, ideal for heat management. Comparing these materials dynamic adsorption performance at temperatures near and far from the onset of phase

change required for heat management resulted in a 20-25% improvement in the "breakthrough capacity" of the heat managed fibers. The thermal front developed in the fiber beds were compared between fibers with active thermal management and fibers with µPCM far from their melting point, showing a reduction in the amplitude of the thermal front created.

8.2.4 Objective 4

Operation and scoping of the potential performance of sub-ambient CO_2 capture via PSA using fiber sorbents

Once the high capacity fiber sorbents had been successfully manufactured, the next step in process development is to operate and work to develop a deeper understanding of the performance of the sub-ambient PSA unit using these materials, discussed in Chapter Seven. To this end single bed pressure swing adsorption cycles in 75 fiber of 50 weight % MIL-101(Cr)-cellulose acetate fiber sorbents were packed into 3/8" Swagelok ® modules were performed at a variety of operating conditions to begin to probe the real-world potential of these materials for the sub-ambient CO_2 capture process. Purities as high as XX% with relatively low recoveries of XX% were found for the single bed cycles using the MIL-101(Cr) fibers, demonstrating the materials could purify CO_2 from flue gas. As single bed cycles are effectively the simplest form of PSA, we expect significant performance improvement to be attainable with more complex cycle design, albeit with potential tradeoffs in PSA productivity. Preliminary cycles were performed using thermally modulated µPCM-MIL-101(Cr) fiber sorbents, but the low weight loading of adsorbent material in these fibers led to limitations on the purity and recovery which could

be attained due to system dead-volumes flattening the response of change in operating parameters.

8.3   Future Directions

8.3.1   *The Role of Polyvinylpyrrolidone in Fiber Sorbent Phase Inversion*

One conclusion reached as a portion of the work of this dissertation was the finding that high ratios of polyvinylpyrrolidone: cellulose acetate enabled the leaching of smaller than 1-micron adsorbent from the polymer filament during the solvent exchange. While this knowledge will be useful for the development of future fiber sorbents, more valuable information could be gained by studying the mechanism of sorbent leaching due to PVP. PVP is a valuable additive in the fiber sorbent manufacturing process, as its viscosity-enhancing properties allow for the fraction of cellulose acetate in the fiber to be reduced, which in turn boosts the feasible weight fraction of adsorbent particles within the fiber.

A parametric study of different fiber sorbent dope compositions should allow for the probing of the exact role of PVP to the leaching behavior. Fiber spinning of multiple different adsorbent materials (varying particle size and particle density) using dopes of comparable viscosity but different PVP: polymer ratio should be performed. By characterizing the degree of particle leaching via thermogravimetric analysis, as well as qualitative (scanning electron microscopy) and quantitative (Hg Porosimetry to determine fiber pore size distribution) studies of the fiber morphology a deeper understanding of the role of PVP in fiber sorbent spinning can be realized. Ultimately, the discovery of the mechanisms of sorbent leaching which may occur in the fiber spinning process will be key to further developing the fiber sorbent platform.

8.3.2   Multi-bed Sub-ambient Pressure Swing Adsorption

The work discussed in Chapter 7 of this dissertation found that sorbent productivity and CO_2 recovery are greatly limited in the case of single bed pressure swing adsorption performed at a laboratory scale. While a variety of factors play a role in the less than stellar performance of the system, more complicated cycle designs can help to improve the performance of the PSA system. The single bed experiments run as part of this dissertation do offer some insight into the limitations of the MIL-101(Cr) fiber sorbent platform for application to sub-ambient CO_2 capture. As mentioned in the introduction of this dissertation, a truly optimized adsorptive separation will leverage all possible avenues (cycle design, sorbent design, and contactor design) to reach the best performance. This dissertation developed the sorbent and contactor, but there is still an opportunity to optimize the cycles for these materials.

The PSA system used for experiments in this work can begin to probe the performance improvement of more complex cycle designs. Of particular interest to the MIL-101(Cr), fiber sorbent platform would be the addition of one or more pressure equalization steps, and a light product pressurization. The lower than required recoveries and productivities for economical sub-ambient CO_2 capture could be improved simultaneously, with little loss in purity through the application of both pressure equalization and light product pressurization. While adding additional steps to an adsorption cycle typically reduces the productivity of the system (due to the cycle taking longer to complete), adding steps to improve recovery could prove more important. By keeping more of the CO_2 in the light product and blowdown inside the adsorption system the recovery should be improved significantly. With that said, less gas will be treated in

each cycle since more gas is being recycled between the beds, so the tradeoff between productivity improvement due to boosted recovery, versus less overall gas being treated per cycle (and second) will be an important balance to achieve.

8.3.3   Post-Spinning Synthesis of MOF Fiber Sorbents

As fiber adsorbents are still in their technological adolescence, there are great opportunities to develop methods of manufacturing to overcome some of the more problematic steps in the fiber sorbent production process.[1] While MIL-101(Cr) and UiO-66 both proved to be good adsorbents for sub-ambient capture, a thorough review of the CoRE MOF database has shown several adsorbents have greater potential for sub-ambient PSA.[2] All but one of these adsorbents lack the required stability to be spun, so the development of alternative approaches to incorporating materials into fiber sorbents will be necessary to get these truly exceptional materials into the fiber morphology. The work of Pimentel et al. offers an interesting jumping-off point, with the spinning of reactant seeds to promote targeted growth of adsorbent inside the fiber, allowing for the production of HKUST-1 fiber adsorbents that could not otherwise be spun.[3] Two main challenges exist for generalizing that approach to other fibers. First, the chemistry (hydroxy double salt intermediate synthesis of MOFs) has only been extended to a few of the most common adsorbents. An interesting direction the field of MOF synthesis has gone in since that publication has been the synthesis of MOFs from solid reactant systems, particularly via mechanochemical synthesis. While mechanochemical synthesis is probably not going to be a path forward for post-spinning synthesis, perhaps the materials capable of being synthesized from solid reactants can also be produced from one solid reactant (seed material) with the other reactants dissolved in a solvent. The discovery of adaptations in

the adsorbent synthesis that could suit the fiber platform post-spinning should continue to be a great area of interest in giving flexibility to the fiber sorbent platform.

8.3.4   *Carbon Molecular Sieve Fiber Sorbents for Kinetic PSA*

Carbon molecular sieves are a class of kinetic adsorbent already being applied in industry for rapidly cycled pressure swing adsorption in oxygen production. While Zeolites, MOFs, amino-silicas, and polymers loaded with amines have already been manufactured into fiber sorbents,[4] carbonaceous materials, and particularly CMS materials offer opportunities for the fiber sorbent platform to be applied to a whole new area of the separation. An opportune direction to further develop fiber sorbents would be to build off the recent developments in carbon molecularly sieve hollow fiber membrane production and instead produce hollow or monolith carbon molecular sieve fiber sorbents.[5,6] These materials would be manufactured in a similar way to the CMS membranes (retaining the mesoporous CMS backbone via polymer selection and/or crosslinking), but instead of spinning fibers with a skin layer to perform the separation, the entire CMS fiber backbone could be used for RPSA separation of gases. Recent advances in polymer synthesis and pyrolysis methodology have allowed for the fine-tuning of the pore size distribution of CMS materials to serve many different applications.[6] As polymeric fiber spinning without concern for the skin layer greatly simplifies the manufacturing process, the application of CMS fiber sorbents could allow for these materials to make a more immediate impact on many challenging separations, where the spinning of CMS hollow fiber membranes may prove especially difficult, the concept of this is presented in **Figure 8-1**.
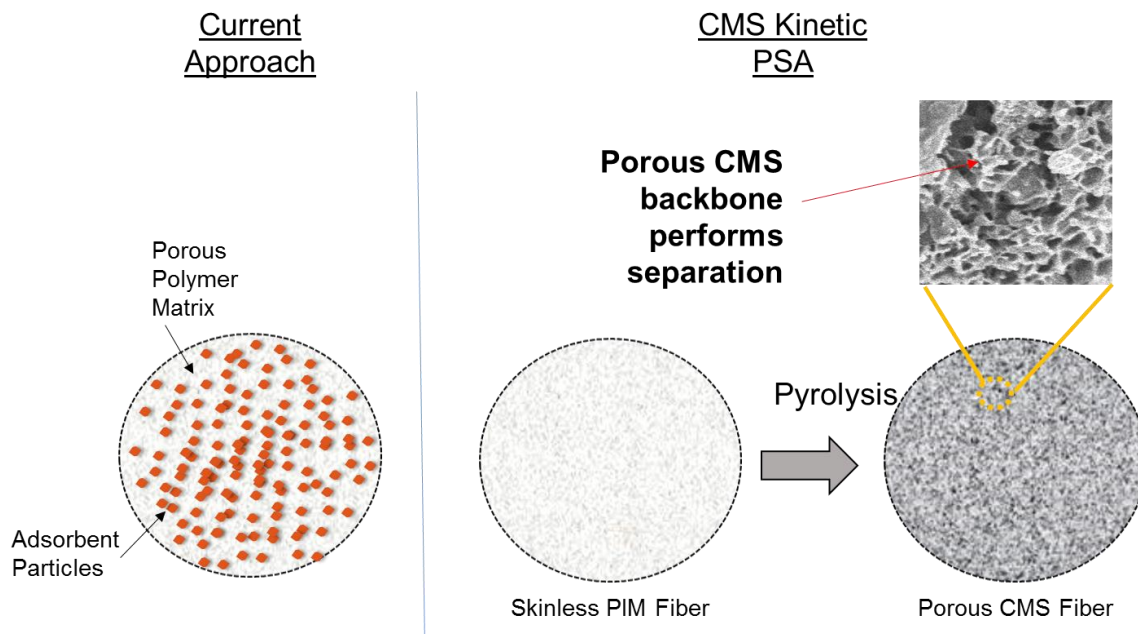
Figure 8-1. Incorporating new PIM CMS materials offers a simpler manufacturing as compared to membrane spinning for diffusion based separarations

8.3.5 *Experimental Comparison of Different Structures for PSA*

In Chapter 7 preliminary results were shown comparing MIL-101(Cr) fiber sorbents to MIL-101(Cr)-µPCM fiber sorbents. In general, these sorts of comparisons between differently structured sorbents or structured geometries are rarely performed or reported, due to a variety of challenges. For the community as a whole, the fundamental information collected from experiments like fixed bed breakthroughs and desorption profiles can be combined with high fidelity modeling do a good job of providing proof of the benefits of new structured sorbent contactors. Still, designing and performing experimental comparisons between differently structured contactors is an area of study that can and should be expanded upon.[1,4]

311

While the main impediment to these studies is the inherent time commitment required to optimize an adsorption cycle with multiple different adsorbent structures, a less discussed challenge, particularly of experiments run at lab or bench scale (which may be less relevant at pilot scale), is how to design experiments for a fair comparison. As structured contactors like fibers and monoliths will tend to have a lower sorbent density inside the same bed volume[4], one approach would be to compare beds containing the same sorbent mass expanding the volume of the structured beds. This comparison may prove unfair since the larger volume may lead to more prevalent heat fronts in one geometry or the other. Similarly, comparing with the same bed volume may undersell the structured contactors since there is *less* adsorbent material available to treat the gas, reducing the maximum productivity that can be achieved for the same bed. In the end, this is among the reason why the simulation work that is already carried out is so important, as it can allow for all these variables to be compared holistically, without hundreds or thousands of man-hours. Still, additional exploration of this space experimentally at lab and bench-scale will be key to providing the evidence to convince decision-makers of the potential of structured contactors.

8.4   References

1.   Lee YH, Jeong J, Kim K, Hyun T, Jamal A, Koh D-Y. Microporous Materials in Scalable Shapes: Fiber Sorbents. *Chemistry of Materials.* 2020/09/08 2020;32(17):7081-7104.

2.   Park J, Lively RP, Sholl DS. Establishing Upper Bounds on CO_2 Swing Capacity in Sub-Ambient Pressure Swing Adsorption via Molecular Simulation of Metal-Organic Frameworks. *Journal of Materials Chemistry A.* 2017.

3.   Pimentel BR, Fultz AW, Presnell KV, Lively RP. Synthesis of Water-Sensitive Metal-Organic Frameworks within Fiber Sorbent Modules. *Ind. Eng. Chem. Res.* May 2017;56(17):5070-5077.

4.   DeWitt SJA, Sinha A, Kalyanaraman J, Zhang F, Realff MJ, Lively RP. Critical Comparison of Structured Contactors for Adsorption-Based Gas Separations. *Annual Review of Chemical and Biomolecular Engineering.* 2018;9(1):129-152.

5.   Koh D-Y, McCool BA, Deckman HW, Lively RP. Reverse osmosis molecular differentiation of organic liquids using carbon molecular sieve membranes. *Science.* 2016;353(6301):804-807.

6.   Ma Y, Jue ML, Zhang F, Mathias R, Jang HY, Lively RP. Creation of Well-Defined "Mid-Sized" Micropores in Carbon Molecular Sieve Membranes. *Angewandte Chemie International Edition.* 2019;58(38):13259-13265.

APPENDIX A. MODELLING OF SUB-AMBIENT FIBER PSA AT INDUSTRIAL SCALE

A number of references are made to Pareto frontiers calculated to support the case studies carried out in Chapter 4. This Appendix details the methods and results generated by collaborators in support of

A.1   Molecular Modelling Details

Molecular modeling of adsorption of single-component CO_2 and N_2 adsorption in MOFs UiO-66 and MIL-101(Cr) were performed by Grand Canonical Monte Carlo (GCMC) simulations[2-4] using the RASPA simulation package[5,6]. As-distributed MOF .cif files from the RASPA package[5,6] were used for the crystal structures of UiO-66 and MIL-101(Cr). To perform GCMC appropriate force fields are needed to describe non-bonding interactions such as van der Waals and Coulombic interactions for sorbate/sorbent and sorbate/sorbate interactions. Standard force fields were used to compute van der Waals interaction, namely the UFF[7] and the TraPPE[8] force field. Lennard-Jones parameters for MOF atoms and quadrupolar CO_2, N_2 molecules were taken from UFF and TraPPE force field, respectively. Sorbate/sorbent interactions were defined with Lorentz-Berthelot mixing rules.[9] Truncated potentials with tail corrections are applied where Lennard-Jones interactions are truncated at 12 Å. Simulation boxes are expanded to at least 26 Å along *x*, *y*, and *z* dimensions. Periodic boundary conditions were defined in all dimensions, and adsorbents and adsorbates were approximated as rigid. Coulombic interactions were

modeled pairwise with a long-range Ewald summation scheme.[10] These interactions are computed via the DDEC point charges for MOF atoms[11-13] and TraPPE charges for CO_2 and N_2 molecules[5,6].

All GCMC simulations included 5,000 initialization cycles to equilibrate the positions of the atoms in the system followed by 50,000 production cycles. Initial tests indicated good convergence using these numbers of cycles. A Monte Carlo cycle consists of N steps where N is the number of molecules in the system. Attempted Monte Carlo moves include translation, rotation, regrowth, reinsertion, deletion and insertion of sorbates at the identical probabilities; either accepted or rejected according to Boltzmann-type weighting criteria.

A.2   VPSA Process Modelling

A fixed-bed packed with thermally-modulated fiber composites was considered in the applied VPSA cycle modeling. A complete account of details describing this model can be found in Rubiera Landa et al[14]. Table A-1 below lists the equations for full-order modeling of VPSA cycles applied in this publication. Table A-2 & Table A-3 provide auxiliary expressions that supplement the set of PDEs. The parameter values applied in this model are given in Table A-119 & Table A-10.

Table A-1. Dynamic fiber-composite packed-bed adsorber equations.

Mass Balance for component i
$$\frac{\partial c_i}{\partial t} + \frac{1-\epsilon}{\epsilon}\,(1-\psi)\,\varphi\,\rho_{\mathrm{MOF}}\frac{\partial q_i}{\partial t} = -\frac{\partial}{\partial z}\,(uc_i) + D_{\mathrm{ax},i}\frac{\partial^2 c_i}{\partial z^2}, \quad i = 1, \ldots, N.$$
Adsorbed-phase concentrations
$$\frac{\partial q_i}{\partial t} = k_i\,(q_i^{\star} - q_i), \quad i = 1, \ldots, N.$$
Total mass balance
$$\frac{\partial}{\partial t}\left(\frac{p}{\Re T}\right) + \frac{1-\epsilon}{\epsilon}\,(1-\psi)\,\varphi\,\rho_{\mathrm{MOF}}\sum_{i=1}^{N}\frac{\partial q_i}{\partial t} = -\frac{\partial}{\partial z}\left(u\frac{p}{\Re T}\right).$$
Energy balance
$$\hat{\rho}_g\hat{C}_g\frac{\partial T}{\partial t} - \frac{\partial p}{\partial t} + \frac{1-\epsilon}{\epsilon}\frac{\partial H_s}{\partial t} = -\frac{\partial}{\partial z}\left(u\hat{h}_g\right) + \frac{\partial}{\partial z}\left(k_g\frac{\partial T}{\partial z}\right) + \frac{1-\epsilon}{\epsilon}\frac{\partial}{\partial z}\left(k_{f,\mathrm{eff.}}\frac{\partial T}{\partial z}\right) + \frac{1-\epsilon}{\epsilon}\dot{\mathfrak{S}}.$$ $$\frac{\partial H_s}{\partial t} = \frac{\partial}{\partial t}H_{\mathrm{PCM}} + \frac{\partial}{\partial t}H_{\mathrm{MOF}} + \frac{\partial}{\partial t}H_{\mathrm{poly.}} + \sum_{i=1}^{N}\frac{\partial}{\partial t}H_{i,\mathrm{ads.}}.$$ $$\frac{\partial}{\partial t}H_{\mathrm{PCM}} = \psi\left[\rho_{\mathrm{PCM}}C_{\mathrm{PCM}} + \rho_{\mathrm{PCM}}\frac{\mathrm{d}}{\mathrm{d}T}\lambda_{\mathrm{PCM}}\right]\frac{\partial T}{\partial t}$$ $$\frac{\partial}{\partial t}H_{\mathrm{MOF}} = (1-\psi)\,\varphi\,\rho_{\mathrm{MOF}}C_{\mathrm{MOF}}\frac{\partial T}{\partial t}$$ $$\frac{\partial}{\partial t}H_{\mathrm{poly.}} = (1-\psi)\,(1-\varphi)\,\rho_{\mathrm{poly.}}C_{\mathrm{poly.}}\frac{\partial T}{\partial t}$$ $$\sum_{i=1}^{N}\frac{\partial}{\partial t}H_{i,\mathrm{ads.}} = (1-\psi)\,\varphi\,\rho_{\mathrm{MOF}}\frac{\partial}{\partial t}\left[\sum_{i=1}^{N}q_i\,\hat{C}_{i,\mathrm{ads.}}T\right]$$ $$\frac{1-\epsilon}{\epsilon}\dot{\mathfrak{S}} = \frac{1-\epsilon}{\epsilon}\,(1-\psi)\,\varphi\,\rho_{\mathrm{MOF}}\sum_{i=1}^{N}(-\Delta H_{\mathrm{ads.},i})\frac{\partial q_i}{\partial t}.$$
Momentum balance
$$u = -\beta_{\mathrm{bed}}\frac{\partial p}{\partial z} \qquad \beta_{\mathrm{bed}} \equiv \frac{1}{\mu_g}\left[\frac{r_f^2 - 3r_{\mathrm{fs}}^2}{8} + \frac{1}{2}\frac{r_{\mathrm{fs}}^4}{r_{\mathrm{fs}}^2 - r_f^2}\ln\left[\frac{r_{\mathrm{fs}}}{r_f}\right]\right].$$

Table A-2. Auxilary expressions and Equations

Total bed porosity

$$\epsilon = \frac{\epsilon_f + \left[\dfrac{1 - \phi_p}{\phi_p} \right]}{1 + \left[\dfrac{1 - \phi_p}{\phi_p} \right]}$$

Phase ratio

$$\frac{1 - \epsilon}{\epsilon} = \frac{\left[\dfrac{\phi_p}{1 - \phi_p} \right]}{\left[\dfrac{\phi_p}{1 - \phi_p} \right] \epsilon_f + 1} \left(1 - \epsilon_f \right)$$

Mass transfer

$$k_i = k_i^{\text{macro}} \frac{c_i}{q_i^\star}, \quad q_i^\star = f(c, T), \quad i = 1, \dots, N.$$

$$k_i^{\text{macro}} = \frac{8}{r_f^2} D_{fp,i} \left[\frac{\epsilon_f}{1 - \epsilon_f} \right] \frac{1}{(1 - \psi) \varphi \rho_{\text{MOF}}}$$

$$D_{fp,i} = D_{g,i} \frac{\epsilon_f}{\tau_f^2}, \quad i = 1, \dots, N.$$

$$D_{g,i} = 0.0018583 \sqrt{T^3 \left[\frac{1}{M_{\text{N}_2}} + \frac{1}{M_{\text{CO}_2}} \right]} \left[\frac{1}{p \left[\sigma_{12}^{\text{LJ}} \right]^2 \Omega^{\text{LJ}}} \right]$$

Fiber tortuosity estimation

$$\tau_f = 1.0 - \ln \left[\epsilon_f \right].$$

Volumetric ratio of PCM to solids in fiber composite

$$\psi := \frac{V_{\text{PCM}}}{V_{\text{PCM}} + V_{\text{MOF}} + V_{\text{poly.}}} = \frac{\omega_{\text{PCM}}/\rho_{\text{PCM},s}}{\omega_{\text{PCM}}/\rho_{\text{PCM},s} + \omega_{\text{MOF}}/\rho_{\text{MOF}} + \omega_{\text{poly.}}/\rho_{\text{poly.}}}.$$

Volumetric ratio of MOF to combined volume of polymer and MOF

$$\varphi := \frac{V_{\text{MOF}}}{V_{\text{MOF}} + V_{\text{poly.}}} = \frac{\omega_{\text{MOF}}/\rho_{\text{MOF}}}{\omega_{\text{MOF}}/\rho_{\text{MOF}} + \omega_{\text{poly.}}/\rho_{\text{poly.}}}$$

Weight fractions of fiber components

$$\omega_{\text{PCM}} = f(\omega_{\text{MOF}}) = 1.0 - \omega_{\text{MOF}} - \omega_{\text{poly.}}$$

Table A-3. Smooth Interface model applied in fiber composite modeling

$$\lambda_{PCM} = f(T) = \frac{\Delta H_{fus.}}{1 + \exp\left[-\dfrac{T - T_{fus.}}{\varsigma_{tr.}}\right]} \quad \frac{d}{dT}\lambda_{PCM} = \frac{\Delta H_{fus.}\exp\left[\dfrac{T_{fus.} - T}{\varsigma_{tr.}}\right]}{\varsigma_{tr.}\left[1 + \exp\left[\dfrac{T_{fus.} - T}{\varsigma_{tr.}}\right]\right]^2}$$

$$\rho_{PCM,s} - \frac{\rho_{PCM,s} - \rho_{PCM,l}}{1 + \exp\left[-\dfrac{T - T_{ph.}}{\varsigma_{ph.}}\right]} \quad C_{PCM} = f(T) = C_{PCM,s} - \frac{C_{PCM,l} - C_{PCM,s}}{1 + \exp\left[-\dfrac{T - T_{ph.}}{\varsigma_{ph.}}\right]}$$

Appropriate boundary conditions and initial conditions required for VPSA-cycle modeling are given in Table A-4 & Table A-5.

Table A-4. Boundary Conditions (BCs) for 4-step VPSA cycle w/ LPP operation

at $z = 0$	at $z = L$
Counter-current pressurization	
$\dfrac{\partial}{\partial z} y_i(t, z = 0) = 0,\ i = 1, \ldots, N$; $u(t, z = 0) = 0$; $\dfrac{\partial}{\partial z} p(t, z = 0) = 0$; $\dfrac{\partial}{\partial z} T(t, z = 0) = 0.$	$y_i(t, z = L) = y_{i,\mathrm{Pr}},\ i = 1, \ldots, N$; $u(t, z = L) = f_{\mathrm{valve}}(\Delta p, T, \cdots)$; $\dfrac{\partial}{\partial z} p(t, z = L) = -\dfrac{1}{\beta_{\mathrm{bed}}} u(t, z = L)$; $T(t, z = L) = T_{\mathrm{Pr}}.$
Adsorption	
$y_i(t, z = 0) = y_{i,\mathrm{feed}},\ i = 1, \ldots, N$; $u(t, z = 0) = u_{\mathrm{feed}}$; $\dfrac{\partial}{\partial z} p(t, z = 0) = -\dfrac{1}{\beta_{\mathrm{bed}}} u(t, z = 0)$; $T(t, z = 0) = T_{\mathrm{feed}}.$	$\dfrac{\partial}{\partial z} y_i(t, z = L) = 0,\ i = 1, \ldots, N$; $u(t, z = L) = -\beta_{\mathrm{bed}} \dfrac{\partial}{\partial z} p(t, z = L)$; $p(t, z = L) = p_{\mathrm{Ad}} = p_{\mathrm{high}}$ $\dfrac{\partial}{\partial z} T(t, z = L) = 0.$
Co-current blowdown	
$\dfrac{\partial}{\partial z} y_i(t, z = 0) = 0,\ i = 1, \ldots, N$; $u(t, z = 0) = 0$; $\dfrac{\partial}{\partial z} p(t, z = 0) = 0$; $\dfrac{\partial}{\partial z} T(t, z = 0) = 0.$	$\dfrac{\partial}{\partial z} y_i(t, z = L) = 0,\ i = 1, \ldots, N$; $u(t, z = L) = u_{\mathrm{Bd}}$; $\dfrac{\partial}{\partial z} p(t, z = L) = -\dfrac{1}{\beta_{\mathrm{bed}}} u(t, z = L)$; $\dfrac{\partial}{\partial z} T(t, z = L) = 0.$
Counter-current evacuation	
$\dfrac{\partial}{\partial z} y_i(t, z = 0) = 0,\ i = 1, \ldots, N$; $u(t, z = 0) = u_{\mathrm{Ev}}$; $\dfrac{\partial}{\partial z} p(t, z = 0) = -\dfrac{1}{\beta_{\mathrm{bed}}} u(t, z = 0)$; $\dfrac{\partial}{\partial z} T(t, z = 0) = 0.$	$\dfrac{\partial}{\partial z} y_i(t, z = L) = 0,\ i = 1, \ldots, N$; $u(t, z = L) = 0$; $\dfrac{\partial}{\partial z} p(t, z = L) = 0$; $\dfrac{\partial}{\partial z} T(t, z = L) = 0.$

Valve expression applied in the BC for the pressurization step.

$u = \min[\, u_1, u_2 \,] = f_{\mathrm{valve}}(\Delta p, T, \cdots)$ $u_1 = k_V\, p_{\mathrm{high}}\ \sqrt{\mathrm{abs}\left[\dfrac{1}{\bar{M}_g}\left[1 - \left(\dfrac{p}{p_{\mathrm{high}}}\right)^2 \right] \right]} \qquad u_2 = k_V\, p_{\mathrm{high}}\ \sqrt{\mathrm{abs}\left[\dfrac{1}{\bar{M}_g}\left[1 - \left(\dfrac{1}{p_{\mathrm{crit.}}}\right)^2 \right] \right]}$ $p_{\mathrm{crit.}} = \left[\dfrac{2}{1+\gamma} \right]^{\frac{\gamma}{1-\gamma}}$ $\qquad\qquad\qquad\qquad \bar{M}_g = y_{\mathrm{N}_2} M_{\mathrm{N}_2} + y_{\mathrm{CO}_2} M_{\mathrm{CO}_2}$

Table A-5. Initial Conditions (ICs) for 4-step VPSA cycle w/ LPP operation.

$$
\begin{aligned}
&y_i(t = 0, z) = y_{i0}, \quad i = 1, \ldots, N \\
&q_i(t = 0, z) = q_{i0} = q_{i0}^{\star} \\
&p(t = 0, z) = p_0 \\
&T(t = 0, z) = T_0 \\
&x(t = 0, z) = x_0 \\
&x_0 = \left[\, y_{10}, \ldots, y_{N0}, q_{10}, \ldots, q_{N0}, p_0, T_0 \,\right]^T
\end{aligned}
$$

Cyclic operation was implemented by with the following ICs for the kth step as follows:

Counter-current pressurization	$x_k(t_{\text{Pr,start}}, z) = \begin{cases} x_0 & \text{for} \quad k = 1, \\ x_{k-1}(t_{\text{Ev,end}}, z) & \text{otherwise.} \end{cases}$
Adsorption	$x_k(t_{\text{Ad,start}}, z) = x_k(t_{\text{Pr,end}}, z).$
Co-current blowdown	$x_k(t_{\text{Bd,start}}, z) = x_k(t_{\text{Ad,end}}, z).$
Counter-current evacuation	$x_k(t_{\text{Ev,start}}, z) = x_k(t_{\text{Bd,end}}, z).$

The VPSA cycle performance is estimated using the set of performance metrics listed in Table A-6.

Table A-6. Process Performance Parameters

Purity
$$\Phi_{\text{Pu},i} = \frac{n_i^{\text{E}}}{n_{\text{tot}}^{\text{E}}} = \frac{n_i^{\text{E}}}{\sum\limits_{i=1}^{N} n_i^{\text{E}}}.$$
Recovery
$$\Phi_{\text{Re},i} = \frac{n_i^{\text{E}}}{n_{i,\text{Pr}} + n_{i,\text{feed}}}.$$
Productivity
$$\Phi_{\text{Prod},i} = \frac{n_i^{\text{E}}}{m_{\text{MOF}}\, t_{\text{cycle}}},$$
Specific energy consumption
$$\Phi_{\text{En},i} = \frac{W_{\text{Pr}} + W_{\text{Ad}} + W_{\text{Bd}} + W_{\text{Ev}}}{n_i^{\text{E}}}.$$ $$W_{\text{Pr}} = 0.$$ $$W_{\text{Ad}} = \int_{t_{\text{Ad,start}}}^{t_{\text{Ad,end}}} \frac{1}{\eta_{\text{compr.}}} \frac{\gamma}{\gamma - 1}\, p(t, z = L)\, Q(t, z = L) \left[\left(\frac{p(t, z = L)}{p_{\text{fg}}} \right)^{\frac{\gamma - 1}{\gamma}} - 1 \right] \mathrm{d}t.$$ $$W_{\text{Bd}} = 0.$$ $$W_{\text{Ev}} = \int_{t_{\text{Ev,start}}}^{t_{\text{Ev,end}}} \frac{1}{\eta_{\text{vac.}}} \frac{\gamma}{\gamma - 1}\, p(t, z = 0)\, Q(t, z = 0) \left[\left(\frac{p(t, z = 0)}{p_{\text{Ev}}} \right)^{\frac{\gamma - 1}{\gamma}} - 1 \right] \mathrm{d}t.$$

In the case of MOFs MIL-101(Cr) and UiO-66, we applied Ideal Adsorbed Solution Theory (IAST)[15] to estimate mixture equilibrim with governing equations given in Table A-7 below. A hybrid routine combining the solution method reported by Rubiera Landa et al.[16] and the generalized FastIAS method of O'Brien & Myers[17] warranted efficiency & robustness in the equilibrium calculations queried by the dynamic adsorber modeling.

Table A-7. Equations of IAST

Description	Equation
Raoult's law	$c_i = c_{\text{tot}}\, y_i = c_i^0(T, \pi)\, x_i$
Equilibrium condition	$\Pi \equiv \Pi_1 \overset{!}{=} \cdots \overset{!}{=} \Pi_N$
Spreading pressure	$\Pi_i = f(c_i^0) \equiv \dfrac{\mathcal{A}}{\mathfrak{R}\,T}\pi_i(c_i^0) = \displaystyle\int\limits_0^{c_i^0} \dfrac{q_i^0}{s}\,\mathrm{d}s$
Closure	$\displaystyle\sum_{i=1}^N x_i = \sum_{i=1}^N \dfrac{c_i}{c_i^0} = 1$
Total adsorbed phase concentration	$q_{\text{tot}} = \left[\displaystyle\sum_{i=1}^N \dfrac{x_i}{q_i^0}\right]^{-1} = \left[\displaystyle\sum_{i=1}^N \dfrac{1}{q_i^0}\dfrac{c_i}{c_i^0}\right]^{-1}$
Adsorbed phase concentration for component i	$q_i = q_{\text{tot}}\, x_i, \quad i = 1, \ldots, N$

Single-component adsorption isotherm equations were parameterized from molecular modeling results for N_2 and CO_2 species adsorbed by both MOFs. We fit the in-silico equilibrium data to the dual-site Langmuir (DSL) equation for each gas. These adsorption isotherms are displayed in Figure A-1 and the corresponding parameters are listed in Table A-9.

For zeolite 13X, we applied the extended dual-site Langmuir model (Table A-8) for mixture equilibrium evaluation with corresponding parameters reported by Haghpanah et al.[18] (listed in Table A-9). We assumed that these parameter values are also valid in the sub-ambient temperature range investigated for the MOFs.

Table A-8. Extended dual-site Langmuir equation

$$c_i = \frac{p}{\Re T} y_i \qquad b_{i1} = b_{i10} \exp\left[\frac{B_{i1}}{T}\right], \quad b_{i2} = b_{i20} \exp\left[\frac{B_{i2}}{T}\right],$$

$$q_i = q_{i1}^{\text{sat}} \frac{b_{i1}c_i}{1 + b_{11}c_1 + b_{12}c_2} + q_{i2}^{\text{sat}} \frac{b_{i2}c_i}{1 + b_{21}c_1 + b_{22}c_2}, \quad i = 1, 2.$$
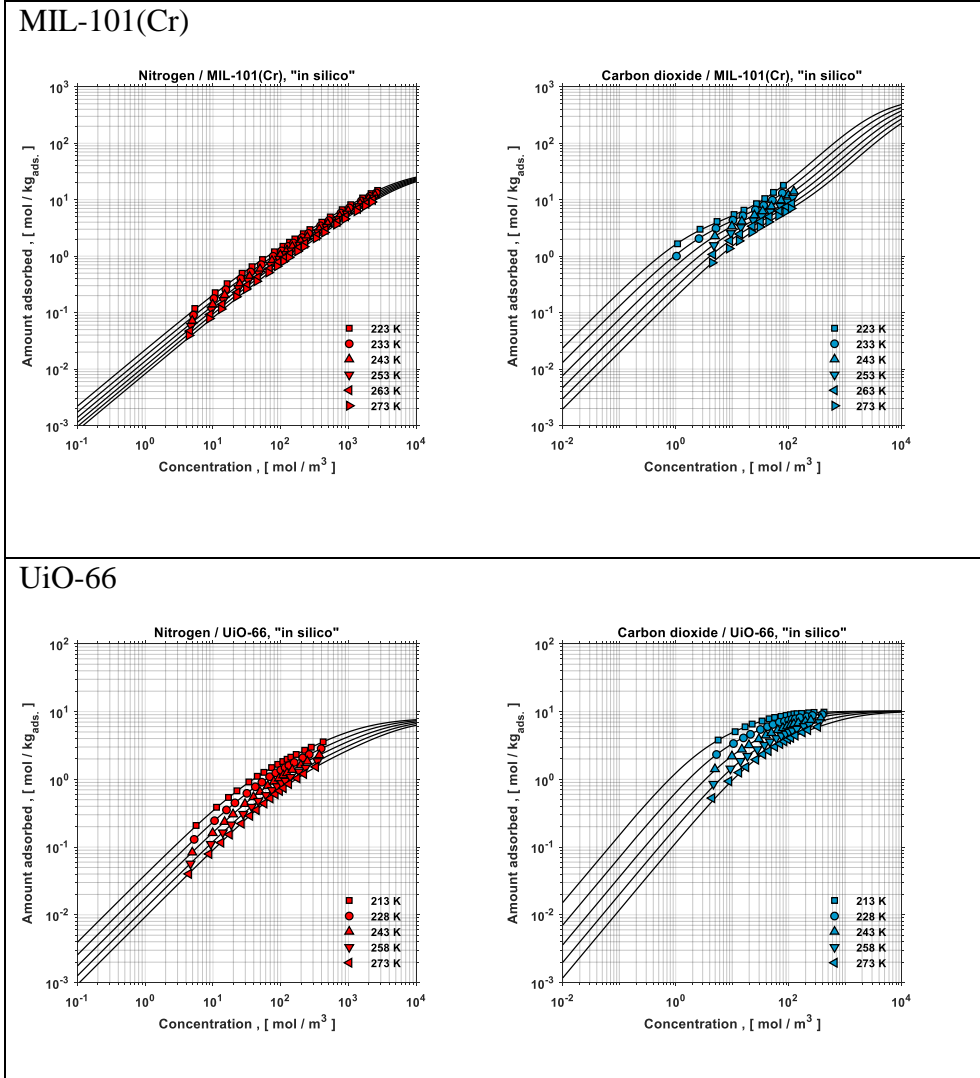
MIL-101(Cr)

UiO-66

Figure A-1. In-silico single-component equilibrium data for nitrogen and carbon dioxide adsorbed by MOFs MIL-101(Cr) & UiO-66.

Table A-9. Parameter values for adsorption equilibrium equations

Nitrogen							
	q_{11}^{sat}	q_{12}^{sat}	b_{110}	b_{120}	B_{11}	B_{12}	Isoteric heat, $\Delta H_{ads.,i}$
MIL-101(Cr)	33.7	0.98	1.2e-5	6.7e-6	672.6	1702	-11867
UiO-66	1.71	6.421	2.8e-5	1.4e-6	1390	1431	-10102
Zeolite 13X	5.84	0.0	2.5e-6	0.0	1900.4	0.0	-17863
Carbon dioxide							
	q_{21}^{sat}	q_{22}^{sat}	b_{210}	b_{220}	B_{21}	B_{22}	Isoteric heat, $\Delta H_{ads.,i}$
MIL-101(Cr)	660.8	4.033	2.9e-8	3.7e-7	2036	3173	-27298
UiO-66	5.7	4.5	2.1e-8	3.1e-6	3057	2445	-23052
Zeolite 13X	3.09	2.54	8.65e-7	2.63e-8	4407.2	4292.8	-38692

The partial differential equations (PDEs) with corresponding BCs and ICs are solved by applying a Method-Of-Lines (MOL) approach[19]. Application of a finite-volume (FVM) discretization along the spatial coordinate, with the flux-limiter function recommended by Koren[20] to avoid spurious oscillations, yields an ordinary differential equation (ODE) system to be integrated in time—see among others, Rubiera Landa et al.[16] and references cited therein. The variable adaptive-step, multiple-stepping time integration scheme of Gear[21] is applied to obtain the solutions to this ODE system. All calculations were performed with the problem-solving environment MATLAB[22] on a PC desktop with Intel Xeon® CPU running at 3.07 GHz and 24 GB RAM.

Table A-10. Simulation parameters.

Parameter	Symbol	Value	Units
Molar heat capacity (gas phase)	$\hat{C}_g$	30.5	J/mol·K
Molar heat capacity (adsorbed phase)	$\hat{C}_{ads.}$	30.5	J/mol·K
Heat capacity (MOF)	C_{MOF}	600 (MIL-101(Cr), UiO-66); 1000 (zeolite 13X)	J/kg·K
Heat capacity (polymer)	$C_{poly.}$	1465	J/kg·K
Axial dispersion coefficient	$D_{ax,i}$	0.00075	m²/s
Compression efficiency	$\eta_{compr.}$	0.7	-
Evacuation efficiency	$\eta_{evac.}$	0.3	-
Fiber porosity	ϵ_f	0.65	-
Packing fraction of fiber bed	ϕ_p	0.69	-
Ratio of gas heat capacities	γ	1.4	-
Gas heat conductivity	k_g	2.5e-2	W/m·K
Polymer heat conductivity	$k_{poly.}$	1.9e-1	W/m·K
Valve coefficient	k_V	2.5e-5	m·g$^{1/2}$/s·Pa·mol$^{1/2}$
Bed length	L	1.0	m
Molecular weight (N₂)	M_{N_2}	28.0	g/mol
Molecular weight (CO₂)	M_{CO_2}	44.0	g/mol
Gas viscosity	μ_g	1.5e-5	Pa·s
Ideal gas constant	$\Re$	8.3144	J/mol·K
Single fiber radius	r_f	25.0e-5	m
Free-surface radius	r_{fs}	30.0e-5	m
Density (MOF)	ρ_{MOF}	1100 (MIL-101(Cr)); 1210 (UiO-66); 1130 (zeolite 13X)	kg/m³
Density (polymer)	$\rho_{poly.}$	1180	kg/m³
Lennard-Jones collision diameter (N₂)	$\sigma_{N_2}^{LJ}$	3.7	Å
Lennard-Jones collision diameter (CO₂)	$\sigma_{CO_2}^{LJ}$	3.8	Å
Lennard-Jones collision diameter (CO₂/N₂ pair)	σ_{12}^{LJ}	1.5	Å
Temperature of operation	$T_{op.}$	243.15	K
Blow-down gas velocity	u_{Bd}	0.1	m/s
Evacuation gas velocity	u_{Ev}	1.5	m/s
Single fiber volume	v_f	2.0e-7	m³
Free-surface volume	v_{fs}	8.6e-8	m³
Collision integral value, Lennard-Jones (LJ)	Ω^{LJ}	1.3	-
Weight fraction of polymer in fiber composite	$\omega_{poly.}$	0.3	-

Additionally, we parametrized the smooth-interface model that represents the phase-change in the fiber composite with the values listed in Table A-11.

Table A-11. Parameterization of smooth-interface model for PCM phase-transitions

Parameter	Symbol	Value	Units
PCM heat capacity (liquid)	$C_{PCM,l}$	2140	J/kg·K
PCM heat capacity (solid)	$C_{PCM,s}$	2900	J/kg·K
PCM heat of transition	$\Delta H_{fus.}$	150.0e3	J/kg
PCM heat conductivity (liquid)	$k_{PCM,l}$	0.15	W/m·K
PCM heat conductivity (solid)	$k_{PCM,s}$	0.17	W/m·K
PCM density (liquid)	$\rho_{PCM,l}$	760	kg/m^3
PCM density (solid)	$\rho_{PCM,s}$	880	kg/m^3
Smoothing parameter	$\varsigma_{tr.}$	1.5	-
Temperature of transition	$T_{fus.}$	243.15	K

We treat the VPSA-cycle simulation as a black-box and apply the multi-objective optimization algorithm 'Surrogate Optimization of Computationally Expensive Multiobjective Problems (SOCEMO)', developed by Müller[23] and implemented in MATLAB[22]. This multi-objective optimizer has been designed specifically to address expensive-to-evaluate black-box functions, allowing us to compute Pareto frontiers efficiently, at a fraction of the computational cost required with other commonly applied genetic algorithms[18]. We compute Pareto frontiers for recovery vs. purity for each of the adsorbents considered, i.e., MIL-101(Cr), UiO-66, and zeolite 13X. The values of the bounds for each decision variable considered in the optimization runs are listed in Table A-12. Parameters specific to the SOCEMO optimizer are given in Table A-13

Table A-12. Decision variables and corresponding bounds

Decision Variable	Symbol	Lower Bound	Upper Bound	Units
Adsorption pressure	p_{high}	12.0	20.0	atm
Gas velocity of feed	u_{feed}	0.10	1.0	m/s
Adsorption step time	t_{Ad}	15.0	120.0	s
Evacuation pressure	p_{Ev}	0.10	0.35	atm
MOF weight fraction in fiber	ω_{MOF}	0.15	0.40	-

Table A-13.SOCEMO optimizer configuration parameters

Optimizer Parameters	Values
Number of decision variables	5
Seeding	'random'
Function evaluation budget	150
Function tolerance	1.0e-3

A.3 Pareto Frontier Data

The following section gives all data related to the two sets of Pareto optimizations run for the thermally-managed fiber sorbents. Figure A-2 and Table A-14 to Table A-19 show the results for the 14% CO_2, 86% N_2 feed first used to confirm the need for the downstream liquefaction. 13X performance gets worse with decreasing temperature, indicating it may not be appropriate for use in sub-ambient conditions. Figure A-3, and Table A-20 and Table A-21 show the complete results for the optimization run for the 17% CO_2, 83% N_2 feed used for the analysis in Chapter 4 of the main text.
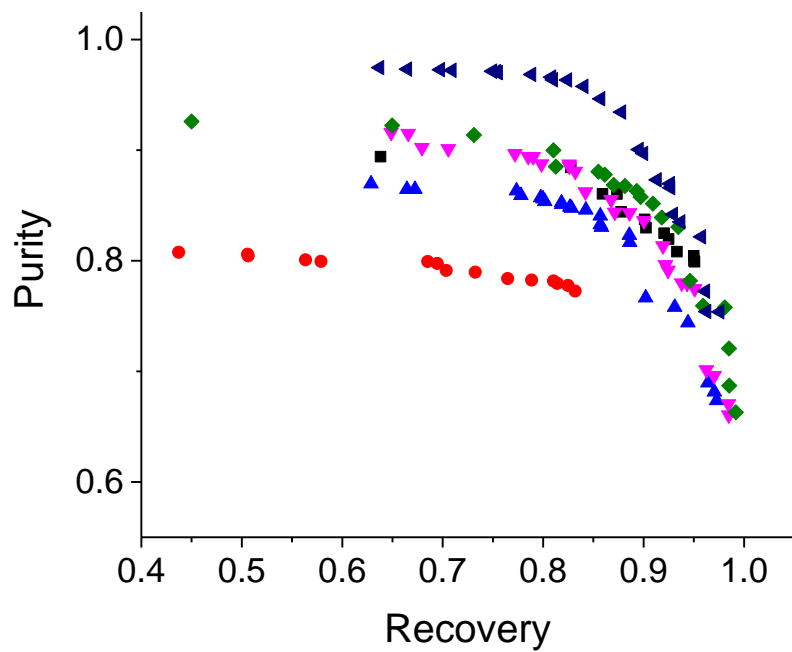
Figure A-2. Pareto frontier of Purity vs Recovery for a variety of thermally managed fiber sorbents at multiple temperatures for a feed of 14% CO_2, 86% N_2. (black) 13X at 298K, (red) 13X at 273K, (blue) UiO-66 at 273K (pink) UiO-66 at 243K, (green) MIL-101(Cr) at 273K, (navy) MIL-101(Cr) at 243K.

Table A-14. Pareto conditions for 13X fiber sorbents at 298 K for a feed of 14% CO$_2$, 86% N$_2$.

Recovery	()	0.951	0.950	0.950	0.933	0.925	0.920	0.902	0.901	0.878	0.874	0.859	0.827	0.638
Purity	()	0.799	0.800	0.804	0.808	0.820	0.825	0.830	0.837	0.844	0.860	0.860	0.884	0.894
Productivity	(mol kg^{-1} sec^{-1})	0.0103	0.0104	0.0107	0.0111	0.0113	0.0111	0.0112	0.0117	0.0118	0.0123	0.0125	0.0133	0.0124
Cycle Time	(sec)	76.3	77.1	76.1	75.4	77.9	78.8	78.1	77.9	78.8	78.9	77.0	81.9	89.7
Pressure	(bar)	12.7	12.4	12.2	12.7	12.3	12.2	12.2	12.2	12.2	16.8	17.1	20.3	20.3
Vacuum	(bar)	0.101	0.102	0.102	0.101	0.102	0.102	0.102	0.102	0.102	0.101	0.101	0.101	0.101
MOF Fraction	(%)	40.0	39.2	39.1	38.0	38.1	39.2	39.1	39.1	39.1	40.0	40.0	40.0	40.0
µPCM Fraction	(%)	35.0	35.8	35.9	37.0	36.9	35.8	35.9	35.9	35.9	35.0	35.0	35.0	35.0
Polymer Fraction	(%)	25	25	25	25	25	25	25	25	25	25	25	25	25

Table A-15. Pareto conditions for 13X fiber sorbents at 273 K for a feed of 14% CO₂, 86% N₂.

Recovery ()	0.832	0.825	0.814	0.810	0.789	0.765	0.732	0.703	0.695	0.685	0.579	0.564	0.506	0.506
Purity ()	0.773	0.778	0.780	0.782	0.782	0.784	0.790	0.791	0.798	0.799	0.799	0.801	0.804	0.806
Productivity (mol kg⁻¹ sec⁻¹)	0.0094	0.0098	0.0094	0.0098	0.0099	0.0098	0.0100	0.0101	0.0103	0.0101	0.0102	0.0100	0.0101	0.0101
Cycle Time (sec)	77.0	75.4	79.0	76.9	76.1	76.9	76.8	76.4	77.6	79.9	77.6	79.6	80.8	81.2
Pressure (bar)	12.2	12.2	12.2	12.2	12.6	13.4	12.2	12.2	12.4	12.3	13.0	13.4	12.3	12.4
Vacuum (bar)	0.101	0.101	0.101	0.101	0.101	0.101	0.101	0.101	0.101	0.101	0.101	0.101	0.101	0.101
MOF Fraction (%)	40.0	40.0	40.0	40.0	40.0	40.0	40.0	40.0	40.0	40.0	40.0	40.0	40.0	40.0
µPCM Fraction (%)	35.0	35.0	35.0	35.0	35.0	35.0	35.0	35.0	35.0	35.0	35.0	35.0	35.0	35.0
Polymer Fraction (%)	25	25	25	25	25	25	25	25	25	25	25	25	25	25

Table A-16. Pareto conditions for MIL-101(Cr) fiber sorbents at 273 K for a feed of 14% CO_2, 86% N_2.

Recovery	O	0.992	0.985	0.985	0.981	0.959	0.946	0.935	0.918	0.909	0.897	0.893	0.881
Purity	O	0.663	0.687	0.721	0.758	0.759	0.782	0.831	0.839	0.852	0.858	0.863	0.868
Productivity	(mol kg⁻¹ sec⁻¹)	0.0099	0.0113	0.0126	0.0141	0.0136	0.0148	0.0163	0.0165	0.0170	0.0179	0.0183	0.0186
Cycle Time	(sec)	98.4	95.1	93.2	93.1	93.8	94.6	98.3	99.6	102.2	102.8	99.9	98.6
Pressure	(bar)	12.2	12.6	13.0	13.6	13.6	13.7	14.4	14.4	13.6	13.5	14.2	14.5
Vacuum	(bar)	0.101	0.102	0.112	0.117	0.121	0.115	0.122	0.122	0.121	0.117	0.121	0.127
MOF Fraction	(%)	35.7	33.6	33.2	32.8	34.6	33.2	36.0	35.1	34.6	32.8	34.2	34.5
µPCM Fraction	(%)	39.3	41.4	41.8	42.2	40.4	41.8	39.0	39.9	40.4	42.2	40.8	40.5
Polymer Fraction	(%)	25	25	25	25	25	25	25	25	25	25	25	25

Recovery	O	0.870	0.861	0.855	0.813	0.810	0.731	0.650	0.450	0.384
Purity	O	0.869	0.878	0.881	0.885	0.900	0.914	0.922	0.926	0.928
Productivity	(mol kg⁻¹ sec⁻¹)	0.0178	0.0181	0.0188	0.0187	0.0203	0.0178	0.0218	0.0196	0.0195
Cycle Time	(sec)	105.1	106.7	105.8	102.3	103.6	129.5	108.1	121.1	122.6
Pressure	(bar)	13.6	13.6	13.6	14.6	14.0	12.6	16.6	15.5	15.8
Vacuum	(bar)	0.112	0.112	0.112	0.127	0.134	0.105	0.137	0.111	0.108
MOF Fraction	(%)	34	34	33	34	33	34	30	33	33
µPCM Fraction	(%)	41	41	42	41	42	41	45	42	42
Polymer Fraction	(%)	25	25	25	25	25	25	25	25	25

Table A-17. Pareto conditions for MIL-101(Cr) fiber sorbents at 243 K for a feed of 14% CO_2, 86% N_2.

Recovery	O	0.991	0.976	0.963	0.962	0.957	0.937	0.930	0.927	0.926	0.913	0.900	0.895
Purity	O	0.671	0.754	0.754	0.772	0.822	0.835	0.842	0.866	0.870	0.873	0.897	0.901
Productivity		0.0119	0.0149	0.0147	0.0156	0.0181	0.0184	0.0177	0.0200	0.0189	0.0204	0.0202	0.0203
Cycle Time (sec)		98.4	106.4	103.8	105.2	111.0	112.0	117.3	117.5	122.4	118.0	127.6	128.0
Pressure (bar)		13.0	13.0	13.0	13.0	13.0	13.2	12.4	13.0	12.4	13.2	12.4	12.4
Vacuum (bar)		0.101	0.101	0.101	0.101	0.101	0.101	0.106	0.101	0.113	0.101	0.113	0.113
MOF Fraction (%)		35.9	35.9	35.9	35.4	35.4	35.4	37.3	35.4	37.6	35.4	37.6	37.6
μPCM Fraction (%)		39.1	39.1	39.1	39.6	39.6	39.6	37.7	39.6	37.4	39.6	37.4	37.4
Polymer Fraction (%)		25	25	25	25	25	25	25	25	25	25	25	25

Recovery	O	0.857	0.840	0.824	0.810	0.808	0.788	0.755	0.753	0.749	0.709	0.698	0.665
Purity	O	0.946	0.958	0.963	0.964	0.966	0.968	0.970	0.971	0.971	0.972	0.973	0.973
Productivity (mol kg⁻¹ sec⁻¹)		0.0285	0.0296	0.0300	0.0300	0.0299	0.0294	0.0282	0.0289	0.0289	0.0280	0.0285	0.0301
Cycle Time (sec)		127.6	131.9	135.4	135.1	138.1	141.0	146.2	146.1	146.4	149.2	148.8	140.9
Pressure (bar)		14.5	14.8	14.9	14.8	14.8	14.9	14.8	14.8	14.8	14.8	14.8	15.4
Vacuum (bar)		0.108	0.106	0.103	0.103	0.103	0.103	0.103	0.103	0.103	0.103	0.103	0.110
MOF Fraction (%)		32.0	31.5	31.2	30.6	31.2	31.2	32.0	31.2	31.2	32.1	31.2	30.1
μPCM Fraction (%)		43.0	43.5	43.8	44.4	43.8	43.8	43.0	43.8	43.8	42.9	43.8	44.9
Polymer Fraction (%)		25	25	25	25	25	25	25	25	25	25	25	25

Table A-18. Pareto conditions for UiO-66 fiber sorbents at 273 K for a feed of 14% CO$_2$, 86% N$_2$.

Recovery (O)	0.973	0.970	0.964	0.944	0.931	0.902	0.886	0.886	0.858	0.857	0.857	0.843
Purity (O)	0.674	0.681	0.690	0.744	0.758	0.766	0.817	0.823	0.830	0.833	0.841	0.846
Productivity (mol kg⁻¹ sec⁻¹)	0.0090	0.0095	0.0097	0.0113	0.0118	0.0118	0.0135	0.0138	0.0142	0.0145	0.0146	0.0149
Cycle Time (sec)	91.1	90.2	89.9	89.9	91.2	93.4	95.4	95.2	93.5	92.4	94.5	94.5
Pressure (bar)	12.2	12.2	12.6	14.6	16.6	15.6	16.2	16.6	18.0	18.1	18.0	18.1
Vacuum (bar)	0.120	0.116	0.116	0.116	0.102	0.102	0.102	0.102	0.103	0.106	0.102	0.102
MOF Fraction (%)	40.0	38.7	38.7	39.7	40.0	40.0	39.3	39.3	39.9	39.3	39.9	40.0
µPCM Fraction (%)	35.0	36.3	36.3	35.3	35.0	35.0	35.7	35.7	35.1	35.7	35.1	35.0
Polymer Fraction (%)	25	25	25	25	25	25	25	25	25	25	25	25

Recovery (O)	0.828	0.827	0.819	0.818	0.802	0.800	0.798	0.778	0.773	0.672	0.664	0.629
Purity (O)	0.848	0.848	0.851	0.852	0.854	0.856	0.857	0.859	0.863	0.865	0.865	0.870
Productivity (mol kg⁻¹ sec⁻¹)	0.0151	0.0149	0.0147	0.0148	0.0149	0.0153	0.0155	0.0150	0.0151	0.0150	0.0152	0.0154
Cycle Time (sec)	93.4	95.1	96.6	96.1	96.5	95.1	94.3	97.6	98.4	98.2	98.0	98.6
Pressure (bar)	18.0	18.2	18.1	18.1	18.1	18.0	18.1	18.2	18.2	17.6	17.6	18.0
Vacuum (bar)	0.102	0.101	0.102	0.106	0.102	0.102	0.102	0.101	0.101	0.109	0.109	0.109
MOF Fraction (%)	39.9	39.6	39.9	39.9	40.0	39.9	40.0	39.6	40.0	39.5	39.9	38.7
µPCM Fraction (%)	35.1	35.4	35.1	35.1	35.0	35.1	35.0	35.4	35.0	35.5	36.3	36.3
Polymer Fraction (%)	25	25	25	25	25	25	25	25	25	25	25	25

Table A-19. Pareto conditions for UiO-66 fiber sorbents at 243 K for a feed of 14% CO$_2$, 86% N$_2$.

Recovery	O	0.985	0.984	0.970	0.963	0.951	0.943	0.938	0.924	0.922	0.919	0.900	0.886	0.871
Purity	O	0.661	0.671	0.696	0.701	0.775	0.779	0.780	0.791	0.796	0.813	0.836	0.843	0.844
Productivity (mol kg⁻¹ sec⁻¹)		0.0130	0.0137	0.0118	0.0118	0.0150	0.0150	0.0138	0.0142	0.0144	0.0161	0.0170	0.0171	0.0169
Cycle Time (sec)		92.1	90.5	105.1	105.6	100.7	101.2	109.3	110.7	109.0	104.1	106.4	106.6	105.6
Pressure (bar)		12.3	12.7	12.3	12.3	14.5	14.3	12.2	12.2	12.2	14.4	14.6	14.9	14.9
Vacuum (bar)		0.101	0.101	0.101	0.101	0.101	0.101	0.101	0.101	0.103	0.101	0.101	0.102	0.107
MOF Fraction (%)		32.2	32.2	40.0	40.0	38.9	39.0	40.0	39.6	39.6	39.0	39.0	39.0	39.0
µPCM Fraction (%)		42.8	42.8	35.0	35.0	36.1	36.0	35.0	35.4	35.4	36.0	36.0	36.0	36.0
Polymer Fraction (%)		25	25	25	25	25	25	25	25	25	25	25	25	25

Recovery	O	0.868	0.842	0.832	0.826	0.826	0.798	0.790	0.785	0.772	0.706	0.679	0.666	0.649
Purity	O	0.855	0.862	0.881	0.885	0.887	0.888	0.894	0.894	0.897	0.901	0.902	0.915	0.916
Productivity (mol kg⁻¹ sec⁻¹)		0.0171	0.0199	0.0178	0.0179	0.0184	0.0176	0.0179	0.0181	0.0184	0.0184	0.0181	0.0186	0.0186
Cycle Time (sec)		109.1	105.9	116.2	117.4	116.6	118.1	120.6	119.5	120.0	119.2	121.1	125.6	127.0
Pressure (bar)		14.9	14.1	14.8	14.8	14.9	14.8	14.6	14.6	14.7	14.8	14.8	18.1	18.1
Vacuum (bar)		0.102	0.103	0.102	0.102	0.102	0.102	0.105	0.105	0.105	0.106	0.107	0.102	0.102
MOF Fraction (%)		39.5	33.6	39.8	40.0	39.4	39.8	40.0	39.8	38.9	39.8	39.8	39.9	39.9
µPCM Fraction (%)		35.5	41.4	35.2	35.0	35.6	35.2	35.0	35.2	36.1	35.2	35.2	35.1	35.1
Polymer Fraction (%)		25	25	25	25	25	25	25	25	25	25	25	25	25
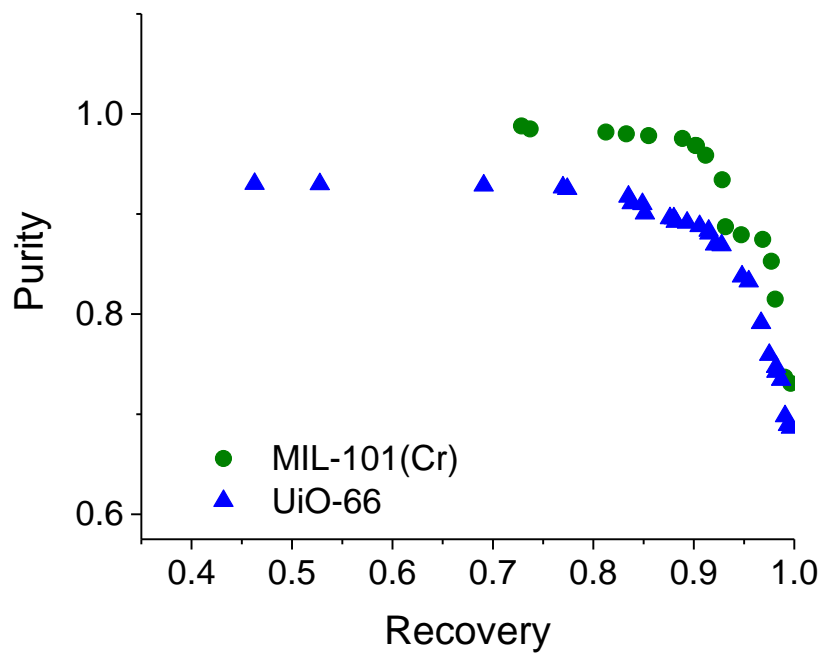
Figure A-3. Pareto frontier of Purity vs Recovery for 17% CO_2, 83% N_2 at 243 K operating temperature. (blue triangles) UiO-66, (green circles) MIL-101(Cr).

Table A-20. Pareto conditions for MIL-101(Cr) fiber sorbents at 243 K for a feed of 17% CO_2, 83% N_2.

Recovery ()	0.996	0.990	0.981	0.977	0.969	0.947	0.932	0.928	0.912	0.903	0.902	0.889	0.855	0.833
Purity ()	0.731	0.737	0.815	0.853	0.875	0.879	0.887	0.934	0.959	0.968	0.969	0.975	0.978	0.980
Productivity (mol kg⁻¹ sec⁻¹)	0.0167	0.0170	0.0204	0.0252	0.0274	0.0271	0.0252	0.0327	0.0352	0.0369	0.0376	0.0382	0.0380	0.0379
Cycle Time (sec)	94.6	94.6	98.3	96.4	97.6	96.8	104.3	105.6	112.3	114.2	113.2	114.6	114.6	114.0
Pressure (bar)	12.5	12.2	18.2	20.2	20.2	20.0	18.2	20.2	20.2	20.2	20.2	20.2	17.9	17.9
Vacuum (bar)	0.103	0.103	0.101	0.101	0.101	0.103	0.101	0.103	0.101	0.102	0.102	0.103	0.109	0.119
MOF Fraction (%)	31.1	30.9	34.7	32.4	32.2	32.7	34.7	32.4	32.4	31.3	31.1	31.1	31.6	31.6
µPCM Fraction (%)	43.9	44.1	40.3	42.6	42.8	42.3	40.3	42.6	42.6	43.7	43.9	43.9	43.4	43.4
Polymer Fraction (%)	25	25	25	25	25	25	25	25	25	25	25	25	25	25

Table A-21. Pareto conditions for UiO-66 fiber sorbents at 243 K for a feed of 17% CO_2, 83% N_2.

Recovery (0)	Purity (0)	Productivity (mol kg⁻¹ sec⁻¹)	Cycle Time (sec)	Pressure (bar)	Vacuum (bar)	MOF Fraction (%)	µPCM Fraction (%)	Polymer Fraction (%)
0.997	0.687	0.0124	97.5	12.6	0.105	38.6	36.4	25
0.994	0.689	0.0128	97.3	12.7	0.101	37.7	37.3	25
0.991	0.698	0.0127	95.0	12.5	0.112	38.2	36.8	25
0.987	0.734	0.0140	99.3	14.0	0.102	40.0	35.0	25
0.982	0.742	0.0143	96.4	15.1	0.101	40.0	35.0	25
0.982	0.747	0.0146	94.1	15.1	0.116	40.0	35.0	25
0.975	0.759	0.0149	93.4	15.4	0.116	37.7	37.3	25
0.967	0.791	0.0160	101.4	12.7	0.101	40.0	35.0	25
0.955	0.833	0.0172	105.3	14.0	0.102	40.0	35.0	25
0.948	0.838	0.0175	104.5	14.0	0.102	40.0	35.0	25
0.928	0.869	0.0187	108.0	14.0	0.102	40.0	35.0	25
0.921	0.870	0.0189	108.9	12.7	0.101	36.8	38.2	25
0.915	0.881	0.0192	110.7	13.9	0.101	40.0	35.0	25
0.915	0.883	0.0192	110.5	14.1	0.101	40.0	35.0	25

Recovery (0)	Purity (0)	Productivity (mol kg⁻¹ sec⁻¹)	Cycle Time (sec)	Pressure (bar)	Vacuum (bar)	MOF Fraction (%)	µPCM Fraction (%)	Polymer Fraction (%)
0.906	0.888	0.0192	111.5	13.9	0.101	40.0	35.0	25
0.893	0.891	0.0194	111.2	14.1	0.101	40.0	35.0	25
0.882	0.892	0.0197	110.8	13.6	0.103	38.4	36.6	25
0.880	0.896	0.0202	110.7	13.6	0.103	37.5	37.5	25
0.876	0.896	0.0206	109.5	13.8	0.104	38.0	37.0	25
0.851	0.901	0.0211	109.9	12.7	0.101	37.1	37.9	25
0.849	0.910	0.0209	113.1	13.8	0.104	38.0	37.0	25
0.838	0.911	0.0211	112.2	13.8	0.104	37.5	37.5	25
0.835	0.917	0.0198	120.1	13.8	0.103	39.9	35.1	25
0.774	0.925	0.0194	125.3	13.8	0.103	39.9	35.1	25
0.770	0.927	0.0195	126.7	13.9	0.102	40.0	35.0	25
0.691	0.929	0.0194	127.5	14.1	0.102	39.9	35.1	25
0.528	0.930	0.0186	132.8	14.3	0.102	40.0	35.0	25
0.463	0.930	0.0178	138.6	14.3	0.102	40.0	35.0	25

A.4 References

1.   James RZ, Alexander; Keairns, Dale; Turner, Marc; Woods, Mark; Kuehn, Norma. Cost and Performance Baseline for Fossil Energy Plants Volume 1: Bitumimous Coal and Natural Gas to Electricity: NETL;2019.

2.   Düren T, Bae Y-S, Snurr RQ. Using molecular simulation to characterise metal–organic frameworks for adsorption applications. *Chemical Society Reviews.* 2009;38(5):1237-1247.

3.   Coudert F-X, Fuchs AH. Computational characterization and prediction of metal–organic framework properties. *Coordination Chemistry Reviews.* 2016/01/15/ 2016;307:211-236.

4.   Li J-R, Ma Y, McCarthy MC, et al. Carbon dioxide capture-related gas adsorption and separation in metal-organic frameworks. *Coordination Chemistry Reviews.* 2011/08/01/ 2011;255(15):1791-1823.

5.   Dubbeldam D, Calero S, Ellis DE, Snurr RQ. RASPA: molecular simulation software for adsorption and diffusion in flexible nanoporous materials. *Molecular Simulation.* 2016/01/22 2016;42(2):81-101.

6.   Dubbeldam D, Torres-Knoop A, Walton KS. On the inner workings of Monte Carlo codes. *Molecular Simulation.* 2013/12/01 2013;39(14-15):1253-1292.

7.   Rappe AK, Casewit CJ, Colwell KS, Goddard WA, Skiff WM. UFF, a full periodic table force field for molecular mechanics and molecular dynamics simulations. *Journal of the American Chemical Society.* 1992/12/01 1992;114(25):10024-10035.

8.   Martin MG, Siepmann JI. Transferable Potentials for Phase Equilibria. 1. United-Atom Description of n-Alkanes. *The Journal of Physical Chemistry B.* 1998/04/01 1998;102(14):2569-2577.

9.   Allen MPT, D.J. *Computer Simulation of Liquids*. New York: Oxford University Press; 1987.

10.   Wells BA, Chaffee AL. Ewald Summation for Molecular Simulations. *Journal of Chemical Theory and Computation.* 2015/08/11 2015;11(8):3684-3695.

11.   Manz TA, Sholl DS. Chemically Meaningful Atomic Charges That Reproduce the Electrostatic Potential in Periodic and Nonperiodic Materials. *Journal of Chemical Theory and Computation.* 2010/08/10 2010;6(8):2455-2468.

12.   Manz TA, Sholl DS. Improved Atoms-in-Molecule Charge Partitioning Functional for Simultaneously Reproducing the Electrostatic Potential and

Chemical States in Periodic and Nonperiodic Materials. *Journal of Chemical Theory and Computation.* 2012/08/14 2012;8(8):2844-2867.

13.   Watanabe T, Manz TA, Sholl DS. Accurate Treatment of Electrostatics during Molecular Adsorption in Nanoporous Crystals without Assigning Point Charges to Framework Atoms. *The Journal of Physical Chemistry C.* 2011/03/24 2011;115(11):4824-4836.

14.   Rubiera Landa HOLRPK, Y; Realff, M.j. Theoretical Investigation of Vacuum pressure-swing adsorptoin processes applying thermally modulated fiber composite adsorbents.

15.   Myers AL, Prausnitz JM. Thermodynamics of mixed-gas adsorption. *AIChE Journal.* 1965;11(1):121-127.

16.   Landa HOR, Flockerzi D, Seidel-Morgenstern A. A method for efficiently solving the IAST equations with an application to adsorber dynamics. *AIChE Journal.* 2013;59(4):1263-1277.

17.   O'Brien JA, Myers AL. A comprehensive technique for equilibrium calculations in adsorbed mixtures: the generalized FastIAS method. *Ind. Eng. Chem. Res.* 1988/11/01 1988;27(11):2085-2092.

18.   Haghpanah R, Majumder A, Nilam R, et al. Multiobjective Optimization of a Four-Step Adsorption Process for Postcombustion CO_2 Capture Via Finite Volume Simulation. *Ind. Eng. Chem. Res.* 2013/03/20 2013;52(11):4249-4265.

19.   Schiesser WE. *The Numerical Method of LInes: Integration of Partial Differential Equations*: Academic Press; 1991.

20.   Vreugdenhil CBK, B. *Numerical Methods for Advection Diffusion Problems: Notes on Numerical Fluid Mechnaics*. Berlin: Vieweg; 1993.

21.   Gear CW. *Numerical INitial Value Problems in Ordinary Differential Equations*: Prentice Hall PTR; 1971.

22.   *MATLAB* [computer program]. Version 9.6.0. (R2019a). Natick, MA: The MathWorks Inc.; 2019.

23.   Müller J. SOCEMO: Surrogate Optimization of Computationally Expensive Multiobjective Problems. *INFORMS Journal on Computing.* 2017;29(4):581-596.